Cyclic Nucleotide Regulation of Excitation-Contraction Coupling in Cardiac Myocytes

by
Claire Y. Zhao

A dissertation submitted to Johns Hopkins University in conformity with the requirements for the degree of Doctor of Philosophy

Baltimore, Maryland

April, 2016

ABSTRACT

The balanced signaling between the two cyclic nucleotides (cNs) cAMP and cGMP in the cN cross-talk signaling network plays a critical role in regulating cardiac contractility. In particular, the signaling network imposes both stimulatory and inhibitory regulatory actions on L-type calcium (Ca^{2+}) channel (LCC), which initiates Ca^{2+}-induced Ca^{2+} release (CICR) and excitation-contraction (EC) coupling. Many therapeutic agents have been developed to selectively inhibit or stimulate proteins in the aforementioned pathway, in the attempt to manage and treat heart failure (HF). Nonetheless, it has been challenging to obtain a comprehensive systems-level understanding of the signal transduction mechanisms of the cN cross-talk signaling network, in part because of the participation of multiple phosphodiesterases (PDEs) in the common tasks of cN degradation, the complex interactions between the signaling proteins, and the large number of tightly-coupled EC coupling-related phosphorylation targets of the network. Accordingly, this work developed multi-scale, biophysically-detailed, and experimentally-validated computational models to study the cN cross-talk signaling network and its regulation of LCC. By precisely defining and quantifying biochemical reactions involved, this work bridged causal gaps between the characteristics of individual molecular components and the collective responses of the signaling network and its regulation of electrophysiology. Through predictive modeling and integrative analysis, this work provide insights into cellular mechanisms that are difficult to elucidate with experimentation alone and serves as solid foundation towards data-driven and simulation-guided medicine.

Academic Advisor:

Dr. Raimond L. Winslow, Ph.D.
Raj and Neera Singh Professor, Department of Biomedical Engineering, Institute for Computational Medicine
Director, Institute for Computational Medicine, Johns Hopkins University Whiting School of Engineering and School of Medicine
Director, Center for Cardiovascular Bioinformatics and Modeling, Johns Hopkins University Whiting School of Engineering and School of Medicine

Thesis Committee (alphabetically by last names):

Dr. Gordon F. Tomaselli, M.D.
Michel Mirowski MD Professor, Division of Cardiology
Professor of Medicine
Chief, Division of Cardiology
Co-Director, Heart and Vascular Institute
Johns Hopkins University School of Medicine

Dr. Natalia A. Trayanova, Ph.D.
Murray B. Sachs Professor, Department of Biomedical Engineering, Institute for Computational Medicine
Johns Hopkins University School of Medicine

Dr. Raimond L. Winslow, Ph.D.
Professor, Department of Biomedical Engineering
Johns Hopkins University School of Medicine

ACKNOWLEGEMENTS

In order to give strength and substance to model predictions, a mathematical model should, in the most succinct of languages, integrate large amounts of information from various sources and capture the essence of biological phenomena in question. I have been fortunate to be able to discuss the various aspects of my research with many subject experts worldwide and to interact with many mentors. A special Acknowledgement Chapter is dedicated to them.

I would like to thank my PI, Dr. Raimond L. Winslow, for sharing his vision and excitement for the field of computational medicine and biology, and for providing instrumental insight and guidance through all stages of my research. I would also like to thank members of the Winslow Lab for their support. I would like to thank my thesis committee members, Drs. Gordon Tomaselli, Natalia Trayanova, and Raimond Winslow, for their feedback. I appreciate the Biomedical Engineering community at JHU and the university for providing a vibrant, productive, and enjoyable environment in which to live and work.

I am grateful to the Natural Sciences and Engineering Research Council (NSERC) of Canada for awarding me with four years of scholarship. I am thankful to my past education and experiences, which gave me the ability, confidence, and determination to succeed. I appreciate every one of the people and events that transformed me into a better individual. My special gratitude goes to my parents for standing by me through the many ups and downs of this transformation. This dissertation is dedicated to you.

Table of Contents

List of Tables

List of Figures

Chapter 1. Introduction

1.1. Heart failure

Millions of people worldwide are affected by Heart failure (HF) [1], a pervasive public health problem. In the United States alone, an estimated one in nine deaths is related to HF, with costs projected to more than double in about fifteen years, from 30.7 billion USD in 2012 to 69.7 billion USD in 2030. HF is a condition characterized by weakened and enlarged ventricles which leads to insufficient blood supply to the body's tissues [1]. Patients with HF develop symptoms gradually and are more prone to arrhythmia and sudden cardiac death [1]. At the cellular level of the cardiac myocytes, HF is characterized by impaired inotropic signaling, calcium mismanagement, and altered myofilament function [2, 3]. In order to fully comprehend cardiac changes causing HF, in this work, we investigate normal functions under healthy conditions, serving as a benchmark against which changes in disease can be elucidated.

1.2. Cardiac excitation-contraction coupling

Excitation-contraction (EC) coupling is the process by which electrical excitation leads to mechanical contraction of cardiac myocytes (Fig. 1.1). The membrane potential is the voltage difference between the inside and outside of the cell. Associated with each heartbeat, it is of a characteristic shape, known as the action potential (AP) [4]. At the beginning of each heartbeat, the cell is stimulated by an electrical signal from a

neighboring cell. As membrane potential rises from rest to a threshold, sodium (Na^+) channels are being activated. Upon further membrane depolarization due to influx of Na^+ current (I_{Na}), L-type calcium (Ca^{2+}) channels (LCCs) open, allowing Ca^{2+} to enter the cell. As this trigger Ca^{2+} binds to and prompts the opening of the Ryanodine Receptors (RyRs), Ca^{2+} from the sarcoplasmic reticulum (SR) Ca^{2+} store is being released into the cytoplasm of the cell. This process is commonly referred to as Ca^{2+}-induced Ca^{2+} release (CICR) [5]. The increased Ca^{2+} concentration ($[Ca^{2+}]$) in the cytosol allows Ca^{2+} to bind to troponin anchored to myofilaments, inducing a conformational change in troponin and initiating contraction through shortening of the myofilaments [5]. CICR is the dominant factor in explaining the link between excitation and contraction in heart muscle [6]. It is frequently accessed by a measure named EC coupling gain, usually estimated by the peak SR Ca^{2+} release flux divided by the peak flux of Ca^{2+} across the cell membrane [6]. It is voltage-dependent due to the reduction in driving force for the LCC and subsequent decrease in dyadic $[Ca^{2+}]$ as membrane potential increases [7].

Fig. 1.1. Overview of EC coupling and PKA and PKG regulation of LCC.

Ca^{2+} plays a key role in coordinating EC coupling, from entering the cell through the LCC, to triggering CICR, and finally initiating contraction of the myofilaments [6]. Among regulation of other proteins critical to EC coupling, the cyclic nucleotide (cN) cross-talk signaling network delivers both stimulatory (green arrow) and inhibitory (red arrow) regulatory actions on LCCs via PKA- and PKG-mediated phosphorylation. Figure adapted from Bers [5].

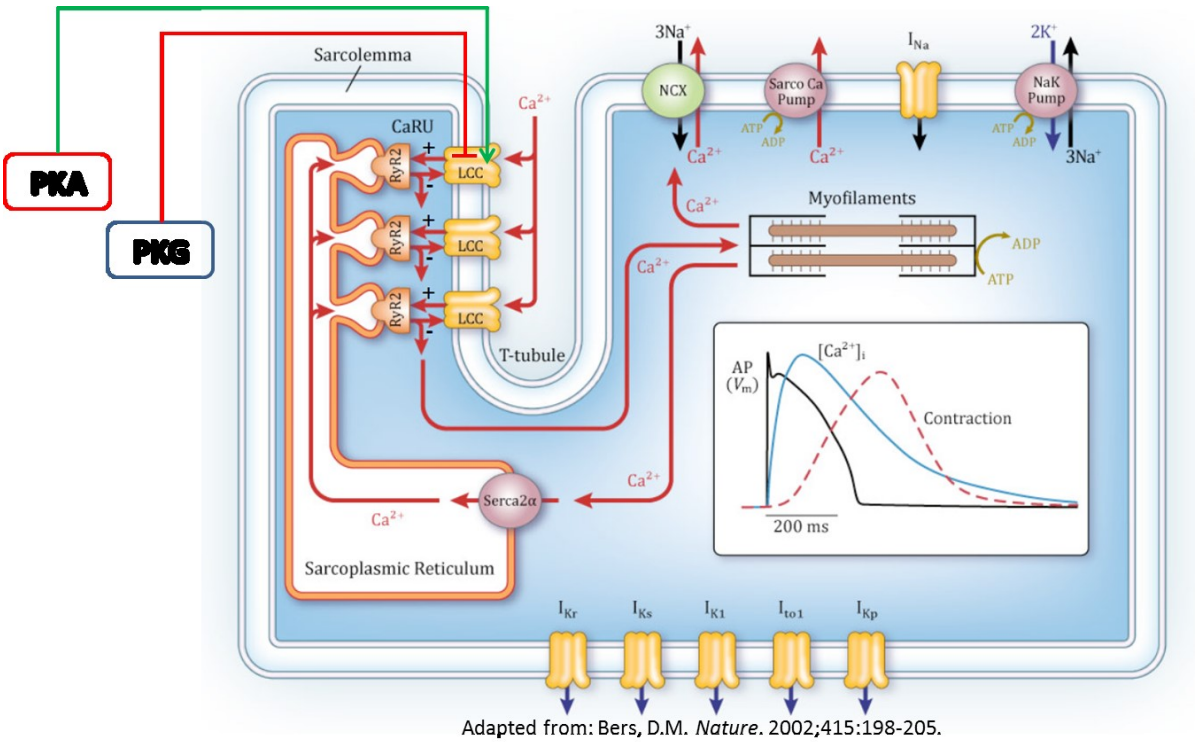

The activation of potassium (K^+) channels as I_{CaL} flows into the cell, generates an opposing outward K^+ current (I_K) that shapes the plateau phase of the AP [4]. As LCC gradually inactivates, I_K dominates over I_{CaL}, driving AP back to rest [4]. Cytosolic [Ca^{2+}] declines as Ca^{2+} is extruded from the cell primarily via Na^+/Ca^{2+} exchanger (NCX) or pumped back into the SR through the SR Ca^{2+} (SERCA) pump [4]. As Ca^{2+} declines, Ca^{2+} dissociates from the myofilaments and the cell begins to relax [5]. Via protein phosphorylation, PKA and PKG regulate a variety of proteins in the EC coupling process, including LCCs, phospholamban (PLB), and Troponin I (TnI) for both PKA [5] and PKG [2, 8, 9]. This dissertation focuses on Protein Kinase A (PKA) - and Protein Kinase G (PKG)-mediated regulation of the LCCs, which initiates the EC coupling process (Fig. 1.1).

1.3. Cyclic nucleotide cross-talk signaling network in cardiac myocytes

The cyclic nucleotides (cNs), cAMP (Cyclic Adenosine-3′, 5′-Monophosphate) and cGMP (Cyclic Guanosine-3′, 5′-Monophosphate), are intricately-regulated second messengers that regulate the response of cardiac myocyte to external and internal stimuli [10-12]. The information encoded in these second messengers are amplified many folds in the responses of downstream targets, such that cellular responses can change dramatically upon minute alternations to these signals [10-12]. The cN cross-talk signaling network regulates the dynamics of both cNs and is composed of the β-adrenergic pathway, NO/cGMP/PKG pathway, and mechanisms for cN hydrolysis that also form the basis for cross-talk between the two aforementioned pathways.

Stimulation of the β-adrenergic signaling pathway, which controls the synthesis of cAMP, enhances cardiac inotropy and lusitropy [5, 13]. On the contrary, activation of the Nitric Oxide (NO)/cGMP/PKG pathway, which control the production of cGMP, tends to attenuate cardiac contractility [8, 10, 14-16] and is also observed to exert antagonistic actions to β-adrenergic tone [17-20]. As a result, delicate balance between cAMP and cGMP signals is required for normal cardiac contraction [17, 18, 21-28]. The degradation of cNs are controlled by distinctively regulated phosphodiesterases (PDEs), which are PDEs 1, 2, 3, 4, and 5 within the cN cross-talk signaling network of cardiac myocytes [29-32]. The coordinated regulation of PDE activities by both cN signals bridge together the β-adrenergic and NO/cGMP/PKG pathways, forming pathway cross-talk. The cN

signals regulate the function of many downstream ion channels and exchangers involved in excitation-contraction (EC) coupling by activating their respective kinases, PKA and PKG, to phosphorylate these targets [2, 5, 33].

1.4. Cyclic nucleotide cross-talk signaling network and heart failure

Prominent remodeling of the components comprising the cN signaling network is observed in HF, including changes in expression levels and possible spatial re-organization of signaling proteins, that causes altered and/or untargeted cN signals and aberrant phosphorylation of target proteins [3, 34-37]. These remodeling disturbs the delicate balance between the cNs and may ultimately lead to cardiac dysfunction [3, 34-37]. For instance, ablation of specific PDE activities through pharmacological inhibition or gene depletion is observed to promote cardiac apoptosis [38], accelerates development of heart failure (HF) [39] and increases likelihood of cardiac arrhythmias [39, 40]. The importance of delicate regulation by distinct PDE families is also reflected by their isoform-specific alternations in cardiac diseases [3, 39, 41-43]. As examples, PDE2 upregulation in the failing heart is observed to attenuate β-adrenergic signaling [43], decreased PDE3 activity promotes cardiac myocyte apoptosis [41], and PDE4 downregulation is associated with arrhythmias in cardiac hypertrophy and HF [39]. Drugs that restore specific PDE activities [44], such as PDE3 activity in ischemic and dilated cardiomyopathies [45] and PDE1 and PDE4 activities in cardiac ischemia [46] have a cardio-protective effect. In addition, PDE5 inhibition is shown to exert cardio-protective

effects in various cardiac pathologies, such as HF, cardiac hypertrophy, and ventricular arrhythmias [9, 47-49]. In this work, we investigate normal signal transduction mehchanisms under healthy conditions, serving as benchmarks against which the impact of changes in cN cross-talk signaing in HF can be fully comprehended.

1.5. History of cyclic nucleotide and signaling research

The cAMP and cGMP signaling systems, together referred to as the cN signaling system, are among the earliest identified signal transduction systems [50]. In 1957, a series of research led to the discovery of cAMP as a factor that stimulates phosphorylase [51]. By 1958, its synthetic activity through adenylate cyclase (AC) and degrading activity through PDE had been described. On the other hand, the second messenger concept where extra-cellular hormones and neurotransmitters bind to cell-surface receptors and their signals are transduced into an intracellular messenger has not caught much attention until the early 1970s [52]. The development of accessible assays that provide meaningful measurement of cAMP in 1971 brought an explosion of activity and interest in characterizing the signal pathway that led to the discovery of G-proteins and PKA [52]. Among the various signaling systems capable of exerting positive inotropic effects in humans, the β-adrenergic signaling pathway is the most powerful by which heart rate and contractility are physiologically regulated and maintained [53].

The discovery of cGMP followed similar trajectory as that of cAMP [52]. Synthesized in 1960 [54], the biological importance of cGMP was identified in 1963 as a natural product in urine [55]. By 1969, the enzymes for the synthesis and degradation of

cGMP have also been discovered [56]. The search for a cGMP-dependent kinase similar to PKA soon followed the appreciation of cGMP as an intracellular second messenger [56]. In 1970, PKG is chromatographically separated from partially purified protein kinases that contained both PKA and PKG [57]. It was not until the 1980s the hormone that stimulated the synthesis of cGMP was discovered, first identified as endothelial-derived relaxant factor (EDRF) and later realized to be nitric oxide (NO) [58]. For the heart, research on the NO/cGMP/PKG pathway exploded following the discovery that cardiac myocytes constitutively expressed NO synthase (NOS), an enzyme that catalyzes NO synthesis, in the 1990s [59].

Investigation of the PDEs began with the discovery of cAMP and cGMP [58]. In 1958, the enzymatic activity of PDE has been discovered as the cellular activity for the hydrolysis of the 3′, 5′ phosphodiester bond of cAMP to yield 5′-AMP [60]. Shortly after its discovery, the molecular diversity of PDE was recognized as gel filtration and ion exchange chromatography of tissue extracts revealed multiple peaks of PDE activities [50]. The present-day nomenclature of PDEs are based on the genes of which they are products, their biochemical properties, regulation, and sensitivity to pharmacological agents [32]. PDEs are classified to Classes I, II, II, with mammalian PDEs belonging to Class I, which is now further organized into elevan structurally-related but functionally distinct PDE gene families, PDEs 1–11 [61]. The cytoplasm of cardiac myocytes primarily contains PDEs 1–5 [17, 62, 63].

The importance of research concerning cN and signal transduction mechanisms has been recognized by the award of several Nobel Prizes [64]:

1. 1971 — Earl W. Sutherland Jr, for his discoveries concerning the mechanisms of action of hormones through cAMP.
2. 1992 — Edmond H. Fischer and Edwin G. Krebs, for their discoveries concerning reversible protein phosphorylation as a biological regulatory mechanism.
3. 1994 — Alfred G. Gilman and Martin Rodbell, for their discovery of G proteins and the roles of these proteins in signal transduction in cells.
4. 1998 — Robert F. Furchgott, Louis J. Ignarro and Ferid Murad, for their discoveries concerning NO and cGMP as signaling molecules in the cardiovascular system.
5. 2000 — Arvid Carlsson, Paul Greengard and Eric R. Kandel, for their discoveries concerning signal transduction in the nervous system.
6. 2012 — Robert J. Lefkowitz and Brian K. Kobilka, for their studies of G-protein-coupled receptors.
7. 2013 — Martin Karplus, Michael Levitt and Arieh Warshel, for the development of multiscale models for complex chemical systems.

Today, it is established that PDEs are essential components of cN signaling [65]. New therapeutic agents are being developed on the basis of their ability to potently and selectively inhibit PDE isoenzymes [32]. On the other hand, the precise mechanisms of the cN signaling pathways in modulating tissue-specific intracellular signaling remains to be established [31, 32, 63, 65, 66]. As such, research into cN signal transduction continues to expand after over half a century of scientific investigation. The extensive knowledge of cN systems accumulated by past research enabled the work in this dissertation, which aims to reveal the interactions of signal components in the cN cross-talk network in cardiac myocytes.

Chapter 2. Interaction between Phosphodiesterases in the Regulation of the Cardiac β-Adrenergic Pathway

2.1. Abstract

In cardiac myocytes, the second messenger cAMP is synthesized within the β-adrenergic signaling pathway upon sympathetic activation. It activates Protein Kinase A (PKA) mediated phosphorylation of multiple target proteins that are functionally critical to cardiac contractility. The dynamics of cAMP are also controlled indirectly by cGMP-mediated regulation of phosphodiesterase isoenzymes (PDEs). The nature of the interactions between cGMP and the PDEs, as well as between PDE isoforms, and how these ultimately transduce the cGMP signal to regulate cAMP remains unclear. To better understand this, we have developed mechanistically detailed models of PDEs 1 – 4, the primary cAMP-hydrolyzing PDEs in cardiac myocytes, and integrated them into a model of the β-adrenergic signaling pathway. The PDE models are based on experimental studies performed on purified PDEs which have demonstrated that cAMP and cGMP bind competitively to the cyclic nucleotide (cN)-binding domains of PDEs 1, 2, and 3, while PDE4 regulation occurs via PKA-mediated phosphorylation. Individual PDE models reproduce experimentally measured cAMP hydrolysis rates with dose-dependent cGMP regulation. The fully integrated model replicates experimentally observed whole-cell cAMP activation-response relationships and temporal dynamics upon varying

degrees of β-adrenergic stimulation in cardiac myocytes. Simulations reveal that as a result of network interactions, reduction in the level of one PDE is partially compensated for by increased activation of others. PDE2 and PDE4 exert the strongest compensatory roles among all PDEs. In addition, PDE2 competes with other PDEs to bind and hydrolyze cAMP and is a strong regulator of PDE interactions. Finally, an increasing level of cGMP gradually out-competes cAMP for the catalytic sites of PDEs 1, 2, and 3, suppresses their cAMP hydrolysis rates, and results in amplified cAMP signaling. These results provide insights into how PDEs transduce cGMP signals to regulate cAMP and how PDE interactions affect cardiac β-adrenergic response.

Key Words: Phosphodiesterase, cyclic nucleotides, β-adrenergic pathway, signaling networks, cardiac myocytes, computational model.

2.2. Introduction

Cyclic nucleotide (cN) phosphodiesterase isoenzymes (PDEs) regulate intracellular levels of the second messengers, cyclic adenosine-3′, 5′-monophosphate (cAMP) and cyclic guanosine-3′, 5′-monophosphate (cGMP), by controlling their degradation. They are ubiquitous in mammalian cells and are critical to the regulation of numerous physiological processes, such as cell signal transduction, proliferation and differentiation, apoptosis, and metabolism [30, 61, 67]. In the cardiovascular system, through controlling the degradation of cAMP, distinct PDE isoenzymes regulate contractility and relaxation, cell growth/survival, and cardiac structural remodeling [17, 29, 68]. Ablation of specific

PDE activities through pharmacological inhibition or gene depletion is observed to promote cardiac apoptosis [38], accelerates development of heart failure (HF) [39] and increases likelihood of cardiac arrhythmias [39, 40]. The importance of delicate regulation by distinct PDE families is also reflected by their isoform-specific alternations in cardiac diseases [3, 39, 41-43]. As examples, PDE2 upregulation in the failing heart is observed to attenuate β-adrenergic signaling [43], decreased PDE3 activity promotes cardiac myocyte apoptosis [41], and PDE4 downregulation is associated with arrhythmias in cardiac hypertrophy and HF [39]. Drugs that restore specific PDE activities [44], such as PDE3 activity in ischemic and dilated cardiomyopathies [45] and PDE1 and PDE4 activities in cardiac ischemia [46] have a cardio-protective effect. However, it has been challenging to obtain a quantitative understanding of the contribution of different PDEs in modulating intracellular signaling [30, 32, 50, 52, 63, 65], in part because the participation of multiple PDEs in the common task of cAMP degradation creates complex interactions between them. Accordingly, in this work, we develop and apply quantitative, experimentally-based models of the PDE network to better understand these complex interactions.

As shown in Fig. 2.1, synthesis of cAMP (dark red oval) is governed by the β-adrenergic pathway (red shaded background) in response to elevated catecholamines (e.g. norepinephrine and epinephrine) [10-12]. These ligands bind to and activate β-adrenergic receptors (β-ARs), which via a G-protein (Gs) mediated process activate adenylyl cyclase (AC), the enzyme which catalyzes cAMP synthesis [5, 34]. PDEs 1–4 (orange symbols) are primarily responsible for the degradation of cAMP (yellow shaded background) in cardiac myocytes [17, 29-32, 62, 63, 69]. The cAMP-hydrolyzing activities of PDEs 1, 2,

and 3 are in turn modulated by their interaction with cGMP (dark blue oval) [29, 61, 70]. The net cAMP signal controls the level of protein kinase A (PKA) activation (isoforms PKA-I and PKA-II [71]), and hence, its phosphorylation of downstream targets to regulate contraction and relaxation of cardiac myocytes [5, 29].

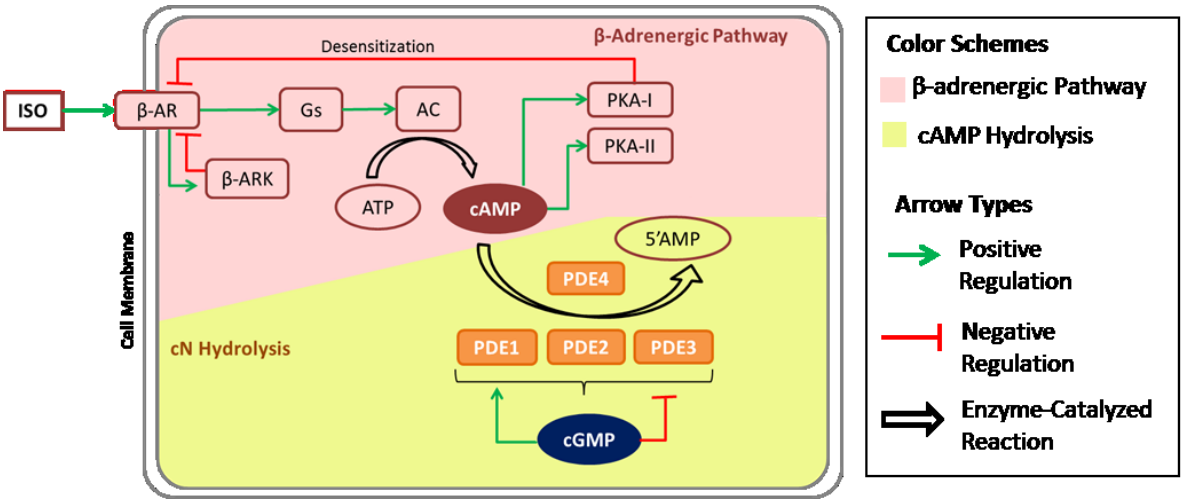

Fig. 2.1. PDEs in the cardiac β-adrenergic signaling pathway.

PDEs 1 – 4 (orange symbols) hydrolyze cAMP (yellow shaded background) generated by the β-adrenergic signaling pathway (red shaded background). cGMP in turn regulates the hydrolytic activity of PDEs 1, 2, and 3. Schematic for the β-adrenergic pathway is adapted from Saucerman et al. [71].

cAMP- and cGMP-mediated regulation of the individual PDEs has been studied primarily in protocols using purified protein extracts of individual PDE isoenzymes [29-31]. We therefore lack a systems level understanding of their network interactions. In addition, existing computational models of the β-adrenergic pathway [71-76] have not incorporated isoform-specific reaction mechanisms of PDE isoenzymes or their cGMP-mediated regulation. Therefore, the ways in which cGMP influences β-adrenergic

response through PDE activities, and the specific roles of each individual PDE isoenzyme in the regulation of β-adrenergic responses remains un-quantified [31, 32, 52, 63, 65]. Here, we present a biophysically-detailed kinetic model of the β-adrenergic pathway with integrated PDE isoenzyme activity as shown in Fig. 2.1. Models of PDEs 1–4 are developed and incorporated into an existing model of the β-adrenergic pathway [71]. This new model both reconstructs and predicts experimental data describing cAMP hydrolysis activities and regulation by cGMP.

The model is used to investigate the regulation of PDEs and β-adrenergic response by changes in cGMP concentration ([cGMP]). Three major findings are presented here. First, simulations reveal the nature of network interactions between distinct isoforms of PDEs, and indicate that activities of PDE2 and PDE4 adjust to compensate for reduced activity of other PDEs including themselves, a behavior which we refer to as "strong coupling". Second, it is demonstrated that PDE2 exerts control over PDE interactions and cytosolic cAMP signals, which is masked in cAMP readouts under PDE2 inhibition by compensatory actions of other PDEs. Finally, with increasing [cGMP], cGMP out-competes cAMP for binding to the catalytic sites of PDEs 1–3, thereby suppressing cAMP hydrolysis rates of these PDEs, leading to a net accumulation of cytosolic cAMP. This contradicts the hypothesis that cAMP concentration ([cAMP]) can be suppressed through cGMP interactions with the PDEs [17, 77, 78], at least on the global whole-cell/cytosolic level.

2.3. Materials and methods

The model presented here expands upon the single, lumped PDE cAMP degradation component of the Saucerman et al. β-adrenergic pathway model [71] to include the activities of multiple PDEs and their cAMP- and cGMP-mediated regulation, while the remainder of the signaling pathway remains the same as that of the original model [71]. Model constraints, equations, and parameters are listed in Appendix A Sect. A.2, A.4, and A.5, respectively.

2.3.1. Model formulation of cN-mediated regulation of PDE activities

Panels A–D in Fig. 2.1 show state diagrams of cN-mediated regulation of cAMP degradation activities for PDEs 1–4 respectively. Each of the PDE isoenzymes are modeled as dimers of two identical subunits [61, 65, 71, 79, 80]. For simplicity, each panel of Fig. 2.2 shows only one of the two subunits. All mammalian PDE subunits are made up of a catalytic and a regulatory domain [32, 61, 65], denoted by the letters "C" and "R" respectively. The catalytic domain (oval) contains a conserved active site (semi-circular socket) that can bind either cAMP or cGMP [32, 61, 65]. The regulatory domains differ markedly among PDEs [61] and consequently are denoted by symbols of different shapes in Fig. 2.2. Among PDEs 1–4, only PDE2 contains a cN-binding site in its regulatory domain, namely the GAF-B regulatory domain [61, 70, 81].

As shown in Fig. 2.2A, both cNs compete for binding to the catalytic domain of PDE1. In PDE2 (Fig. 2.2B), both cNs compete for binding to both the regulatory and catalytic domains. Allosteric activation of PDE2 enzymatic activity is induced by binding of either cN to the GAF-B regulatory domain (vertical transitions). This regulates the

binding affinity of cNs for the catalytic domain (horizontal transitions). The PDE3 model (Fig. 2.2C) also incorporates competitive binding of both cNs to the catalytic domain. Finally, as shown in Fig. 2.2D, PKA-mediated phosphorylation of PDE4 induces a conformational change (vertical transitions), allowing the PKA-phosphorylated form to hydrolyze cAMP with faster maximal rate than does the non-phosphorylated form (horizontal transitions).

Fig. 2.2. Mechanistic models for PDEs.

PDE monomer subunits are shown with catalytic domains (ovals, denoted by "C") and regulatory domains (varied shapes, denoted by "R") for PDEs 1–4 in (A)–(D) respectively. Active sites within catalytic domains that bind cAMP and/or cGMP are represented by semi-circular sockets; the GAF-B regulatory domain of PDE2 is represented by open rectangular socket. Reversible and irreversible reactions are denoted by double-headed and single-headed arrows respectively. ***(A) – (C)*** Competitive binding of cAMP and cGMP to PDEs 1 – 3 respectively. ***(D)*** cAMP hydrolysis by PDE4 is regulated by PKA-mediated phosphorylation.

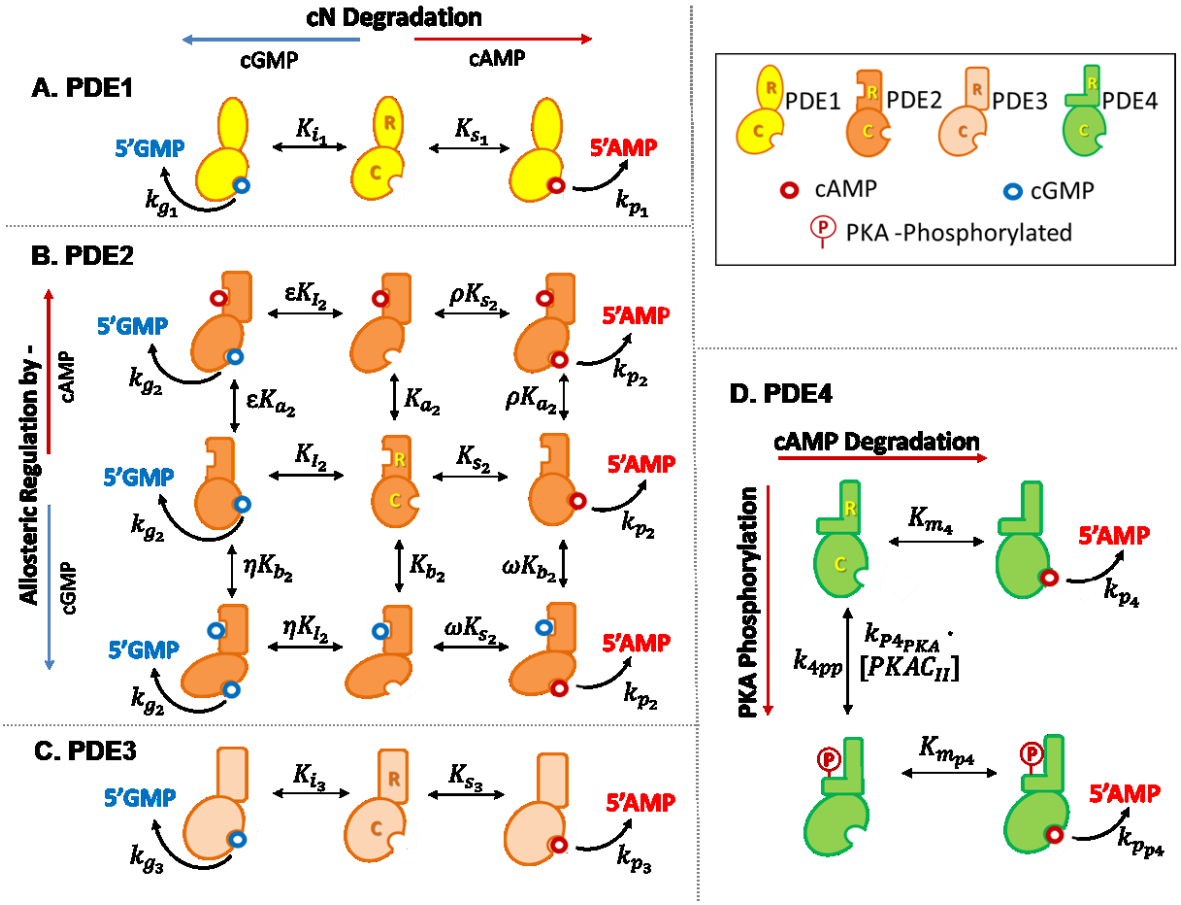

Reactions consisting of binding of cNs to PDEs, PDE conformational changes, and cN degradation via breakage of the 3′-cyclic phosphate bond are assumed to reach equilibrium rapidly with respect to the time-scale of other reactions in the signaling network. This assumption is supported by experiments demonstrating near instantaneous decay of cN signals upon withdrawal of PDE 1–4 inhibitors [63, 82, 83] and upon increased PDE activation [84]. Parameters "K" denote binding affinities, whereas parameters "k" denote rate constants. The final degraded products 5′-AMP and 5′-GMP are inactive in cN signaling pathways [61]. Equations and the experimental basis for each PDE model in Fig. 2.2 are given in Appendix A Sect. A.4.2 and A.6. PDE parameters are

set within the ranges identified in the cited literature where available, as tabulated in Appendix A Sect. A.5.2.

2.3.2. Model formulation and analysis of cGMP regulation of the β-adrenergic pathway

All four PDE models (Fig. 2.2) are integrated into the β-adrenergic model of Saucerman et al. [71] by replacing its lumped PDE cAMP degradation component. The relative cAMP hydrolysis rates of PDEs 1–4 are constrained using data from Rochais et al. [85] and Verde et al. [86] (Appendix A Fig.A.4). All figures, including those in the Supplement, are produced with the same set of parameters and initial conditions (Appendix A Sect. A.5). For model analysis, we also defined control, low, medium, and high concentrations of input isoproterenol ([ISO]) and [cGMP] (Appendix A Sect. A.3.1).

2.4. Results

2.4.1. Model validation

Having constrained the individual models for PDEs 1–4 to reproduce experimental data [31-32] (Appendix A Sect. A.2.1), we tested the ability of each model to reconstruct experimental data not included in the fitting process. The PDE1 model reproduces cAMP hydrolysis rates in the presence of 6.25 μM cGMP as reported by Yan et al. [87] (Fig. 2.3A). At 1 μM cAMP, the PDE2 cAMP hydrolysis rate (Fig. 2.3B) is potentiated by cGMP in a concentration dependent manner. The PDE2 cAMP hydrolysis rate is

approximately twice that of basal rate under maximal stimulation at ~ 3 μM cGMP. With further increases of [cGMP], PDE2 potentiation diminishes, with suppression occurring at and above ~ 30 μM cGMP. This dome-shaped relationship agrees with in vitro assay data for PDE2 [88-90]. As shown in Appendix A Fig.A.2. Experimental validation of PDE2 cAMP hydrolysis., the sigmoidal shape of the PDE2 cAMP hydrolysis curve measured in the presence of cAMP alone predicts experimental results [91-93], and the simulated EC50 concentration (36 μM) agrees with average values from experiments [29, 94, 95]. As shown in Fig. 2.3C, the cGMP-dependent rate of cAMP hydrolysis by PDE3 agrees with experiment [96]. Behavior of the integrated signaling network model is validated against cN measurements from Wild-Type (WT) adult rat ventricular myocytes (Fig. 2.3 D and E). In Fig. 2.3D, the dose-response of whole-cell [cAMP] as a function of [ISO] (at basal [cGMP]) both with (blue) and without (black) the non-specific PDE inhibitor IBMX agree qualitatively with experimental data [97, 98]. In addition, the model approximates the time course of cytosolic cAMP transients in response to acute β-adrenergic stimulation (Fig. 2.3E) [97, 99] as well as to specific PDE inhibitors [85] (Appendix A Fig.A.5). The agreement of the model with a wide range of experiments indicates the assumptions underlying model mechanisms are reasonable.

Fig. 2.3. Experimental data predicted by the model.

(A) PDE1 cAMP hydrolysis rate with 6.25 μM cGMP (normalized to maximum rate) versus data of Yan et al. [87]. ***(B)*** PDE2 cAMP hydrolysis rates (1 μM cAMP) as a function of [cGMP] versus data of Prigent et al. [88]. Hydrolysis rates are normalized against cAMP hydrolysis rate at 1 μM cAMP without cGMP. ***(C)*** PDE3 cAMP hydrolysis rates as a function of [cGMP] versus data of He et al. [96] at 0.2 μM cAMP.

Rates are normalized to cAMP hydrolysis rates at 0.2 µM cAMP without cGMP. (A) – (C) shows data (dots) from experiments performed using purified PDEs. ***(D)*** ISO dose-response relationship of [cAMP], both with (blue) and without (black) 100 µM PDE inhibitor IBMX versus data of Vila-Petroff et al. [97] and Kuznetsov et al. [98]. ***(E)*** Time-varying [cAMP] in response to 10 nM ISO versus data of Vila-Petroff et al. [97] (filled black dots) and Zaccolo et al. [99] (hollow blue dots). (D) and (E) Simulations are performed with basal [cGMP] of 10 nM from Götz et al. [100].

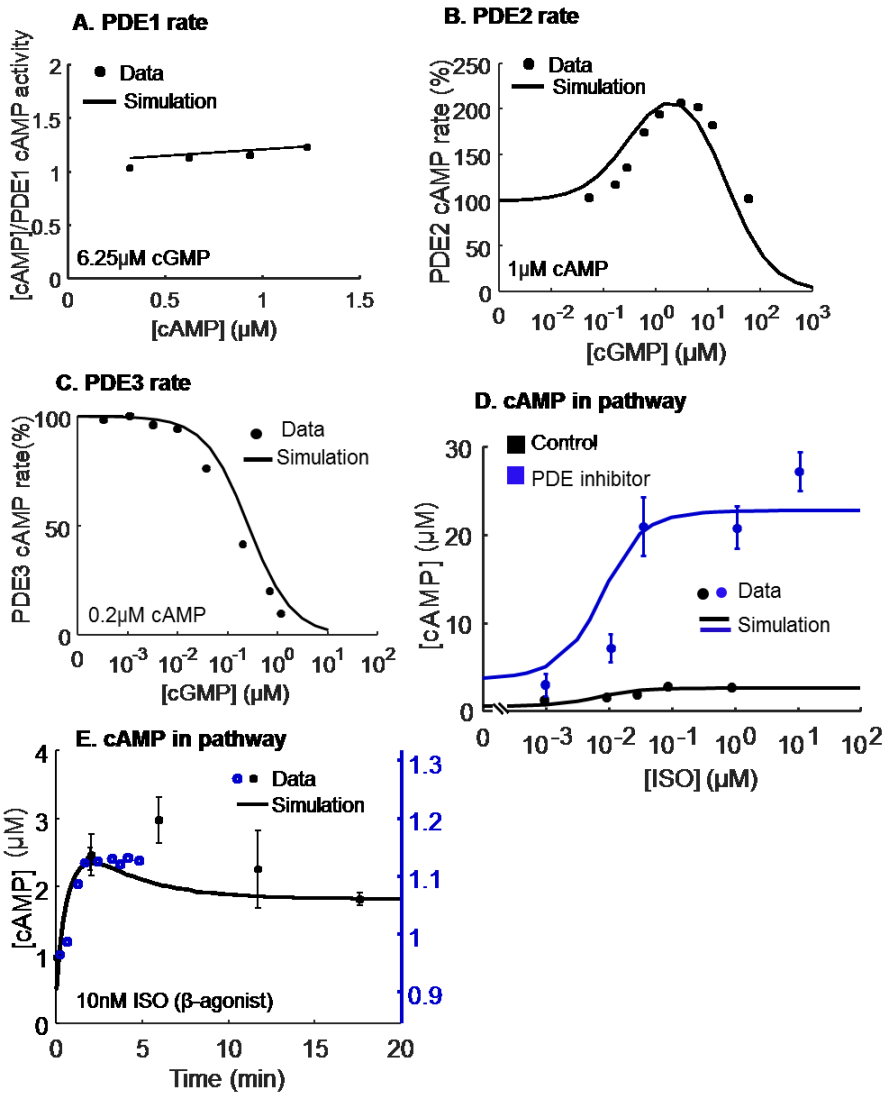

2.4.2. cAMP dynamics arises from tight interactions between PDEs

Multiple PDE isoenzymes hydrolyze cAMP simultaneously, making regulation of cAMP degradation a tightly coupled and intertwined reaction system. Fig. 2.4 shows results of simulations designed to tease apart the relationships between individual PDEs. It depicts the response of the β-adrenergic pathway when PDE2 (Fig. 2.4A–4C) or PDE4 (Fig. 2.4D–4F) is inhibited during and after β-adrenergic stimulation. Inhibition of PDE2 produces little change in both whole-cell [cAMP] (Fig. 2.4A) and PKA activation (Fig. 2.4B) before or after ISO application. Fig. 2.4C shows that an increase of the PDE4 cAMP hydrolysis rate (green line) compensates for the ablation of PDE2 activity (red line). Inhibition of PDE4 (Fig. 2.4D) produces a large increase in whole-cell [cAMP] which is greater than that which occurs in response to 10 nM ISO stimulation alone, resulting in further activation of PKA-I and PKA-II (Fig. 2.4E, black and grey lines respectively). Fig. 2.4F shows that the increase in PDE2 hydrolysis activity (red line) upon PDE4 inhibition, together with smaller increases from PDE1 (black line) and PDE3 (blue line), provide partial compensation for the loss of PDE4 activity (green line) to limit the overall rise in whole-cell [cAMP]. Fig. 2.4 demonstrates that cAMP dynamics arise from tight interactions between the PDEs.

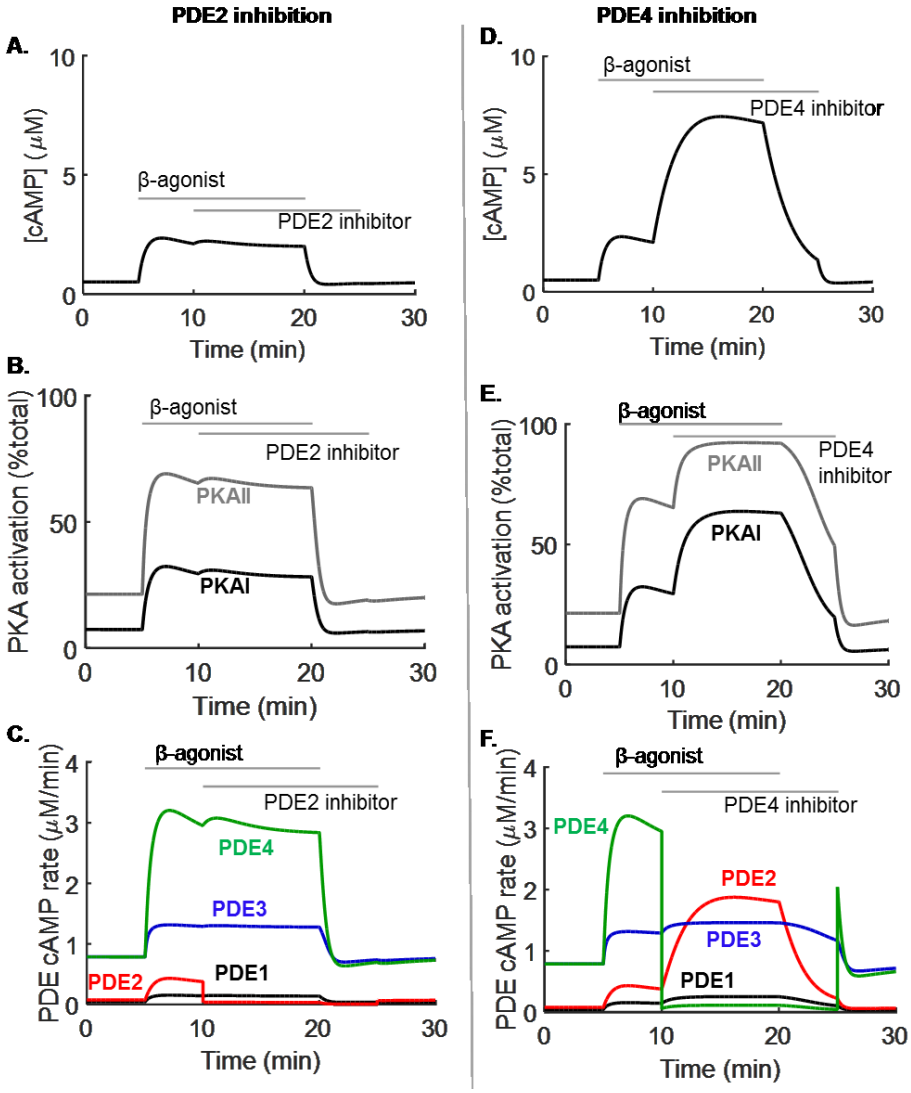

Fig. 2.4. Compensatory interactions of PDEs in the β-adrenergic pathway.

Responses of the β-adrenergic pathway to 10 nM ISO and subsequent inhibition of PDE2 in ***(A – C)*** or PDE4 in ***(D – F)***. Shown are whole-cell [cAMP] in ***(A, D)***, activation of PKA-I (black) and PKA-II (grey) in ***(B, E)***, and hydrolysis rates of PDEs 1 – 4 (black, red, blue, and green lines respectively) in ***(C, F)***. All simulations are performed with basal [cGMP] of 10 nM from Götz et al. [100].

In order to characterize interaction between the PDEs, we simulated inhibition of a specific PDE isoenzyme with simultaneous application of 10 nM ISO and varying [cGMP] and recorded PDE rate changes from that without PDE inhibition (Fig. 2.5 and S9). Under 10 nM ISO and the indicated [cGMP], Fig. 2.5 shows percent increases in the activities of each PDEs upon PDE4 inhibition, relative to their respective hydrolysis rates before inhibition at basal [cGMP] of 10 nM and 10 nM ISO. At 10 nM cGMP, the percent rate increases of Fig. 2.5A correspond approximately to that at the termination of concomitant β-agonist stimulation and PDE4 inhibition in Fig. 2.4F above. As shown in Fig. 2.5A, the compensatory increase in PDE2 rate (red line) is the greatest among the PDEs across all levels of [cGMP], with magnitudes that scale with varying degrees of PDE4 inhibition (Fig. 2.5B). Conversely, increases in PDE4 rates respond similarly to varying levels of PDE2 inhibition (Appendix A Fig.A.9), despite the small total PDE rate increases. As shown in Appendix A Fig.A.10A–D, PDE3 inhibition is also partially compensated for by primarily an increase in PDE4 activity and a smaller magnitude of increase in PDE2 activity. PDE4 rate is also increased in response to inhibition of PDE1 (Appendix A Fig.A.10E). Consequently, PDE2 and PDE4 show the strongest coupling among the PDEs in cAMP hydrolysis because either one can partially compensate for reduced activity of the other, and for reduced PDE3 activity.

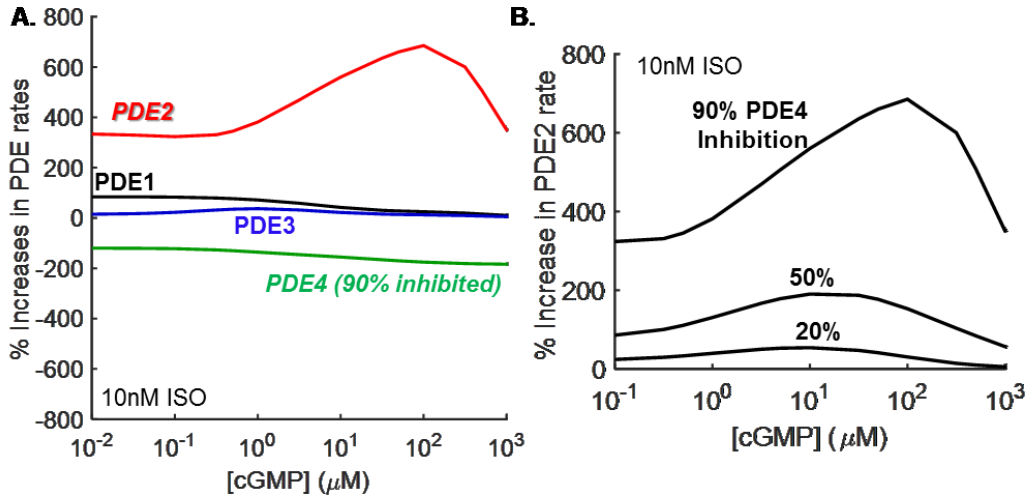

Fig. 2.5. PDE2 compensation for PDE4 inhibition.

Percent increases in PDE rates upon PDE4 inhibition relative to their respective rates prior to inhibition under 10 nM ISO and basal [cGMP] (10 nM). Varying degrees of PDE4 inhibition is simulated with simultaneous ISO stimulation under the indicated [cGMP] for 30 min. ***(A)*** Percent increases in the hydrolysis rates of PDEs 1–4 upon 90% PDE4 inhibition are shown with black, red, blue, green lines respectively. ***(B)*** Percent increases in PDE2 cAMP hydrolysis rate upon 20%, 50%, and 90% PDE4 inhibition.

These model results show that the interpretation of experiments investigating the roles of multiple PDEs by measuring [cAMP] in response to application of selective blockers can be confounded by network interactions between the different PDEs. For instance, many experiments show no or negligible changes in whole-cell [cAMP] before and after PDE2 inhibition [23, 43, 85, 101-106]. Figs. 4 and 5 demonstrate that multiple PDE isoenzymes work together to lessen changes to the cAMP signal when some of the PDE mechanisms are altered. Much greater increases in [cAMP] than that in Fig. 2.4D would result without PDE2 compensation (Appendix A Fig.A.11B), although increases in

PDE2 rates (Fig. 2.4F) cannot fully prevent [cAMP] increases due to PDE4_inhibition (Fig. 2.4D). Reciprocally, PDE4 can also partially compensate for the rises in [cAMP] due to PDE2 inhibition (Appendix A Fig.A.11A). As a result, the aforementioned experimental approach [23, 43, 85, 101-106] underestimates cAMP degradation by the inhibited PDE, because it does not account for compensatory actions of the remaining PDEs.

2.4.3. cGMP regulates PDE2 cAMP hydrolysis in a biphasic manner

The cAMP binding affinity is significantly lower for PDE2 (Appendix A Fig.A.2) than those for the other PDEs [17, 29, 32, 107], making it more resistant to activation by cNs [29, 94]. Furthermore, the fact that cytosolic [cAMP] does not rise appreciably upon PDE2 inhibition (Fig. 2.4A) can lead to the inference that PDE2 plays little role in cAMP regulation in the cytosol of cardiac myocytes [62, 69, 102, 103]. To examine this, model PDE2 hydrolysis rate is shown as a percentage of the total hydrolysis rate by all PDEs (i.e. PDEs 1–4) at each [ISO] and indicated [cGMP] (Fig. 2.6A).

Fig. 2.6. PDE2 cAMP hydrolysis rates under cGMP regulation.

(A) Proportion of total cAMP hydrolysis attributed to PDE2 as a function of ISO stimulation and concomitant applications of cGMP at 10 nM (control), 1 μM, 5 μM, and 50 μM. ***(B)*** Percentages of PDE2 with cAMP (solid black) and cGMP (solid grey) occupying its catalytic domain under 1 μM ISO as a function of [cGMP]. Percentages of PDE2 with unoccupied free catalytic domains are shown in dashed grey line. The dotted vertical lines correspond to elevated [cGMP] simulated in (A) (i.e. 1 μM, 5 μM, and 50 μM cGMP).

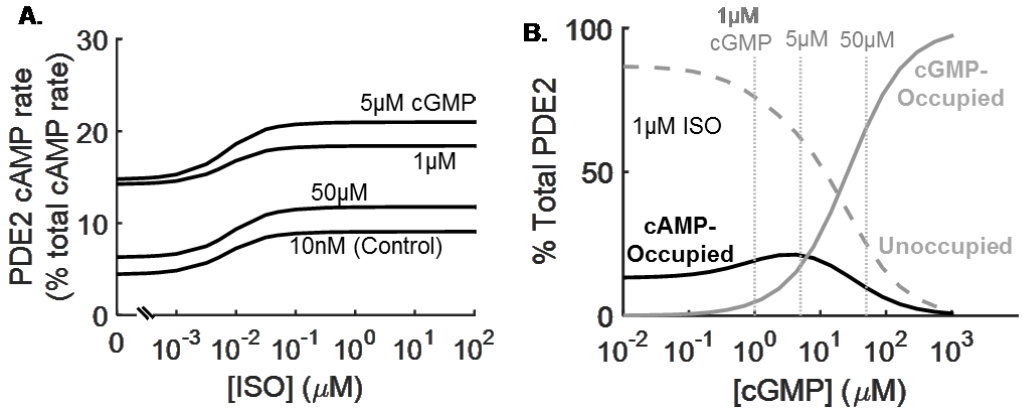

Simulations shown in Fig. 2.6A demonstrate that PDE2 is responsible for a non-negligible proportion of cAMP degradation (up to ~ 22%) in the cytosol of cardiac myocytes, which increases with increasing levels of ISO stimulation. Under control [cGMP] (10 nM), PDE2 is responsible for hydrolyzing ~ 5% of cytosolic cAMP under basal conditions (i.e. no ISO), and up to ~ 10% at higher [ISO]. Addition of cGMP changes the behavior of PDE2 in the pathway. At higher [cGMP] of 1 μM and 5 μM, the proportion of cytosolic cAMP hydrolyzed by PDE2 increases to ~ 15% respectively with no ISO and up to ~ 22% at high [ISO]. Under these elevated [cGMP] (e.g. 1 μM and 5 μM), PDE2 surpasses PDE1 and PDE3 to become the second most potent regulator after PDE4. However, at 50 μM cGMP, the activity of PDE2 is suppressed close to that at basal [cGMP].

As shown in Fig. 2.6B, this cGMP-dependent biphasic response in PDE2 cAMP hydrolysis (Fig. 2.6A) arises from the fact that the proportion of PDE2 with cAMP occupying its catalytic domain (Fig. 2.6B, solid black line) is in the range of ~ 15 – 20% at lower [cGMP] (e.g. 1 μM and 5 μM), but is suppressed to much lower levels at [cGMP]

above ~ 10 μM. At these high [cGMP], cGMP successfully competes with cAMP to bind the PDE2 catalytic binding site and cGMP-bound PDE2 (solid grey line) dominates. Although cGMP stimulates PDE2 hydrolytic activity upon binding to the GAF-B regulatory domain (Fig. 2.2B), high [cGMP] can still suppress cAMP hydrolysis by preventing cAMP-binding at the catalytic site.

2.4.4. Activation of the β-adrenergic pathway is potentiated by cGMP

Understanding the way in which cGMP regulates β-adrenergic function is challenging due to the complex behavior of the individual PDEs (Figs. 2 and 6) and their interactions (Fig. 2.4). To better understand this regulation, activation of the β-adrenergic pathway at different [cGMP] was simulated. Increasing [cGMP] increases the amplitude of whole-cell cAMP transients as well as PKA-I and PKA-II activation (Appendix A Fig.A.6 A–C). This occurs as result of a net decrease in PDE cAMP hydrolysis rates (Appendix A Fig.A.6D). Fig. 2.7A–C shows percent increases in steady state, cellular-average [cAMP], PKA-I and PKA-II activation in response to elevated [cGMP] of 1 μM, 5 μM, and 50 μM, relative to that measured at basal [cGMP] (10 nM). At each level of ISO stimulation, an increase in [cGMP] leads to an increase in cellular-average [cAMP] (Fig. 2.7A) as well as increased PKA-I and PKA-II activation (Figs. 7B and C).

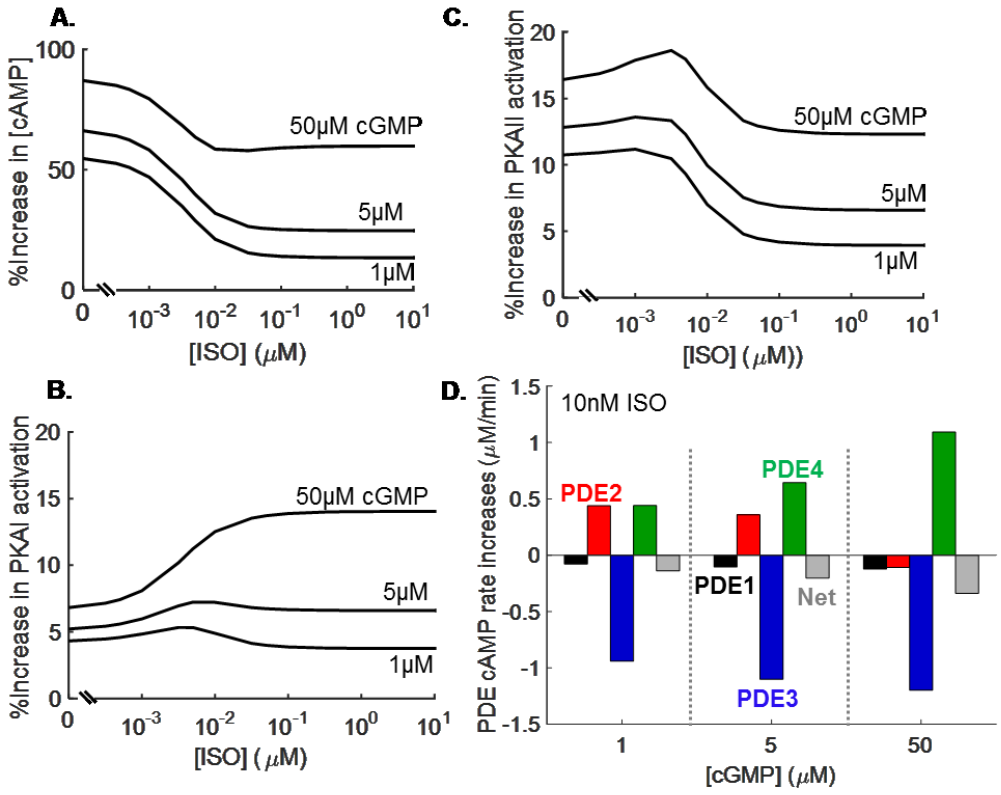

Fig. 2.7. cGMP regulation of β-adrenergic response.

(A) - (C) Percent increases of steady state cellular-average [cAMP] and PKA-I and PKA-II activations are shown respectively under various [cGMP] and [ISO]. Percent increases are shown relative to that measured at basal [cGMP] of 10 nM. ***(D)*** Increases in individual PDE hydrolysis rates (μM/min) with 10 nM ISO and indicated [cGMP] from their respective rates at basal cGMP (10 nM). The shadings for PDEs 1–4 are respectively black, red, blue, and green. The net change in PDE hydrolysis rate is shaded grey.

Fig. 2.7D shows increases in steady state cAMP hydrolysis rates for PDEs 1–4 under elevated [cGMP] from their respective rates under control cGMP (10 nM). There are two distinct modes of PDE interactions underlying the observed increases of whole-

cell cAMP with increasing [cGMP]. First, at 1 μM and 5 μM cGMP, the hydrolysis rates of PDE2 and PDE4 increase (red and green bars respectively); however, the hydrolysis rate of PDE3 (blue) is reduced sufficiently to produce a net reduction in cAMP hydrolysis (grey). Second, at 50 μM cGMP, the hydrolysis rate of PDE2 is decreased to less than the control rate as are those of PDEs 1 and 3. This is due to the fact that at high levels, cGMP overtakes cAMP in its competition for the catalytic sites of PDEs 1, 2, and 3, suppressing their cAMP hydrolysis rate (e.g. Fig. 2.6B). The increase in PDE4 rates (green) is no longer sufficient to compensate, resulting in a larger net reduction of cAMP hydrolysis rate (grey).

2.5. Discussion

2.5.1. Integrative modeling of cN signaling reveals interactions between PDEs

Therapeutic agents have been developed on the basis of their ability to potently and selectively inhibit specific PDE isoenzymes for the treatment of various diseases [32, 108-112]. However, we know relatively little about the mechanisms and contribution of the various PDEs in modulating intracellular signaling [30, 32, 50, 52, 63, 65]. As shown in Fig. 2.1, PDEs 1–4 function synergistically to regulate the strength of β-adrenergic signaling in cardiac myocytes [5, 17, 29-32, 62, 63, 69]. Several factors make it difficult to understand these interactions: 1) PDEs degrade the same cAMP signal that regulates their activities; 2) PDE activities are regulated by cGMP (Fig. 2.2); 3) Multiple PDE

isoenzymes work in concert to hydrolyze cAMP (Fig. 2.1). When the activity of one PDE isoenzyme is altered, activities of others change due to the presence of cAMP-induced negative feedback (Fig. 2.4). For these reasons, biophysically-detailed computational models are useful for studying interactions between different types of PDEs and cGMP, and their role in the regulation of the β-adrenergic pathway.

A wealth of past research on cGMP regulation of PDEs and the β-adrenergic pathway (e.g. Fig. 2.3; Appendix A Fig.A.1–Fig.A.6, Table A.9–Table A.12, Sect. A.5) has allowed us to develop a functionally integrated mechanistic model of cGMP regulation of the β-adrenergic pathway (Fig. 2.1 and Fig. 2.2). Recent live-cell imaging studies, such as those by Nikolaev et al. [84], Herget et al. [83], and Mehel et al. [43], have further advanced our understanding of PDE family regulation. Using the model reported here, we are able to perform in-depth analyses of and tease out the complex interactions underlying these experimental observations. There are three major findings from this work. First, model analyses demonstrate compensatory regulation of PDEs, with PDE2 and PDE4 being the major factors in this compensatory regulation. In particular, the increase in PDE2 rate is the most sensitive of all PDEs to PDE4 inhibition (Fig. 2.4 and Fig. 2.5). Reciprocally, upon PDE2 inhibition, the increase in PDE4 rate is the greatest among the PDEs (Appendix A Fig.A.9). Second, PDE2 regulates cAMP dynamics in a cGMP-dependent manner (Fig. 2.6). Third, cGMP potentiates whole-cell [cAMP] and PKA activation in a concentration-dependent manner (Fig. 2.7).

2.5.2. Tight coupling between PDE2 and PDE4 drives cAMP dynamics

The redundancy of the PDE network, with multiple isoenzymes performing the same hydrolytic function (Fig. 2.1) contributes a degree of robustness to perturbations. Specifically, a decrease of activity of a particular PDE isoenzyme is partially compensated for by the remaining PDE isoenzymes, with PDE2 and PDE4 exhibiting the strongest interdependence among the PDEs (Fig. 2.4, Fig. 2.5, and Appendix A Fig.A.9). Such coupling between PDE isoenzymes may be an important mechanism in stabilizing cAMP dynamics in the heart [3, 42, 113], including disease settings where alterations in isoenzyme-specific PDE expression and/or activity have been implicated [3, 39, 41, 43, 50, 113-115]. Modeling results show that the ability of PDE2 to compensate for reduced activity of PDE4 is particularly strong. Partial PDE2 compensation for reduced PDE4 activity is consistent with experimental data showing that PDE4 inactivation produces only small effects, if any, on basal blood pressure, heart rate, and inotropy [116]. It is clearly established that PDE4 expression is reduced in HF [39, 116, 117]. Our modeling predicts that under this condition PDE2 may partially compensate for the loss of cAMP hydrolytic activity of PDE4. This is a novel insight regarding the role of PDE2 in HF. This compensation will be further enhanced through up-regulation of PDE2 that has been observed in HF [43]. Improved understanding of the modes of interactions between PDEs may therefore provide insights on disease-induced changes in signal transduction and the efficacy of drug actions.

2.5.3. PDE2 integrates cAMP and cGMP signals in regulation of the β-adrenergic pathway

The presence of PDE2 in cardiac myocytes and its degradation of cAMP have been demonstrated in many studies using a variety of experimental techniques, such as chromatography [118, 119], electrophoresis [88], electrophysiological measurements [85, 86], and live-cell imaging [101, 120]. Increased PDE2 expression in HF is observed to blunt β-adrenergic signaling with PDE2 inhibition partially restoring β-adrenergic responsiveness in diseased cardiac myocytes [43]. In addition, adenoviral PDE2 overexpression in healthy cardiac myocytes markedly decreased [cAMP] upon β-adrenergic stimulation with effects reversed by PDE2 inhibition [43]. As highlighted by our PDE2 model (Fig. 2.2B), PDE2 exhibits complex interactions with both cNs, and serves as a nexus through which cGMP influences cAMP dynamics. Our model, therefore, helps tease out the complex interactions and interpret experimental observations.

When interpreted through a quantitative model of the complex interactions involved, the role of PDE2 in cAMP hydrolysis manifested in experiments is exposed. Experiments demonstrate that PDE2 EC50 is at least tenfold higher than the cellular-average [cAMP] and approximately tenfold higher than that of other PDEs [17, 29, 32, 107], therefore appearing to play a minor role in regulating cytosolic cAMP in cardiac myocytes [62, 69, 102, 103]. Simulations reveal that despite these biochemical properties, PDE2 does hydrolyze appreciable amounts of cytosolic cAMP (up to ~ 22%), especially under increased β-adrenergic stimulation (Fig. 2.6A); however, its role is partially masked in the small increases in [cAMP] upon PDE2 inhibition due to the compensatory actions of the remaining PDEs (Fig. 2.4A–C).

Because of its high EC50, PDE2 can be further activated at elevated [cAMP] when other PDE isoenzymes have already reached their maximum hydrolysis capacity. Furthermore, cGMP increases the proportion of cAMP hydrolyzed by PDE2, until very high levels suppress its activity (Fig. 2.6A). This cGMP-mediated dome-shaped biphasic behavior of PDE2 cAMP hydrolysis rate arises from the competitive binding of cNs to its regulatory and catalytic domains (Fig. 2.6B and Fig. 2.2B). In addition, as the changes in PDE rates (Fig. 2.5) reflect the dome-shaped hydrolysis curves of PDE2 (Fig. 2.6), it can be seen that cGMP regulation of PDE2 influences the activities of other PDEs, and therefore shapes synergistic interactions between them. Our simulations show the aforementioned PDE2 behaviors exist without having to hypothesize the existence of a specialized nano-compartment with elevated cN levels or limited expression of other PDEs [23]. However, our work does not rule out the existence of such micro-domains. In such cases, PDE2 will exert an even greater control over cAMP dynamics than that shown in Figs. 5 and 6, as it would be further activated by the higher [cAMP], and/or be the only PDE isoenzyme appreciably degrading cAMP.

2.5.4. Whole-cell cAMP is potentiated by cGMP

The model demonstrates that cGMP potentiates cellular-average cAMP signals, resulting in increased PKA activation due to a net reduction of hydrolysis rates across all PDEs (Fig. 2.7A–C). The cGMP-mediated dome-shaped biphasic behavior of PDE2 cAMP hydrolysis rate contributes two modes of PDE interaction underlying the observed cAMP potentiation in the cellular average sense (Fig. 2.7D). Upon sensing lower [cGMP] (e.g. 1–5 μM, Fig. 2.7D), the increases in PDE2 and PDE4 rates serve to compensate for the

suppressed PDE3 rate. At higher [cGMP] (e.g. 50 μM, Fig. 2.7D), PDE2 rate is suppressed and contributes to, instead of compensating for, cGMP-mediated cAMP potentiation. In the latter case, despite PDE4's large contribution to cAMP degradation, the strength of PDE4-mediated feedback driven by the elevated [cAMP] is not sufficient to completely compensate for the suppression of other PDE activities (Fig. 2.7D). Model results therefore suggest that, in mammalian cardiac myocytes, reduction of β-adrenergic response, as measured by whole-cell [cAMP] and PKA activation, upon stimulation of the Nitric Oxide (NO)/cGMP/Protein Kinase G (PKG) pathway is not likely to be mediated by cGMP regulation of the PDEs. In fact the model predicts that this regulation potentiates [cAMP] and PKA activation. This is contrary to what has been previously hypothesized based on observations of responses of downstream targets of the β-adrenergic pathway [17, 77, 78], at least on the global whole-cell/cytosolic level. Instead, we speculate that the inhibitory activities may result from pathways downstream of the PDEs, such as PKG-mediated phosphorylation of downstream targets. This prediction of the model could be tested experimentally.

2.5.5. Model rationale, limitations, and future work

In order to study synergistic interactions between multiple PDE families in regulating whole-cell cAMP dynamics, we focused on studying the signal transduction mechanisms, particularly with regard to the PDEs, and sought to quantify the biochemistry of the signal components (Fig. 2.2) and cGMP regulation of cAMP dynamics (Fig. 2.1). Recent advances in spatiotemporally-resolved recording of cAMP signals [36, 63, 67, 121-124] now make it possible to measure the compartmentalized activities of different

PDEs. For instance, in the SERCA/PLB/AKAP signalosome, PDE3A1 phosphorylation by PKA is recently shown to promote its targeting to the signalosome, where it may modulate [cAMP] in a highly localized manner [125]. Our model lacks such compartmentalization, and extending the model to allow its use in studying the diversification of cN signals in subcellular micro-domains is an important next step. The current model does not incorporate the bidirectional functional relationships between cAMP and cGMP, which (respectively) potentiate and attenuate cardiac contractility [5, 8, 13]. To advance our investigation of the cAMP-cGMP cross-talk signaling network, we are incorporating more mechanistic models of cGMP dynamics guided by recent advancements in cGMP recording [100, 120]. Further extensions to the model must ultimately include regulation of transmembrane channels and calcium cycling proteins, and incorporation of these mechanisms into integrative models of the ventricular myocyte.

2.5.6. Multi-scale modeling bridges causal link between individual signaling protein characteristics and collective pathway response

This multi-scale model mechanistically integrates interactions between the cNs within the domains of each PDE isoenzymes to the emergent network responses of the β-adrenergic pathway. By enabling system-level analysis, the model provides insight regarding the ways in which each distinct PDE regulates cAMP signals, and the ways in which cAMP signals feed-back to influence the behavior of each PDE. In particular, the synergistic, compensatory behaviors of PDE2 and PDE4 would not have been revealed without this network-level analysis. Further studies of the signaling pathway will reveal how isoform-specific changes in PDE expression in hypertrophy and HF [22, 46, 126] contribute to

disease-related remodeling. Understanding information processing through signaling pathways is critical to deciphering the mechanisms behind observed physiological responses in health and disease.

2.6. Conclusions

We have developed a computational model of the β-adrenergic pathway to investigate the roles and interactions of distinctively-regulated PDEs 1–4, in regulating cAMP signal dynamics in the cardiac myocyte. Using the model, we have shown that 1) PDE2 and PDE4 exhibit the strongest coupling among the PDEs; 2) PDE2 and its regulation by cGMP regulate cAMP dynamics; and 3) The presence of cGMP potentiates whole-cell [cAMP], which subsequently increases PKA activation.

Disclosures

None declared.

Acknowledgements

This work was supported by Natural Sciences and Engineering Research Council (NSERC) of Canada scholarships, CGS M-377616-2009 and PGSD3-405041-2011, awarded to C.Y.Z, and National Heart Lung and Blood Institute (NHLBI) of the USA grant R01 HL105239. Matlab source code is available from the authors. An SBML model description will be submitted to the EBI Biomodels database.

Appendix A. Supplementary Material for the β-Adrenergic–PDE Model

Chapter 3. Roles of Phosphodiesterases in the Regulation of the Cardiac Cyclic Nucleotide Cross-Talk Signaling Network

3.1. Abstract

The balanced signaling between the two cyclic nucleotides (cNs) cAMP and cGMP plays a critical role in regulating cardiac contractility. Their degradation is controlled by distinctly regulated phosphodiesterase isoenzymes (PDEs), which in turn are also regulated by these cNs. As a result, PDEs facilitate communication between the β-adrenergic and Nitric Oxide (NO)/cGMP/Protein Kinase G (PKG) signaling pathways, which regulate the synthesis of cAMP and cGMP respectively. The phenomena in which the cAMP and cGMP pathways influence the dynamics of each other are collectively referred to as cN cross-talk. However, the cross-talk response and the individual roles of each PDE isoenzyme in shaping this response remain to be fully characterized. We have developed a computational model of the cN cross-talk network that mechanistically integrates the β-adrenergic and NO/cGMP/PKG pathways via regulation of PDEs by both cNs. The individual model components and the integrated network model replicate experimentally observed activation-response relationships and temporal dynamics. The model predicts that, due to compensatory interactions between PDEs, NO stimulation in the presence of sub-maximal β-adrenergic stimulation results in an increase in cytosolic cAMP accumulation and corresponding increases in PKA-I and PKA-II activation;

however, the potentiation is small in magnitude compared to that of NO activation of the NO/cGMP/PKG pathway. In a reciprocal manner, β-adrenergic stimulation in the presence of sub-maximal NO stimulation results in modest cGMP elevation and corresponding increase in PKG activation. In addition, we demonstrate that PDE2 hydrolyzes increasing amounts of cAMP with increasing levels of β-adrenergic stimulation, and hydrolyzes increasing amounts of cGMP with decreasing levels of NO stimulation. Finally, we show that PDE2 compensates for inhibition of PDE5 both in terms of cGMP and cAMP dynamics, leading to cGMP elevation and increased PKG activation, while maintaining whole-cell β-adrenergic responses similar to that prior to PDE5 inhibition. By defining and quantifying reactions comprising cN cross-talk, the model characterizes the cross-talk response and reveals the underlying mechanisms of PDEs in this non-linear, tightly-coupled reaction system.

Key Words: Cyclic nucleotide cross-talk signaling network; Phosphodiesterases; β-adrenergic pathway; NO/cGMP/PKG pathway; Cardiac myocytes; Computational model.

3.2. Introduction

The two cyclic nucleotides (cNs), cyclic adenosine-3′, 5′-monophosphate (cAMP) and cyclic guanosine-3′, 5′-monophosphate (cGMP), are intricately-regulated second messengers. Phosphodiesterase isoenzymes (PDEs) rely on the feedback of both cAMP and cGMP signals to modulate the rate at which they degrade these two cNs [63, 95, 124]. The integration of these feedback signals provides the means for communication between

the β-adrenergic and Nitric Oxide (NO)/cGMP/Protein Kinase G (PKG) signaling pathways, which regulate the synthesis of cAMP and cGMP respectively. The phenomenon whereby one cN signal influences the dynamics of the other is commonly referred to as cN cross-talk [17, 18, 25]. It is known that stimulation of the β-adrenergic and NO/cGMP/PKG pathways exert opposing physiological responses, with the former enhancing cardiac inotropy and lusitropy [5, 13] and the latter attenuating cardiac contractility [8, 10, 14-16] and antagonizing β-adrenergic tone [17-19, 21-23, 25-27, 42, 43]. Furthermore, many signaling components in the network are perturbed in cardiac hypertrophy and heart failure (HF), potentially contributing to disease remodeling [3, 34-37]. As a result, it is important to understand the regulatory mechanisms that maintain balance between the cN signals in both health and disease.

Fig. 3.1. Cyclic nucleotide cross-talk signaling network.

(A) The cN cross-talk signaling network model is composed of the β-adrenergic pathway (red background), the NO/cGMP/PKG signaling pathway (blue background), and cross-talk between them (yellow background). Cross-talk is mediated by PDEs 1–5. In the regulation of cAMP- ***(B)*** and cGMP- ***(C)*** hydrolysis, cNs exert positive (green arrows) or negative (red arrows) regulation of PDE activities. In particular, PDE2 hydrolysis rate of either cN is stimulated (green arrow) by low concentrations of the other cN but is suppressed (red arrow) if the concentrations are sufficiently high. To avoid crowding the figure, the hydrolysis reactions of cNs are omitted in (B) and (C), which would have been drawn as red arrows originating from each PDE to cAMP in (B) and cGMP in (C). Instead, hydrolysis of cAMP and cGMP are respectively represented by ovals of faded red in (B) and faded blue in (C).

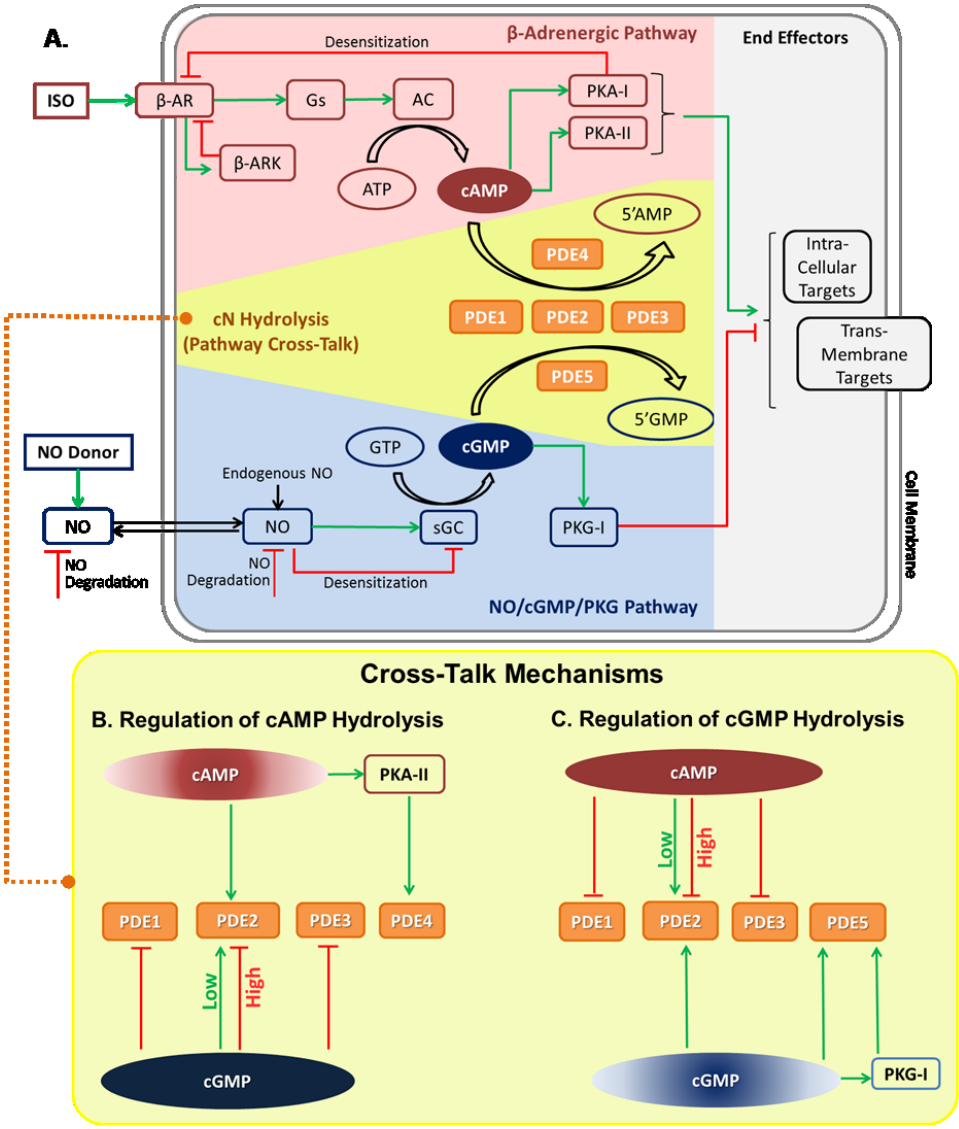

The complex interactions comprising cN cross-talk, and the participation of multiple PDEs in the common task of cN degradation make understanding the nature of these regulatory mechanisms challenging [32, 52, 63, 65]. As shown in Fig. 3.1A, the synthesis of cAMP and cGMP is regulated by the β-adrenergic pathway (red background) and the NO/cGMP/PKG pathway (blue background) in response to external and/or internal stimuli [10-12]. Synthesis of cAMP is catalyzed by adenylyl cyclase (AC) via a

stimulatory G-protein (Gs) mediated process that occurs when catecholamines (e.g. norepinephrine and epinephrine) bind to and activate β-adrenergic receptors (β-ARs) [34]. Synthesis of cGMP is catalyzed by soluble guanylate cyclase (sGC) in response to an increase in NO concentration ([NO]) [8, 16]. In cardiac myocytes, the degradation of cAMP and cGMP are primarily catalyzed by PDEs 1–5, each with its own unique biochemical characteristics and regulatory mechanisms [17, 29-32, 62, 63, 69] (yellow background). PDEs 1, 2, and 3 are capable of hydrolyzing both cNs, while PDE4 and PDE5 are specific to cAMP and cGMP respectively. The coordinated regulation of PDEs 1, 2, and 3 activities by both cNs thus functionally bridge together the β-adrenergic and NO/cGMP/PKG pathways. The net cN signals regulate downstream targets (gray background) via phosphorylation of these targets by Protein Kinase A (PKA) (isoforms PKA-I and PKA-II) and/or PKG (Fig. 3.1A). As examples, these targets include L-type calcium (Ca^{2+}) channels (LCCs), phospholamban (PLB), and Troponin I (TnI) for both PKA [5] and PKG [2, 8, 9].

The cross-talk between β-adrenergic and NO/cGMP/PKG pathways consists of a variety of cN-mediated reactions that regulate PDE activities (Fig. 3.1A and B). As shown in Fig. 3.1B, cAMP degradation is regulated by PDEs 1–4 in cardiac myocytes [17, 29-32, 62, 63, 69]. As a form of negative feedback, cAMP can stimulate its own degradation through activation of PDEs 2 and 4 (green arrows) [127]. The presence of cGMP can potentially increase cAMP concentration ([cAMP]) by inhibiting cAMP hydrolysis rates of PDEs 1 and 3 (red arrows) [127]. Depending on its concentration ([cGMP]), cGMP can either inhibit or potentiate [cAMP] by regulating PDE2 cAMP hydrolysis activity (alternating red/green arrows) [127]. As shown in Fig. 3.1C, cGMP

dynamics depend on the activities of PDEs 1, 2, 3, and 5 [29, 31, 62, 69]. Negative feedback on [cGMP] is accomplished by cAMP- and cGMP-dependent activation of PDE2 and cGMP-dependent activation of PDE5 [31, 62, 69, 128]. The presence of cAMP can potentially increase [cGMP] by inhibiting cGMP degrading activities of PDEs 1 and 3, while either inhibiting or potentiating [cGMP] by regulating PDE2 cGMP hydrolysis activity depending on [cAMP] [31, 62].

cAMP- and cGMP-mediated regulation of PDEs 1–5 has been studied primarily in protocols using purified protein extracts [29-31]. The interpretation of experiments investigating the roles of multiple PDEs by measuring [cAMP] and/or [cGMP] in response to application of selective PDE inhibitors can be confounded by compensatory network interactions between the remaining PDEs [127]. As a result, it is difficult to attain a system level understanding of the signaling network that bridges the causal link between the characteristics of individual signaling proteins and the collective response of the entire network. To address this, we present a biophysically-detailed kinetic model of the cN cross-talk network (Fig. 3.1A) that includes mechanistic models of cN regulation of PDEs 1–5 (Fig. 3.1B–C). Three major novel predictions emerge from this model. First, simultaneous NO stimulation in the presence of sub-maximal β-adrenergic stimulation results in potentiation of whole-cell β-adrenergic response; reciprocally, β-adrenergic stimulation in the presence of sub-maximal NO stimulation results in increased [cGMP] and PKG activation. These increases, however, are small in magnitude when compared to direct activation of the NO/cGMP/PKG pathway by NO and the β-adrenergic pathway by isoproterenol (ISO). Second, PDE2 degrades increasing proportions of cAMP with increasing β-adrenergic stimulation; however, it degrades more cGMP under decreasing

[NO]. Finally, the compensatory actions of PDE2 under selective PDE5 inhibition regulate the enhanced [cGMP] and PKG activation and maintain whole-cell β-adrenergic response similar to that prior to PDE5 inhibition.

3.3. Materials and methods

In a previously developed model, we studied PDE regulation of cAMP and response of the β-adrenergic pathway by treating [cGMP] as a model parameter [127]. Here, we extend this model by incorporating a mechanistic description of cGMP production and degradation. Details of the model are presented in the Supplement. Symbols are defined in Appendix B Sect. B.1; Sect. B.2 provides all model equations; Sect. B.3 defines and gives nominal values for model parameters; Sect. B.4 lists state variable initial conditions. Synthesis of cGMP is modeled by incorporating a NO/sGC model by Batchelor et al. (Eqs. 15–20 Appendix B Sect. B.2.2) [129]. Models for PDEs 1–4 (Appendix B Sect. B.2.3) are those described previously in Zhao et al. [127], with PDEs 1–3 now regulating cGMP degradation as well as cAMP degradation (Fig. 3.1). Based on the newly developed model of PKG activation by cGMP (Eqs. 40–43 Appendix B Sect. B.2.5; rationale Appendix B Sect.B.5.2), the description of PDE5 degradation of cGMP is modified from that in Batchelor et al. [129] to explicitly include PDE5 activation upon phosphorylation by PKG [128, 130-134] (Eq. 32 Appendix B Sect. B.2.3; rationale Sect.B.5.1). In order to replicate experimental protocols [63, 82, 97, 99], NO release from the NO donor SNAP is modeled according to existing literature [135-141] (Eqs. 12–14 Appendix B Sect. B.2.2; rationale Sect. B.5.3). Experimental conditions for data depicted

in figures are summarized in Appendix B Sect. B.8. Model signaling components are constrained by experimental data (Appendix B Sect. B.6.1–B.6.3) in conjunction with the experimentally determined ranges for model parameters (Appendix B Sect. B.3). The individual PDE component models are integrated within the rest of the network according to constraints in Appendix B Sect. B.6.2. The remaining model components and parameters are unchanged from those presented in Zhao et al. [127] and Batchelor et al. [129]. Model integration allowed for the construction of the entire cN signaling network which includes all biochemical actions outlined in Fig. 3.1. All figures contained in this paper, including those in the Supplement, are generated with the same set of parameters and state variable initial conditions.

3.4. Results

3.4.1. Validation of individual PDE models

The PDE models were validated against experimental data describing their interaction with cAMP and cGMP (Fig. 3.2), after being constrained by a separate set of experiments (Appendix B Sect. B.6.1). These model validation data (Fig. 3.2 dotted symbols) have not been used in the model fitting process. Data in Fig. 3.2A, B, and D (dotted symbols) are at different [cAMP] and [cGMP] than those used to constrain the respective PDE models (Appendix B Fig.B.3A–C) from the same experimental studies. As shown in Fig. 3.2A, the PDE1 model reproduces cAMP hydrolysis rates at constant [cGMP] (6.25 μM) while varying [cAMP] as reported by Yan et al. [87]. In addition, it

replicates cGMP hydrolysis rates at constant [cAMP] (6.25 μM) while varying [cGMP] as reported by Yan et al. [87] (Fig. 3.2B). As shown in Fig. 3.2C, the PDE2 model replicates the dome-shaped cAMP hydrolysis curve as a function of [cGMP] reported by Prigent et al. [88], as well as cAMP regulation of PDE2 cGMP hydrolysis with 10 μM [cGMP] (Fig. 3.2D) observed by Russell et al. [142]. When only one cN is present in the reaction system, the PDE2 EC50s (half-maximal activation concentrations) for both cAMP and cGMP hydrolysis also agree with experimental averages [29, 65] (Appendix B Fig.B.7). As shown in Fig. 3.2E and F respectively, PDE3 cAMP and cGMP hydrolysis are suppressed by the other cN, in agreement with experimental data of He et al. [96].

Fig. 3.2. Experimental validation of PDE models.

Experimental data predicted by the PDE models. Dotted symbols are experimental data (obtained from purified PDEs); lines are simulation results. ***(A)*** PDE1 cAMP hydrolysis rate at 6.25 μM [cGMP] (normalized to the maximum rate) versus data of Yan et al. [87]. ***(B)*** Normalized PDE1 cGMP hydrolysis rate at 6.25 μM [cAMP] versus data of Yan et al. [87]. ***(C***) Effects of [cGMP] on PDE2 cAMP hydrolysis rates (1 μM [cAMP]) compared to data of Prigent et al. [88]. Reported rates are normalized against rate without cGMP. ***(D)*** PDE2 cGMP hydrolysis rates (10 μM [cGMP]) as a function of [cAMP] compared to data of Russell et al. [142], normalized to that without cAMP. ***(E)*** PDE3 cAMP hydrolysis (0.2 μM [cAMP]) as a function of [cGMP] versus data of He et al. [96], normalized to that without cGMP. ***(F)*** Normalized PDE3 cGMP hydrolysis (0.2 μM [cGMP]) versus data of He et al. [91].

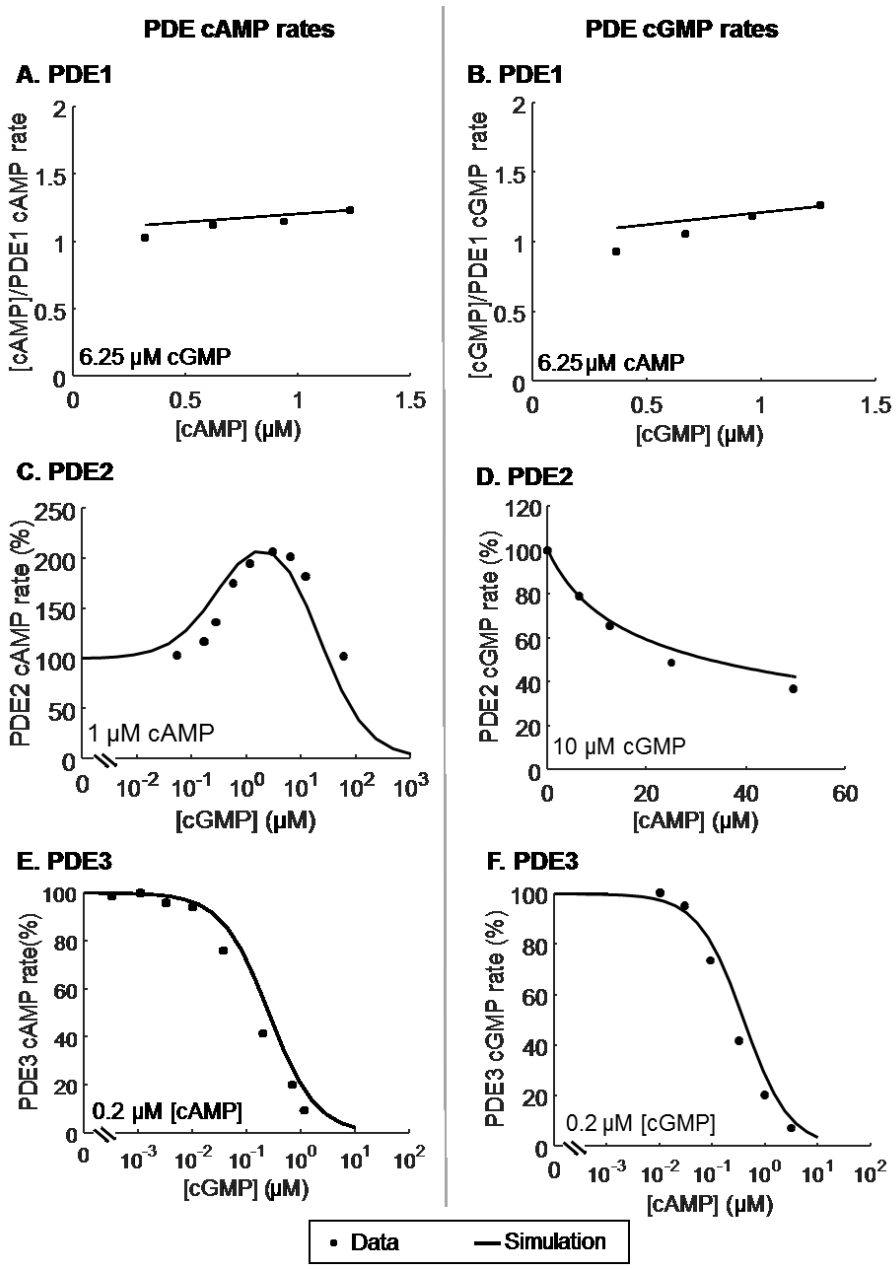

3.4.2. Validation of the integrated signaling network model

The behavior of the full signaling network model (Fig. 3.1) is validated by comparison with experimental data obtained from rat cardiac ventricular myocytes (Fig. 3.3 dotted symbols), which have not been used in model development. The model qualitatively

replicates whole-cell [cAMP] responses to ISO with (blue) and without (black) inhibition of PDEs by IBMX (Fig. 3.3 A) as measured by Vila-Petroff et al. [97] (blue dots) and Kuznetsov et al. [98] (black dots). In addition, the model approximates the time course of cytosolic [cAMP] transients in response to acute β-adrenergic stimulation (Fig. 3.3 B) as reported by Vila-Petroff et al. [143] (filled black dots) and Zaccolo et al. [99] (hollow blue dots) and to specific PDE inhibitors according to Rochais et al. [85] (Appendix B Fig.B.8).

Fig. 3.3. Experimental validation of cross-talk signaling network model.

Model predicts experimental data from rat cardiac ventricular myocytes. Dotted symbols are experimental data; lines are simulation results. ***(A)*** Dose-response relationship of [cAMP] in response to ISO, with (blue) and without (black) the PDE inhibitor IBMX (100 μM), versus data of Vila-Petroff et al. [97] (blue dots) and Kuznetsov et al. [98] (black dots). ***(B)*** Simulated [cAMP] time course in response to 10 nM [ISO] compared to data of Vila-Petroff et al. [143] (filled black dots) and Zaccolo et al. [99] (hollow blue dots). ***(C)*** Simulated [cGMP] with (gray bar) and without 100 μM [IBMX] (white bar) in the absence and presence of SNAP (100 μM) compared to data of Castro et al., 2006 [82] (black dots) and 2010 [128] (blue dots). ***(D)*** Simulated [cGMP] time course under 100 μM [SNAP] perfusion followed by 100 μM [IBMX] application compared to data of Castro et al. [82]. ***(E)*** Simulated [cGMP] time course in presence of SNAP (100 μM) with intermittant application of the specific PDE inhibitors EHNA (PDE2 inhbitor, 10 μM) and Sildenafil (Sil, PDE5 inhibitor, 0.1 μM), and the non-specific PDE inhibitor (100 μM [IBMX]) compared to data of Castro et al. [82]. (C)–(D) Details on simulations and data processing are provided in Appendix B Sect.B.8.1.

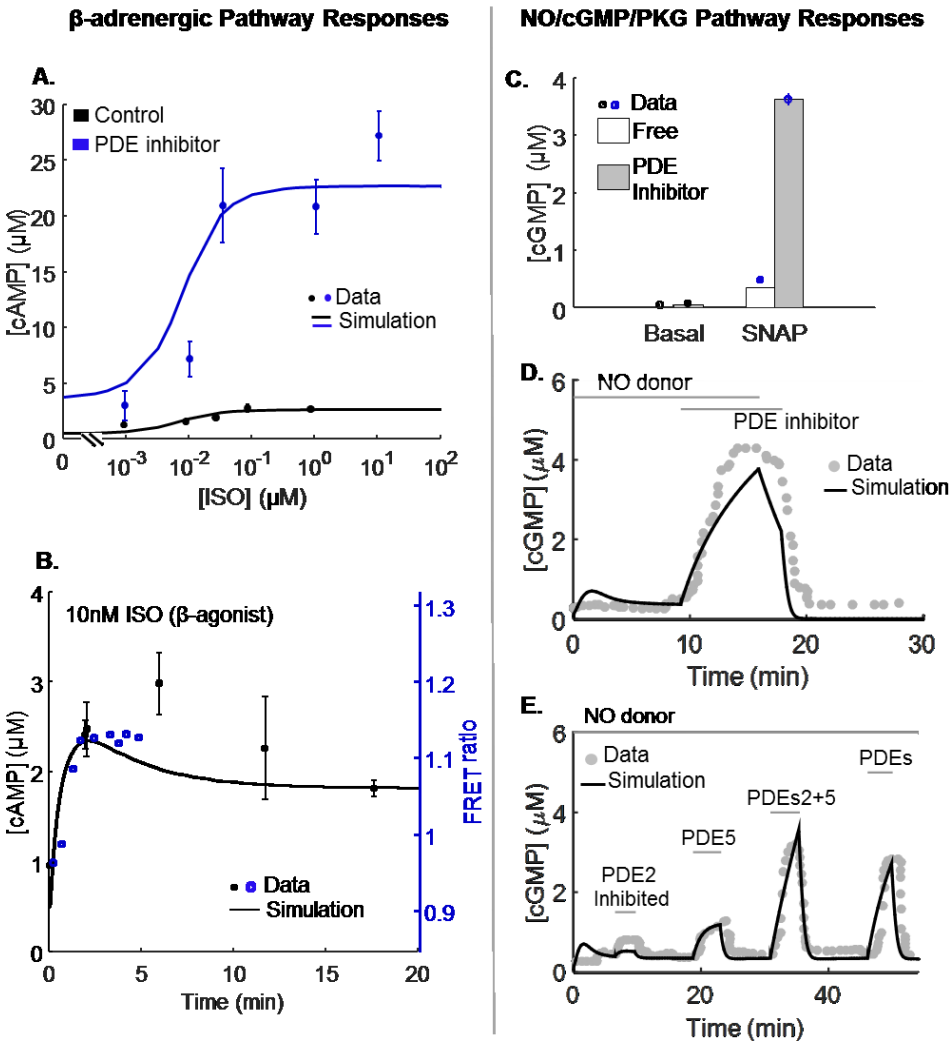

The model replicates experimentally measured [cGMP] under basal, non-stimulated conditions (Fig. 3.3 C, first two columns) [82, 128] as measured by Castro et al., 2006 [82] (black dots), both before (gray) and after (white) inhibition of all PDEs by IBMX. The basal [cGMP] of ~ 10 nM (first column) also agrees with data of Götz et al. [100]. In addition, simulated [cGMP] under NO stimulation from SNAP follows data of Castro et al., 2010 [128] (blue dots), before (gray) and after (white) IBMX application

(Fig. 3.3 C, last two columns). Furthermore, the temporal dynamics of [cGMP] accumulation and degradation approximates data from Castro et al. [82] with SNAP and subsequent IBMX application (Fig. 3.3 D). Finally, as shown in Fig. 3.3 E, [cGMP] time course under specific PDE inhibitors for PDE2 and PDE5 agrees with data of Castro et al. [82]. Details on simulations and data processing for Fig. 3.3 C–E are provided in Appendix B Sect. B.8.1. The agreement of the model with data from a wide range of experiments (Fig. 3.2 and Fig. 3.3; Appendix B Fig.B.3–Fig.B.8) indicates the assumptions underlying model mechanisms are reasonable.

3.4.3. β-adrenergic pathway and NO/cGMP/PKG pathway responses are potentiated upon NO and ISO stimulation respectively via cN cross-talk

Cross-talk between the cN pathways refers to the signaling mechanisms by which β-adrenergic stimulation leads to PKG activation and/or NO elevation leads to PKA activation, i.e. the phenomenon whereby one pathway's input signal influences the response of another pathway. The responses of the pathways to their respective stimuli are referred to as the direct responses, which consist of changes in β-adrenergic responses upon ISO stimulation and changes in NO/cGMP/PKG pathway responses upon NO stimulation. In Fig. 3.4, we compare the cross-talk responses (right-hand axes, gray color scheme) to the direct responses of each pathway (left-hand axes, black color scheme). As shown in Fig. 3.4A–C (black lines), under 1 nM ISO, increasing [NO] via an increase in [SNAP] leads to substantial activation of the NO/cGMP/PKG pathway, with large increases in [cGMP] (Fig. 3.4A) and PKG activation (Fig. 3.4B and C). Comparatively,

increases in the β-adrenergic cross-talk responses measured in terms of [cAMP] and activation of PKA-I and PKA-II are smaller in magnitude (Fig. 3.4A–C respectively, gray lines). In order to fully characterize the cross-talk responses, percent increases in β-adrenergic pathway activations are calculated under varying [ISO] with low, medium, and high [SNAP] of 5 nM, 50 nM, and 500nM (Appendix B Fig.B.9A–C). It can be seen that the NO cross-talk effects on the β-adrenergic pathway increases with [NO], reaching up to ~ 30% in potentiation of [cAMP] and activation of PKA-I and PKA-II. On the other hand, this cross-talk response diminishes with increasing [ISO], reaching negligible values for [ISO] above 100 nM (Appendix B Fig.B.9A–C). Under the same simulation protocol, the percent increases in [cGMP] and PKG activation (Appendix B Fig.B.10A and B) are comparable in magnitude as those for the β-adrenergic pathway (Appendix B Fig.B.9A–C).

Fig. 3.4. Cross-talk responses as compared to direct pathway responses.

Direct and cross-talk responses are shown in black and gray respectively. ***(A)–(C)*** NO-elicited direct response in the NO/cGMP/PKG pathway (black) is compared to its cross-talk response in the β-adrenergic pathway (gray) at 1 nM [ISO] and with varying [SNAP]. ***(D)–(F)*** ISO-elicited direct response of the β-adrenergic pathway (black) is compared to its cross-talk response in the NO/cGMP/PKG pathway (gray) at 5 nM [SNAP] and with varying [ISO]. ***(A)*** [cGMP] versus [cAMP]. ***(B)*** PKG versus PKA-I activation as a percentage of total [PKG] and [PKA-I] respectively. ***(C)*** PKG versus PKA-II activation as a percentage of total [PKG] and [PKA-II] respectively. ***(D)*** [cAMP] versus [cGMP]. ***(E)*** PKA-I versus PKG activation as a percentage of total [PKA-I] and

[PKG] respectively. ***(F)*** PKA-II versus PKG activation as a percentage of total [PKA-II] and [PKG] respectively.

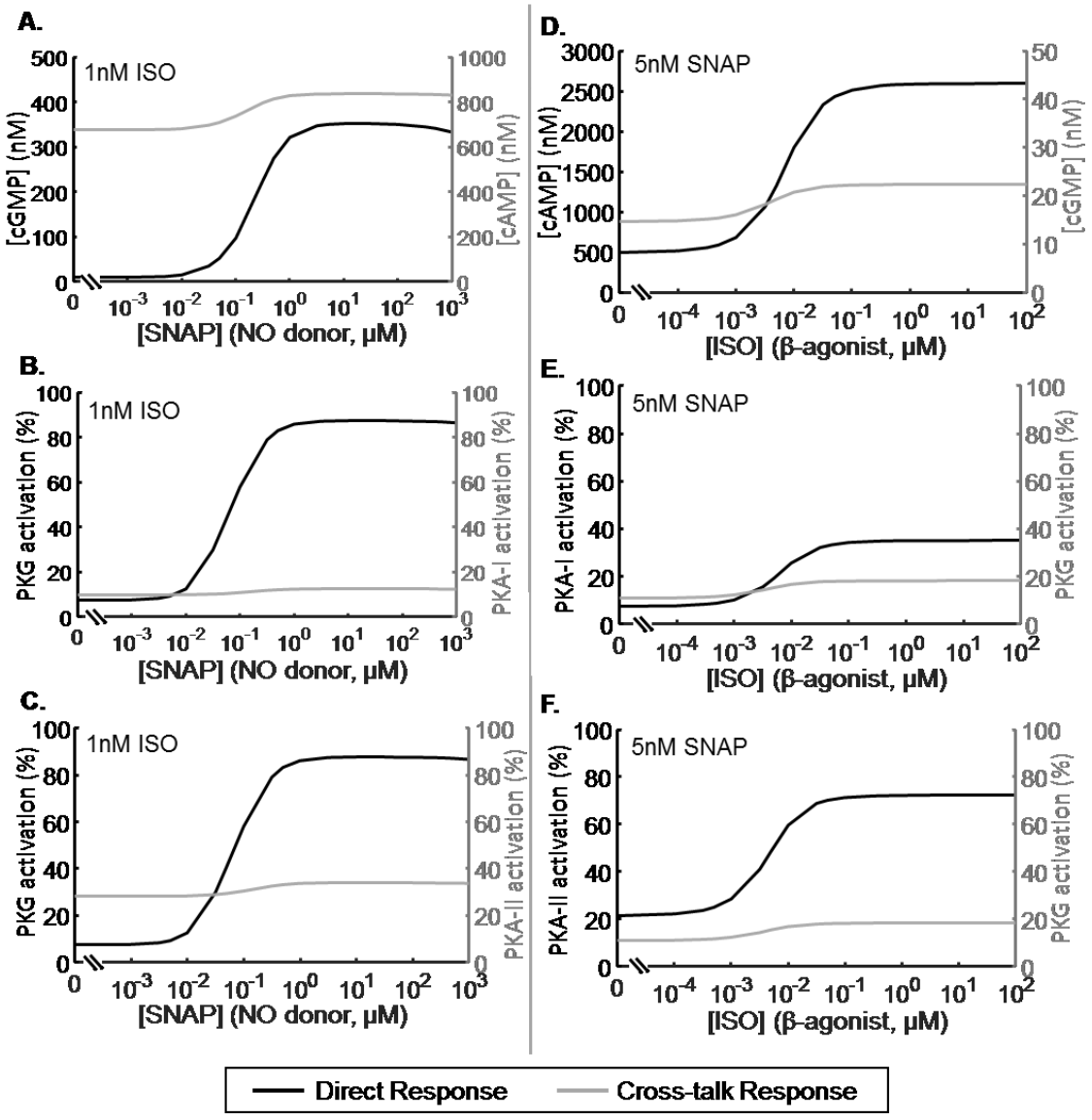

In addition, the β-adrenergic response is substantially activated by increasing [ISO] under 5 nM [SNAP], with large increases in [cAMP], PKA-I activation, and PKA-II activation (Fig. 3.4D–F respectively, black lines). Under the same simulation protocol,

the cross-talk response in the NO/cGMP/PKG pathway is also potentiated by ISO, although the increase in [cGMP] (Fig. 3.4D, gray line) and PKG activation Fig. 3.4E and F, gray lines) are relatively small in magnitude compared to that of the direct pathway response (black lines). In Appendix B Fig.B.9D and E, the cross-talk response is characterized by calculating percent increases in NO/cGMP/PKG pathway activation under low, medium, and high [ISO] (1 nM, 10 nM, and 1 μM [ISO] respectively) across various [SNAP]. The potentiation in [cGMP] and PKG activation increases with increasing [ISO], reaching maximal percent increases of ~ 60% and ~ 90% for [cGMP] and PKG activation respectively. The cross-talk response decreases with increasing [SNAP] until reaching a nadir for [SNAP] above 1 μM (Appendix B Fig.B.9D and E). In addition, percent increases in [cAMP] and PKA-I and PKA-II activation (Appendix B Fig.B.10C–E) are an order of a magnitude larger than those for the NO/cGMP/PKG pathway (Appendix B Fig.B.9D and E).

3.4.4. Mechanisms underlying cross-talk responses

Results shown in Fig. 3.5 attempt to tease apart the interactions between PDEs (black, red, blue, green, and cyan for PDEs 1–5 respectively) that give rise to the observed cross-talk responses characterized in Fig. 3.4 and Appendix B Figs. S9 and S10. At both low (1 nM; Fig. 3.5A) and high (1 μM; Fig. 3.5B) [ISO], similar mechanisms account for the observed increase of [cAMP] with increasing [NO] (or [SNAP]). Increasing [NO] increases [cGMP], and cGMP competes with cAMP for the catalytic site of PDE3. This results in a progressive decrease in PDE3 cAMP hydrolysis rate (blue), leading to a net increase in [cAMP]. The observed increases in PDE2 (red) and PDE4 (green) cAMP

hydrolysis rates due to feedback activation by increased [cAMP], and additional allosteric activation of PDE2 by cGMP are not sufficient to compensate for the steep decrease in PDE3 rate, especially at higher [SNAP] (e.g. 50 nM and 500 nM). These changes in PDE rates result in a net decrease in cAMP hydrolysis rates across all PDEs (gray) and larger cAMP accumulation at higher [SNAP]. In Fig. 3.5B, the same [SNAP] under high [ISO] conditions (e.g. 1 μM) produces much smaller changes in PDE rates. This occurs because [cAMP] is elevated in response to strong β-adrenergic stimulation, and cAMP then binds to a larger proportion of PDEs, making them less available to interact with cGMP. As such, increases in [cGMP] result in much less changes in PDE activities under high [ISO] than that under low [ISO]. The much smaller magnitude of decrease in PDE3 rates observed at high [ISO] is further compensated by increases in PDE2 and PDE4 rates, resulting in a smaller net rate increase across all PDEs (Fig. 3.5B). Consequently, the impact of NO stimulation on the β-adrenergic pathway becomes less significant under stronger β-adrenergic stimulation.

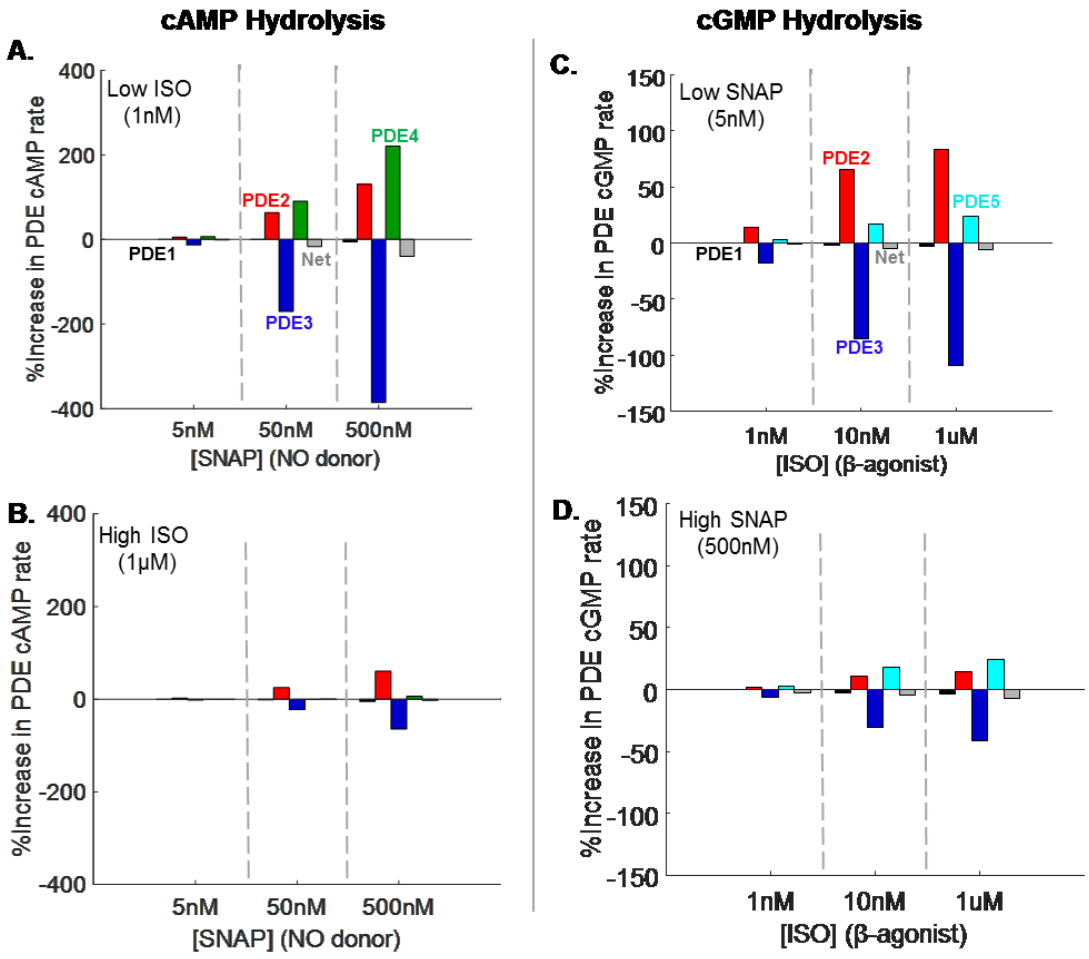

Fig. 3.5. PDE interactions underlying cross-talk response.

Shadings for PDEs 1–5 are respectively black, red, blue, green, and cyan, with gray indicating net increases across all PDEs. ***(A)*** and ***(B)*** Percent increases in PDE cAMP hydrolysis rates, under low (1 nM) and high (1 μM) [ISO] respectively. The percent increases are calculated against PDE2 cAMP hydrolysis rates without SNAP but with the same indicated [ISO]. ***(C)*** and ***(D)*** Percent increases in PDE cGMP hydrolysis rates under low (5 nM) and high (500 nM) [SNAP] and indicated [ISO], normalized to PDE2 cGMP hydrolysis rates before ISO application but under the same indicated [SNAP].

With regard to cGMP hydrolysis, as shown in Fig. 3.5C and D, increases in PDE2 (red) and PDE5 (cyan) rates over a range of [ISO] cannot fully counteract the decreases in PDE3 (blue) and PDE1 (black) cGMP hydrolysis rates, leading to a net decrease in cGMP hydrolysis rate across all PDEs (gray) and therefore the observed [cGMP] accumulation (Fig. 3.4D) and increased PKG activation (Fig. 3.4E). The decreased PDE1 (black) and PDE3 (blue) cGMP hydrolysis rates are due to increased competition of cAMP, arising from β-adrenergic stimulation, over cGMP for binding the catalytic domains of these PDEs. Increases in PDE2 and PDE5 cGMP rates are due to feedback signaling from increased [cGMP], with some additional increase in PDE2 cGMP rate arising from allosteric activation by increased [cAMP]. A comparison of Fig. 3.5D to C, in which an increased [cGMP] lessens the availability of PDEs to interact with cAMP, the impact of ISO stimulation on the NO/cGMP/PKG pathway becomes less significant under stronger NO stimulation (Fig. 3.4D and E).

3.4.5. Role of PDE2 in cN cross-talk network

Using the model, the roles of individual PDEs can be probed in the complete cross-talk network. In particular, because PDE2 exhibits multiple modes of interaction with cAMP and cGMP (Fig. 3.1B and C), it is challenging to experimentally quantify its actions in the cross-talk network. PDE2 cAMP hydrolysis rates can be allosterically activated by cGMP binding to its GAF-B regulatory domain; however, high [cGMP] can also suppress PDE2 cAMP hydrolysis rate as it competes with cAMP for its catalytic domain (Fig. 3.1B). Similarly, lower [cAMP] can increase PDE2 cGMP hydrolysis rate by occupying

GAF-B regulatory domain, while higher [cAMP] can suppress its rate by out-competing cGMP in occupying the catalytic domain (Fig. 3.1C).

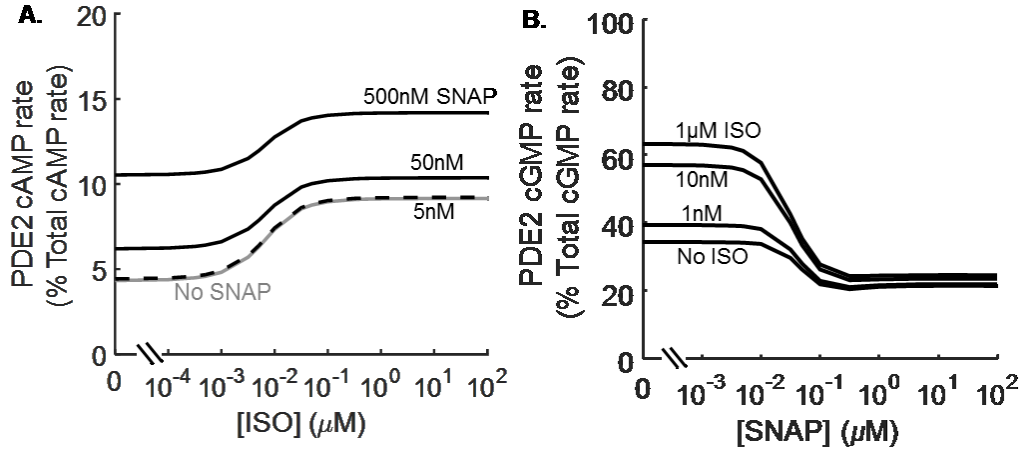

Fig. 3.6. Role of PDE2 in cross-talk signaling network.

(A) Percent cAMP hydrolyzed by PDE2 relative to total cAMP hydrolyzed at each [ISO], without SNAP and with simultaneous applications of 5 nM, 50 nM, and 500 nM [SNAP]. ***(B)*** Percent cGMP hydrolyzed by PDE2 against total cGMP hydrolyzed at each [SNAP], without ISO and with simultaneous applications of 10 nM, 100 nM, and 1 μM [ISO].

Fig. 3.6A shows predicted PDE2 cAMP hydrolysis rates as a percentage of the total cAMP hydrolysis rates of all PDEs; similarly, Fig. 3.6B shows predicted PDE2 cGMP hydrolysis rates as a percentage of the total cGMP hydrolysis rates of all PDEs. The proportion of cAMP degraded by PDE2 increases with increasing [ISO] (Fig. 3.6A). This is due to increased substrate availability from increased cAMP synthesis produced by increased β-adrenergic stimulation. The proportion of cAMP degraded by PDE2 also increased with increased [NO] from SNAP due to allosteric activation of PDE2 and compensation for the competitive inhibition of PDE1 and PDE3 cGMP activities by

cGMP. As shown in Fig. 3.6B, PDE2 is simultaneously responsible for hydrolyzing up to ~ 60% of cGMP. Increasing [ISO] potentiated the proportion of cGMP hydrolyzed by PDE2 across all [SNAP] primarily because PDE2 compensated for the decrease in PDE1 and PDE3 rates arising from competitive inhibition by elevated [cAMP]. On the other hand, increased [cGMP] from increased [SNAP] increased PDE5 cGMP hydrolysis rate such that the proportion of cGMP hydrolyzed by PDE2 is lower at higher [SNAP].

3.4.6. NO/cGMP/PKG activity potentiated by PDE5 inhibition is partially compensated by PDE2

The effect of PDE5 inhibition has been investigated extensively because of its therapeutic promise in treating heart diseases such as cardiac hypertrophy and heart failure [9, 47-49]. The model makes predictions about the impact of PDE5 inhibition on changes in PDE interactions under varying extent of β-adrenergic and NO stimulation (Fig. 3.7). Fig. 3.7 shows effects of strong PDE5 inhibition (90%) on all PDEs (Fig. 3.7A), and varying levels of PDE5 inhibition on PDE2 cGMP hydrolysis rates (Fig. 3.7B), [cGMP] (Fig. 3.7C), and PKG activation (Fig. 3.7D) as [ISO] is varied in the presence of medium level of [SNAP] (50 nM). In order to study the effect of PDE5 inhibition under varying [ISO], percent increase in response is given relative to values prior to PDE5 inhibition at the selected [SNAP] without ISO. As shown in Fig. 3.7A, upon PDE5 inhibition, the compensatory increase in PDE2 cGMP rate is the greatest among the cGMP hydrolyzing PDEs regardless of [ISO], with magnitudes that also scale with the extent of PDE5 inhibition (Fig. 3.7B). The cGMP rate increases in PDEs 1–3 are due to increased cGMP-occupancy of their catalytic domains (Appendix B Fig.B.12A). Reciprocally,

compensatory increase in PDE5 cGMP rates is also the greatest upon PDE2 inhibition (Appendix B Fig.B.11). As a result, among all PDEs, PDE2 and PDE5 compensate most strongly for a reduction in activity of the other, a behavior we refer to as strong coupling. In addition, as shown in Fig. 3.7C and D, PDE5 inhibition leads to sizable increases in [cGMP] and consequently PKG activation.

Fig. 3.7. NO/cGMP/PKG pathway responses under PDE5 inhibition.

All simulation data shown are percent increases upon PDE5 inhibition relative to their respective values prior to inhibition under a medium level of [SNAP] (50 nM) without ISO stimulation. Varying degrees of PDE5 inhibition (20%, 50%, and 90%) is simulated with simultaneous SNAP application under the indicated [ISO] for 30 min. ***(A)*** Percent increases in cGMP hydrolysis rates of PDEs 1–3 and 5 upon 90% PDE5 inhibition. ***(B)–(D)*** respectively, percent increases in PDE2 cGMP rates, [cGMP], and PKG activation upon 20%, 50%, and 90% PDE5 inhibition.

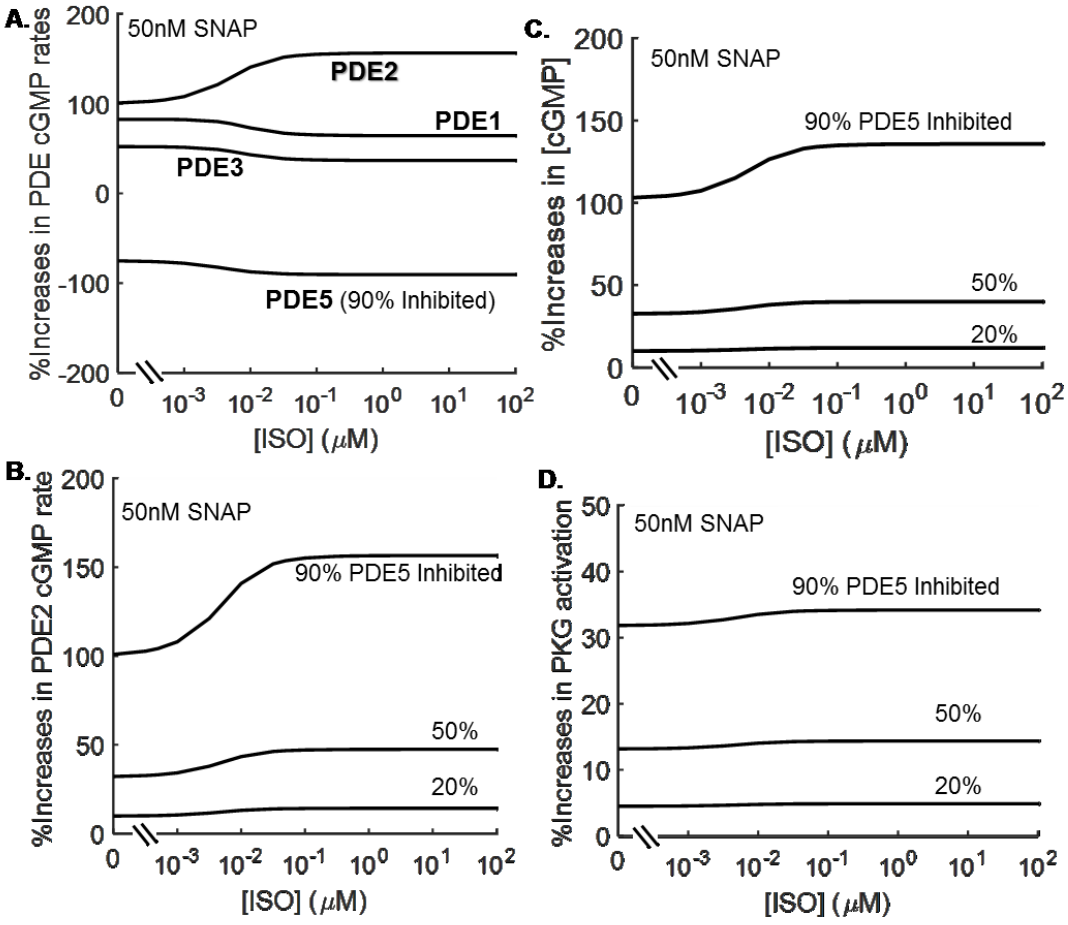

3.4.7. Whole-cell [cAMP] is stabilized under PDE5 inhibition via PDE2 activation

Fig. 3.8 shows the impact of PDE5 inhibition on β-adrenergic response. As shown in Fig. 3.8A, PDE5 inhibition indirectly leads to a decrease in PDE3 cAMP hydrolysis rates. There is also a smaller magnitude of PDE1 cAMP hydrolysis rate decrease, which is less significant due to the smaller overall PDE1 cAMP degradation capacity compared to that of PDE3. Changes in PDE rates are observed because increased [cGMP] from PDE5 inhibition (Fig. 3.7A) competes with cAMP for the catalytic domains of PDEs 1 and 3

(Appendix B Fig.B.12B) and suppresses their cAMP hydrolysis rate. On the other hand, a large increase in PDE2 cAMP hydrolysis rate results from allosteric activation by cGMP and feedback regulation by the elevated [cAMP] (Appendix B Fig.B.12B). The resulting elevation in [cAMP] is therefore almost completely compensated for by PDE2 (Fig. 3.8B). The increase in PDE2 (Fig. 3.8C) and decrease in PDE3 (Fig. 3.8D) rates vary depending on the extent of PDE5 inhibition, preventing changes in β-adrenergic response under PDE5 inhibition regardless of [ISO] (Fig. 3.8B).

Fig. 3.8. β-adrenergic pathway activity under PDE5 inhibition.

All simulation data shown are percent increases upon PDE5 inhibition relative to their respective values prior to inhibition under the same [SNAP] (50 nM) without ISO stimulation (same normalization as in Fig. 3.7). ***(A)*** Percent increases in cAMP hydrolysis rates of PDEs 1–4 upon 90% PDE5 inhibition. ***(B)–(D)*** respectively, percent increases in [cAMP], PDE2 cAMP rates, and PDE3 cAMP rates upon 20%, 50%, and 90% PDE5 inhibition.

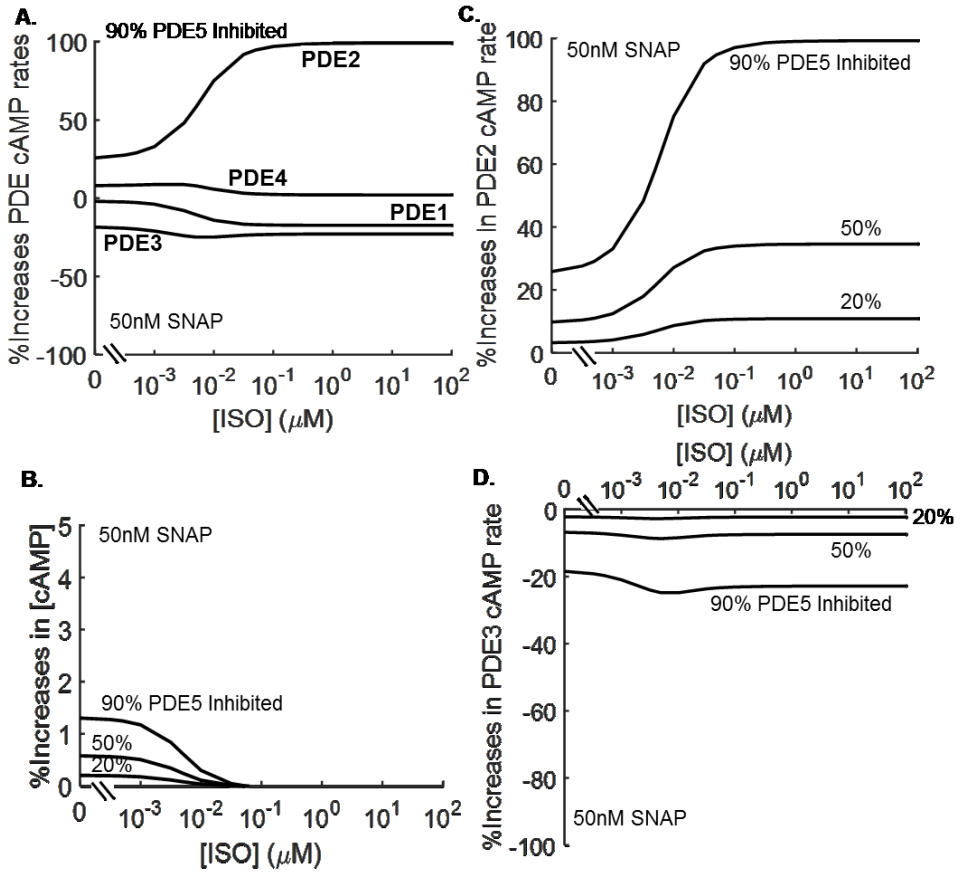

3.5. Discussion

3.5.1. Multi-scale modeling of cN signaling reveals cross-talk responses and mechanisms

By measuring responses downstream of the signaling network, independent activation of the β-adrenergic pathway by β-agonists and the NO/cGMP/PKG pathway by NO are observed to result in antagonistic actions, with the former strengthening and the latter attenuating cardiac contractility [5, 8, 10, 13-16]. Balanced signaling between cAMP and cGMP is crucial in maintaining normal cardiac function, especially when prominent

remodeling of the cN signaling network is also observed in cardiac hypertrophy and heart failure, potentially contributing to altered and/or untargeted cN signals, aberrant phosphorylation of target proteins, and cardiac dysfunction [3, 34-37]. However, relatively little is known about the ways in which different PDE isoforms regulate the cN cross-talk that enables communication between the β-adrenergic and NO/cGMP/PKG pathways. Several factors make it difficult to understand these interactions: a) PDEs degrade the same cAMP and cGMP signals that regulate their activities (Fig. 3.1A); b) multiple PDE isoenzymes function synergistically in the common task of cAMP and cGMP degradation (Fig. 3.1A); c) a variety of positive and negative regulatory relationships exist between PDEs, cGMP, and cAMP (Fig. 3.1B and C). As a result, when the activity of one PDE is altered, the activities of other PDEs will also change to partially compensate for the change in cN signals, activating a subset or all of the many reaction mechanisms identified in Fig. 3.1B–C on a scenario-dependent basis. By precisely defining biochemical reactions comprising the cN cross-talk network (Fig. 3.1), models are useful tools for revealing the mechanisms of PDE interaction underlying the communication between the β-adrenergic and NO/cGMP/PKG pathways.

The model presented here enables analysis of the roles of each PDE in the context of the full signaling network. Model analyses demonstrate that: a) at sub-maximal levels of β-adrenergic stimulation, simultaneous NO stimulation decreases PDE3 cAMP hydrolysis rate, which overcomes increases in PDE2 and PDE4 rates, resulting in a modest increase of whole-cell [cAMP] and the observed NO-mediated potentiation of Protein Kinase A (PKA) activation; b) at sub-maximal levels of NO stimulation, the decreased PDE3 cGMP hydrolysis rates produced by simultaneous β-adrenergic

stimulation overcomes increases in the rates of PDE2 and PDE5, resulting in a net increase of [cGMP] and PKG activation (Fig. 3.4 and Fig. 3.5); c) PDE2 exerts more control of cytosolic [cAMP] and [cGMP] under increasing β-adrenergic stimulation and decreasing NO stimulation (Fig. 3.6); d) due to PDE2 compensation, the anti-adrenergic effect of PDE5 inhibition is mediated via increased PKG activation (Fig. 3.7) while changes in whole-cell β-adrenergic response are kept small (Fig. 3.8). These results reflect that redundancy of the PDEs in the cN signaling network contributes a degree of robustness to perturbations. This compensatory coupling between PDEs may be an important mechanism in controlling cN dynamics in the heart [3, 42, 113], including disease settings where alterations in isoenzyme-specific PDE expression and/or activity have been implicated [3, 39, 41-43, 50, 113-115, 144-146].

3.5.2. PKG is likely to suppress downstream target activity as cross-talk responses are stimulatory

Understanding the effects of NO on biological tissues remains challenging in part because NO, a highly reactive gas, is difficult to manipulate and has many reaction pathways and targets [15, 16, 33, 77, 147-150]. Prior experimental results have found that NO decreases the cardiac functional response to β-adrenergic stimulation [16, 147, 151-153]. For instance, in cardiac ventricular myocytes, pre-stimulated whole-cell LCC current via β-adrenergic pathway stimulation is diminished by increased [NO] [154] and inotropic responses to β-adrenergic stimulation are enhanced in eNOS knockout (eNOS-/-) mice [155]. On the other hand, the exact mechanisms underlying these findings remain unclear [78, 151, 153], in part because vast majority of these experimental readouts have

not been actual cAMP and cGMP signals but have been inferred by their effects on other targets following interventions aimed to alter their concentrations.

To refine our understanding, we precisely defined the signal transduction mechanisms elicited by NO in the cN signaling network in terms of a model. Simulations show that, NO produced modest increases of [cAMP] and PKA activation at levels of [ISO] that do not saturate β-adrenergic response (gray lines in Fig. 3.4A–C and Appendix B Fig.B.9A–C). This potentiation under sub-maximal β-adrenergic stimulation results from increased PDE2 and PDE4 and decreased PDE3 cAMP hydrolysis rates (Fig. 3.5A). Under strong β-adrenergic tone, the PDEs are more fully saturated with cAMP and thus become less available for cGMP binding (Fig. 3.5B); thereby, the β-adrenergic pathway becomes less responsive to NO stimulation (Appendix B Fig.B.9A–C). Our model therefore suggests that, in cardiac myocytes, NO-mediated inhibition of β-adrenergic response is not likely to arise from cGMP-mediated stimulation of PDE cAMP hydrolysis activities. On the global whole-cell/cytosolic level, the proposed mechanism is contrary to previous conclusions that NO suppresses [cAMP] via cN cross-talk based on observations of suppressed β-adrenergic responses of downstream targets upon NO stimulation [17, 77, 78]. The model predicts that despite NO-mediated stimulation of [cAMP] and PKA activation, NO more strongly activates the NO/cGMP/PKG pathway (Fig. 3.4A–C, black lines) and the inhibitory effects of NO on the β-adrenergic responses are likely due to the direct actions of PKG on its molecular targets. This direct response is likely to be strong enough to overcome the additional cross-talk activation, as well as attenuating the ISO-stimulated activation of β-adrenergic pathway. This mechanism is supported by experimental observations that PKG phosphorylates LCCs on α_1- and β-

subunits [156, 157] and that activation of PKG attenuates the β-adrenergic potentiation of LCC single channel open probability [158-161] and whole-cell current [154, 162]. Overall, the model suggests that NO activation of PKG dominates over its positive effects on cAMP/PKA. As a result, the model-predicted NO potentiation of β-adrenergic pathway activity is consistent with experimentally observed NO-mediated anti-adrenergic effects on target actives [16, 147, 151-153]. These predictions of the model could be tested experimentally.

Reciprocally, the model shows that β-adrenergic stimulation can result in increased [cGMP] and subsequent PKG activation (gray lines in Fig. 3.4D–E), especially under lower levels of NO stimulation (Appendix B Fig.B.9D and E). Increased [cAMP] from β-adrenergic stimulation out-competes cGMP for catalytic domains of PDE1 and PDE3 suppressing their cGMP hydrolysis rates, which are not fully counteracted by the compensatory increase in PDE2 and PDE5 rates, leading to a net decrease in cGMP hydrolysis rate across all PDEs. In a manner similar to the diminished cross-talk response of the β-adrenergic stimulation under high [ISO] (Appendix B Fig.B.9A–C), the impact of ISO stimulation on the NO/cGMP/PKG pathway becomes less significant under strong NO stimulation (Appendix B Fig.B.9D and E), because the resulting higher [cGMP] reduces the availability of PDEs to interact with cAMP resulting in smaller changes in PDE rates. At present, experimental studies are limited with respect to the effects of β-adrenergic stimulation on the NO/cGMP/PKG pathway. This may be the case because simultaneous ISO stimulation with NO produced much larger effects on [cAMP] and PKA activation (Appendix B Fig.B.10C–E) than on [cGMP] and PKG activation (Appendix B Fig.B.9D and E). On the other hand, Sumii and Sperelakis showed that ISO

stimulated whole-cell LCC current is inhibited by PKG [163]. In addition, it has long been established that β-adrenergic stimulation of LCC occurs via PKA-phosphorylation of the channel [164]. Interpreting these data through the model, we expect that β-adrenergic activation of PKA is likely to dominate over its potentiation of the NO/cGMP/PKG pathway. This is supported by our simulation result that direct effect of ISO on β-adrenergic pathway activation (black) is much more pronounced than its cross-talk effect (gray) on the NO/cGMP/PKG pathway (Fig. 3.4D–E).

3.5.3. PDE2 serves as a nexus in cAMP-cGMP cross-talk

PDE2 exhibits complex interactions with both cNs and serves as a nexus for cAMP-cGMP cross-talk. Increased PDE2 expression in HF is observed to blunt β-adrenergic signaling with PDE2 inhibition partially restoring β-adrenergic responsiveness in diseased cardiac myocytes [43]. Adenoviral PDE2 overexpression in healthy cardiac myocytes also markedly decreased [cAMP] upon β-adrenergic stimulation with effects reversed by PDE2 inhibition [43]. However, PDE2 EC50s are at least tenfold higher than the cellular-average [cAMP] and [cGMP], and approximately tenfold higher than that of other PDEs [17, 29, 32, 107], properties which are replicated by the model (Appendix B Fig.B.7). By itself, these high EC50s suggest that PDE2 would play a minor role in regulating cytosolic cAMP and cGMP in cardiac myocytes [62, 69, 102, 103]. When interpreted through a quantitative model which accounts for the complex interactions among PDEs, the role of PDE2 in cN hydrolysis manifested in experiments is exposed.

PDE2 hydrolyzes a larger proportion of cAMP than what may be inferred from the minute changes in [cAMP] observed upon PDE2 inhibition [62, 69, 102, 103]. Via

negative feedback by cAMP, the hydrolysis rates of the remaining PDEs increase to compensate for the loss of PDE2 activity. Therefore the negligible net change in [cAMP] under PDE2 inhibition is not a true reflection of the proportion of cAMP hydrolyzed by PDE2 [127]. By direct measurement of its hydrolysis activity, simulations reveal that despite having an EC50 at least tenfold higher than the other PDEs, PDE2 is responsible for hydrolyzing a sizable proportion of cAMP in the cross-talk (Fig. 3.6A). Simulation also reveals that PDE2 hydrolyzes larger proportions of cGMP than it does cAMP. It exerts more control of cGMP with increasing [ISO] but lower [NO]. In addition, because of its high EC50s, PDE2 can be further activated at elevated [cAMP] and [cGMP] when other PDE isoenzymes have already reached their maximum hydrolysis capacity. As a result, PDE2 may exert a greater functional role than previously concluded based on experiments which showed only small changes of cN signals upon PDE2 inhibition [62, 69, 102, 103].

3.5.4. Anti-adrenergic effect of PDE5 inhibition is facilitated by PDE2

Selective inhibition of PDE5 has been intensively investigated because of its potential cardio-protective effects in various cardiac pathologies, such as heart failure, cardiac hypertrophy, and ventricular arrhythmias [9, 47-49]. Model simulations provide insights into the effects of PDE5 inhibition on changes in PDE interactions under differing conditions of β-adrenergic and NO stimulation (Fig. 3.7 and Fig. 3.8). The model demonstrates that PDE5 inhibition is partially compensated for by an increase in PDE2 cGMP rate Fig. 3.7A); therefore, [cGMP] and PKG activation are prevented from further elevation above the observed respective maxima (Fig. 3.7C and D). Modeling results

further show that PDE2 strongly compensates for the reduced activity of PDE5 and, similarly, that PDE5 strongly compensates for PDE2 inhibition, (Fig. 3.7 and Appendix B Fig.B.11). In addition, an increase in PDE2 cAMP rates prevented an increase in β-adrenergic activation under PDE5 inhibition, especially at high [ISO] (Fig. 3.8), which could have resulted from decline in PDE3 cAMP rates due to competitive inhibition by the elevated [cGMP] (Fig. 3.7). As a result, the anti-adrenergic effect of PDE5 inhibition is likely mediated by PKG phosphorylation of downstream targets, instead of suppressing cAMP via pathway cross-talk. Such anti-adrenergic effect is further facilitated by the prevention of sizable increases in β-adrenergic activation (Fig. 3.8). This is a novel insight regarding the role of PDE2 in HF. This compensation will be further enhanced through inhibition of PDE5 in HF and cardiac hypertrophy, as both PDE2 and PDE5 are up-regulated [43, 144-146].

3.5.5. Model rationale, limitations, and future work

Our current study focuses on investigating PDE interactions that give rise to cross-talk behavior of the cN signaling network (Fig. 3.1). Recent advances have revealed that many signaling components in the network form compartments and/or multi-protein signaling complexes ("signalosomes") [36, 63, 67, 121-124]. With advancements in methods for spatiotemporally-resolved recording of cAMP [36, 63, 67, 121-124] and cGMP [82, 120, 165], extending the model to include these additional mechanisms is an important next step to understand diversification of cN signals in subcellular micro-domains and communication between these cellular compartments. Under conditions exhibiting high [cGMP], cAMP-cGMP positive cross-talk is likely to be more substantial

than that shown in Fig. 3.4 [127]. In addition, NO-derived cGMP and natriuretic peptide (NP)-derived cGMP reside in distinct subcellular compartment [82, 166], exerting differential regulation of β-adrenergic responses [17, 77, 78, 120, 167]. Functional re-distribution of PDEs between these two cGMP compartments has been observed in diseased cardiac myocyte [120, 165, 166]. These discoveries together with more in-depth analysis of the cN cross-talk signaling network provide new opportunities for model expansion in future research. Changes in cN signals can be magnified many folds in the responses of downstream targets. For instance, LCCs, critical to cardiac excitation-contraction coupling [7, 168], respond sensitively to β-adrenergic stimulation [5, 169]. Important next steps will be extensions of the signaling model to study its regulation of transmembrane channels and calcium cycling proteins, and eventually for the model to be incorporated into integrative models of the ventricular myocyte.

3.6. Conclusions

We developed a computational model of the cN cross-talk signaling network (Fig. 3.1) that mechanistically integrates the β-adrenergic and the NO/cGMP/PKG pathways (Fig. 3.2 and Fig. 3.3) to investigate the roles of distinctively-regulated PDE isoenzymes in regulating cAMP and cGMP signal dynamics. Using the model, we deciphered the underlying mechanisms of three model observations a) via cN cross-talk, β-adrenergic pathway and NO/cGMP/PKG pathway responses are potentiated upon stimulation by NO and β-agonist respectively (Fig. 3.4 and Fig. 3.5), but this cross-talk response is dominated by the direct response; b) PDE2 exerts increasing control of cytosolic [cAMP]

under higher β-adrenergic stimulation, but exerts increasing control of [cGMP] at decreasing levels of NO stimulation (Fig. 3.6); c) due to compensatory action by PDE2, PDE5 inhibition enhanced [cGMP] and PKG activation but not whole-cell β-adrenergic response (Fig. 3.7 and Fig. 3.8).

Disclosures

None declared.

Acknowledgements

This work was supported by Natural Sciences and Engineering Research Council (NSERC) of Canada scholarships, CGS M-377616-2009 and PGSD3-405041-2011, awarded to C.Y.Z, and National Heart Lung and Blood Institute (NHLBI) of the USA grant R01 HL105239.

Appendix B. Supplementary Material for the cN Signaling Network Model

Chapter 4. Mechanisms of the Cyclic Nucleotide Cross-Talk Signaling Network in Cardiac L-Type Calcium Channel Regulation

4.1. Abstract

Regulation of L-type calcium (Ca^{2+}) channel (LCC) gating is critical to shaping the cardiac action potential (AP) and triggering the initiation of excitation-contraction (EC) coupling in cardiac myocytes. The cyclic nucleotide (cN) cross-talk signaling network, which encompasses the β-adrenergic and the Nitric Oxide (NO)/cGMP/Protein Kinase G (PKG) pathways and their interaction (cross-talk) through distinctively-regulated phosphodiesterase isoenzymes (PDEs), regulates LCC current via Protein Kinase A- (PKA) and PKG-mediated phosphorylation. Due to the tightly-coupled and intertwined biochemical reactions involved, it remains to be clarified how LCC gating is regulated by the signaling network from receptor to end target. In addition, the large number of EC coupling-related phosphorylation targets of PKA and PKG makes it difficult to quantify and isolate changes in L-type Ca^{2+} current (I_{CaL}) responses regulated by the signaling network. We have developed a multi-scale, biophysically-detailed computational model of LCC regulation by the cN signaling network that is supported by experimental data. LCCs are modeled with functionally distinct PKA- and PKG-phosphorylation dependent gating modes. The model exhibits experimentally observed single channel characteristics, as well as whole-cell LCC currents upon activation of the cross-talk signaling network.

Simulations show 1) redistribution of LCC gating modes explains changes in whole-cell current under various stimulation scenarios of the cN cross-talk network; 2) NO regulation occurs via potentiation of a gating mode characterized by prolonged closed times; and 3) due to compensatory actions of cross-talk and antagonizing functions of PKA- and PKG-mediated phosphorylation of LCC, the effects of individual inhibitions of PDEs 2, 3, and 4 on I_{CaL} are most pronounced a low levels of β-adrenergic stimulation. Consequently, the model reveals underlying mechanisms of observed LCC current behavior under various stimulation scenarios of the signaling network. These results provide insights into how cN signals transduced via the cN cross-talk signaling network are integrated via LCC regulation in the heart.

Key Words: Phosphodiesterases, cyclic nucleotides, signaling network, L-type calcium channel, cardiac myocytes, computational model.

4.2. Introduction

The cardiac voltage-gated L-type calcium (Ca^{2+}) channels (LCCs) initiate and coordinate a series of events that give rise to cardiac myocyte action potential (AP) and contraction and relaxation within each heartbeat [170, 171]. Activated upon membrane depolarization, the LCCs allow Ca^{2+} influx across the sarcolemma [5]. This small amount of Ca^{2+} through LCCs triggers the opening of ryanodine receptors (RyRs) which allow larger amounts of Ca^{2+} to be released from the sarcoplasmic reticulum (SR) Ca^{2+} store, a process known as Ca^{2+}-induced Ca^{2+} release (CICR) [5, 172]. The elevated Ca^{2+}

concentration ([Ca^{2+}]) promotes Ca^{2+} binding to myofilaments, initiating contraction [173, 174]. The process from electrical excitation to mechanical contraction of the myocyte is referred to as the cardiac excitation-contraction (EC) coupling [5, 7].

Fig. 4.1. Model representation of LCC regulation by the cN cross-talk signaling network.

(A) The cN cross-talk signaling network model from Zhao et al. [175] is composed of the β-adrenergic and NO/cGMP/PKG pathways (red and blue color schemes respectively) as well as the PDEs that regulate cN degradation (yellow color scheme). The PDEs are in turn regulated by the cNs; therefore, they also facilitate cross-talk between the β-adrenergic and NO/cGMP/PKG pathways [127, 175]. The entire signal network transduces stimuli (e.g. ISO and NO) to the activation of PKA and PKG, which then respectively deliver stimulatory (green arrow) and inhibitory (red arrow) control of LCC (grey color scheme). Model schematics adapted from Zhao et al. [175]. (B) Each individual LCC undergo voltage- and Ca2+-dependent gating (left) and an independent process of voltage-dependent inactivation (VDI) (right), according to a model from Greenstein and Winslow [176]. PKA- and PKG-mediated phosphorylation of LCC promotes LCCs into district gating modes, characterized by distinct gating parameters f_{modei} (blue) and g_{modei} (red). Model schematics adapted from Greenstein and Winslow [176].

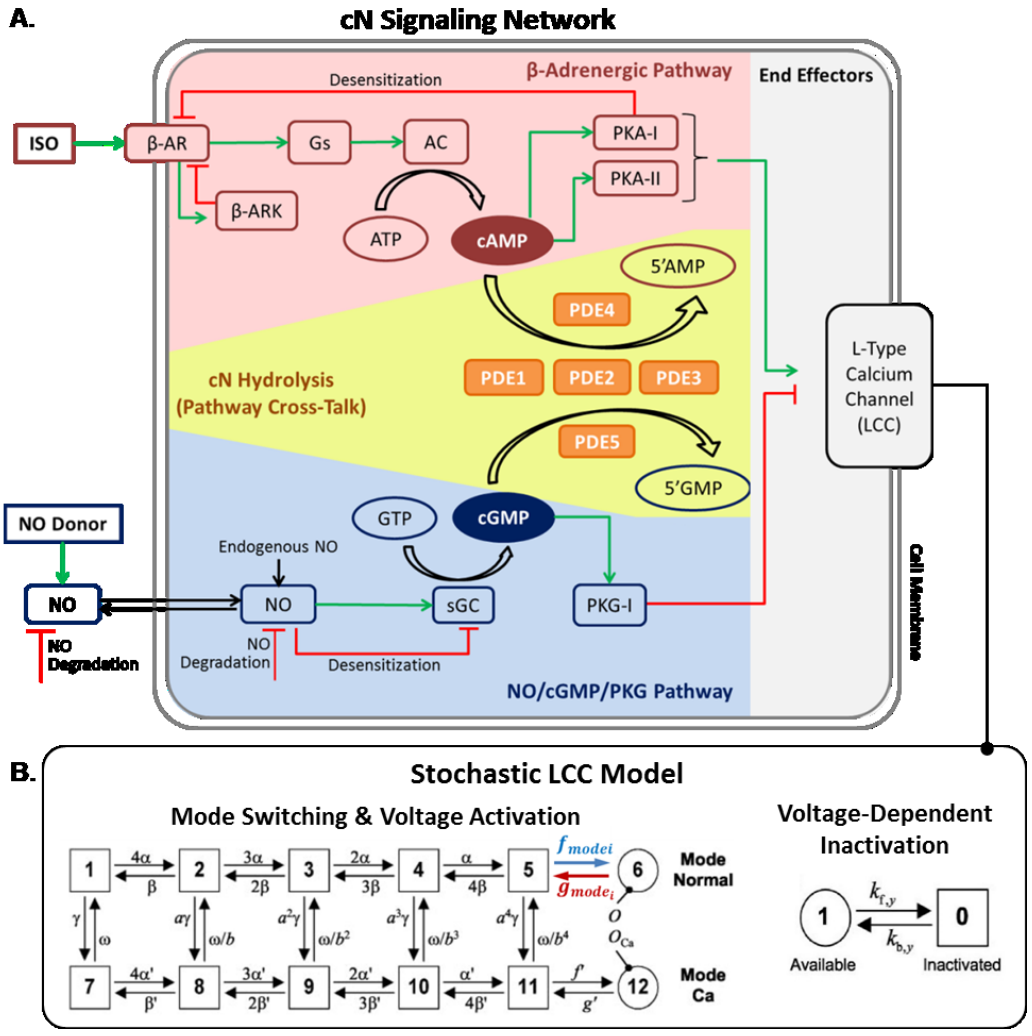

The cyclic nucleotide (cN) cross-talk signaling network (Fig. 4.1A) can deliver both stimulatory (green arrow) and inhibitory (red arrow) regulatory influences on LCCs (Fig. 4.1B). It regulates the dynamics of the two cyclic nucleotides (cNs), cyclic adenosine-3′, 5′-monophosphate (cAMP) and cyclic guanosine-3′, 5′-monophosphate (cGMP), as well as the subsequent activation of protein kinase A (PKA) and protein kinase G (PKG) [127, 175]. Our previous work constructed a mechanistic model of the cN cross-talk signaling network [127, 175], which is composed of the β-adrenergic signaling pathway (red color scheme), nitric oxide (NO)/cGMP/PKG signaling pathway

(blue color scheme), and the cross-talk between them (yellow color scheme) as facilitated by five distinctively regulated families of phosphodiesterases (PDEs) (orange boxes). As shown in Fig. 4.1B, the random openings and closings of LCC is a result of Ca^{2+} dependent inactivation (CDI) (vertical transitions) and voltage activation (horizontal transitions) (left model) and a voltage-dependent inactivation (VDI) process (right model) [176]. This stochastic gating behavior giving rise to the whole cell L-type Ca^{2+} current (I_{CaL}) is further regulated by gating mode switching (colored transitions, Fig. 4.1B, left model) in response to the cN cross-talk signaling network via PKA- and PKG-mediated phosphorylation of the channel [5, 9].

Stimulation of the β-adrenergic and NO/cGMP/PKG pathways promote opposing physiological responses, with the former enhancing cardiac inotropy and lusitropy [5, 13] and the latter attenuating cardiac contractility [8, 10, 14-16] and antagonizing β-adrenergic tone [17-19, 21-28]. Many signaling components in the cN signaling network are also altered in cardiac hypertrophy and heart failure (HF) [3, 34-37]. Furthermore, changes in I_{CaL} leads to alterations in EC coupling and is a key mechanism in AP duration (APD) prolongation, a hallmark of HF [168, 177], and in increasing the likelihood of early after-depolarizations (EADs) [178]. Despite its physiological significance, mechanisms of LCC regulation by the cN cross-talk signaling network remain to be further investigated. First, the large number of EC coupling-related PKA and PKG phosphorylation targets [5, 9] and the interdependence of these targets in CICR and/or EC coupling [172] make it challenging to quantify and isolate the changes of I_{CaL} caused by cN cross-talk network regulation. In addition, the behavior of the PKA and PKG signals that regulate LCCs are non-intuitive due to the large number of interacting

proteins in the cN cross-talk signaling network (Fig. 4.1A) [127, 175]. Furthermore, the means through which the two kinases, PKA and PKG, simultaneously phosphorylate the same LCC target needs to be clarified.

As a result, multiple mechanisms may underlie observed changes in I_{CaL} upon activation of the signaling network. In order to dissect the role of cN cross-talk signaling network in its regulation of LCC, we constructed an integrative mathematical model that allows dynamic regulation of stochastic LCC gating as a function of β-adrenergic and NO stimulation (Fig. 4.1). Three insightful predictions emerge from this model. First, changes in I_{CaL} under varying extents of stimulation of the cN cross-talk network can be explained by redistribution of LCCs among four distinct gating modes. Second, NO suppression of I_{CaL} occurs via potentiation of a gating mode characterized by prolonged closed times, which mirrors the fact that β-adrenergic stimulation of I_{CaL} is a result of promoting a distinct gating mode characterized by prolonged open times [179, 180]. Finally, individual inhibitions of PDEs 2, 3, and 4 produce no changes in I_{CaL} under basal, non-stimulated conditions. The resultant changes in I_{CaL} are more pronounced at lower, instead of higher levels, of β-adrenergic stimulation. These aforementioned I_{CaL} behaviors are due to two major compensatory actions that attempts to lessen changes in I_{CaL}: 1) mechanisms comprising cN cross-talk that stabilizes cAMP and cGMP concentrations ([cAMP] and [cGMP]); and 2) redistribution between distinct gating modes of LCCs in response to PKA-PKG-mediated phosphorylation.

4.3. Materials and methods

The complete model described in this work (Fig. 4.1) is referred to as the cN signaling-LCC model, consisting of three modules: 1) the cN signaling network model; 2) the PKA-PKG-LCC model; and 3) the LCC gating model. We integrate previously developed cN cross-talk signaling network model from Zhao et al. [175] with a LCC model from Greenstein and Winslow [176], originally developed by Jafri et. al. [181], through PKA- and PKG- mediated regulation of the channel (Fig. 4.2), with details of model construction explained below. We aimed to construct the simplest model with minimal alternations to existing models and that will explain the most experimental data. Further details of the model are presented in the Supplement: symbols are defined in Appendix C Sect. C.1; Sect. C.2 provides all model equations; Sect. C.3 defines and gives nominal values for model parameters; Sect. C.4 lists state variable initial conditions. In addition, Appendix C Sect. C.4 and Sect. C.6 provide details on simulations conditions and additional simulation results respectively. All figures contained in this paper, including those in Appendix C, are generated with the same set of parameters and state variable initial conditions.

4.3.1. The cN cross-talk signaling network model

We incorporated a previously-developed model of the cN cross-talk signaling network (Fig. 4.1A) that described the communication between the β-adrenergic and the NO/cGMP/PKG pathways through mechanistic models of PDEs 1, 2, 3, 4, and 5 [175, 182]. PDEs 1, 2, and 3 can hydrolyze both cAMP and cGMP, while PDE4 and PDE5 are

respectively cAMP- and cGMP- specific [175, 182]. The PKA and PKG activities predicted by this model are used to drive the PKA-PKG-LCC model described below.

4.3.2. The PKA-PKG-LCC model

For the PKA-PKG-LCC model (Fig. 4.2), the proportion of LCCs in each state is a function of activated PKA-II and PKG-I, whose activity are, in turn, regulated by the cN cross-talk signaling network model described above. As shown in Fig. 4.2A, the distribution of LCCs between the "Unavailable" and "Available" States will determine the number of channels available for opening. Increased activation of PKA-II promotes more channels to become available (white) from their unavailable states (grey shaded). This transition is opposed by increased PKG activity. This is supported by experimental evidence that activation of PKA increase [160, 179, 180] and activated PKG suppresses channel availability [160, 161].

It has been demonstrated that PKA phosphorylation of at least one Serine site on LCC is related to its β-adrenergic response [164, 183] and that LCCs have PKG phosphorylation sites [156, 157]. In addition, by comparing putative PKA and PKG phosphorylation sites on LCC as reviewed by Benitah, et al. [49], Harvey et al. [164], Keef et al. [78], and van der Heyden et al. [184], PKA and PKG have distinct phosphorylation sites on LCC, except Serine 1928. However, the functional role of Serine 1928 in LCC β-adrenergic regulation has been challenged by Ganesan et al. [185]. As a result, our model (Fig. 4.2B) assumes that PKA and PKG have distinct phosphorylation sites on LCC and therefore that LCC can be non-, PKA-, PKG-, and PKA-and-PKG phosphorylated (grey boxes on top). LCCs phosphorylated by PKA and

PKG are respectively denoted by red and blue symbols of encircled “P”, with the phosphorylation rates proportional to the activities of the respective kinases (i.e. activated PKA and PKG).

Fig. 4.2. State diagram for PKA-PKG-LCC Model.

The PKA-PKG-LCC Model regulates LCC channel availability (A) and distribution of LCCs among four distinct gating modes (B). (A) The proportion of channels in the available (white) and unavailable (grey shaded) states are determined by the extent of PKA-II and PKG activation. This transition is opposed by increased PKG activity. (B) Increased activations of PKA and PKG promote the channels to be phosphorylated by the respective kinases, with dephosphorylation regulated by protein phosphatase, PP2A. Phosphorylation by PKA and PKG are respectively denoted by red and blue symbols with encircled “P”. Clockwise from upper-left corner, the proportions of channels in each of non-, PKA-, PKA-and-PKG-, and PKG-phosphorylated states (grey-shaded boxes on top) correspond to distinct gating modes of Mode 1, Mode A, Mode AG, and Mode G (white boxes at the bottom).

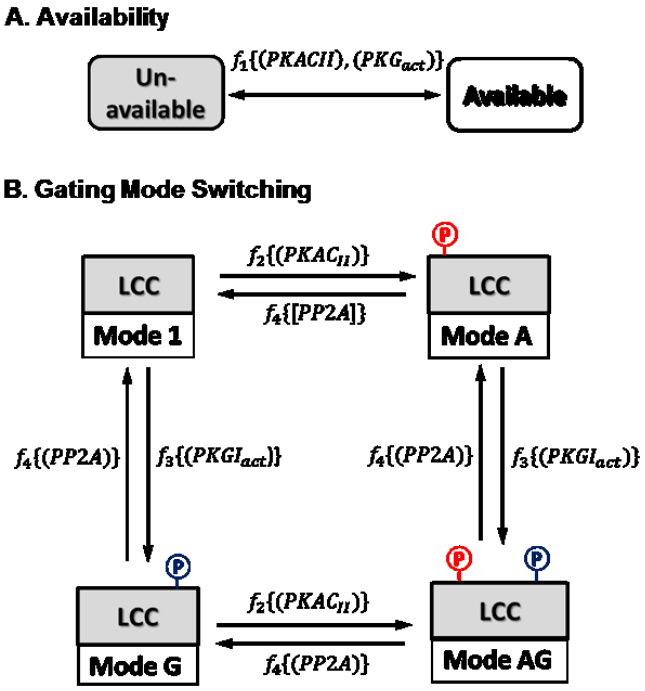

In order clockwise from the upper-left-hand corner of Fig. 4.2B, we modeled four distinct patterns of channel openings and closings or gating modes, namely Mode 1, Mode A, Mode AG, and Mode G (white boxes), corresponding respectively to the four phosphorylation states, non-, PKA-, PKA-and-PKG, and PKG-phosphorylated (grey boxes). Based on experimental literature, Mode 1 is the predominant mode of LCC gating under basal, non-stimulated conditions, characterized by repeated brief openings [176, 179]. Mode A is a high-activity gating mode, characterized by prolonged channel openings [179, 180]. β-adrenergic stimulation redistributes the relative proportions of channels in each modes, such that Mode A is favored over Mode 1 [179, 180]. Under PKG activation, histogram of channel closed times show a multi-exponential distribution with widely differing means [159, 161, 186], indicating the existence of at least one more gating mode other than Mode 1. This gating mode is characterized by a reduction of

channel open probability [158, 161, 186, 187] through prolonged channel closed time with no effects on channel open time or single channel conductance in cardiac myocytes [158, 186]. Here, we name this PKG-induced LCC gating mode as Mode G. The aforementioned Mode G characteristics are also observed in in other cell types, such as chromaffin cells [159, 188]. Single channel recordings show that activation of PKG suppresses the channel open probability and ensemble currents of LCCs pre-stimulated by activated PKA, so that these properties become similar to that observed under basal, non-stimulated conditions [158, 159]. We name this mode that arises from stimulation of both PKA and PKG as Mode AG.

In our model (Fig. 4.2B), we assumed that PP2A activity governs LCC dephosphorylation relating to modal redistribution. This is supported by the finding that, Mode A gating is coupled to a site dephosphorylated by PP2A by using inhibitors of differential sensitivity to PP1 and PP2A [189]. Furthermore, the model (Fig. 4.2) assumes that PKA-II, instead of PKA-I, is the predominant form regulating LCC, in that the rate constants related to PKA-phosphorylation is a function of activated PKA-II (i.e. $PKACII$). This is supported by the fact that PKA-II is localized near the LCC, whereas PKA-I is diffused throughout the cytosol [6, 71]. These assumptions are also consistent with prior modeling studies of LCC phosphorylation by PKA [71, 74]. In addition, the regulatory processes controlling LCC availability (Fig. 2A) and modal gating distribution (Fig. 2B) are assumed to be independent. It is also assumed that LCC phosphorylation (Fig. 2) occurs independently of voltage- and Ca^{2+}-dependent gating (Fig. 1). These assumptions are consistent with previous models describing kinase-mediated phosphorylation of LCC [74, 79, 180, 190].

4.3.3. The LCC gating model

The LCC model (Fig. 4.1B) is adopted from Greenstein and Winslow [176], originally developed by Jafri et al. [181]. In this model, LCCs undergo voltage- and Ca^{2+}-dependent gating (Fig. 4.1B, left) and an independent process of voltage-dependent inactivation (VDI) (Fig. 4.1B, right). LCC is composed of four independent subunits (Fig. 4.1B, left). While all subunits needs to be in the open configuration for the channel to conduct current (State 6 and State 12), transition to closed configuration of any one or more of the subunits (States 1–5 and States 7–11) will close the channel (i.e. no conductance). Voltage-dependent transition to open states (State 6 and State 12) occur upon membrane depolarization, when the channel undergo transition from left to right. With elevated [Ca^{2+}], CDI occurs as a result of downward transitions from Mode Normal (top row) to Mode Ca^{2+} (bottom row), in which transition into open state (State 12) is rare, thereby effectively inactivates the channel. In addition, as shown in the model on the right in Fig. 4.1B, depolarization promotes transitions from the available state (State 1) to the unavailable inactivated state (State 0), as depicted in the Hodgkin-Huxley type gating model for VDI.

Parameters for LCCs gating in Mode 1 is the same as that from the original model by Greenstein and Winslow [176], henceforth referred to as the baseline LCC model. Mode A gating is obtained by dividing the reverse rate from the open state (State 6) by a factor of 10 (i.e. $g_{modeA} = g_{mode1}/10$) while all other parameters remain the same as the baseline model of Greenstein et al. [180]. Similarly, Mode G gating is obtained by dividing the forward rate to State 6 by a factor of 2 (i.e. $f_{modeG} = f_{mode1}/2$). Mode AG gating, corresponding to LCC phosphorylated by both PKA and PKG, is assumed to

incorporate parameter adjustments for both Mode A and Mode G (i.e. $g_{modeAG} = g_{mode1}/10$ and $f_{modeAG} = f_{mode1}/2$). The theoretical basis for adjustments of gating parameters is explained in Appendix C Sect. C.5.1. The stochastic simulation of LCC model is achieved through Markov process simulation. Briefly, for each time step, dt, a uniformly distributed random variable is generated and is used to determine which state the Markov processes governing LCC gating (Fig. 4.1B) transitions into, if a transition occurs. Unless otherwise indicated, $[Ca^{2+}]$ is clamped at 4 μM for the entire duration of the simulation, which approximates $[Ca^{2+}]$ in pipette solutions containing Ca^{2+} buffers (e.g. EGTA) typically employed in single channel recordings [191] (Appendix C Sect.). In order to avoid extreme values from stochastic simulations, all peak I_{CaL} currents are generated from currents smoothed out by moving average of 0.5 msec window so that high frequency fluctuations in the sub-msec timescale are smoothed out.

4.4. Results

4.4.1. Model validation of single channel behavior

The behavior of the entire model (Fig. 4.3) reproduces experimental results obtained from single channel recordings of LCCs (Fig. 4.3 dots), under various extents of stimulation by β-agonist, isoproterenol (ISO) and NO donor, SNAP. For LCC channel availability (Fig. 4.3A) and gating mode distribution (Fig. 4.3B), four stimulation scenarios are investigated: "Basal" representing non-stimulated condition and "ISO", "SNAP", and "ISO+SNAP" representing maximal stimulation by the indicated reagent.

As shown in Fig. 4.3A, percent of LCCs available under basal conditions is ~ 25%, in agreement with result of Greenstein et al. [180]. Consistent with data by Schröder et al. [161], under maximal ISO stimulation, availability increases ~ 50% from that of basal conditions, to ~ 40%. Availability is suppressed below that of basal condition under maximal NO stimulation, either by itself or simultaneously with maximal ISO, qualitatively replicating data by Schröder et al. [161] and Carabelli et al. [159]. As shown in Fig. 4.3B, under basal conditions (first group), almost all channels gate in Mode 1 (black) with the rest gating in Mode A (red) and, upon maximal β-adrenergic stimulation (second group), channels originally gating in Mode 1 shift to Mode A so that percent LCCs in Mode A increases to ~ 20%, replicating results from Greenstein et al. [180]. Additionally, model predicts distribution of channel gating modes under SNAP and ISO+SNAP conditions (Fig. 4.3B, third and last group respectively). Compared to that under basal conditions, more channels gate in Mode G (blue) under SNAP stimulation (Fig. 4.3B, third group). Under simultaneous ISO and SNAP stimulation (Fig. 4.3B, last group), percent LCCs in Mode A and Mode G respectively are similar to those under ISO and SNAP conditions. In addition, percent LCC in Mode AG (green) is the highest under ISO+SNAP condition among the four stimulation scenarios.

Fig. 4.3. LCC single channel properties under cN cross-talk signaling regulation.

Model reproduces experimental data. Dotted symbols are experimental data; lines and bars are simulation results. (A) and (B) Simulation are performed under four stimulation conditions, “Basal” (no stimuli), “ISO” ([ISO] = 10 μM), “SNAP” ([SNAP] = 100 μM), and “ISO+SNAP” ([ISO] = 10 μM and [SNAP] = 100 μM, applied simultaneously). (B)–(D) Gating modes Mode 1, Mode A, Mode G, and Mode AG are respectively represented

by the black, red, blue, and green color schemes. **(A)** Percent of LCCs available under basal, ISO, SNAP, ISO+SNAP conditions versus results of Greenstein et al. [180], Schröder et al. [161], Schröder et al. [161], and Carabelli et al. [159] respectively. **(B)** Distribution of gating modes under four stimulation conditions, versus data for Basal and ISO conditions from Greenstein et al. [180]. **(C)** Mean open (first group) and closed (second group) times for channels gating in each mode. Mean channel open times for Mode 1 (black) and Mode A (red) versus data by Yue et al. [179], that for Mode G versus data by Tohse and Sperelakis [186]. Mean closed time for Mode 1, Mode A, Mode G, and Mode AG respectively versus results by Scrhöder et al. [161], Greenstein et al. [180] and Yue et al. [179], Tohse and Sperelaskis [186], and Klein et al. [160]. Currents are elicited by 150 msec pulses to 0 mV from a holding potential of – 80 mV. The mean open and closed times of each gating mode are calculated from independent simulation of 500 sweeps, with distribution shown in Appendix C Fig.C.1.

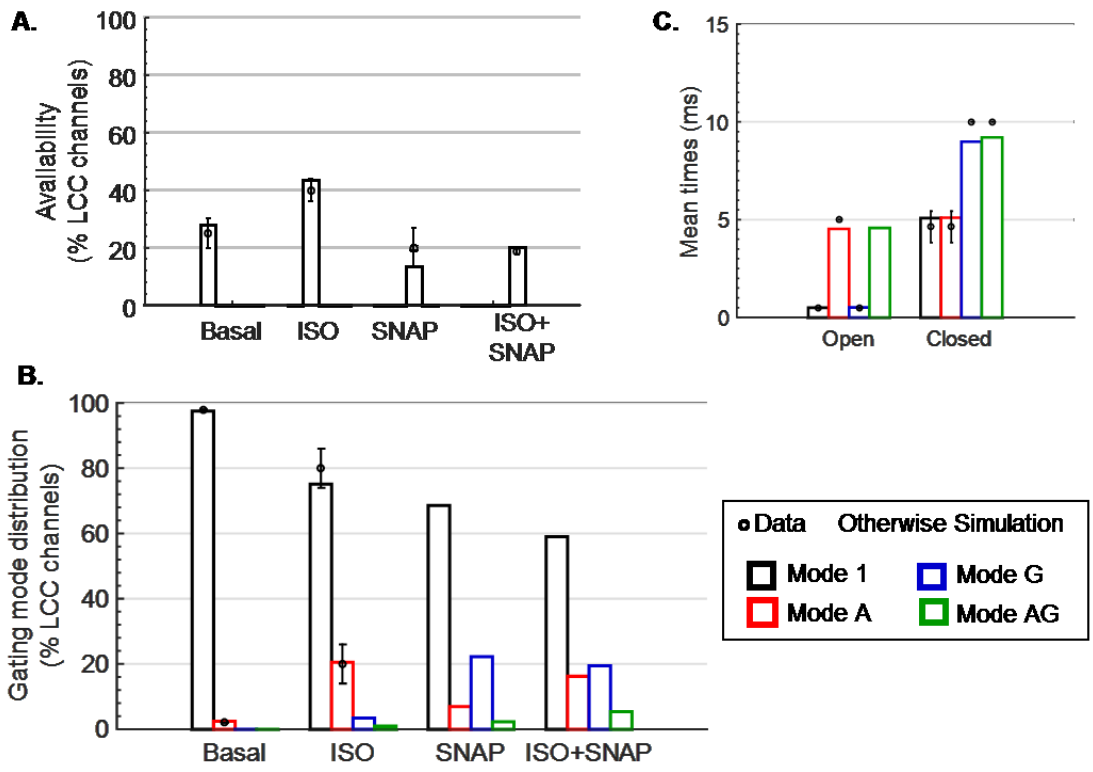

As shown in Fig. 4.3C, mean LCC channel open (first group) and closed (second group) times are calculated from stochastic simulation of five hundred LCCs for each gating mode (bars) and compared to experimental data (dots). The model replicates mean channel open times (first group) of ~ 0.5 msec for Mode 1 (black) and of ~ 5 msec for Mode A (red) consistent with Yue et al. [179] and Greenstein et al. [180]. Mean closed times for Mode 1 is ~ 5 msec in agreement with data by Schröder et al. [161]; that of Mode A is similar to Mode 1, consistent with that from Greenstein et al. [180] and Yue et al. [179]. In addition, model agrees with data by Tohse and Sperelakis [186] that the mean open time of channels gating in Mode G (blue) is approximately the same as that in Mode 1 at ~ 0.5 msec with the Mode G mean closed time at approximately twice that of basal at ~ 10 msec. Finally, the mean closed time of Mode AG (green) is similar to that of

Mode G, consistent with data by Klein et al. [160]. Model predicts that the mean open time of Mode AG is ~ 5 msec, similar to that of Mode A.

4.4.2. Model validation of whole-cell L-type calcium current

Fig. 4.4A and B respectively show the model ensemble current and peak current-voltage (IV) relations of the whole-cell L-type Ca^{2+} current, I_{CaL}. In Fig. 4.4A, whole cell LCC ensemble currents are elicited by 150 msec test potentials of 0 mV from a holding potential of – 40 mV (top row) under the aforementioned four stimulation scenarios, Basal (black), ISO (red), SNAP (blue), and ISO+SNAP (green). As shown, β-adrenergic stimulation potentiates the magnitude of I_{CaL} (red) from that under basal conditions (black), consistent with that observed by Katsube et al. [169] and Kameyama et al. [192]. The model also qualitatively reproduces NO suppression of basal I_{CaL} (blue) as that measured by Grunshin et al. [193] and Wahler and Dollinger [154]. Finally, under ISO+SNAP condition (green), I_{CaL} is suppressed below that observed under ISO alone and the peak current is similar to that under basal conditions. The model behavior that SNAP suppresses I_{CaL} pre-stimulated by ISO is consistent with data by Abi-Gerges et al. [194] and Wahler and Dollinger [154].

In Fig. 4.4B, the means (dots) and ranges (error bars) of peak I_{CaL} arising from stochastic LCC gating are calculated from six independent simulations for each test potential of the voltage protocol (top row). The peak IV relations obtained from these simulation results (thicker solid lines) are compared to experimental data (dots connected with dotted lines). The model reproduces IV curve under basal conditions (black), consistent with the original model of Greenstein & Winslow [176]. In addition, the

extents of IV curve potentiation under ISO (red) qualitatively agrees with data by Katsube et al. [169]. The extent of IV curve suppression due to maximal NO stimulation (blue) agrees with that measured by Sumii and Sperelakis [163]. The IV curve under simultaneous maximal ISO and NO stimulation (green) returns to approximately that observed under basal conditions, a behavior consistent with that observed by Wahler and Dollinger et al. [154]. The model behavior that NO suppresses ISO pre-stimulated I_{CaL} is also consistent with that reported by Abi-Gerges et al. [194].

Fig. 4.4. Regulation of whole-cell I_{CaL} by the cN cross-talk signaling network.

Simulation are performed under four stimulation conditions, "Basal" (no stimuli, black), "ISO" ([ISO] = 10 μM, red), "SNAP" ([SNAP] = 100 μM, blue), and "ISO+SNAP" ([ISO] = 10 μM and [SNAP] = 100 μM applied simultaneously, green). **(A)** Whole cell LCC ensemble currents elicited by 150 msec test potentials of 0 mV from a holding potential of – 40 mV (top row). **(B)** Data are shown in thin lines and are connected with dotted lines; simulations are shown in thicker lines and are connected with solid lines. The peak IV curve under basal conditions (black) versus data from Greenstein & Winslow [176]. The extents of IV curve changes under ISO (red), SNAP (blue), and ISO+SNAP (green) conditions versus data by Katsube et al. [169], Sumii and Sperelakis [163], and Wahler and Dollinger et al. [154] respectively. For simulation data, the means (dots) and ranges (error bars) of results due to stochastic LCC gating are shown for six independent simulations. Currents are elicited by test potentials of 150 msec duration over the range of - 40 mV to + 60 mV in 10 mV steps from a holding potential of - 40 mV (top row).

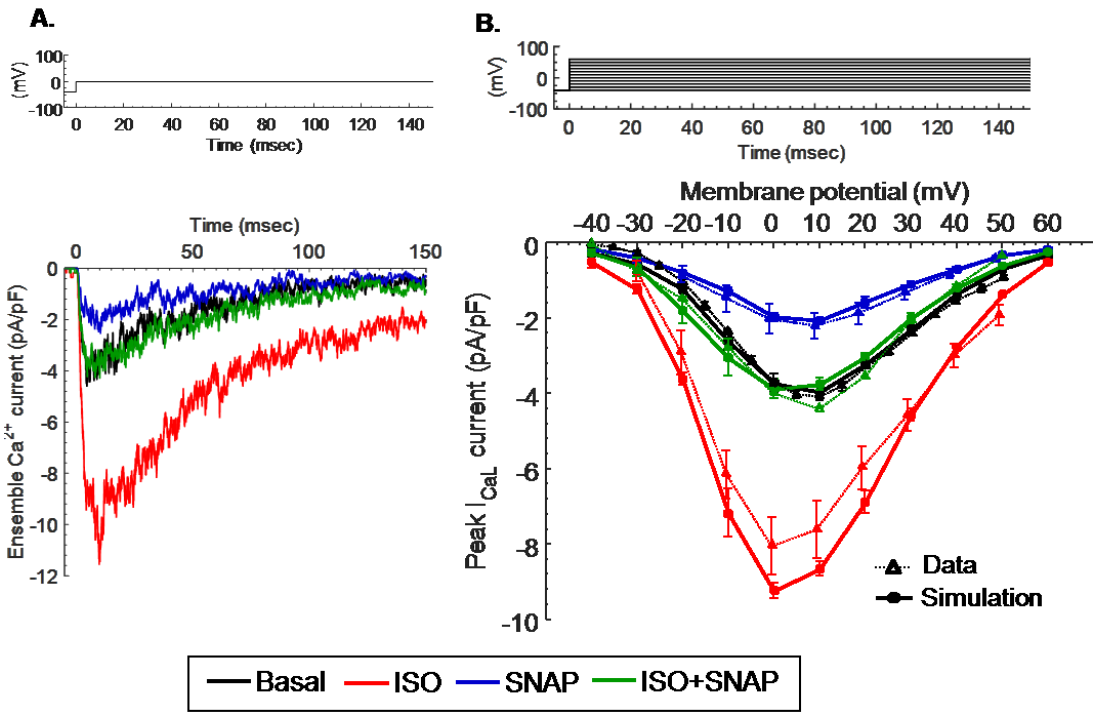

4.4.3. Regulation by cN signaling network of LCC current

Results shown in Fig. 4.5 attempts to elucidate changes in availability and gating mode distribution under various extents of cN cross-talk stimulation that that give rise to the observed whole-cell I_{CaL}. As shown in Fig. 4.5A, the model replicates percent increases in peak I_{CaL} over that under basal I_{CaL} (grey line) across varying [ISO] as measured by Katsube et al. [169] (black dots), with steep increases in current occurring over the range of ~ 5 nM to 50 nM [ISO]. Model demonstrates this is due to increase in channel availability (Fig. 4.5B) over the aforementioned range of [ISO]. In addition, with increased β-adrenergic stimulation, more channels begin to gate in Mode A (red) from Mode 1 (black), while the number of channels gating in Mode G (blue) and Mode (AG) remain very low across [ISO] (Fig. 4.5C).

Fig. 4.5. Redistribution of LCC gating modes by the cN cross-talk signaling network.

LCC gating behavior under varying [ISO] (no SNAP) (A–C) and under varying [SNAP] with 10 μM ISO and without ISO (D–G). (A) and (D) The mean (dot) and range of Peak I_{CaL} (error bar) of six independent stochastic simulations are shown. **(A)** Percent increases in Peak I_{CaL} under varying [ISO] over that under basal I_{CaL} (no ISO or SNAP) (grey line) versus data by Katsube et al. [169] (black dots). (E) Peak I_{CaL} under varying [SNAP] without ISO (black) and with 10 μM [ISO] (grey). **(B)** and **(E)** Percent of LCCs available. Percent of LCCs gating in Mode 1 (black), Mode A (red), Mode G (blue), Mode AG (green) are shown for varying [ISO] (C), varying [SNAP] **(F)**, and varying [SNAP] under simultaneous ISO stimulation (10 μM) **(G)**.

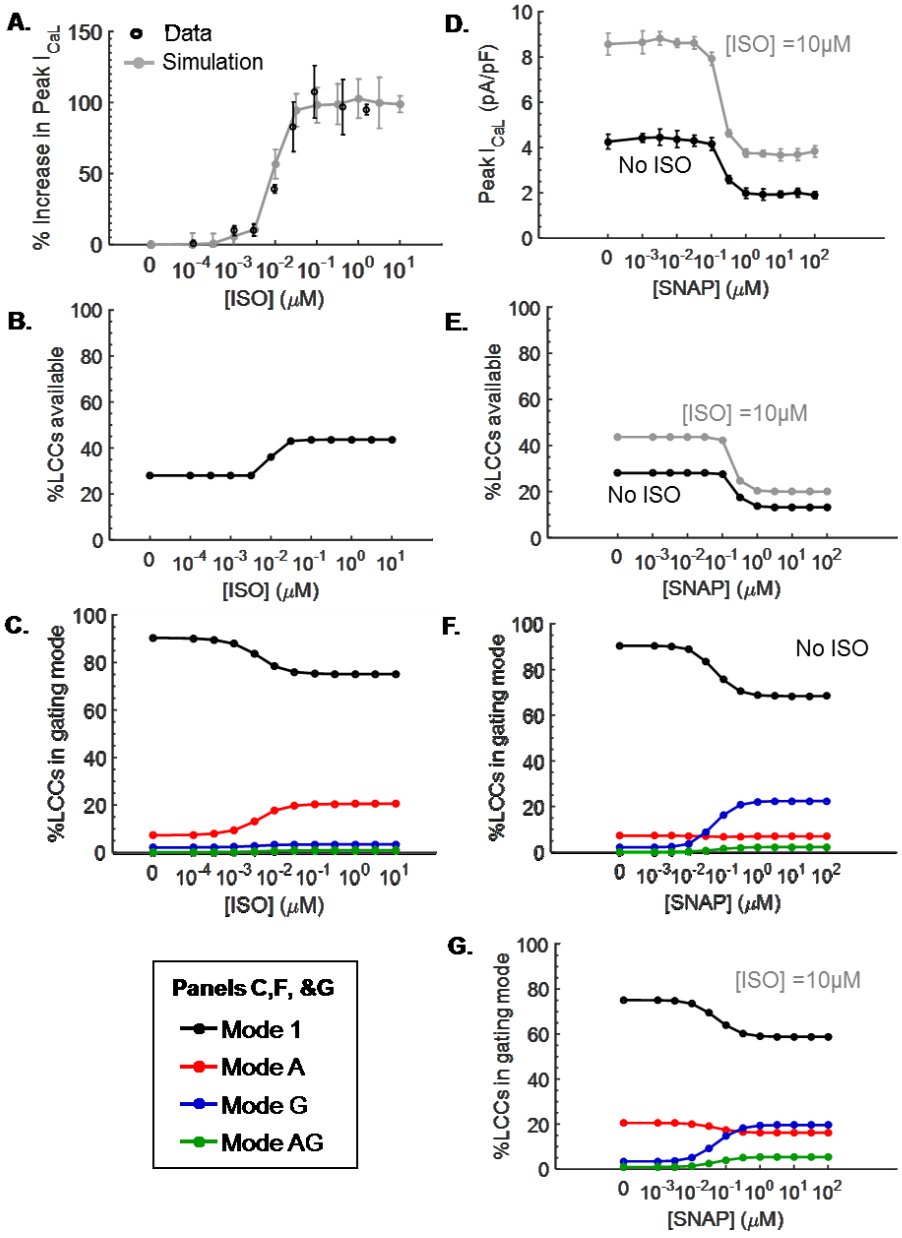

Using the model, we also investigated the changes in I_{CaL} over varying [NO] as donated from SNAP without (black) and with (grey) simultaneous [ISO] stimulation of 10 μM (Fig. 4.5D). As shown, with or without ISO, low [NO] does not have much effect on I_{CaL}; it is not until sufficiently high [NO] does suppression of I_{CaL} occur. Comparing against peak I_{CaL} levels without ISO (black), simultaneous ISO stimulation leads to an

increase in I_{CaL} (grey) that is more pronounced at lower than higher [SNAP]. High [SNAP] is able to completely abolish the increase in I_{CaL} pre-stimulated by ISO (grey), such that, at high [SNAP], I_{CaL} return to that observed under low [SNAP] without ISO (black). On the other hand, the addition of ISO did not shift the range of [NO] over which I_{CaL} exhibited most change. Model demonstrates that channel availability is suppressed at high [SNAP] either without (grey) or with (black) ISO. Compared to SNAP alone, it is potentiated by addition of ISO across all [SNAP] (Fig. 4.5E, grey vs. black). Fig. 4.5F shows the proportion of LCCs in each of the four gating modes under varying [SNAP] in the absence of ISO. Increase in [SNAP] caused an increased proportion of channels gating in Mode G (blue) from their original Mode 1 gating mode (black), while proportions gating in Mode A (red) and Mode AG (green) remain fairly constant across [SNAP] with a very slight increase in Mode AG. Compared to modal distribution under SNAP alone (Fig. 4.5E), an increase in Mode A gating (red) is the most prominent change caused by addition of ISO, with magnitude of increase slightly higher at lower [SNAP] (Fig. 4.5G). On the other hand, Mode AG (green) is slightly more pronounced with high [SNAP] under the maximal β-adrenergic stimulation. In short, model shows that β-adrenergic and NO stimulation primarily arises from potentiation of Mode A and Mode G gating respectively.

In Appendix C Fig.C.2 and Fig. 4.6, model reveals the behavior of the signaling network driving LCC regulation shown in Fig. 4.4 and Fig. 4.5. Despite large increases in the activities of all cAMP-hydrolyzing PDEs, PDEs 1–4 (Appendix C Fig.C.2C), [cAMP] and subsequent PKA activation (Appendix C Fig.C.2A and B respectively) are substantially increased at elevated [ISO]. Comparably, ISO-induced increases in [cGMP]

and PKG activity (Appendix C Fig.C.2D and E respectively) as a result of PDE interaction in cN cross-talk (Appendix C Fig.C.2F) [175] are small in magnitude. The large increase in β-adrenergic activation (Appendix C Fig.C.2A–C) overcomes cross-talk activation of the NO/cGMP/PKG pathway (Appendix C Fig.C.2A–C) leading to promotion of Mode A gating, which dominates over the slight increases in Mode G and Mode AG gating, leading to increased peak I_{CaL} (Fig. 4.5A–C). In Fig. 4.6, signal transduction mechanisms under varying [SNAP] stimulation are investigated for the observed LCC responses in Fig. 4.6D–G. Increasing [SNAP] results in increasing [cAMP] (Fig. 4.6A) and subsequent PKA activation (Fig. 4.6B), without (black) or with (grey) simultaneous ISO. As shown in Fig. 4.6C and D, this behavior is due to cross-talk mechanisms [175]. The activity of PDE3 (blue) is suppressed under higher [SNAP], because increased [cGMP] (Fig. 4.6E) competitively binds to its catalytic domain diminishing cAMP-occupancy [127]. The rise in PDE2 (red) and PDE4 (green) activities partially compensated for the loss of PDE3 activity (blue). Comparing that under high to low [ISO] (Fig. 4.6D vs. C), PDE2 compensation for decreased PDE3 activity is more pronounced under high [ISO], because PDE4 (green) is saturated and no longer responsive to changes in the pathway (Fig. 4.6D).

Fig. 4.6. Role of cN cross-talk in LCC regulation.

(A) and **(B)** respectively, [cAMP] and percent active PKA-II under varying [SNAP] without (black) and with ISO (10 μM). **(C)** cAMP hydrolysis rates for PDEs 1, 2, 3 and 4 (black, red, blue, and green respectively) for simulation without ISO. **(D)** Similar to C, for simulation with ISO. **(E)** and **(F)** respectively, [cGMP] and percent active PKG under varying [SNAP] without (black) and with ISO (10 μM). **(G)** and **(H)** The cGMP

hydrolysis rates for PDEs 1, 2, 3 and 5 (black, red, blue, and cyan respectively) for simulation without and with ISO respectively.

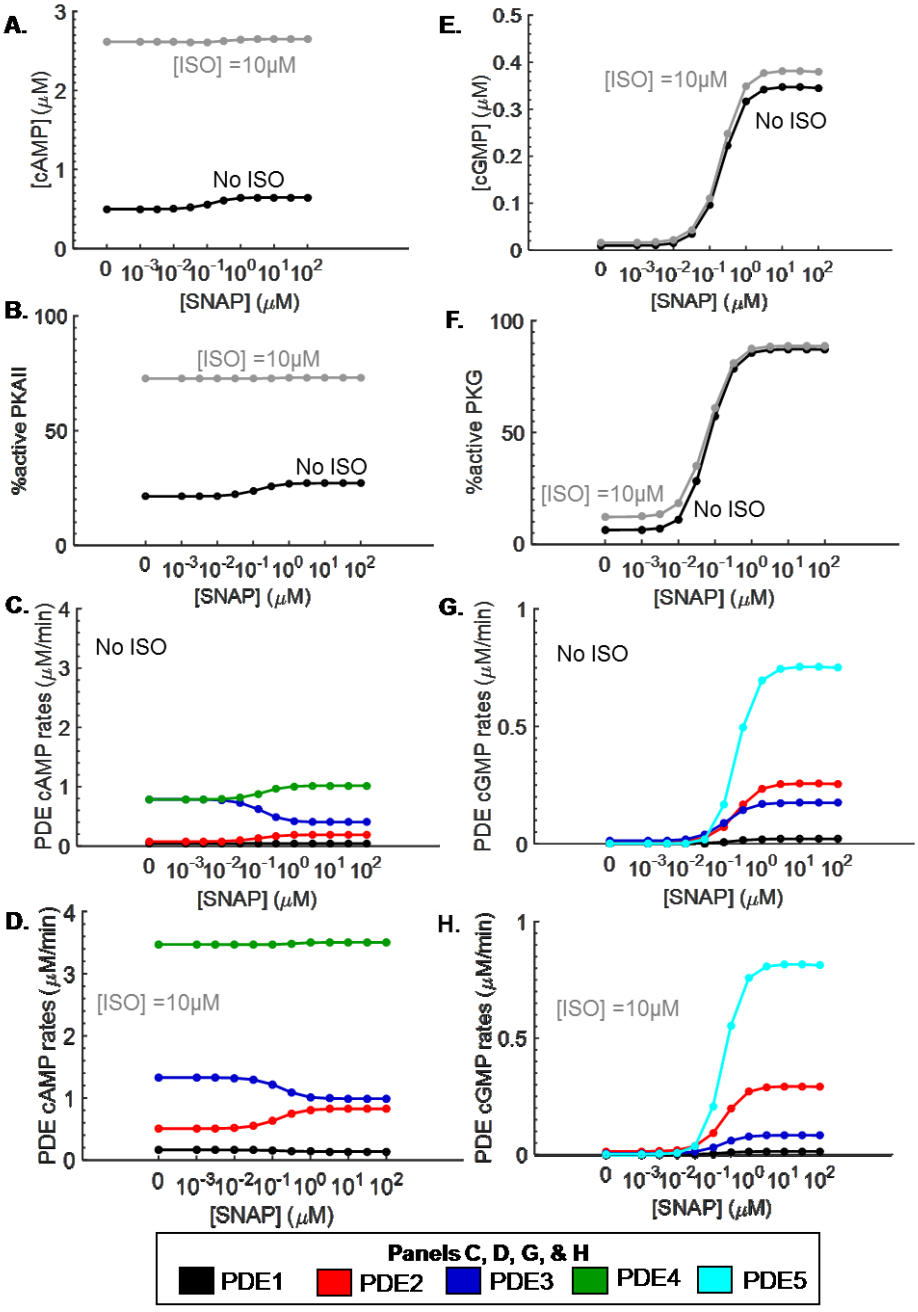

Because saturation of PDE activities at high ISO led to higher [cAMP] and PKA activation (Fig. 4.6A and B respectively, grey vs. black), Mode A gating (red) is more

favored under simultaneous SNAP and ISO stimulation (Fig. 4.6G) versus SNAP alone (Fig. 4.6F), giving rise to the upward shift of the curve representing peak I_{CaL} upon addition of ISO across [SNAP] (Fig. 4.6D, grey vs. black). The suppression of peak I_{CaL} curves at high [SNAP] (Fig. 4.5D, grey and black) is driven by the NO/cGMP/PKG pathway (Fig. 4.6E–H). In response to increased [NO] with (grey) or without (black) [ISO], activation of PKG (Fig. 4.6F) substantially increased from the rise in [cGMP] (Fig. 4.6E). For both cases with and without [ISO], this is due to saturation of cGMP hydrolysis activities of PDEs 1 (black), 2 (red), 3 (blue), and 5 (cyan) (Fig. 4.6G and H). Upon addition of ISO (Fig. 4.6H), despite the decrease in PDE3 rate from cAMP competition, PDE2 rate increased sufficiently to compensate. As a result, for both cases, with increasing [SNAP], the substantial increase in PKG activation overcomes the cross-talk response of increased PKA activation. Consequently, with increasing [NO], suppression of LCC availability and Mode A gating and increase in Mode G gating (Fig. 4.5E–G) lead to suppression of peak I_{CaL} (Fig. 4.5D).

4.4.4. Role of PDE inhibition on LCC regulation under basal conditions

Fig. 4.7A shows overlapping peak IV curves for I_{CaL} IV under control conditions (black) and under PDEs 2, 3, and 4 inhibition (red, blue, and green respectively) when neither the β-adrenergic nor the NO/cGMP/PKG is stimulated. Model therefore predicts that individual inhibition of PDEs 2, 3, and 4 under basal, non-stimulated conditions does not alter peak I_{CaL} appreciably, consistent with that reported by Verde et al. [86]. Using our model, we dissected the mechanism behind this phenomenon (Fig. 4.7B–E). As shown in Fig. 4.7B, the percent increases in [cAMP] (red) and [cGMP] (blue) under individual

inhibition of these PDEs are extremely low. For each PDE inhibition case, our model further teased out changes in cAMP hydrolysis rates of PDEs 1, 2, 3, and 4 (Fig. 4.7C, black, red, blue, and green bars respectively) as well as the changes in cGMP hydrolysis rates for PDEs 1, 2, 3, and 5 (Fig. 4.7C, black, red, blue, and cyan respectively), with the net change indicated in grey. It is to be noted, for all cases (Fig. 4.7C and D), the net PDE rate changes (grey) are very much the same as the decrease in rate of the inhibited PDE. This indicates that the remaining PDEs have not compensated much for the loss of the inhibited PDE through cross-talk or feedback mechanisms. This is because, without β-adrenergic or NO stimulation, [cAMP] and [cGMP] are so low and their changes due to PDE inhibition so small (Fig. 4.7B) that they are unable to cause noticeable changes in PDE activities (Fig. 4.7C and D). Despite the absence of cross-talk compensation, PKA (red) and PKG (blue) activities are hardly affected by the small changes in [cN] (Fig. 4.7E). As a result, channel availability (percent increase less than 0.1% for all cases) and modal distribution (Fig. 4.7F) remain similar to control condition, as a result individual inhibition of PDEs 2, 3, and 4 has no effect on I_{CaL} under basal condition (Fig. 4.7A).

Fig. 4.7. Result of individual PDE inhibition on I_{CaL} under basal condition.

All simulations are performed under basal non-stimulated condition, without ISO or NO stimulation. Results are compared to responses prior to the indicated PDE inhibition. **(A)** Peak IV curves for I_{CaL} under control condition without PDE inhibition (black) and with 90% inhibition of PDE2 (red), PDE3 (blue), and PDE4 (green). Currents are elicited from a holding potential of – 50 mV to test potentials of 300 msec duration from - 40 mV to + 50 mV in 10 mV increments. The mean (dot) and ranges (error bar) of three runs are shown for each IV curve. Under PDE 2, 3, and 4 inhibition, percent increases in [cAMP]

(red) and [cGMP] (blue) are shown in **(B)**, increases in PDE cAMP hydrolysis rates in **(C)**, increases in PDE cGMP hydrolysis rates in **(D)**, percent increases in PKA (red) and PKG (blue) activation in **(E)**, and percent increases in gating modes **(F)**. (C) and (D) The increases in hydrolysis rates for PDEs 1, 2, 3, 4, and 5 are shown in black, red, blue, green, and cyan respectively, with the net rate shown in grey. (F) Percent increases in gating modes, Mode 1, A, G, and AG are shown in black, red, blue, and green outlined bars respectively.

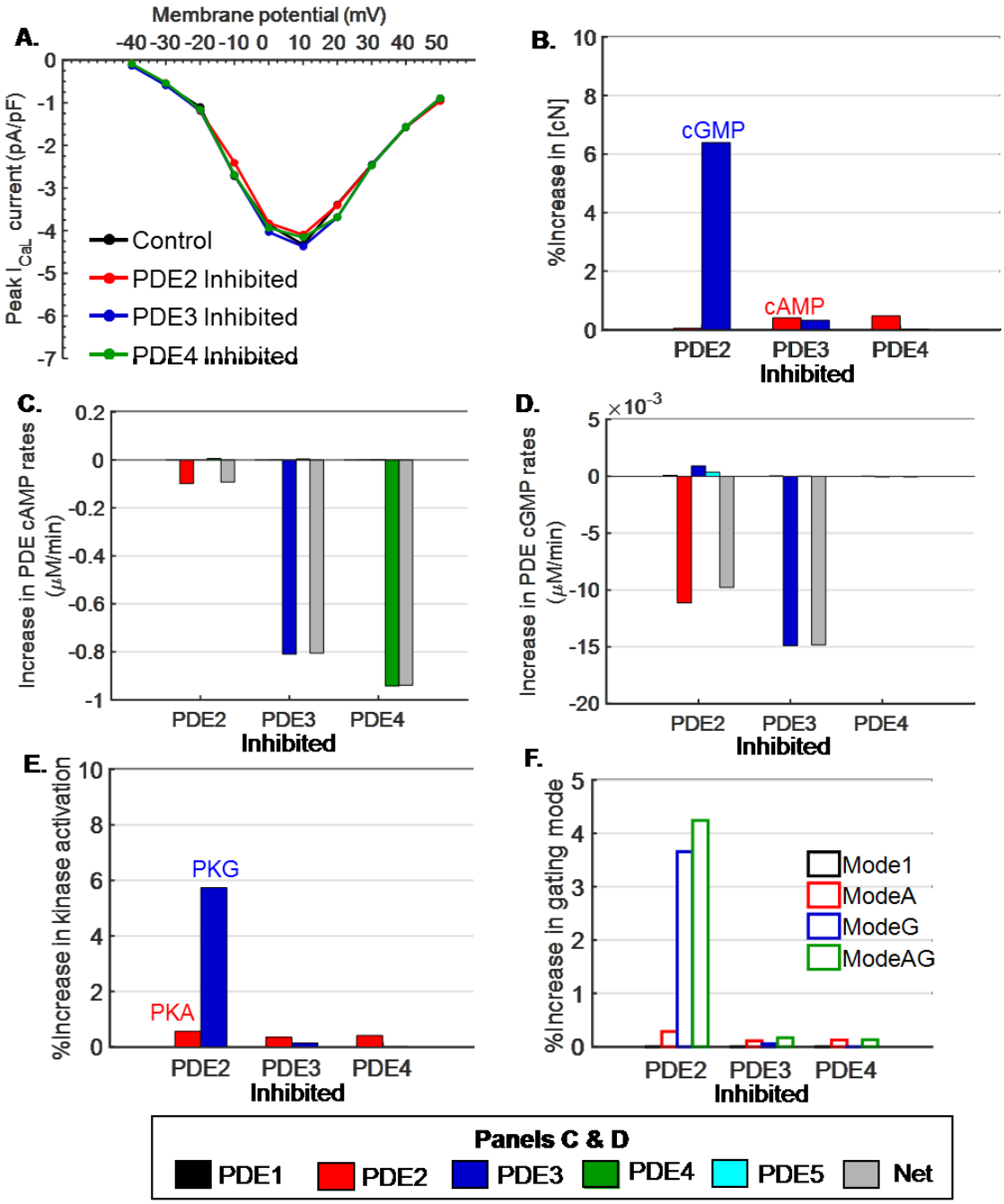
A.
Membrane potential (mV)
-40 -30 -20 -10 0 10 20 30 40 50
Peak I_{CaL} current (pA/pF)
Control
PDE2 Inhibited
PDE3 Inhibited
PDE4 Inhibited
B.
%Increase in [cN]
cGMP
cAMP
PDE2 PDE3 PDE4
Inhibited
C.
Increase in PDE cAMP rates (μM/min)
PDE2 PDE3 PDE4
Inhibited
D.
$\times 10^{-3}$
Increase in PDE cGMP rates (μM/min)
PDE2 PDE3 PDE4
Inhibited
E.
%Increase in kinase activation
PKG
PKA
PDE2 PDE3 PDE4
Inhibited
F.
%Increase in gating mode
Mode1
ModeA
ModeG
ModeAG
PDE2 PDE3 PDE4
Inhibited
Panels C & D
PDE1 PDE2 PDE3 PDE4 PDE5 Net

4.4.5. Role of PDE inhibition on LCC regulation under β-adrenergic stimulation

In Fig. 4.8, responses of the model under individual inhibition of PDEs 2, 3, and 4 are shown for 1 nM, 10 nM, and 1 μM [ISO] which are indicated respectively by white, light grey, and dark grey color schemes. The potentiation of peak I_{CaL} currents under 1 nM ISO (white bars) under PDE 2, 3, and 4 inhibition are consistent with that reported by Verde et al. [86] (Fig. 4.8A). Simulation also indicates PDE inhibitions exert the most impact on peak I_{CaL} under lower (white and light grey), instead of high (dark grey) [ISO] (Fig. 4.8A). We proceed to dissect the mechanisms underlying the observed I_{CaL} regulation for each case of PDE inhibition. Under PDE2 inhibition, higher [ISO] results in larger increases in [cAMP] and PKA activation (Fig. 4.8B and C respectively). Stimulation by 10 nM [ISO] (light grey) further increased I_{CaL} from that under 1 nM (white), but stimulation by 1 μM [ISO] does not affect I_{CaL} by much (dark grey). As such, increased β-adrenergic activation (Fig. 4.8B and C) does not necessarily correlate to increased potentiation of I_{CaL} (Fig. 4.8A). Fig. 4.8D and E reveals that, among the three PDEs inhibited, PDE2 inhibition caused the most increase in [cGMP] and PKG activation, despite of having the smallest increase in [cAMP] and PKA activation (Fig. 4.8B and C). The extent of increases in [cGMP] and PKG activation also increased with increasing [ISO]. By decreasing channel availability, promoting Mode G gatin, and keeping Mode A gating low (Appendix C Fig.C.3), this elevated PKG activation under low β-adrenergic tone (Fig. 4.8B and C) is sufficient to suppress PKA-mediated increases in I_{CaL}, until completely annihilating it under high [ISO] (Fig. 4.8A).

In contract to PDE2 inhibition, for PDE3 inhibition, higher [ISO] results in smaller, instead of larger, increases in [cAMP] (Fig. 4.8B). Furthermore, increasing [ISO] results in decreased, instead of increased, magnitude of changes in [cGMP] and subsequent PKG activation (Fig. 4.8D and E). The magnitude of changes in I_{CaL} decrease with higher [ISO] (Fig. 4.8A) (i.e. inversely correlates with [ISO]), but positively correlates with changes in [cAMP], PKA activation, [cGMP], and PKG activation. The increases in PKA activation (Fig. 4.8C) also positively correlate with that of [cAMP] (Fig. 4.8B). This indicates that the cross-talk mechanisms regulating cAMP and cGMP dynamics is the primary regulator of I_{CaL} under PDE3 inhibition. The responses under PDE4 inhibition are similar to that under PDE3 inhibition in terms of changes in I_{CaL} decreased under high [ISO] (Fig. 4.8A) and that these I_{CaL} changes positively correlate with changes in PKA and PKG activation (Fig. 4.8C and E respectively). However, in contrast to that under PDE3 inhibition, increases in [cAMP] become larger, rather than smaller, under higher [ISO] (Fig. 4.8B). The extent of PKA activation (Fig. 4.8C) inversely, rather than positively, correlates with that of [cAMP] (Fig. 4.8B). This is because PKA activation saturated from the steep rise in [cAMP] (Fig. 4.8B). These observations indicate that regulation of I_{CaL} under PDE4 inhibition operates under a distinct cross-talk mechanism, but similar PKA-PKG-LCC interaction, compared to that under PDE3 inhibition.

Fig. 4.8. Result of PDE inhibition on I_{CaL} under β-adrenergic stimulation.

Individual inhibitions of PDE 2, 3, and 4 (abscissa) under [ISO] of 1 nM (white), 10 nM (grey), and 1 μM (dark grey). Percent increases in model responses are shown with respect to those prior to the indicated PDE inhibition. For PDE 2, 3, and 4 inhibition

respectively, 10 μM EHNA, 1 μM Cilo, and 0.3 μM Rol have been applied in accordance with Verde et al. [86]. **(A)** Increases of peak I_{CaL} over control under low, median, and high levels of [ISO] under PDE 2, PDE 3, and PDE 4 inhibition (first, second, and last bar groups respectively). The mean (dot) and ranges (error bar) of peak I_{CaL} from three runs are shown for each bar. **(B) – (E)** respectively, percent increases in [cAMP], [cGMP], PKA-II activation, and PKG activation under the indicated PDE inhibition over control for each [ISO].

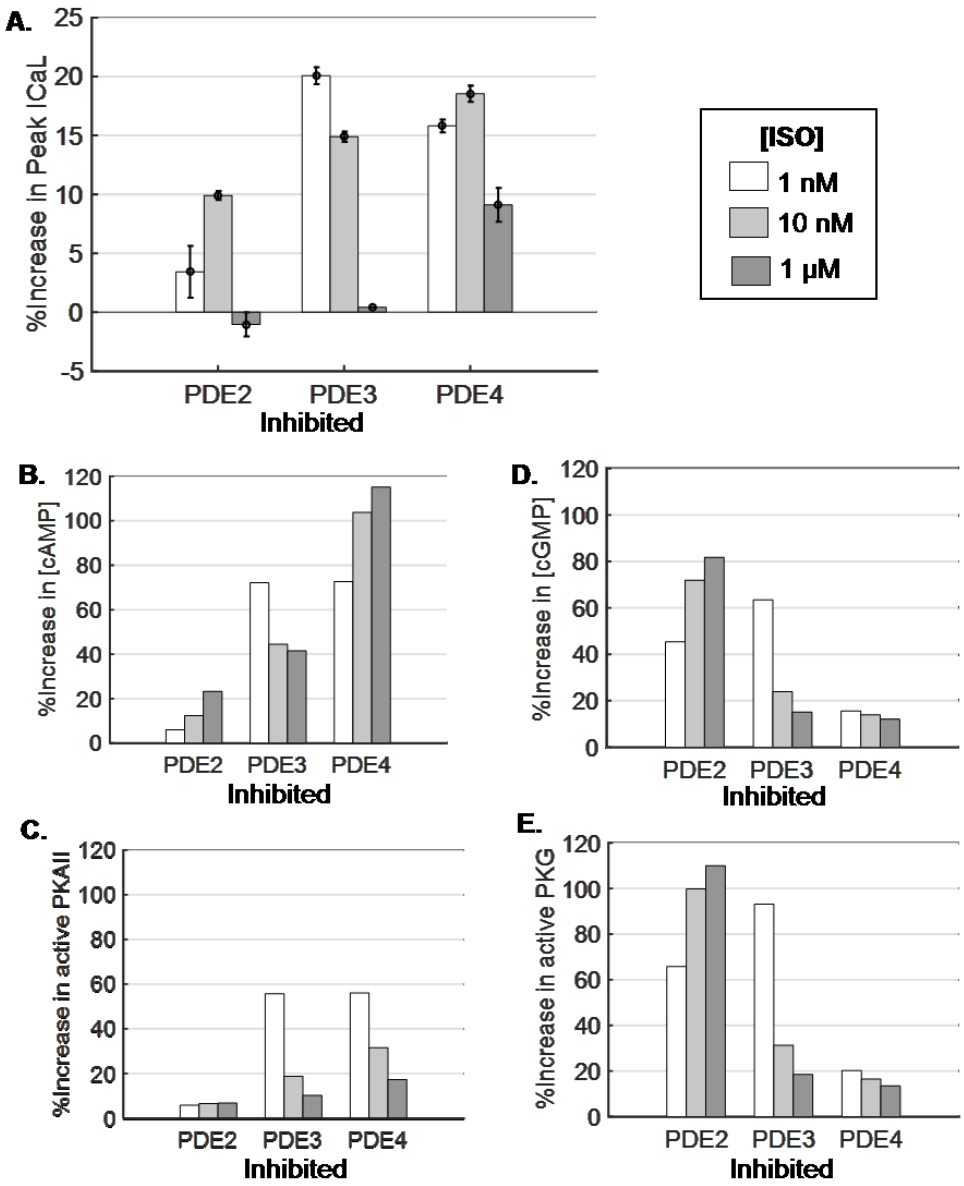

In order to further explain observations made on Fig. 4.8, we teased out PDE interactions in response of the indicated PDE inhibition as influenced by cross-talk mechanisms (Fig. 4.9). Under the same simulation protocol as that of Fig. 4.8, Fig. 4.9 shows the differences in cN hydrolysis rates of each PDE prior to and after the indicated PDE inhibition, in terms of cAMP (Fig. 4.9A–C) and cGMP (Fig. 4.9D–F) degradation,

for each of the three levels of ISO stimulation. All three [ISO] are sufficient to induce changes in the non-inhibited PDEs. The rate increases of these remaining PDEs (positive values) partially compensated for the loss of the inhibited PDE, such that the net decrease in rate (grey) is less in magnitude than the rate suppression of the inhibited PDE. This indicates that cross-talk mechanisms are activated by ISO stimulation, because changes in [cAMP] and [cGMP] are sufficiently large.

Fig. 4.9. PDE interaction underlying β-adrenergic regulation of I_{CaL}.

cN hydrolysis rates for PDEs 1, 2, 3, 4, and 5 are shown in black, red, blue, green, and cyan respectively. The net changes in rates under individual inhibition of PDEs 2, 3, and 4 (first, second, and third bar group respectively) are shown in grey. Increases in PDE rates are obtained by subtracting rates after the indicated PDE inhibition form those prior to inhibition. Simulation protocol is the same as that employed in Fig. 4.8. **(A) – (C)** Increases in cAMP hydrolysis rates of PDEs 1, 2, 3, and 4 as well as net cAMP rate changes across all PDEs are shown for [ISO] of 1 nM, 10 nM, and 1 μM respectively. **(D) – (F)** Increases in cGMP hydrolysis rates of PDEs 1, 2, 3, and 5 and net rate changes are shown for [ISO] of 1 nM, 10 nM, and 1 μM respectively.

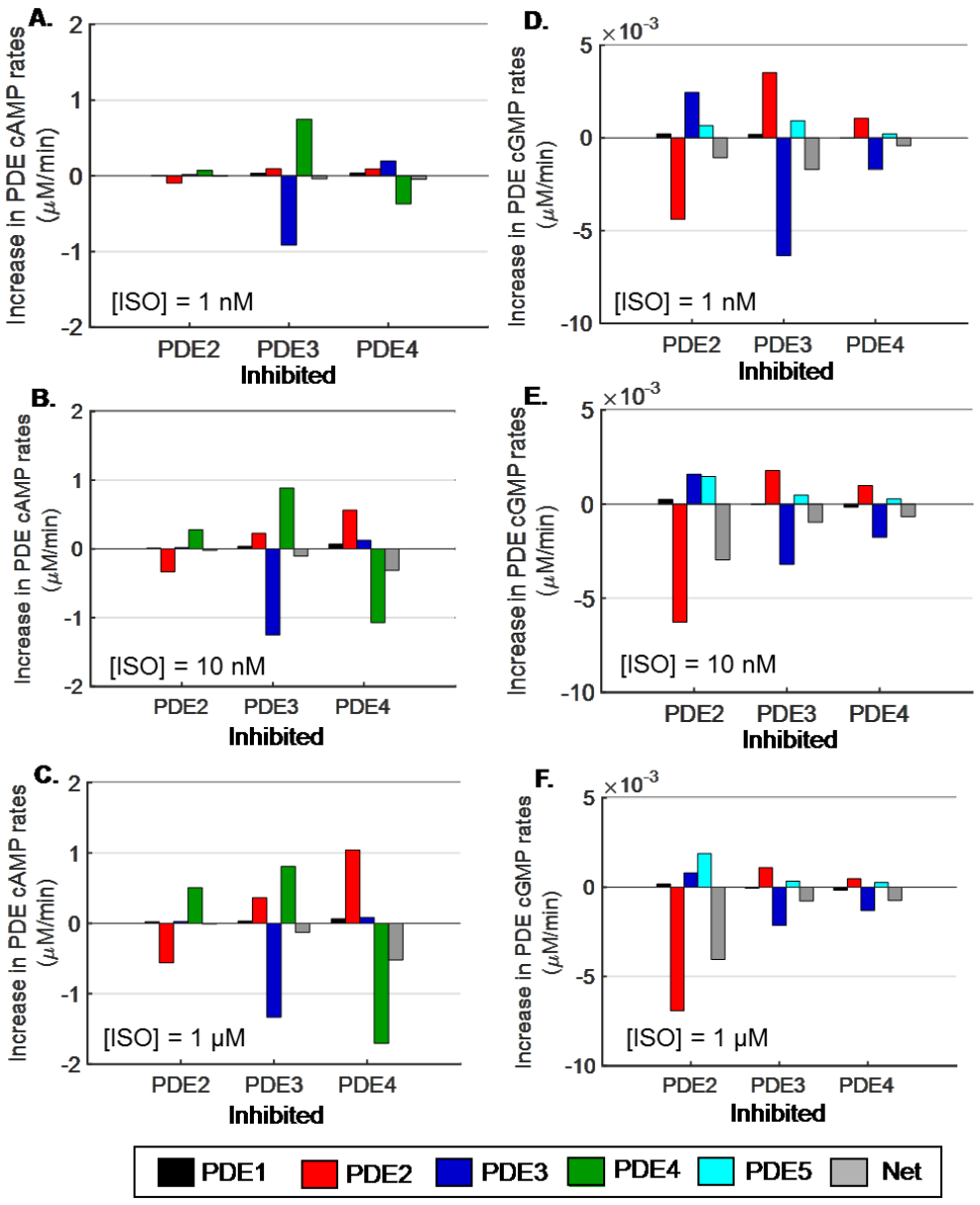

Among the three PDE inhibitions, PDE2 inhibition resulted in the least changes in PDE cAMP hydrolysis rates (Fig. 4.9A–C). In addition, PDE4 almost completely compensated for the loss of PDE2 activity; therefore, the net change in cAMP hydrolysis rate (grey) is near zero, leading to the smallest increases in β-adrenergic tone with increasing [ISO] (Fig. 4.8B and C). On the other hand, for cGMP hydrolysis, the

increase in PDE3 (blue) and PDE5 (cyan) cGMP hydrolysis rates cannot compensate for PDE2 inhibition (red) (Fig. 4.9D–F, first groups), giving rise to the largest net decrease in cGMP hydrolysis rates (grey) among PDE inhibitions (Fig. 4.9D–F, first groups). Furthermore, the magnitudes of the net decreases in cGMP hydrolysis rates (grey) are enlarged with increasing [ISO]. This is because, with increasing [ISO], and therefore accumulation of [cAMP], the loss of PDE2 cGMP activity increases in magnitude with allosteric activation by cAMP, but the compensatory PDE3 activity is inhibited by competitive binding from increased [cAMP], while PDE5 activity is not sufficiently amplified through cGMP-mediated feedback or allosteric activation [127, 175] (Fig. 4.9D–F). As a result, with increasing [ISO], PKA-mediated potentiation of I_{CaL} is more and more opposed by PKG-mediated suppression of I_{CaL}, leading to the small changes in I_{CaL} relative to other PDE inhibitions, which becomes even smaller under high [ISO] (Fig. 4.8A).

For both PDE3 and PDE4 inhibitions, changes in cGMP dynamics are comparatively small (Fig. 4.9D–F, second and third groups); therefore, the β-adrenergic pathway becomes the principal driver behind the observed changes in I_{CaL} (Fig. 4.8A). As changes in PKG activity and therefore changes in its subsequent interaction with LCC are no longer prominent, cN cross-talk, which drives cAMP dynamics and subsequent PKA activation, becomes increasingly important in I_{CaL} regulation. As shown in Fig. 4.9A–C (second groups), under PDE3 inhibition, PDE4 (green) is the greatest and a potent compensator in cAMP hydrolysis, together with additional compensation from PDE2 (red). In constrast, for PDE4 inhibition (Fig. 4.9A–C, third group), increase in PDE2 (red), though greatest among the remaining PDEs, cannot completely compensate

for the loss of PDE4 (green), especially at higher [ISO]. Additionally, with increasing [ISO], the magnitudes of net changes in cAMP hydrolysis rate (grey) increases, as amplified losses of PDE4 activity becomes more difficult to be compensated by PDE2. This leads to larger [cAMP] rises under PDE4 inhibition than PDE3 inhibition, as well as increased accumulation of [cAMP] with higher [ISO] under PDE4 inhibition. Consequently, for PDE4 inhibition, it is the saturation of cAMP-mediated PKA activation that prevented further increases in I_{CaL} than that under PDE2 inhibition (Fig. 4.8A).

4.5. Discussion

4.5.1. Integrative modeling dissects mechanisms underlying LCC regulation by cN signaling cross-talk signaling network

The cN cross-talk signaling network (Fig. 4.1A) is able to deliver both stimulatory and inhibitory regulations to the LCC (Fig. 4.1B), which has been shown to be essential for the initiation and coordination of cardiac electrical and mechanical properties, such as CICR, AP, and EC coupling [170, 171]. On the other hand, LCC regulation by the cN cross-talk signaling network remains perplexing, in part because it has been challenging to decipher the functional role of the numerous interdependent mechanisms contributing to I_{CaL} regulation. First of all, the quantification of changes in I_{CaL} caused by cN cross-talk network regulation is hindered by difficulty in isolating the impact of cN cross-talk signaling network on I_{CaL} from the large number of PKA and PKG phosphorylation targets in the tightly coupled CICR and EC coupling process [5, 9, 172]. In addition, the

intertwined signal transduction mechanisms in the cN cross-talk signaling network renders the behavior of PKA and PKG signals acting on LCC non-intuitive (Fig. 4.1A) [127, 175]. The investigation is further complicated by the simultaneous phosphorylation of the same LCC target by two kinases, PKA and PKG, as well as the molecular complexity of the LCC channel itself [164].

In order to explain the functional role of the cN cross-talk signaling network in its regulation of LCC, we constructed a mechanistic computational model (Fig. 4.1 and Fig. 4.2) by functionally integrating our previously validated model of the signaling pathway [127, 175] with an existing LCC model [176, 181]. The complete model describes I_{CaL} regulation via dynamic interactions among PKA, PKG, and LCCs as a function of extra-cellular stimuli. It reproduces experimentally observed LCC single channel (Fig. 4.3) and whole cell current (Fig. 4.4 and Fig. 4.5A) characteristics as regulated by the signaling network. To our knowledge, this is the first model accounting for regulation of LCC by the cN signaling network through its simultaneous phosphorylation by two kinases, PKA and PKG. We demonstrated that PKA- & PKG-mediated regulation of channel open and closed times explains changes in whole-cell LCC currents under β-adrenergic and NO stimulation (Fig. 4.3–Fig. 4.5). In addition, NO-mediated suppression of basal and β-adrenergic pre-stimulated I_{CaL} occurs via potentiation of LCC Mode G gating. Finally, individual inhibitions of PDEs 2, 3, and 4 are compensated through cross-talk mechanisms as well as PKA- and PKG-mediated redistribution of LCC gating modes, so that their effect on I_{CaL} is absent under basal conditions and is most prominent a lower levels of β-adrenergic stimulation (Fig. 4.7–Fig. 4.9 and Fig.C.3).

4.5.2. PKA and PKG-mediated LCC gating mode redistribution explains regulation of I_{CaL}

Much of the functional effects of signaling on and kinase regulation of LCC remains to be understood, in part because there are many confounding factors regarding channel regulation [49, 195] and the difficulty in relating channel phosphorylation sites to functional changes in currents [164]. To refine our understanding, our model explained cN regulation of LCC currents in the simplest of terms by relating whole cell L-type Ca^{2+} current (I_{CaL}) to the fundamental parameters describing the opening and closing of a single LCC channel. This approach makes it possible to include information on PKA- and PKG-phosphorylated LCC gating properties derived from single-channel experiments [159-161, 179, 180, 186], which would otherwise be impossible if a more phenomenological model were employed. In model simulation, comparing to basal conditions (Fig. 4.3A and B, "Basal"; Fig. 4.3C, Mode 1 in black), PKA phosphorylation increases channel availability (Fig. 4.3A, "ISO") and the number of channels gating in Mode A (Fig. 4.3B, "ISO"), which is characterized by prolonged open time (Fig. 4.3C, red). This is consistent with the experimental results of Yue et al. [179], who demonstrated the existence of a distinct gating mode with very long-lasting openings as a result of ISO stimulation. Model further related this gating scheme to whole-cell I_{CaL} in that that model reproduces the potentiation of IV-curve under maximal ISO stimulation (Fig. 4.4B) and the full extent of I_{CaL} potentiation under varying [ISO] (Fig. 4.5A) as observed by Katsube et al. [169]. As a result, model elucidated single-channel behavior under full extent of β-adrenergic stimulation (Fig. 4.4, red and Fig. 4.5A–C).

Furthermore, PKG phosphorylation decreases channel availability (Fig. 4.3A, "SNAP") and potentiates gating in Mode G (Fig. 4.3B, "SNAP"), which is characterized by increased channel closed time (Fig. 4.3C, blue). This is consistent with observations by Tohse and Sperelakis that channel closed time is doubled, while channel open time and single channel conductance remain the same as control cells when PKG is fully activated by hydrolysis-resistant cGMP analogue (8-bromo-cGMP) [186]. Schröder et al. [161] additionally demonstrated decrease in channel availability under NO stimulation, which the model is consistent with. Model further relates this gating scheme to the suppression of IV curve of peak whole-cell I_{CaL} under maximal PKG activation (Fig. 4.4B, blue) as observed by Sumii and Sperelakis [163]. Additionally, model shows dual phosphorylation of LCC by both PKA and PKG returns channel availability to approximately that of basal conditions (Fig. 4.3A, "ISO+SNAP"), consistent with experimental data that by Carabelli et al. [159]. Dual phosphorylation also promotes Mode AG gating, a mode characterized by prolonged open and closed times (Fig. 4.3C, green). This is consistent with hypothesis by Carabelli et al. [159] that the effects of PKA and PKG phosphorylation on single channel gating are additive, which is also reflected by that the LCC Markov model for Mode AG (Fig. 4.1B) incorporates parameter adjustments of both Mode A and Mode G (i.e. $g_{modeAG} = g_{mode1}/10$ and $f_{modeAG} = f_{mode1}/2$). Our model reveals that such arrangement of gating schemes is sufficient to account for NO suppression of pre-stimulated I_{CaL} through β-adrenergic activation (Fig. 4.4B, green). This is consistent with experimental finding by Wahler and Dollinger [154] that subsequent NO stimulation returns LCC IV curve back to that observed under basal conditions.

4.5.3. Model elucidates regulation of I_{CaL} through NO/cGMP/PKG signaling axis

Activation of the NO/cGMP/PKG pathway suppresses pre-stimulated I_{CaL} is consistently observed by various groups [154, 162, 163, 194, 196-201]. On the other hand, its activation has yielded complex results, including increased [202], decreased [193, 203], or unchanged [194, 196] I_{CaL} under basal conditions in the absence of ISO. In addition, while the hypothesis that PKA-mediated phosphorylation of LCC is required for I_{CaL} potentiation under β-adrenergic stimulation is fairly established, LCC phosphorylation by PKG is less studied. We modeled PKG-mediated phosphorylation of LCC (Fig. 4.2), which is supported by studies demonstrating PKG phosphorylation sites on LCC [156, 157]. Besides data shown in Fig. 4.4B by Sumii and Sperelakis [163], NO-mediated suppression of basal I_{CaL} is also reported by other groups [193, 203, 204], in support of our model scheme (Fig. 4.1 and Fig. 4.2) and simulation results (Fig. 4.3–Fig. 4.6). Additionally, Ziolo et al. [203] further demonstrated that the observed I_{CaL} suppression is reversed upon application of PKG inhibitor.

Furthermore, the following experimental results in mammalian cardiac ventricular myocytes, obtained by stimulation and/or inhibition of NO/cGMP/PKG pathway at various points in the signaling cascade, also indirectly support our model results. First, decreasing cellular [NO], via NOS inhibitor, NO scavengers, or NOS knockout (eNOS-/-), has a stimulatory effect on basal I_{CaL} [155, 205, 206]. Second, basal I_{CaL} is suppressed by activation of NO/cGMP/PKG pathway through methods other than manipulating [NO], such as stimulating sGC or perfusion of cGMP or cGMP analogue [158, 201, 203, 207, 208]. Finally, increase of basal and pre-stimulated I_{CaL} is observed under inhibition of the

NO/cGMP/PKG cascade through methods other than decreasing [NO], such as inhibiting sGC [206, 209]. In addition, the following experiments support a direct interaction between LCC and PKG employed in our model. First, PKG-mediated suppression of LCC gating is potentiated in PKG-I transgenic mice over-expressing PKG [161]. Second, inhibitory effects of PKG on I_{CaL} is shown to persist under PDE inhibition and phosphatase inhibition and ablates under PKG inactivation [163]. Finally, when I_{CaL} was enhanced by Bay K 8644, which prolongs channel mean open times without increasing [cAMP] [210], the enhanced basal I_{CaL} was also reduced by activating PKG [163]. Taken together, the above experimental results support our model by demonstrating the inhibitory regulation of the NO/cGMP/PKG pathway on I_{CaL} and direct interaction of PKG with LCC, independent of possible confounding factors such as changes in [cAMP] and phosphatase activity via cross-talk mechanisms. For the experiments that showed no effect [194, 196] or slight stimulation [202] of I_{CaL} by NO stimulation, we believe the cause may be variation in experimental protocols, for instance NO, a highly reactive gas, is difficult to manipulate and has many cardiac reaction pathways and targets [15, 16, 33, 77, 147-150]. In fact, our model simulation shows that there is virtually no effect on I_{CaL} when [NO] is low; suppression only occurs when NO reaches a sufficiently high concentration (above ~ 50 nM) (Fig. 4.4, green; Fig. 4.5D, black).

Because our model allows dynamic transition between gating modes upon activation of the cN signaling pathway (Fig. 4.1 and Fig. 4.2), we are able to explain the observed whole-cell I_{CaL} in terms of changes in signaling and subsequent changes in LCC. With increased [ISO], substantial increase in [cAMP] and subsequent PKA activation (Fig. S2) overcome the slight increase in ISO-induced PKG activation (Fig. S2)

due to cN cross-talk [175], leading to increase in channel availability (Fig. 4.5B) and shift to Mode A gating (red) (Fig. 4.5C), finally results in steep increases in current over the range of ~ 5 nM to 50 nM [ISO] (Fig. 4.5A). We also discovered that NO-mediated suppression of I_{CaL} occurs via potentiation of Mode G (blue) gating (Fig. 4.5D–G). Activation of the NO/cGMP/PKG pathway is strong under NO stimulation that it overcomes β-adrenergic potentiation through cN cross-talk (Fig. 4.6). In addition, model shows that PKA and PKG phosphorylation of LCC exerts antagonistic effects on I_{CaL} (Fig. 4.5). This is supported by experimentally finding that NO ablates the increase in pre-stimulated I_{CaL} through activation of the β-adrenergic pathway [154, 162, 163, 194, 196-201] and the converse that β-adrenergic activation also stimulates PKG-inhibited I_{CaL} [163], although the latter of which is not usually performed experimentally.

Our model also shows that the occurrence of Mode AG (green) is rare, regardless of the extents of stimulation of the cN cross-talk network (Fig. 4.5C, F, and G). Mode AG therefore contributes the least to L-type Ca^{2+} current among the four gating modes modeled. This result adheres with intuition that the probability of simultaneous occurrence of two events (phosphorylation by both PKA and PKG) is low due to multiplying the probabilities of the individual events (individual phosphorylation by PKA and PKG), assuming independence of the two events. To the best of our knowledge, there is currently no experimental evidence explicitly demonstrating dependence of PKA- and PKG-mediated phosphorylation of LCC. As a result, our model made the above independence assumption, which eliminated the need to constrain the additional model states exposed if dependence were assumed with experimental data.

This study assumed that PKG phosphorylation rate of LCC is equal to that of PKA (i.e.$k_{cat\_PKG} = k_{cat\_PKA}$), in the absence of experimental data (Appendix C Sect. C.3.2). We examined our results on I_{CaL} regulation (Fig. 4.5, Fig.C.3, and Fig. 4.6) through sensitivity analysis (Appendix C Sect. C.6.2) of increasing (Fig.C.4–Fig.C.6) and decreasing (Fig.C.7–Fig.C.9) k_{cat_PKG} by a factor of ten. Comparing the results from this sensitivity analysis and figures from the original model, ten-fold variations in k_{cat_PKG} do not produce significant changes in model outputs on LCC currents, LCC gating, or cN cross-talk signaling (Fig.C.4–Fig.C.9). This is because channel dephosphorylation rate (k_{PP2A}) is much larger than the PKA and PKG kinase phosphorylation rates (k_{cat_PKA} and k_{cat_PKG} respectively) and, therefore, dominates the behavior of the PKA-PKG-LCC model (Fig. 4.2). As a result, our key findings are not likely to be affected by uncertainty in the exact value of PKG phosphorylation rate of LCC (k_{cat_PKG}).

4.5.4. Change in I_{CaL} is mitigated by cN cross-talk and redistribution of distinct gating modes

Due to the tightly-coupled and intertwined reaction network (Fig. 4.1) [127, 175], it has been difficult to resolve the following two mechanisms underlying LCC regulation: 1) regulation of PKA and PKG activation via cN cross-talk (Mechanism 1); and 2) LCC interaction with activated PKA and PKG (Mechanism 2). Consequently, it has been debated if activation of the NO/cGMP/PKG pathway exerted its effect on LCC through PKG-mediated phosphorylation or its influence on PKA activation [78, 151, 153]. Analysis through our model is able to distinguish LCC regulation exerted by these two

mechanisms. Our model therefore serves as a powerful tool for interpreting experiments on cN signaling and I_{CaL} interaction.

Our model demonstrates that the effects of PDE inhibition on I_{CaL} are most pronounced under low levels of β-adrenergic stimulation (Fig. 4.8A), but absent under basal conditions (Fig. 4.7A), consistent with that reported by Verde et al. [86]. Our model further revealed the mechanisms behind this phenomenon (Fig. 4.7–Fig. 4.9 and Fig.C.3). As shown in Fig. 4.7C and D, the net PDE rate change (grey) is very much the same as the decrease in rate of the inhibited PDE, indicating that the remaining PDEs do not compensate much for the loss of the inhibited PDE through cross-talk mechanisms. This is because, under basal conditions, [cN] and its change under PDE inhibition are too minute to activate noticeable changes in PDE activities. As a result, PKA (red) and PKG (blue) interaction with LCC cannot produce sufficient changes in channel availability or modal distribution for a change in I_{CaL} to occur (Fig. 4.7E). Because PKA-PKG-LCC interaction is preserved as that of control cells and PDE compensation virtually non-existent under basal conditions, the absence of effects under PDE inhibition is primarily a result of Mechanism 2.

Under β-adrenergic stimulation, the cell activates both Mechanism 1 and Mechanism 2 to compensate for PDE inhibition. I_{CaL} increased the least under PDE2 inhibition, because increase in PDE4 rate prevented large increases in [cAMP] due to PDE2-PDE4 coupling [211] (Mechanism 1). In addition, PKG activation under low β-adrenergic tone suppressed PKA-mediated increases in I_{CaL} (Fig. 4.8 and Fig. 4.9) (Mechanism 2). For both PDE3 and PDE4 inhibitions, β-adrenergic pathway becomes the principal driver in I_{CaL} regulation, as changes in PDE cGMP activities are small

compared to that under PDE2 inhibition and to changes in PDE cAMP activities (Fig. 4.9D–F). For PDE3 inhibition, the extents of changes in I_{CaL} (Fig. 4.8A) positively correlate with changes in PKA activation (Fig. 4.8C) and with that of [cAMP] (Fig. 4.8B), which is compensated by increase in PDE2 and PDE4 rates (Fig. 4.9) (Mechanism 1). For PDE4 inhibition, increase in PDE2 activity partially degraded the excess cAMP and saturation of PKA activation by cAMP prevented further increase of channels gating in Mode A (Fig. 4.8 and Fig. 4.9) (Mechanism 1). Understanding of these mechanisms will contribute to more precise manipulation of I_{CaL} through this pathway.

4.5.5. Model rationale, limitations, and future work

Our current study focuses on functionally linking cN cross-talk signaling to LCC channel regulation (Fig. 4.1). Recent advances have revealed that many signaling components in the model (Fig. 4.1) form compartments and/or multi-protein signaling complexes ("signalosomes") [36, 63, 67, 121-124, 212]. For instance, in addition to β-adrenergic pathway compartmentalization [213-216], NO-derived cGMP and natriuretic peptide (NP)-derived cGMP are discovered to reside in distinct subcellular compartment [82, 166] and exert differential regulation of β-adrenergic responses, [17, 77, 78, 120, 167], with functional significance in diseased cardiac myocyte [120, 165, 166]. With advancements in methods for spatiotemporally-resolved recording of cNs [36, 63, 67, 82, 120-124, 165] and in understanding molecular basis of compartmentalization [123, 217-221], extending the model to include these additional mechanisms serves to understand how cN signals are diversified in subcellular micro-domains, how coherent signaling is orchestrated between these compartments, and how down-stream effectors respond to the diversified

signals. Due to lack of experimental data, our model did not study the effect, if any, of CDI of LCCs on distribution of gating modes or gating characteristics of each gating mode [222, 223]. Experimental studies using barium (Ba^{2+}) as charge carriers, which eliminate CDI [224, 225], and with mutations affecting CDI [225] demonstrate that variation of the CDI process mostly disturb channel gating kinetics, but not peak I_{CaL}. As a result, we limited our analysis to peak I_{CaL}. We further deomonstrated that varying [Ca^{2+}] between 1 nM and 10 μM does not significantly change model peak I_{CaL} (Appendix C Fig.C.10). We also did not study the interaction between LCCs and Ca^{2+} dynamics in the micro-domain near the mouth of the LCC or the impact of which on CICR [195, 226-229]. In addition, expansion of the model to include altered cN signaling network [3, 34-37] and L-type Ca^{2+} current [168, 177, 178] implicated in cardiac hypertrophy and heart failure (HF) will also help understand disease mechanisms. Aided by advances in experimental findings, modeling compartmentalization and functional integration of the model into a whole-cell myocyte model in future research will help investigate these unanswered questions in local signaling and cN regulation of Ca^{2+} cycling and AP morphology.

4.6. Conclusion

We developed a computational model of LCC regulation by the cN cross-talk signaling network (Fig. 4.1) that functionally integrates signaling and LCC gating to investigate the effect of cN cross-talk on LCC current (Fig. 4.2). Using the model, we deciphered the underlying mechanisms of three model observations: 1) changes in whole-cell current

can be explained by redistribution of LCC gating modes caused by simulation of the cN cross-talk network (Fig. 4.3–Fig. 4.5); 2) NO regulation of I_{CaL} occurs via potentiation of Mode G gating (Fig. 4.5–Fig. 4.6); and 3) The effect of PDEs 2, 3, and 4 inhibition is absent under basal conditions but most pronounced a low levels of β-adrenergic stimulation, because change to I_{CaL} is mitigated by cN cross-talk and redistribution of LCC gating modes (Fig. 4.6–Fig. 4.9).

Disclosures

None declared.

Acknowledgements

This work was supported by Natural Sciences and Engineering Research Council (NSERC) of Canada scholarships, CGS M-377616-2009 and PGSD3-405041-2011, awarded to C.Y.Z, and National Heart Lung and Blood Institute (NHLBI) of the USA grant R01 HL105239.

A portion of the research contained in this manuscript has been presented as a Platform Presentation in Calcium Signaling at the 60th Annual Meeting of the Biophysical Society in March, 2016.

Appendix C. Supplementary Material for the cN Signaling–LCC Model

Chapter 5. Summary and Conclusions

While it has long been known that the HF phenotype exhibits altered EC coupling [4, 230], research has only recently begun to focus on remodeling of the cN cross-talk signaling network as a possible contributing factor [2, 3, 35, 50, 52, 231, 232]. Through a variety of experimental techniques, many of the signaling components comprising the cN signaling network are shown to remodel in HF [3, 34-37]. On the other hand, experiments on the signaling network primarily utilize protocols using purified protein extracts and/or focuses on the measurement of one physiological quantity at a particular spatial-temporal scale [29-31]. Furthermore, the interpretations of experiments are often confounded by complex compensatory network interactions [127, 175, 211]. As a result, it is difficult to attain a systems-level understanding of the signaling network that bridges the causal link between the characteristics of individual signaling proteins and the collective response of the entire network.

Through data-driven multi-scale modeing, this work is able to link the characteristics of individual proteins, to the signaling network, and to the interaction between signaling and electrophysiology. Consequently, analysis results achieve a quantitative and systems-level understanding of the mechanisms functionally significant to cN signaling and its regulation of LCC. The modeling work here is also unique in that it is the first to incorporate the cross-talk between β-adrenergic and NO/cGMP/PKG pathways and detailed description of regulation of LCCs by this signaling network. Thus the model is able to offer mechanistic predictions within each biophysical hierarchy and accross hierarchies, achieveling molecular understanding of the signal network.

Using the models, we addressed our three major aims for the investigatigation of the cN cross-talk signaling network. The first aim is to quantify the molecular mechanisms of cN regulation of PDEs and their influences on β-adrenergic pathway (Chapter 2). The second aim is to study PDE interactions arising from dynamic cN cross-talk within the cN cross-talk signaling network (Chapter 3). The third aim is to identify and analyze functionally significant mechanisms underlying LCC regulation by the signaling network (Chapter 4).

5.1. Mechanistically derived, multi-scale computational model achieves multi-type data integration and fusion

An understanding of the regulatory pathways can be best achieved using an integrated systems approach, incorporating the interplay of cNs and dynamic regulation of LCC by the signaling network. In order to achieve our research aims, we leveraged the extensive work embodied by the following three well-validated state-of-the-art computational models: the β-adrenergic signaling pathway model by the Saucerman lab [71], the NO/sGC/PDE5 model by the Garthwaite lab [129], and the cardiac LCC model from the Winslow lab [176]. The β-adrenergic model [71] includes a representation of cAMP production through ISO-induced activation of AC, cAMP degradation by a lumped PDE component, and the release of active subunits of PKA upon activation by cAMP. The NO/sGC/PDE5 model [129] includes NO-induced sGC activation for cGMP production and cGMP degradation by PDE5 which is in turn activated by cGMP. The LCC model

[176] features realistic voltage activation and inactivation, which is critical to shaping the cardiac AP [233].

In order to functionally integrate the three aforementioned models, modeling efforts in this research fused a multitude of experimental data, effectively leveraging upon the extensive knowledge accumulated in published literature (Fig. 5.1). The biomedical reactions included in the model were represented in the most detailed, mechanistic way possible. In the βAR–PDE model [127] (Chapter 2), we derived mechanistic models of the PDEs based on structural data from X-ray crystallography, amino-acid sequencing and electron density maps, as well as functional data from purified proteins using biochemical assays, sometimes with site-directed mutagenesis of the PDE protein (Fig. 5.1 Items 1–5). In addition, measurements of [cAMP] in live-cell Fluorescent (FRET) imaging and radioimmunoassay (Fig. 5.1 Items 10–11) under various protocols of PDE inhibition informed relative activities of the PDEs within the β-adrenergic pathway.

Fig. 5.1. Multi-scale modeling of cN signaling network.

Experimental methods at their respective biophysical scales (listed in grey boxes) used to constrain and validate the βAR–PDE model [127] (Chapter 2), the cN cross-talk signaling network model [175] (Chapter 3), and the signaling–LCC model (Chapter 4).

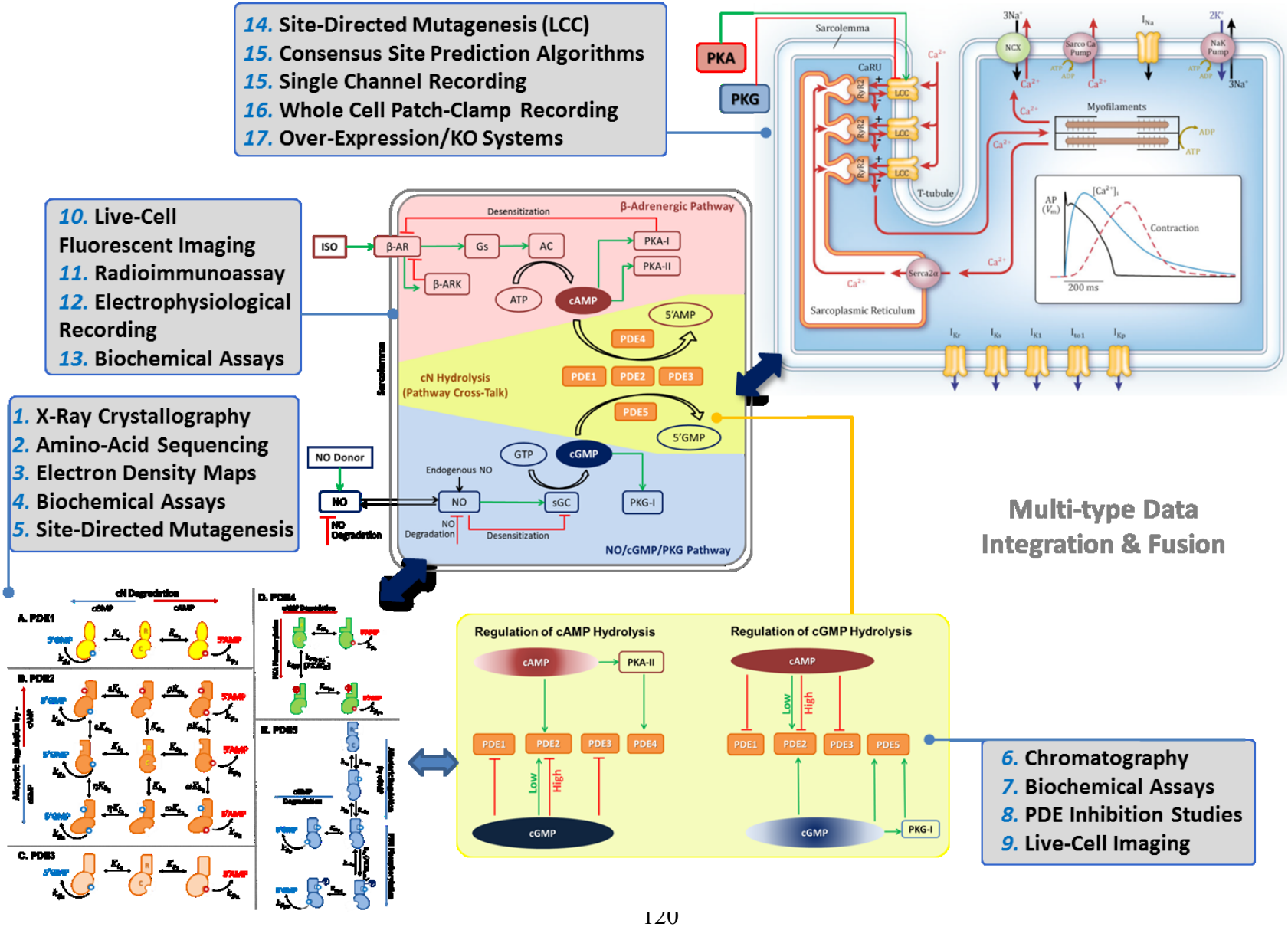
14. Site-Directed Mutagenesis (LCC)
15. Consensus Site Prediction Algorithms
15. Single Channel Recording
16. Whole Cell Patch-Clamp Recording
17. Over-Expression/KO Systems
10. Live-Cell Fluorescent Imaging
11. Radioimmunoassay
12. Electrophysiological Recording
13. Biochemical Assays
1. X-Ray Crystallography
2. Amino-Acid Sequencing
3. Electron Density Maps
4. Biochemical Assays
5. Site-Directed Mutagenesis
PKA
PKG
Sarcolemma
CaRU
T-tubule
Myofilaments
Sarcoplasmic Reticulum
Contraction
ISO
β-AR
Gs
AC
ATP
cAMP
PKA-I
PKA-II
β-ARK
Desensitization
β-Adrenergic Pathway
5'AMP
PDE4
PDE1
PDE2
PDE3
cN Hydrolysis (Pathway Cross-Talk)
PDE5
5'GMP
GTP
cGMP
NO Donor
NO
Endogenous NO
sGC
PKG-I
NO Degradation
Desensitization
NO/cGMP/PKG Pathway
Multi-type Data Integration & Fusion
Regulation of cAMP Hydrolysis
Regulation of cGMP Hydrolysis
Low
High
6. Chromatography
7. Biochemical Assays
8. PDE Inhibition Studies
9. Live-Cell Imaging

The cN cross-talk signaling network model [175] (Chapter 3) incorporated the previously developed PDE models [127] to link the input of ISO and NO to the output of PKA and PKG signals. We quantified the cN cross-talk mechanisms in cardiac myocytes (Fig. 5.1 yellow box), with experimentally-observed steady-state behavior and temporal dynamics of both cN signals obtained from studies utilizing FRET imaging, radioimmunoassay, electrophysiological recording, and biochemical assays under various PDE inhibition protocols (Fig. 5.1 Items 7–9 and 10–13). In addition, chromatography studies (Fig. 5.1 Item 6) provided insights on the relative expressions of different PDE families.

Finally, in the signaling–LCC model (Chapter 4), the cN cross-talk signaling model is mechanistically integrated with a LCC model [176]. In order to achieve this, we used data obtained from single channel and patch clamp recording experiments in control, over-expression, and knockout models as well as LCCs with site-directed mutagenesis. We also incorporated insights obtained from consensus site prediction algorithms (Fig. 5.1 Items 9 and 10).

The mechanisms by which the cN cross-talk signaling network influences cardiac function have been difficult to conceptualize in a unified manner. By integrating the wide-ranges of experimental data listed above, our models developed provided a common framework for these data, which are otherwise not commonly viewed together (Fig. 5.1). These various sources of information give our model predictive power and are subsequently mined for meaning via model simulation and analysis. In addition, our models also allow for the alteration of internal concentrations and rates not necessarily well-controlled or even accessible in experiments, therefore providing a tightly controlled

experimental set-up for predictions unattainable by current technology. Biophysically-based and experimentally-validated computational modeling is a powerful tool for dissecting the integrated behavior of complex biological systems [234]. When coupled with experiments, this approach is particularly insightful for the distillation of critical relationships in complex, intertwined, and often times non-intuitive signaling networks [234].

5.2. Molecular understanding of network behavior is achieved via integrative analysis

The models developed in this work quantified interactions across multiple biological scales, from molecular characteristics of each signaling component, to individual biochemical reactions between components, to the collective architecture of the entire signaling network (Fig. 5.1). They also incorporates mechanisms across multiple temporal scales, from minutes for the net cN signals, to milliseconds at the levels of PDE activities and channel gating. This work therefore reveals the molecular origins of the network phenomena of cN cross-talk and LCC regulation, which is critical to the regulation of cardiac contractility.

Fig. 5.2. Highlight of findings.

Major findings are listed at their respective biophysical scales (blue boxes) from analysis of the βAR–PDE model [127] (Chapter 2), the cN cross-talk signaling network model [175] (Chapter 3), and the Signaling–LCC model (Chapter 4).

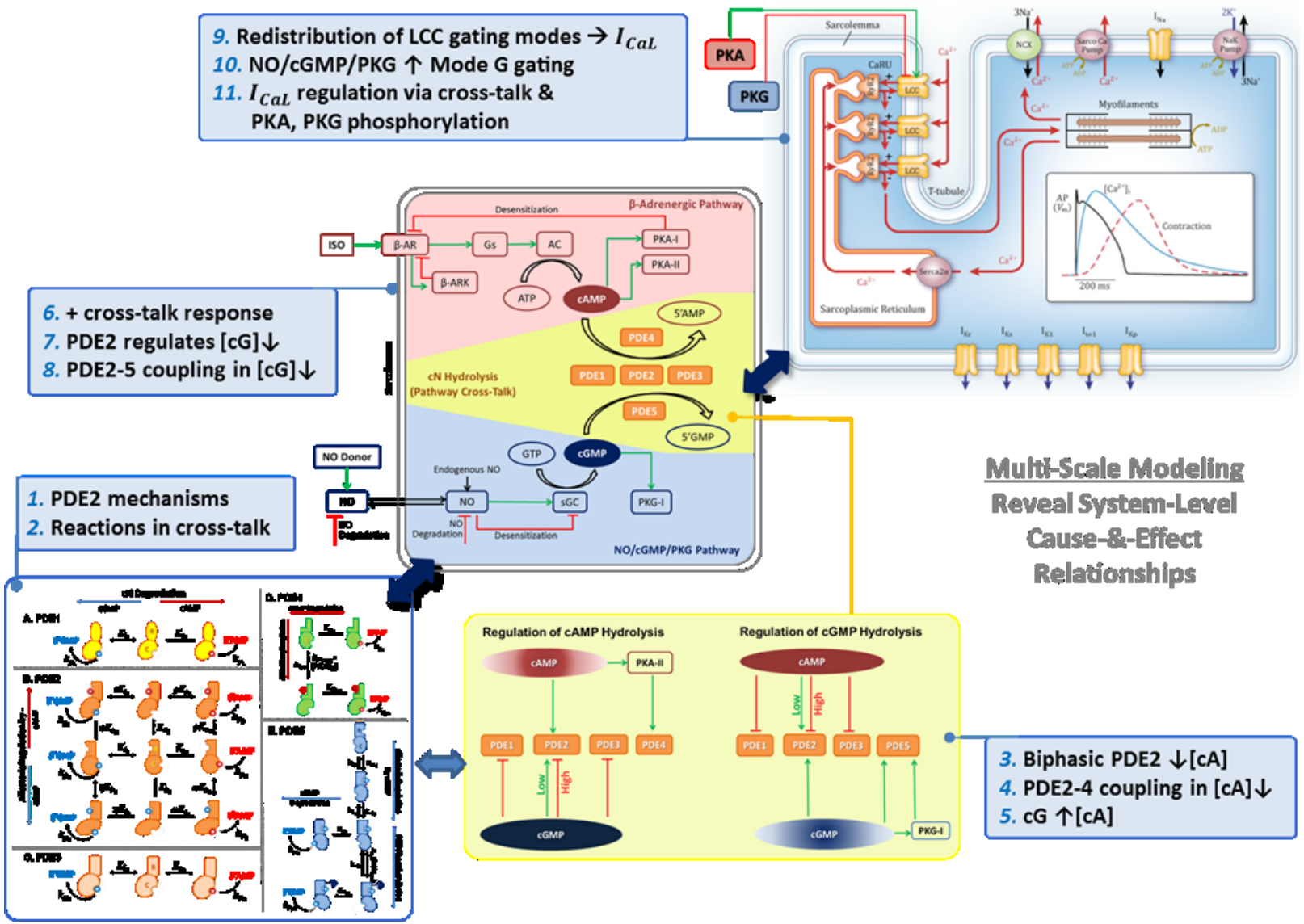
9. Redistribution of LCC gating modes → I_{CaL}
10. NO/cGMP/PKG ↑ Mode G gating
11. I_{CaL} regulation via cross-talk & PKA, PKG phosphorylation
PKA
PKG
Sarcolemma
CaRU
LCC
T-tubule
Myofilaments
Sarcoplasmic Reticulum
Contraction
200 ms
6. + cross-talk response
7. PDE2 regulates [cG]↓
8. PDE2-5 coupling in [cG]↓
β-Adrenergic Pathway
Desensitization
ISO
β-AR
Gs
AC
PKA-I
PKA-II
β-ARK
ATP
cAMP
5'AMP
PDE4
cN Hydrolysis (Pathway Cross-Talk)
PDE1
PDE2
PDE3
PDE5
5'GMP
GTP
cGMP
NO Donor
Endogenous NO
NO
sGC
PKG-I
NO Degradation
Desensitization
NO/cGMP/PKG Pathway
1. PDE2 mechanisms
2. Reactions in cross-talk
Regulation of cAMP Hydrolysis
Regulation of cGMP Hydrolysis
Low
High
3. Biphasic PDE2 ↓[cA]
4. PDE2-4 coupling in [cA]↓
5. cG ↑[cA]
Multi-Scale Modeling Reveal System-Level Cause-&-Effect Relationships

In Zhao et al., 2015 [211] (Chapter 2), a biophysically-detailed computational model is presented that provides insights on how interactions between distinctively regulated phosphodiesterase isoenzymes (PDEs) affect β-adrenergic response in cardiac myocytes [127]. Using these PDE models, the molecular mechanisms by which the PDEs decode information carried in the cGMP signal in β-adrenergic pathway regulation were revealed. The following key results were obtained (Items 1–5):

- PDE2 and PDE4 activities exihbit strong coupling.
- PDE2 regulation of cytosolic cAMP is potentiated at low but suppressed at high [cGMP].
- cGMP potentiates whole-cell [cAMP] and subsequent PKA activation.
- PDEs serve as an integration point for cAMP and cGMP signals.

In Zhao et al., 2016 [175] (Chapter 3), a biophysically-detailed computational model is constructed that provides insights on the cross-talk communication between the β-adrenergic and NO/cGMP/PKG signaling pathways via distinctively-regulated PDEs in cardiac myocytes. The combined model is the most highly integrated cN signaling model to date. Using this model, a precise quantitative understanding of how cGMP and cAMP signals influence each other were obtained by by analyzing the interaction of individual signaling elements in the context of the network architecture. The following key results were obtained (Items 6–8):

- Whole-cell [cAMP] and PKA activation are potentiated by NO stimulation.
- NO/cGMP/PKG pathway response is potentiated by β-adrenergic stimulation.
- PDE2 regulation of cytosolic [cAMP] and [cGMP] depends on PDE interaction.
- PDE2 compensation regulates anti-adrenergic effect of PDE5 inhibition.

Finally, a biophysically-detailed computational model is constructed that provides insights on LCC regulation via PKA- and PKG-mediated phosphorylation (Chapter 4). This is the first model accounting for LCC regulation by the cN signaling network via its interaction with both kinases. The following key results were obtained (Items 9–11):

- Single-channel gating mode redistribution by network explains whole cell LCC current (I_{CaL}) responses.
- NO suppression of I_{CaL} occurs via potentiation of Mode G, characterized by prolonged closed times.
- Changes to I_{CaL} are mitigated by cN cross-talk and redistribution of LCC gating modes.

Chapter 6. Future Directions

With advancements in methods for spatiotemporally-resolved recording of cAMP [36, 63, 67, 121-124] and, more recently, cGMP [82, 120, 165], extending the model to include additional mechanisms in cN regulation is an important next step to understand diversification of cN signals in subcellular micro-domains and communication between these cellular compartments. For instance, in addition to NO-derived cGMP, natriuretic peptide (NP) is also responsible for cGMP synthesis in the cardiac myocytes. The NP-derived cGMP reside in distinct subcellular compartment [82, 166] and is differentially regulated and triggers different responses than the NO-derived cGMP [16, 235]. The two cGMP pools are also shown to be regulated by distinct sets of PDE families [166]. On the other hand, both cGMP pools are critical in cN signal transduction and regulation of cardiac contractility [166, 232].

In addition, computational model can be extended to study the effect of signaling macro-complexes or signalosomes, which organizes signaling components into spatially and/or functional aggregates. For instance, PDE3A1 has recently been shown to participate in the SERCA/PLB/AKAP signalosome, where phosphorylation by PKA promotes its targeting to the signalosome and where it may modulate [cAMP] in a highly localized manner [125]. This is a level of compartmentalization not described in our model. This is a good instance in which modeling can be utilized to study how local and global signaling is orchestrated to achieve coherent cellular communication.

Furthermore, these targets of the cN signaling network include many other proteins critical to cardiac calcium homeostasis and excitation-contraction, in addition to LCCs. For instance, phospholamban (PLB) and Troponin I (TnI) are targets for both

PKA [5] and PKG [2, 8, 9]. Further extensions to the model must ultimately include regulation of transmembrane channels and Ca^{2+} cycling proteins, and incorporation of these mechanisms into integrative models of the ventricular myocyte.

Finally, a model for diseased cardiac myocyte should be developed to study the effect remodeling signaling components in the network on signal transduction and electrophysiology [120, 165, 166]. In cardiomyocytes from hypertrophic hearts, Perera et al. revealed that β-adrenergic receptor-stimulated contractility is amplified by NP/cGMP signaling due to spatial redistribution of PDE2 and PDE3 [120]. In addition, Zhang et al. reported that PDE5 is retargeted to hydrolyze NP-derived cGMP instead of NO-derived cGMP [165]. These recent breakthroughs in spatiotemporally resolved live-cell recordings of cNs (e.g. [120, 165]) have begun to provide new insights and will be valuable in guiding us in the development of computational models for further research in cN cross-talk signaling network.

Regarding LCC regulation, further studies are required to ellucidate the effects of Ca^{2+} dependent inactivation (CDI) on LCC current kinetics, distribution of gating modes, and gating characteristics of each gating mode [222, 223]. In addition, it is also crucial to study interaction between LCCs and Ca^{2+} dynamics in the micro-domain near the mouth of the LCC or the impact of which on CICR [195, 226-229]. Aided by advances in experimental findings, modeling compartmentalization and functional integration of the model into a whole-cell myocyte model will help investigate unanswered questions in cN regulation of Ca^{2+} cycling and AP morphology. Further integration of the models into higher-dimensional tissue models will aid the understanding of Ca^{2+} and AP propagation in the heart.

More in-depth analysis of the cross-talk signaling network represents new opportunities for the model to identify experimental conditions for future studies of cross-talk. Methods such as sensitivity analysis can be utilized to simulate disease conditions and identify drugable targets. The therapeutic potential of the cN signaling network is highlighted in literature [11, 14, 31, 231, 236, 237]; however, the extent to which these changes intervene with the normal operations of the entire signaling network, the cell, and ultimately the whole heart remains to be carefully studied. Useful therapeutic targeting of the myocyte β-adrenergic and NO/cGMP/PKG pathways requires an intimate knowledge of the proteins that regulate it. Mechanistic insights into intracellular signaling pathways hold the promise to developing new treatment for reversing the devastating consequences of HF [2].

Appendix A.Supplementary Material for the β-Adrenergic–PDE Model

A.1. Definition of terminology and symbols

A.1.1. Definition of symbols for signaling network components

	Symbol	Representation
		Phosphodiesterases
1	PDE	Phosphodiesterase, enzyme that catalyzes the breakage of phosphodiester bond in cAMP
2	PDEs	Phosphodiesterase isoenzymes
3	PDE1	Phosphodiesterase gene family 1
4	PDE2	Phosphodiesterase gene family 2
5	PDE3	Phosphodiesterase gene family 3
6	PDE4	Phosphodiesterase gene family 4
		Cyclic nucleotides and hydrolyzed forms
7	cAMP	Cyclic Adenosine-3',5' Monophosphate (second messenger)
8	cGMP	Cyclic Adenosine-3',5' Monophosphate (second messenger)
9	cN	Cyclic Nucleotide, either cAMP or cGMP (second messenger)
10	cNs	Cyclic Nucleotides, both cAMP and cGMP (second

		messengers)
11	5’-AMP	Adenosine 5’-Monophosphate. Hydrolyzed cAMP, after breakage of its phosphodiester bond
		β-adrenergic signaling pathway
12	β-AR	β-Adrenergic Receptor
13	βARK	β-Adrenergic Receptor Kinase
14	Gs	G-protein
15	AC	Adenylyl Cyclase
16	ATP	Adenosine Triphosphate
17	ADP	Adenosine Diphosphate
18	PKA	Protein Kinase A (cAMP-dependent protein kinase)
19	PKA-I	PKA, Type I
20	RI	Regulatory subunit of PKA-I
21	PKACI	Catalytic subunit of PKA-I
22	PKA-II	PKA, Type II
23	RII	Regulatory subunit of PKA-II
24	PKACII	Catalytic subunit of PKA-II

Table A.1. Definition of symbols for signaling pathway components.

A.1.2. Definition of symbols for pharmacological drugs

	Symbol	Full Name	Effects
1	ISO	Isoproterenol	β-AR agonist
2	IBMX	3-isobutyl-1-methylxanthine	Non-specific PDE inhibitor
3	PKI	Protein Kinase Inhibitor	Kinase inhibitor
4	EHNA	Erythro-9-(2-Hydroxy-3-Nonyl) Adenine	PDE2 inhibitor
5	Cilo	Cilostamide	PDE3 inhibitor
6	Rol	Rolipram	PDE4 inhibitor

Table A.2. List of pharmacological drugs.

A.2. Model constraints and additional validation

Each PDE model is optimized individually to in vitro data on purified PDE (Fig.A.1 and the stated conditions below). For a given PDE isoenzyme model, all constraints for that PDE are used simultaneously (i.e. included in the same cost function), together with the ranges for parameters imposed by experiments whenever available (Section 5B Tables, Pages 26-28). Subsequently, the relative proportions of the PDEs were fit to Fig.A.4 (Page 11). Each optimization minimizes the value of a cost function that captures the distance between the data points and the corresponding simulation results through the least-square best fit method. All optimizations are performed in MATLAB (MathWorks Inc.) using the function, fmincon, utilizing the interior-point optimization algorithm. No additional tests of uniqueness of the fit were performed.

A.2.1. Constraints for PDE models

The parameters for the PDE models are constrained by the data shown in Fig.A.1. In addition, they are constrained to ranges identified by experiments whenever available (referenced in Section 5B). All plots in Fig.A.1 are presented in a way that preserves their original appearance in the source literature. To constrain parameters for PDEs 1, 3, and 4, Equations 12, 15, 17 are fitted to data shown in Fig.A.1 (A), (C), and (D) respectively, together with the ranges for parameters imposed by experiments (referenced in Section 5B).

Fig.A.1. Experimental constraints for PDE models.

Dotted symbols represent experimental data; lines represent simulation results. ***(A)*** PDE1 cAMP hydrolysis rate (normalized to the recorded maximum rate) is constrained to normalized data from Yan et al. [87] with 3.125 μM cGMP. ***(B)*** Effects of various [cAMP] on PDE2 cGMP hydrolysis rates, with 0.2 μM cGMP, is constrained by data from Terasaki & Appleman [118]. Rates are normalized to the cGMP rate measured without cAMP. ***(C)*** PDE3 model is constrained to normalized data from Movsesian et al. [238]. The dashed line is fit to rates measured without cGMP (hollow dots), and solid line to rates measured with 0.05 μM cGMP (filled dots). ***(D)*** PDE4 model replicates normalized data from Wang et al. [239].

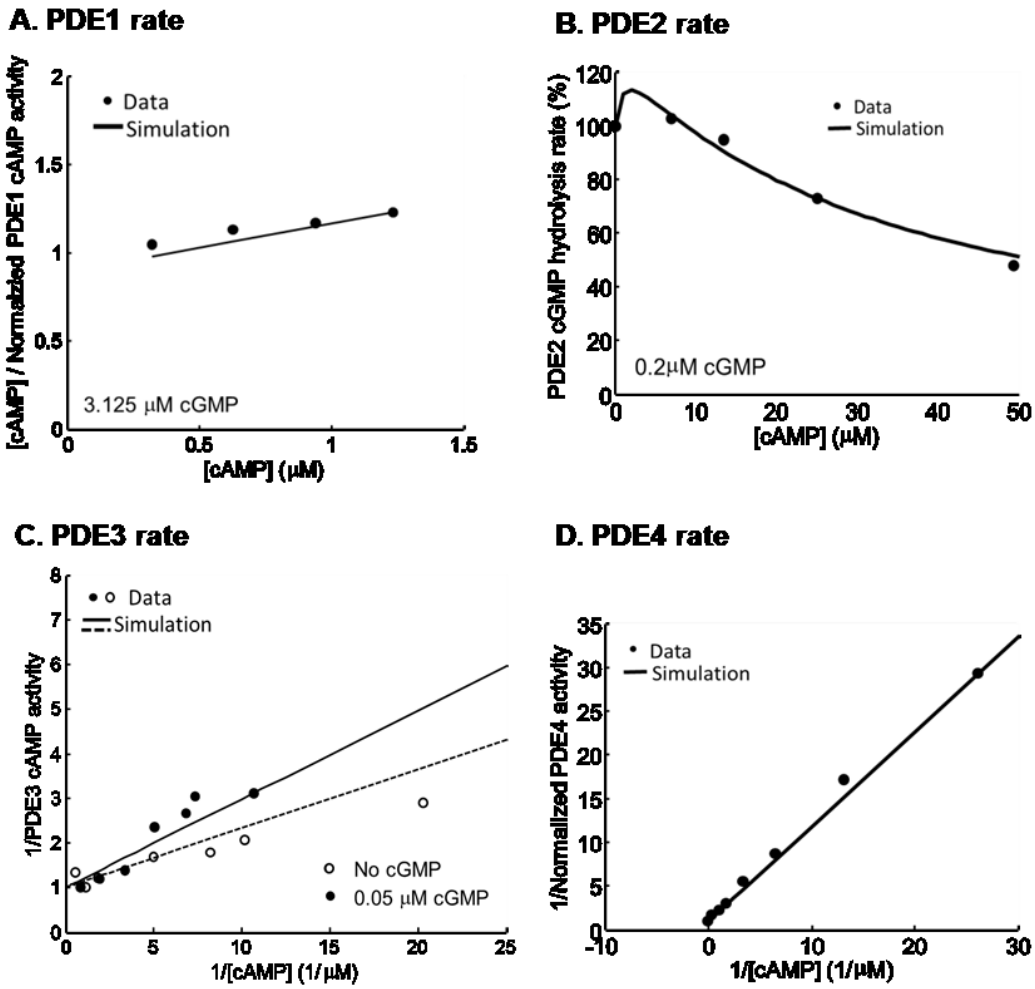

For the PDE2 model, the following constraints are imposed simultaneously to fit Equations 13 and 14, in addition to that shown in Fig.A.1B:

1. Parameters K_{a_2} and K_{b_2} are constrained to the ranges identified by [240, 241] and parameters

   K_{s_2} and K_{I_2} to those identified by [31].

2. The scaling factors, ρ, ω, ε, and η, are constrained to the ranges of (0, 1), because cN binding to GAF-B regulatory domain increases cN binding affinity to catalytic

domain (i.e. decreases dissociation constant). In other words, cN allosteric regulation produces positive cooperativity [30, 241].

3. cAMP-mediated scaling factors (ρ and ε) are required to take on values that are greater than their corresponding cGMP-mediated scaling factors (ω and η) as experiments show less sensitivity of PDE2 to cAMP allosteric regulation [95].
4. The apparent EC50 for cAMP (measured in the absence of cGMP), is constrained to be greater than that for cGMP (measured in the absence of cAMP) [95].
5. The maximal cAMP hydrolysis under cGMP regulation is constrained to occur at [cGMP] above 2 μM [93, 241].
6. Microscopic reversibility is satisfied for each closed loop of the PDE2 model (Fig. 2.2B).

Experimental basis for model construction are explained in Section 6 of the Supplement.

A.2.2. Additional validation of PDE models

We define "model validations" as predictions made using the model that agree with experimental data not included in the fitting process.

Fig.A.2. Experimental validation of PDE2 cAMP hydrolysis.

When cGMP is not present, EC50 of PDE2 cAMP hydrolysis rate (black line) agrees with the average reported by various experimental groups (horizontal error bars) [29, 94, 95]. The range of cellular average [cAMP] [17, 95, 150, 192, 242, 243] is indicted by the shaded grey area.

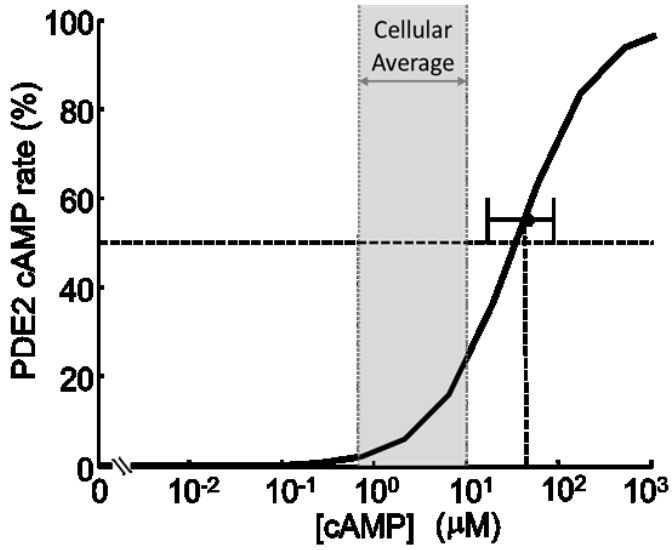

A.2.3. Validation of kinase activation

We define "model validations" as predictions made using the model that agree with experimental data not included in the fitting process.

The PKA model from Saucerman et al. [71] reproduces experimentally measured relationships between PKA activation and [cAMP] (Fig.A.3), with (black) and without (grey) the kinase inhibitor (PKI) [244].

Fig.A.3. Experimental validation of PKA activation.

(A) and ***(B)*** are reproduced according to Saucerman et al. [71] using the present model. ***(A)*** Dependence of PKA activation (normalized) to [cAMP] with (grey) and without (black) protein kinase inhibitor, PKI (60 nM) agree with experimental results of Beavo et

al. [244]. ***(B)*** Hill plot of PKA activation with (grey) and without (black) PKI is reproduced using the same data as (A). Presence of cooperativity is highlighted by the nonlinearity exhibited by $\log(F/(1-F))$, where F is the fraction of PKA activation shown in (A).

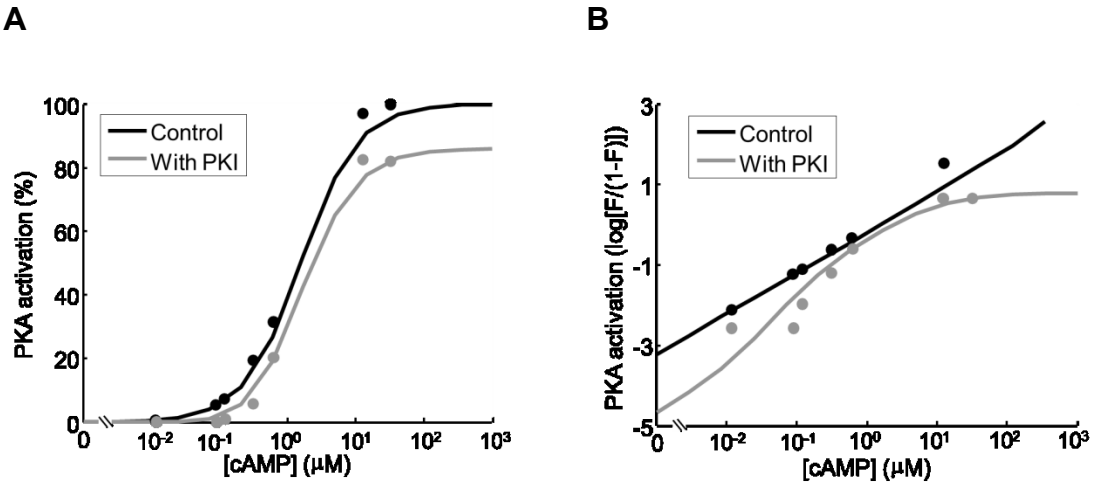

A.2.4. Constraints for cN cross-talk signaling network

Data from Adult Rat Ventricular Myocytes (ARVMs) obtained by Verde et al. [86] and Rochais et al. [85] are shown in grey and black respectively in Fig.A.4. The lower two, closely-matching data sets from Verde et al. [86] and the data averages from Rochais et al. [85] are used to constrain the rates of cAMP hydrolysis by PDEs 1 – 4, namely parameters $Vmax_{PDE1_A}$, $Vmax_{PDE2_A}$, $Vmax_{PDE3_A}$, and $Vmax_{PDE4_A}$ (Section 5B). In addition, the constraint that the hydrolysis rate of PKA-phosphorylated PDE4 is 1.4 times that of non-phosphorylated PDE4 [130, 245] is applied simultaneously.

Fig.A.4. Constraints for maximal PDE cAMP hydrolysis rates.

Data used for constraining cAMP hydrolysis rates ($Vmax$'s) of PDEs 1 – 4 are shown, with the specific PDE inhibited indicated on the abscissa. Percent increase in [cAMP] against total cAMP hydrolyzed (as measured by the non-specific PDE inhibitor, IBMX) upon PDE2, PDE3, and PDE4 inhibition (with inhibitors EHNA, Cilo, and Rol respectively) are shown from Verde et al. [86] (grey) and Rochais et al. [85] (black). Simulation results are show in blue. Data from Verde et al. [86] are displayed in accordance with the original figure, with averages indicated by bar graph. The lower two, closely-matching data sets from Verde et al. [86] and the data averages from Rochais et al. [85] are used to constrain the rates of cAMP hydrolysis by PDEs 1 – 4 to avoid biasing the model. All data are obtained from ARVMs under basal condition (i.e. without ISO).

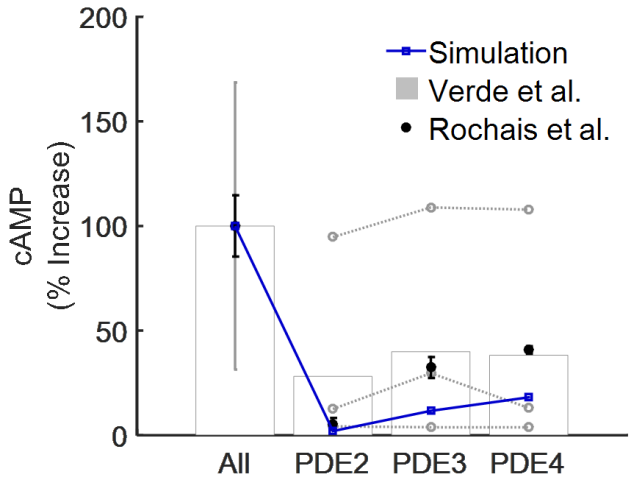

A.2.5. Additional validation for cN cross-talk signaling network

We define "model validations" as predictions made using the model that agree with experimental data not included in the fitting process.

Fig.A.5 below provides additional validation of the contribution of isoform-specific PDEs in regulating [cAMP] upon activation of β1-AR (i.e. β2-AR stimulation is inhibited by ICI [85]). Model closely replicates cAMP time course measured under PDE3 inhibitor (Cilo), PDE4 inhibitor (Rol), and non-specific PDE inhibitor (IBMX), under ISO stimulation, as measured by Rochais et al. [85] from ARVMs.

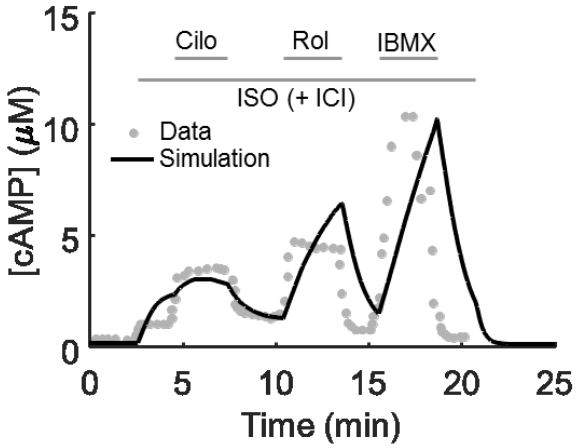

Fig.A.5. cAMP time course under specific PDE inhibitors (Approximated by Model).

Experimental data predicted by the model. Simulated cAMP time course measured under PDE3 inhibitor (Cilo, 1 μM), PDE4 inhibitor (Rol, 10 μM), and non-specific PDE inhibitor (IBMX, 100 μM), under 5 μM ISO stimulation (black line) is compared to that measured by Rochais et al. [85] in ARVMs (grey dots). A concomitant β2-AR antagonist (ICI, 1 μM) was applied in the experiment by Rochais et al. [85], but not simulated by the model.

Potential causes of the slight discrepancy between data and simulation may be the following:

1) We assumed instantaneous application and termination of drug application (i.e. a square wave of drug concentration against time), which may not fully represent the influx and efflux of drugs in this complex experimental setup.

2) We employed a very simplistic model of PDE inhibition by specific PDE inhibitors (Section 4C), with the assumption that the inhibitors will instantaneously ablate target activity.

3) The data include inhibition of β2-AR from concomitant application of ICI with ISO, which is not included in the model. However, it may serve as a good estimate of whole-cell cAMP dynamics.

4) We assumed a very simplistic approach to estimate [cAMP] from CNGC signals, using the calibration curve of the probe (C460W/E583M) against cAMP from Rich et al. [246] as referenced in Rochais et al. [85].

A.3. Results (additional figures)

A.3.1. Stimulus concentrations in simulations

Isoproterenol (ISO) is a commonly applied β-adrenergic receptor agonistic in experiments investigating the β-adrenergic pathway [98, 169, 192, 243, 247], designed to mimic the action of epinephrine (EP) and norepinephrine (NE) signaling in the heart. As shown in Fig.A.6A, typical [ISO] applied in experiments are between 1 nM – 1 μM, and

in some instances up to 10 μM [98, 169, 192, 243, 247]. This range of [ISO] achieves similar ranges of AC activation as epinephrine (EP) and norepinephrine (NE) [248].

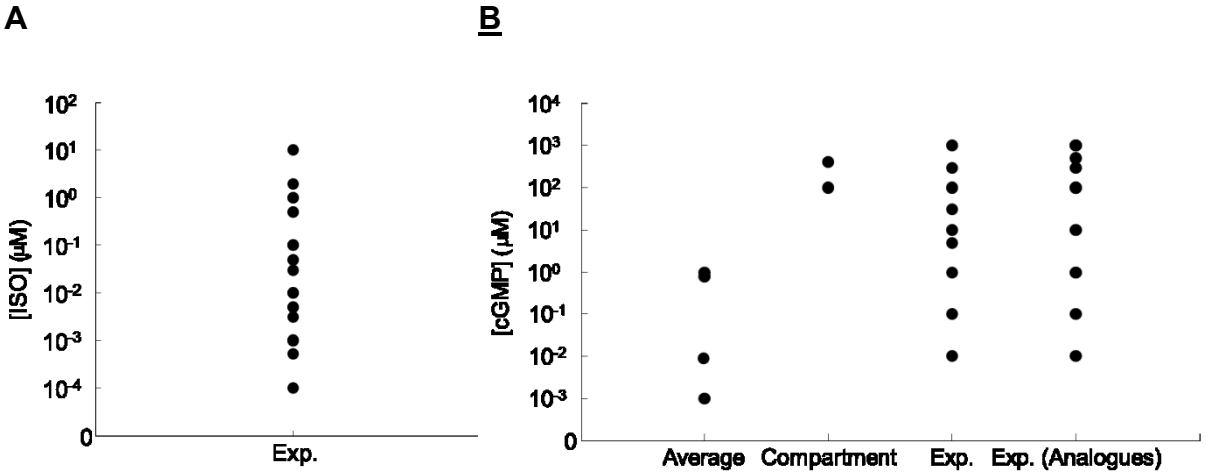

Fig.A.6. Experimentally measured concentrations of ISO and cGMP in experiments in cardiac myocytes.

(A) [ISO] applied in extra-cellular solution in experiments (Exp.) investigating the β-adrenergic pathway in cardiac myocytes. Data are aggregated from five studies [98, 169, 192, 243, 247]. ***(B)*** First two columns respectively show [cGMP] measured in cardiac myocytes and hypothesized to exist in specialized compartments. Last two columns of data respectively show [cGMP] and [cGMP analogues] (8-Br-cGMP and 8-pt-cGMP) applied in intra-pipette solutions in experiments using cardiac myocytes. Data are pooled from thirteen studies [8, 16, 66, 82, 95, 100, 128, 143, 158-161, 163, 186, 204, 249, 250].

Experimental measurements of [cGMP] from the literature are shown in Fig.A.6B. In the rat cardiac myocyte, [cGMP] is estimated to average from 0.001 (1 nM) to 1 μM in quiescent cell and upon increasing levels of NO perfusion [82, 128, 143] (first column). Second column shows [cGMP] is hypothesized compartments [8, 16, 66, 95, 249]. The

third column shows sample data of [cGMP] through intra-pipette delivery to cardiac myocytes in experiments investigating the effect of cGMP on β-adrenergic regulation of ionic currents, which ranges from 0.1 mM to 1 mM [197, 200, 251]. Similarly, [cGMP analogues] used are of up to 1 mM [158-161, 163, 186, 204, 250] (last column). Finally, [cGMP] used in this study agrees with that reported by Zaccolo and Movsesian [17]. Basal (non-stimulated) [cGMP] is set to 10 nM to reflect the recent experimental finding of Götz et al. [100].

From the data gathered in Fig.A.6, we defined the following [ISO] and [cGMP] for use in model simulation and analysis (Table A.3 and Table A.4).

Conditions	[ISO]	Rationale
Control	0	Quiescent cell. Basal conditions
Low [ISO]	1 nM	Lowest concentration used in data gathered
Medium [ISO]	10 nM	[ISO] at the steep part of the [ISO]-[cAMP] dose response curve
High [ISO]	1 μM	Maximal effective [ISO], at which [ISO]-[cAMP] dose response curve saturates.

Table A.3. Concentrations of ISO selected for simulation.

Conditions	[cGMP]	Rationale
Control	10 nM	Cytosolic. Quiescent cell. Steady state, basal conditions. Reflects new data by Götz et al. [100].
Low [cGMP]	1 μM	Low range of experimentally applied intra-pipette [cGMP]. Cellular average, steady state, stimulated conditions.
Medium [cGMP]	5 μM	Median range of experimentally applied intra-pipette [cGMP]. Cellular average, peak transient [cGMP] in some cells. Concentration in compartments.
High [cGMP]	50 μM	High range of experimentally applied intra-pipette [cGMP]. Concentration in compartments.

Table A.4. Concentrations of cGMP selected for model simulation.

A.3.2. Supporting figures

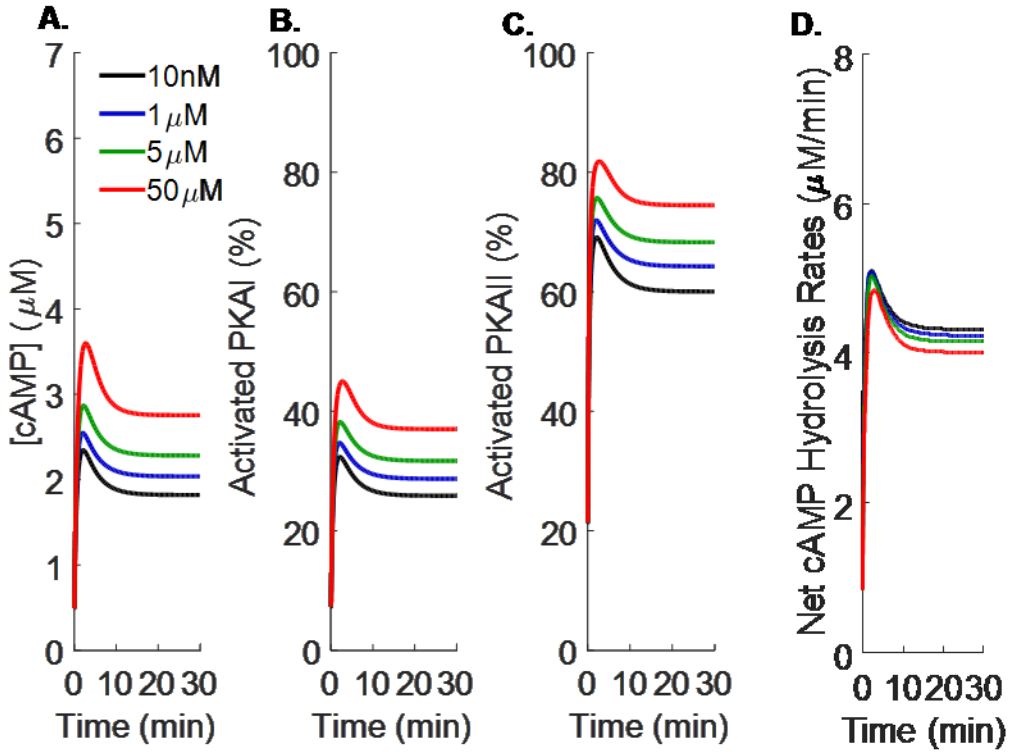

Fig.A.7. Regulation of cAMP transients by varying concentrations of cGMP.

(A) **–** ***(D)*** Sample measurements of the signaling pathway under median [ISO] stimulation (10 nM) together with varying [cGMP]: 10 nM (control), 1 μM, 5 μM, and 50 μM cGMP are indicated by black, blue, green, and red lines respectively. Upon increased [cGMP], [cAMP] transient in ***(A)*** potentiated, leading to increased activation of PKA-I in ***(B)*** and PKA-II in ***(C)***. The potentiation of β-adrenergic responses (A – C) results from a net reduction of cAMP hydrolysis rates across all PDEs in ***(D)***. cGMP-induced potentiation of β-adrenergic responses was observed under other [ISO] as well (not shown).

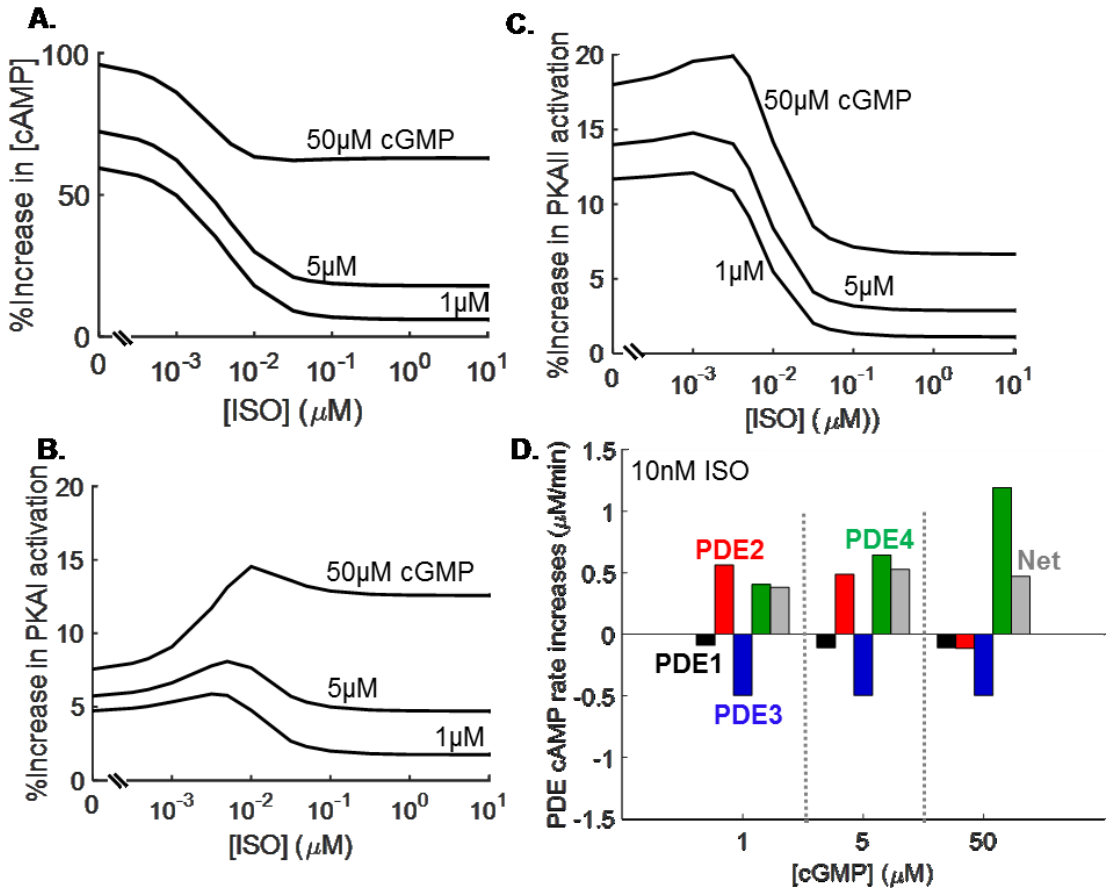

Fig.A.8. cGMP potentiation of β-adrenergic response.

Maximal signal reached across time are shown for β-adrenergic responses under application of various [cGMP] and [ISO]. ***(A) - (C)*** Percent increase of maximal cellular-average [cAMP], PKA-I, and PKA-II activation are shown respectively under various [cGMP] and [ISO]. Percent increases in data are shown relative to that measured at basal [cGMP] (10 nM). ***(D)*** Increases in individual PDE hydrolysis rates (μM/min) with 10 nM ISO and indicated [cGMP] from their respective rates at basal cGMP (10 nM). The shadings for PDEs 1 – 4 are respectively black, red, blue, and green. The net change in PDE hydrolysis rate is shaded grey.

For PDE2 inhibition (Fig.A.9), the percent PDE rate increases on the leftmost of Fig.A.9 (i.e. at 10 nM cGMP) correspond approximately to the PDE rates at the end time point of concomitant ISO and PDE2 inhibition in Fig. 2.4C.

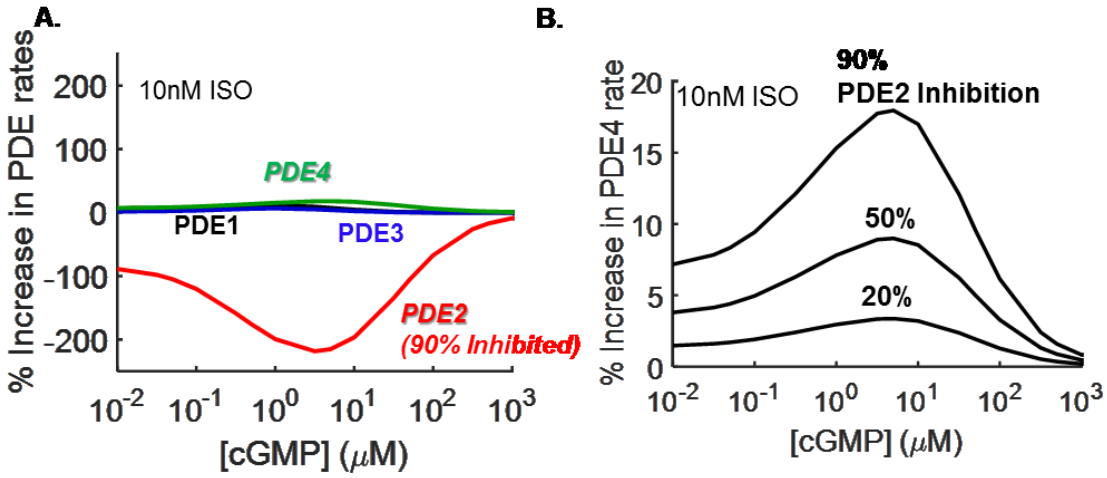

Fig.A.9. cAMP response under PDE2 inhibition.

Percent increases in PDE rates upon PDE2 inhibition relative to their respective rates prior to inhibition under 10 nM ISO and basal [cGMP] (10 nM). Varying degrees of PDE2 inhibition is simulated with simultaneous ISO stimulation under the indicated [cGMP] for 30 minutes. ***(A)*** Percent increases in hydrolysis rates of PDEs 1–4 upon 90% PDE2 inhibition are shown by black, red, blue, and green lines respectively. ***(B)*** Percent increases in PDE4 rate upon 20%, 50%, and 90% PDE2 inhibition.

We also simulated effects of PDE3 and PDE1 inhibition (Fig.A.10A–D and E respectively) on activities of other PDEs. Inhibition of PDE3 produces a small change in both whole-cell [cAMP] (Fig.A.10A) and PKA activation (Fig.A.10B) before or after ISO application. As shown in Fig.A.10C, PDE3 inhibition is primarily compensated for

by an increase in PDE4 activity (green line), and a smaller magnitude of increase in PDE2 activity (red line). At basal conditions of 10 nM ISO and 10 nM cGMP, inhibition of PDE3 produces a reduction in its hydrolytic activity of ~ 1.3 μM/min (Fig.A.10C, blue line). Under these same conditions, PDE4 and PDE2 activities increase by ~ 0.75 and ~ 0.1 μM/min, respectively (Fig.A.10C, green and red lines respectively). As shown in Fig.A.10D, increases in PDE2 (red) and PDE1 (black) are large when compared to their small rate prior to PDE3 inhibition. PDE4 (green) and PDE2 (red) primarily compensated for PDE3 inhibition.

As shown in Fig.A.10E, our model predicts that under these basal conditions, inhibition of PDE1 by 90% results in a small increase of PDE4 activity that partially compensates for reduced PDE1 activity. This is of second order importance because the hydrolytic activity of PDE1 in our model is very low. Compared to the compensatory changes in PDE rates upon inhibition of PDE4 (Figs. 4D–F and 5), inhibition of PDE1 did not produce a significant change in the activity of the other PDEs (Fig.A.10E). This model result is consistent with the experimental result by Bode et al. that the cytosolic expression of PDE1 in rat ventricular myocyte is very low [119].

These results (Fig.A.10) complement our major finding that PDE2 and PDE4 exhibit the strongest coupling among the PDEs, and demonstrate that PDE4 also partially compensates for reductions of PDE3. PDEs 2 and 4 therefore play a key role in compensating for reductions in the activity of other PDEs.

Fig.A.10. cAMP response under PDE3 and PDE1 inhibition.

Responses of the β-adrenergic pathway to 10 nM ISO and subsequent inhibition of PDE3 ***(A – C)***. All simulations are performed with basal [cGMP] of 10 nM [100]. Shown are

whole-cell [cAMP] in ***(A)***, activation of PKA-I (black) and PKA-II (grey) in ***(B)***, and hydrolysis rates of PDEs 1–4 (black, red, blue, and green lines respectively) in ***(C)***. ***(D)*** and ***(E)*** respectively, percent increases in PDE rates upon PDE3 and PDE1 inhibition relative to their respective rates prior to inhibition under 10 nM ISO and basal [cGMP] (10 nM). Percent rate changes in PDEs 1, 2, 3, and 4 are shown in black, red, blue, and green respectively. The indicated PDE inhibition is simulated with simultaneous ISO stimulation under the indicated [cGMP] for 30 minutes.

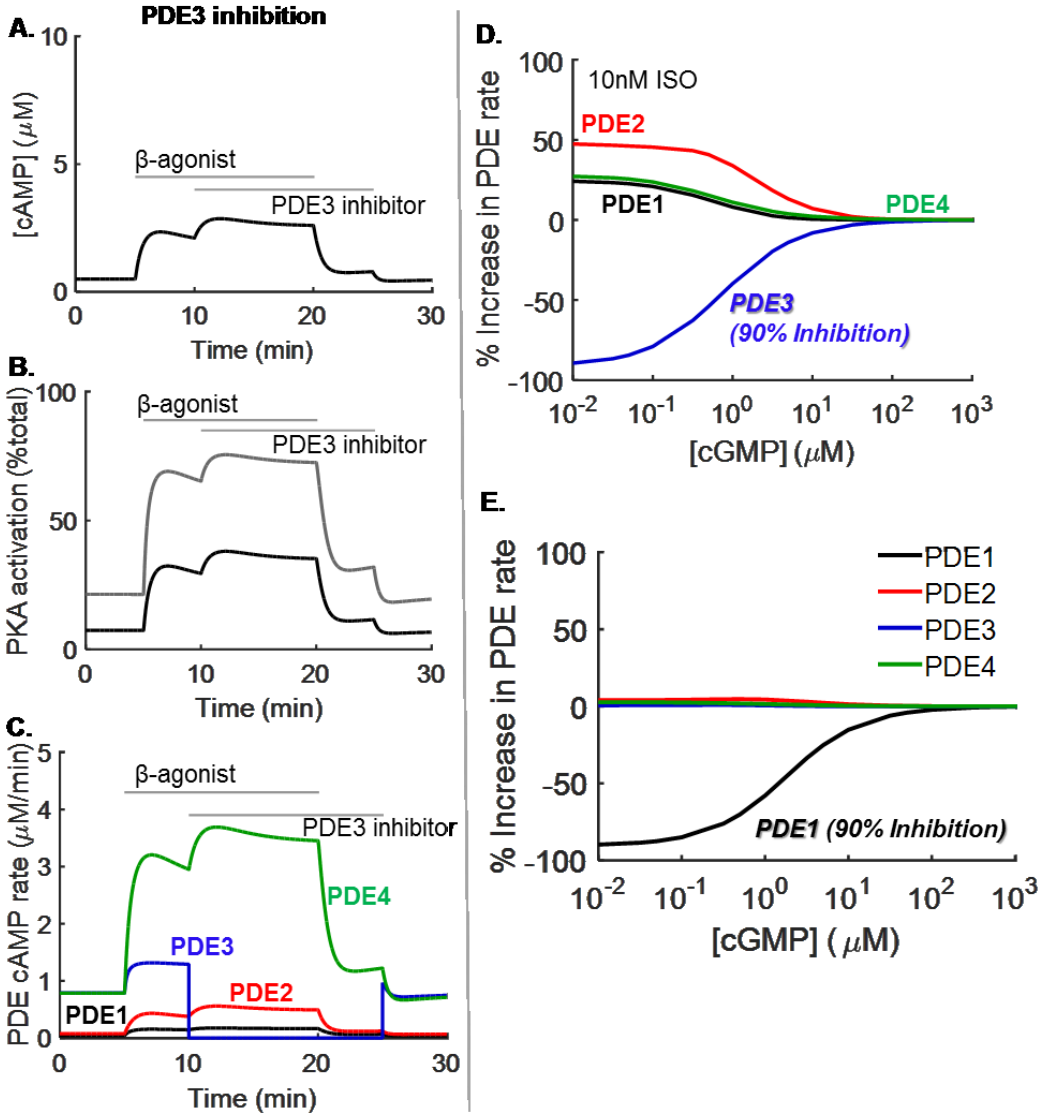

To better quantify the extent of PDE4 compensation of PDE2 activity, we compared [cAMP] under PDE2 inhibition alone (black line) with that of concomitant PDE2 and PDE4 inhibition (grey line) under varying [cGMP] (Fig.A.11A). It can be seen that without compensation by PDE4 (grey line), PDE2 inhibition produced cAMP many folds higher than that under PDE2 inhibition alone (black line). The effect of PDE4 compensation on [cAMP] (grey shaded area) is sizable for PDE2 inhibition.

Similarly, as shown in Fig.A.11B, PDE2 also compensates for a large extent of cAMP increase due to PDE4 inhibition (grey shaded area). It can be seen that without compensation by PDE2 (grey line), PDE4 inhibition produced cAMP many folds higher than that with PDE2 compensation (black line). As a result, PDE2 and PDE4 shows strong coupling, because each has the greatest change in activity and compensated significantly to the inhibition of the other.

Fig.A.11. Coupling between PDE2 and PDE4.

Under varying [cGMP], [cAMP] are reported under 10 nM ISO with the indicated PDEs 90% inhibited. ***(A)*** Compared to inhibition of both PDE2 and PDE4 (grey line), [cAMP] is lower when PDE4 is allowed to compensate for the inhibition of PDE2 (black line). The grey shaded area indicates effect of PDE4 compensation. ***(B)*** Similar to A, Panel B shows the effect on [cAMP] by PDE2 compensation of PDE4 inhibition (grey line), PDE4 inhibition (black line), and extent of PDE2 compensation (grey shaded area).

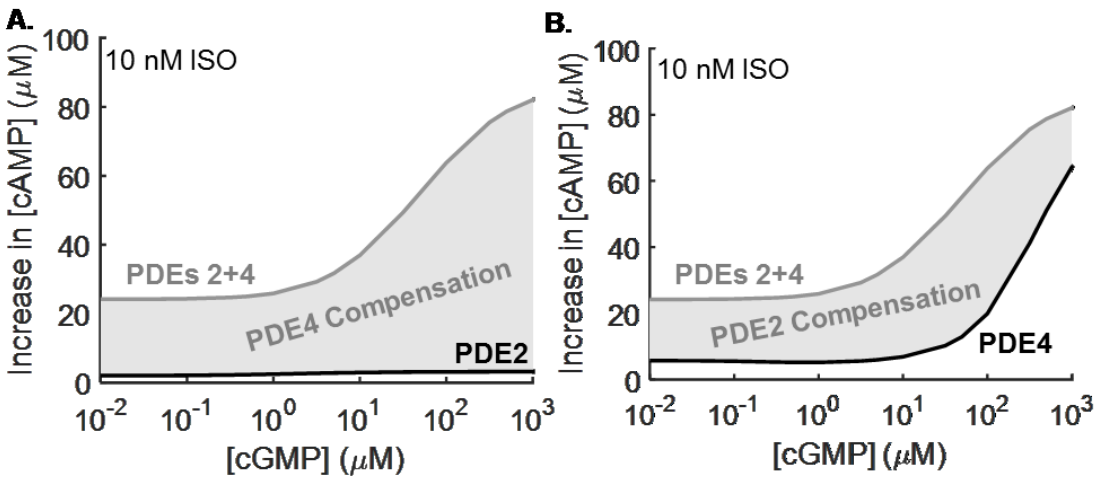

A.4. List of equations

For notation, concentrations of signaling species are enclosed by square brackets, "[ ]". Fractions normalized to total concentrations are not enclosed or are enclosed by round brackets, "( )". Rates of cN production and degradation are prefixed by lower-case of letter "v". Subscript A denotes cAMP hydrolysis related terms. The definitions of state variables, together with their initial conditions, are tabulated in Section 4F. Notations are preserved as much as possible for equations adapted from previous models [71, 129].

A.4.1. Equations for β-adrenergic pathway

Equation 18, which governs cAMP is extended to include degradation by distinctly regulated PDEs 1 – 4. All other equations remain the same as in the original model [71].

Equations for β-AR receptor

$$[L_{tot}] - [LR] - [LRG] - [L] = 0 \quad (1)$$

$$[\beta_1 AR_{act}] - [LR] - [LRG] - [RG] - [\beta_1 AR] = 0 \quad (2)$$

$$[G_{stot}] - [RG] - [LRG] - \left[G_{s\beta\gamma}\right] - [G_s] = 0 \quad (3)$$

$$\frac{d([\beta_1 AR_{act}])}{dt} = \left\{k_{\beta ARK-}[\beta_1 AR_{S464}] - k_{\beta ARK+}([LR] + [LRG])\right\} \ldots$$

$$+ \{k_{PKA-}[\beta_1 AR_{S301}] - k_{PKA+}([PKACI][\beta_1 AR_{act}])\} \quad (4)$$

$$\frac{d([\beta_1 AR_{S464}])}{dt} = k_{\beta ARK+}([LR] + [LRG]) - k_{\beta ARK-}[\beta_1 AR_{S464}] \quad (5)$$

$$\frac{d([\beta_1 AR_{S301}])}{dt} = k_{PKA+}[PKAC_I][\beta_1 AR_{act}] - k_{PKA-}[\beta_1 AR_{S301}] \quad (6)$$

Where:

$[LR] = [L][\beta_1 AR]/K_L$; $[LRG] = [L][\beta_1 AR][G_s]/(K_L K_R)$; $[RG] = [\beta_1 AR][G_s]/K_c$

Equations for Gs activation

$$\frac{d([G_{s\alpha GTPtot}])}{dt} = k_{gact}([RG] + [LRG]) - k_{hyd}[G_{s\alpha GTPtot}] \quad (7)$$

$$\frac{d([G_{s\beta\gamma}])}{dt} = k_{gact}([RG] + [LRG]) - k_{reassoc}[G_{s\alpha GDP}]\left[G_{s\beta\gamma}\right] \quad (8)$$

$$\frac{d([G_{s\alpha GDP}])}{dt} = k_{hyd}[G_{s\alpha GTPtot}] - k_{reassoc}[G_{s\alpha GDP}]\left[G_{s\beta\gamma}\right] \quad (9)$$

Equations for cAMP production

For the following equations, terms governing pharmacological drug Forskolin (Fsk) are removed from the original model [71] because it is not studied in the present model.

$$[G_{s\alpha GTPtot}] - [G_{s\alpha GTP}] - [G_{s\alpha GTP}{:}\,AC] = 0 \quad (10)$$

$$[AC_{tot}] - [G_{s\alpha GTP}{:}\,AC] - [AC] = 0 \quad (11)$$

$$vp_A = \frac{k_{AC_{basal}}[AC][ATP]}{k_{m_{AC_{basal}}} + [ATP]} + \frac{k_{AC_{Gs\alpha}}[AC{:}G_{s\alpha}GTP][ATP]}{k_{m_{GsaGTP}} + [ATP]}$$

Where $[G_{s\alpha GTP}{:}\,AC] = [G_{s\alpha GTP}][AC]/K_{Gs\alpha}$

A.4.2. Equations for phosphodiesterase isoenzymes

The lumped cAMP degradation component in Saucerman et al. [71] is extended to be regulated by PDEs 1 – 4.

Equations for PDE1

Rate of PDE1 degradation of cAMP, with competitive inhibition by cGMP (12)

$$vPDE1_A = \frac{Vmax_{PDE1_A}[cAMP]}{K_{s_1}\left(1 + \frac{[cGMP]}{K_{I_1}}\right) + [cAMP]}$$

Equations for PDE2

Rate of PDE2 cAMP degradation as regulated by cGMP (13)

$$vPDE2_A = \frac{Vmax_{PDE2_A}[cAMP][1 + \frac{[cAMP]}{\rho k_a} + \frac{[cGMP]}{\omega k_b}]}{K_{s_2}\left[1 + \frac{[cAMP]}{K_{a_2}} + \frac{[cAMP][cGMP]}{\varepsilon K_{I_2} K_{a_2}} + \frac{[cGMP]}{K_{I_2}} + \frac{[cGMP]}{K_{b_2}} + \frac{[cGMP]^2}{\eta K_{I_2} K_{b_2}}\right] + \cdots}$$
$$[cAMP][1 + \frac{[cAMP]}{K_{a_2}} + \frac{[cGMP]}{\omega K_{b_2}}]$$

Rate of PDE2 degradation of cGMP as regulated by cAMP (used as model constraint only) (14)

$$vPDE2_G = \frac{Vmax_{PDE2_G}[cGMP][1 + \frac{[cGMP]}{\eta k_{b_2}} + \frac{[cAMP]}{\varepsilon k_{a_2}}]}{k_{I_2}\left[1 + \frac{[cGMP]}{k_{b_2}} + \frac{[cAMP][cGMP]}{k_{s_2} k_{b_2}} + \frac{[cAMP]}{k_{s_2}} + \frac{[cAMP]}{k_{a_2}} + \frac{[cAMP]^2}{\rho k_{s_2} k_{a_2}}\right] + \cdots}$$
$$[cGMP][1 + \frac{[cGMP]}{k_{b_2}} + \frac{[cAMP]}{\varepsilon k_{a_2}}]$$

Equations for PDE3

Rate of PDE3 degradation of cAMP, with competitive inhibition by cGMP (15)

$$vPDE3_A = \frac{Vmax_{PDE3_A}[cAMP]}{K_{s_3}\left(1 + \frac{[cGMP]}{K_{i_3}}\right) + [cAMP]}$$

Equations for PDE4

Fraction of PDE4 phosphorylated by PKA

$$PDE4 = 1 - pPDE4$$

$$\frac{d(pPDE4)}{dt} = k_{p4_{PKA}} \cdot [PKAC_{II}] \cdot PDE4 - k_{4pp} \cdot pPDE4 \quad (16)$$

Rate of cAMP hydrolysis by non-phosphorylated and phosphorylated PDE4 (17)

$$vPDE4_A = \frac{Vmax_{PDE4_A} \cdot PDE4 \cdot [cAMP]}{K_{m_4} + [cAMP]} + \frac{Vmax_{pPDE4_A} \cdot pPDE4 \cdot [cAMP]}{K_{m_{p4}} + [cAMP]}$$

A.4.3. Equations for cN signal dynamics

The asterisks (*) following the originally defined PDE hydrolytic rates denote the rate after inhibition by a pharmacological inhibitor if applied.

Balance equations for cN signals

$$\frac{d[cAMP_{tot}]}{dt} = vp_A - vPDE1_A^* - vPDE2_A^* - vPDE3_A^* - vPDE4_A^* \quad (18)$$

Equations for pharmacological inhibition of PDE activities

$$vPDE1_A^* = vPDE1_A/(1 + \frac{[IBMX]}{Ki_{IBMX\_PDE1}})$$

$$vPDE2_A^* = vPDE2_A/(1 + \frac{[IBMX]}{Ki_{IBMX\_PDE2}} + \frac{[EHNA]}{Ki_{EHNA}}))$$

$$vPDE3_A^* = vPDE3_A/(1 + \frac{[IBMX]}{Ki_{IBMX_{PDE3}}} + \frac{[Cilo]}{Ki_{Cilo}})$$

$$vPDE4_A^* = vPDE4_A/(1 + \frac{[IBMX]}{Ki_{IBMX\_PDE4}} + \frac{[Roli]}{Ki_{Rol}})$$

A.4.4. Equations for kinase activation

Equations for PKA activation

All equations in this section are the same as the original model of Saucerman et al. [71].

PKA-I activation by cAMP and inhibition by PKI are governed by the following equations.

$$2[PKA_{Itot}] - ([RC_I] + [ARC_I] + [A_2RC_I] + [PKAC_I{:}PKI]) - [PKAC_I] = 0 \quad (19)$$

Where

$$[RC_I] = \frac{K_A K_B}{[cAMP]^2}\frac{[PKAC_I]}{K_D}([PKAC_I] + [PKAC_I{:}PKI])$$

$$[ARC_I] = \frac{K_A}{[cAMP]^2}\frac{[PKAC_I]}{K_D}([PKAC_I] + [PKAC_I{:}PKI])$$

$$[A_2RC_I] = \frac{[PKAC_I]}{K_D}([PKAC_I] + [PKAC_I{:}PKI])$$

$$[A_2R_I] = [PKAC_I] + [PKAC_I{:}PKI]$$

$$[PKAC_I{:}PKI] = \frac{[PKAC_I][PKI_{tot}]}{K_{PKI} + [PKAC_I] + [PKAC_{II}]}$$

PKA-II activation by cAMP and inhibition by PKI are governed by the following equations.

$$2[PKA_{II}tot] - ([RC_{II}] + [ARC_{II}] + [A_2RC_{II}] + [PKAC_{II}{:}PKI]) - [PKAC_{II}] = 0 \quad (20)$$

Where

$$[RC_{II}] = \frac{K_A K_B}{[cAMP]^2} \frac{[PKAC_{II}]}{K_D} ([PKAC_{II}] + [PKAC_{II}{:}\,PKI])$$

$$[ARC_{II}] = \frac{K_A}{[cAMP]^2} \frac{[PKAC_{II}]}{K_D} ([PKAC_{II}] + [PKAC_{II}{:}\,PKI])$$

$$[A_2RC_{II}] = \frac{[PKAC_{II}]}{K_D} ([PKAC_{II}] + [PKAC_{II}{:}\,PKI])$$

$$[A_2R_{II}] = [PKAC_{II}] + [PKAC_{II}{:}\,PKI]$$

$$[PKAC_{II}{:}\,PKI] = \frac{[PKAC_{II}][PKI_{tot}]}{K_{PKI} + [PKAC_I] + [PKAC_{II}]}$$

Finally, concentration of pharmacological inhibitor PKI is regulated by the following

$$[PKI] = \frac{K_{PKI}[PKI_{tot}]}{K_{PKI} + [PKAC_I] + [PKAC_{II}]}$$

A.4.5. Equations for cAMP conservation of mass

Equations for cAMP bound to PDEs

cAMP bound to PDEs are governed by the following equations.

$$[APDE2] = [PDE2] \frac{[cAMP]}{k_{a_2}}$$

$$[APDE2A] = [PDE2] \frac{[cAMP]^2}{\rho k_{s_2} k_{a_2}}$$

$$[PDE2A] = [PDE2] \frac{[cAMP]}{k_{s_2}}$$

$$[GPDE2A] = [PDE2] \frac{[cAMP][cGMP]}{\omega k_{s_2} k_{b_2}}$$

$$[APDE2G] = [PDE2] \frac{[cAMP][cGMP]}{\varepsilon k_{i_2} k_{a_2}}$$

Where

$$[PDE2] = \frac{2[PDE2]_{tot}}{D_{PDE2}} / (1 + \frac{[IBMX]}{Ki_{IBMX\_PDE2}} + \frac{[EHNA]}{Ki_{EHNA}})$$

and

$$D_{PDE2} = 1 + \frac{[cAMP]}{k_{a_2}} + \frac{[cAMP][cGMP]}{\varepsilon k_{i_2} k_{a_2}} + \frac{[cGMP]}{k_{i_2}} + \frac{[cGMP]}{k_{b_2}} + \frac{[cGMP]^2}{\eta k_{i_2} k_{b_2}} \ldots + \frac{[cAMP]^2}{\rho k_{s_2} k_{a_2}} + \frac{[cAMP]}{k_{s_2}} + \frac{[cAMP][cGMP]}{\omega k_{s_2} k_{b_2}}$$

Conservation of mass for cAMP

Free [cAMP] is updated from the original model [71] to include the effect of cAMP bound to PDEs.

$$[cAMP] = [cAMP]_{tot} - ([RCcAMP_I] + 2 \cdot [RCcAMPcAMP_I] + 2 \cdot [RcAMPcAMP_I]) \ldots (21)$$
$$-([RCcAMP_{II}] + 2 \cdot [RCcAMPcAMP_{II}] + 2 \cdot [RcAMPcAMP_{II}]) \ldots$$
$$-([APDE2] + 2 \cdot [APDE2A] + [PDE2A] + [GPDE2A] + [APDE2G])$$

A.5. Model parameters

A.5.1. Parameters in β-adrenergic pathway model

Parameters for β-AR receptor

	Parameter	Representation	Value	Unit	Ref.
1	$[\beta_1 AR_{tot}]$	Total concentration of $\beta_1 AR$	0.0132	μM	[71]
2	$[G_{stot}]$	Total concentration of stimulatory G protein	3.83	μM	[71]
3	K_L	Dissociation constant between	0.285	μM	[71]

		β_1AR receptor and its ligand			
4	K_R	Dissociation constant between ligand-bound β_1 AR receptor and G-protein	0.062	μM	[71]
5	K_C	Dissociation constant between unbound β_1 AR receptor and G-protein	33	μM	[71]
6	$k_{\beta ARK+}$	β_1 AR desensitization by β-arrestin	1.1×10^{-6}	ms^{-1}	[71]
7	$k_{\beta ARK-}$	β_1AR re-sensitization	$2k_{\beta ARK+}$	ms^{-1}	[71]
8	k_{PKA+}	β_1AR desensitization by PKA	3.6×10^{-6}	$\mu M^{-1}ms^{-1}$	[71]
9	k_{PKA-}	β_1AR re-sensitization	$0.62k_{PKA+}$	ms^{-1}	[71]

Table A.5. Parameters for β-adrenergic receptor regulation.

Parameters for GS activation

	Parameter	Representation	Value	Unit	Ref.
1	k_{gact}	$G_{s\alpha}$activation	0.016	ms^{-1}	[71]
2	k_{hyd}	$G_{s\alpha}$hydrolysis	8×10^4	ms^{-1}	[71]
3	$k_{reassoc}$	$G_{s\alpha}$reassociation	1.2	$\mu M^{-1}ms^{-1}$	[71]

Table A.6. Parameters for G-protein activation.

Parameters for cAMP production

	Parameter	Representation	Value	Unit	Ref.

1	$[AC_{tot}]$	Total concentration of adenylyl cyclase	0.0497	μM	[71]
2	$[ATP]$	Total concentration of ATP	5×10^3	μM	[71]
3	$K_{Gs\alpha}$	AC activation by $G_{s\alpha}$	315	μM	[71]
4	k_{AC_basal}	Basal AC activity	2×10^{-4}	ms^{-1}	[71]
5	k_{m_basal}	Basal AC affinity for ATP	1.03×10^3	μM	[71]
6	$k_{AC\_Gs\alpha}$	AC activity with $G_{s\alpha}$ activation	8.5×10^2	ms^{-1}	[71]
7	$k_{m\_Gs\alpha GTP}$	$AC: G_{s\alpha}$ affinity for ATP	315	μM	[71]

Table A.7. Parameters for AC catalyzed production of cAMP.

Parameters for PKA activation

	Parameter	Representation	Value	Unit	Ref.
1	$[PKA_{Itot}]$	Total concentration of PKA-I	0.59	μM	[71]
2	$[PKA_{IItot}]$	Total concentration of PKA-II	0.025	μM	[71]
3	K_A	Dissociation constant between one cAMP-bound PKA (ARC) and second cAMP (A)	9.14	μM	[71]
4	K_B	Dissociation constant between unbound PKA (RC) and cAMP (A)	1.64	μM	[71]
5	k_D	Dissociation constant between two cAMP bound regulatory subunit (A2R) and catalytic	4.375	μM	[71]

		subunit (C) of PKA			

Table A.8. Parameters for cAMP activation of PKA.

A.5.2. Parameters for phosphodiesterase models

Parameters for PDE1

	Parameter	Representation	Value	Unit	Ref.
1	K_{i_1}	PDE1 affinity to cAMP	0.983	μM	[252]
2	K_{s_1}	PDE1 affinity to cGMP	0.764	μM	[252]
3	$Vmax_{PDE1_A}$	Maximal homotropic cAMP hydrolytic rate	5.0×10^{-6}	$\mu M/ms$	FIT

Table A.9. Parameters for PDE1 model.

Parameters for PDE2

	Parameter	Representation	Value	Unit	Ref.
1	K_{a_2}	Dissociation constants for cAMP binding to GAF-B regulatory domain	0.2286	μM	[240, 241]
2	K_{b_2}	Dissociation constants for cGMP binding to GAF-B regulatory domain	0.0654	μM	[240, 241]
3	K_{s_2}	Dissociation constants for cAMP binding to catalytic domain	32.451	μM	[31]
4	K_{I_2}	Dissociation constants for cGMP	22.2176	μM	[31]

		binding to catalytic domain			
5	ρ	Scaling factor for $k_{s_{PDE2}}$ upon cAMP biding to GAF-B regulatory domain for cAMP-regulated cAMP hydrolysis	0.9791	--	[30]
6	ω	Scaling factor for $k_{s_{PDE2}}$ upon cGMP biding to GAF-B regulatory domain	0.8638	--	[253]
7	ε	Scaling factor for $k_{I_{PDE2}}$ upon cAMP biding to GAF-B regulatory domain cAMP-regulated cGMP hydrolysis	0.668	--	FIT
8	η	cGMP-activated, cGMP hydrolysis Scaling factor for $k_{I_{PDE2}}$ upon cGMP biding to GAF-B regulatory domain cGMP-regulated cGMP hydrolysis	0.375	--	[241]
9	$Vmax_{PDE2_A}$	Maximum homotropic rate cGMP hydrolysis	2.20×10^{-4}	$\mu M /ms$	FIT
10	$[PDE2]_{tot}$	Total concentration of PDE2	5×10^{-3}	μM	[72]

Table A.10. Parameters for PDE2 model.

Parameters for PDE3

	Parameter	Meaning	Value	Unit	Ref.
1	K_{s_3}	cAMP affinity to catalytic domain	0.133	μM	[254]
2	K_{i_3}	cGMP affinity to catalytic domain	0.101	μM	[254]
3	$Vmax_{PDE3_A}$	Maximum rate of cAMP hydrolysis	2.5×10^{-5}	$\mu M /ms$	FIT

Table A.11. Parameters for PDE3 model.

Parameters for PDE4

	Parameter	Representation	Value	Units	Ref.
1	$k_{4_{PKA}}$	Rate of PDE4 phosphorylation	7.5×10^{-3}	$\mu M^{-1} ms^{-1}$	[74]
2	$k_{4_{pp}}$	Rate of PDE4 dephosphorylation	1.5×10^{-3}	ms^{-1}	[74]
3	K_{m_4}	cAMP affinity to catalytic domain of the non-phosphorylated PDE4	1.122	μM	[130, 245]
4	$K_{m_{p4}}$	cAMP affinity to catalytic domain of the non-phosphorylated PDE4	K_{m_4}	μM	[130, 245]
5	$Vmax_{PDE4_A}$	Maximum rate of cAMP hydrolysis by the non-	1.0×10^{-4}	$\mu M/ms$	FIT

		phosphorylated PDE4			
6	$Vmax_{pPDE4_A}$	Maximum rate of cAMP hydrolysis by the phosphorylated PDE4	$1.4 \cdot Vmax_{PDE4}$	$\mu M/ms$	[130, 245]

Table A.12. Parameters for PDE4 model.

Parameters for pharmacological reagents

	Parameter	Representation	Value	Unit	Ref.
1	Ki_{IBMX_PDE1}	IC50 of IBMX inhibition of PDE1 activity	11	μM	[255]
2	Ki_{IBMX_PDE2}	IC50 of IBMX inhibition of PDE2 activity	27.9	μM	[255]
3	Ki_{IBMX_PDE3}	IC50 of IBMX inhibition of PDE3 activity	6	μM	[255]
4	Ki_{IBMX_PDE4}	IC50 of IBMX inhibition of PDE4 activity	30	μM	[130]
5	Ki_{EHNA}	IC50 of EHNA inhibition of PDE2 activity	0.8	μM	[10]
6	Ki_{Cilo}	IC50 of Cilo inhibition of PDE3 activity	5×10^{-3}	μM	[10]
7	Ki_{Rol}	IC50 of Rolipram inhibition of PDE activity	0.2	μM	[256]

Table A.13. Inhibitory constants of pharmacological inhibitors.

	Parameter	Representation	Value	Unit	Ref.
1	$[L_{tot}]$	Total concentration of ligand to β-adrenergic receptor (e.g. isoproterenol (ISO))	0..100	μM	[71]
2	$[IBMX]$	Concentration of PDE inhibitor, IBMX	100	μM	[71, 82]
3	$[PKI_{tot}]$	Concentration of kinase inhibitor, PKI	0.18	μM	[71]

Table A.14. Typical concentrations for pharmacological inhibitors.

Constants for unit conversions

	Parameter	Original Unit	Converted Unit	Multiplication Factor	Ref.
1	cf_{pmolMg_uM}	$pmol/mg\ protein$	μM	0.18	[6]
2	$cf_{pmolGWetWt\_uM}$	$pmol$ $/g\ wet\ weight$	μM	2.43×10^3	[6]
3	$cf_{pmolCell\_pmolM}$	$pmol$ $/100{,}000\ cells$	$pmol$ $/mg\ protein$	0.361	[71]

Table A.15. Constants for unit conversions.

A.6. Initial conditions

Initial conditions for state variables reflect basal conditions, where no pharmacological drugs are applied externally or internally to the cell. The values are obtained from model steady state behavior in simulations starting with a preliminary set of initial conditions.

For the preliminary initial conditions, experimental values are assigned whenever possible, such as [cAMP] and [cGMP]. When experimental measures are not readily available, all components are assumed to be in their non-activated states, and all PDE activities are assumed to be zero. When the model is run from the preliminary initial conditions to obtain steady-state values, the states with experimentally consistent initial values remained in the experimentally recorded range at steady-state.

	State Variables	Representation	Initial Value	Unit	Ref.
1	$[L]$	Ligand to β-adrenergic receptor (e.g. ISO)	0	μM	--
2	$[\beta AR]$	β-adrenergic receptor	0.0101	μM	[71]
3	$[Gs]$	Stimulatory G-protein	3.8288	μM	[71]
4	$[\beta_1 AR_{act}]$	Activated β-receptor	0.0112	μM	[71]
5	$[\beta_1 AR_{S464}]$	Desensitized β-AR by β receptor kinase	0	μM	[71]
6	$[\beta_1 AR_{S301}]$	Desensitized β-AR by PKA-I	0.0020	μM	[71]
7	$[G_{saGTPtot}]$	Total concentration of stimulatory G-protein with GTP bound to its α-subunit	0.0234	μM	[71]
8	$[G_{saGDP}]$	stimulatory G-protein with GDP bound to its α-subunit	0.0006	μM	[71]
9	$[G_{sb\gamma}]$	β and ϒ subunits of the stimulatory G-protein	0.0241	μM	[71]
10	$[G_{saGTP}]$	Free stimulatory G-protein with GTP bound to its α-subunit	0.0209	μM	[71]
11	$[AC]$	Adenylyl Cyclase	0.0472	μM	[71]
12	$vPDE1_A^*$	Rate of cAMP hydrolysis by PDE1	0.0	$\mu M/ms$	--
13	$vPDE2_A^*$	Rate of cAMP hydrolysis by PDE2	0.0	$\mu M/ms$	--
14	$vPDE3_A^*$	Rate of cAMP hydrolysis by PDE3	0.0	$\mu M/ms$	--

15	$(pPDE4)$	PKA phosphorylated PDE4	0.1193	%	--
16	$vPDE4_A^*$	Rate of cAMP hydrolysis by PDE4	0.0	$\mu M/ms$	--
17	$[cAMP_{tot}]$	total [cAMP]	0.6122	μM	[71]
18	$[cAMP]$	free [cAMP]	0.2033	μM	[71]
19	$[cGMP]$	[cGMP]	0.1	μM	[71]
20	$[PKAC_I]$	Dissociated active fragment of PKA-I	0.1072	μM	[71]
21	$[PKAC_{II}]$	Dissociated active fragment of PKA-II	0.306	μM	[71]

Table A.16. Initial conditions for state variables.

A.7. Species and temperature information

A.7.1. Temperature

The physiological temperature of cardiac ventricular myocyte is commonly reported to be 37 ◦C. The temperatures at which data shown in figures were collected are listed in Table A.17 below. The majority of model data were collected at room temperature (~25◦C). No model equation has explicit temperature dependence.

A.7.2. Species

Whenever possible in parameterization of our model, we prioritized on using experimental data from ventricular myocytes or heart tissue. A good portion of our data is from rat ventricular myocytes, because it seems to be the most prevalent in existing literature. Species information for figures is tabulated in Table A.17.

Our baseline β-adrenergic pathway model from Saucerman et al. is based on rat ventricular myocytes [71]. Species information for PDE parameters are listed below:

1) Table A.9: Data are based on PDE1 from human cardiac myocytes [252].
2) Table A.10: Data are based on PDE2 from cloned mouse [240, 241] and human [253], guinea pig cardiac myocytes [72], and review papers [30, 31].
3) Table A.11: Data are based on PDE3 from human myocardium [254].
4) Table A.12: Data are based on PDE4 from recombinant PDE4 [130], mouse cardiac myocytes [245], and a prior model of the β-adrenergic pathway [74].

	Figure	Species	Assay Temp. (◦C)	Ref.
	Manuscript			
1	Fig. 2.3A PDE1 rate	Mouse PDE1 clones	Pre-warmed	[87]
2	Fig. 2.3B PDE2 rate	Purified from rat ventricular myocytes	--	[88]
3	Fig. 2.3C PDE3 rate	Human heart PDE3 clones	30	[96]
4	Fig. 2.3D [ISO] vs. [cAMP]	Rat cardiac myocytes	25	[97, 98]
5	Fig. 2.3E cAMP dynamics	Rat cardiac myocytes	25	[99, 143]
	Supplement			
7	Fig.A.1A PDE1 constraint	Mouse PDE1 clones	Pre-warmed	[87]
8	Fig.A.1B PDE2 constraint	Purified from Rat heart	--	[142]

9	Fig.A.1C PDE3 constraint	Purified from human ventricular tissue	30	[238]
10	Fig.A.1D PDE4 constraint	Human PDE4 clones	23	[239]
11	Fig.A.3 PKA validation	Purified from rabbit skeletal muscle	23	[244]
10	Fig.A.4 PDE constraint	Rat ventricular myocytes	Room	[85, 86]

Table A.17. Species and temperature information for relevant figures.

A.8. Basis for model formulation

The PDE1 model (Fig. 2.2A) is based on in vitro experiment with purified enzyme demonstrating competitive inhibition of cAMP and cGMP [17, 257]. In addition, substrate competition experiments suggest that there is only one catalytic site for both cNs [87].

As shown in Fig. 2.2B, cAMP and cGMP regulation of PDE2 hydrolysis is modeled using a two-site competitive binding scheme, supported by structural and biochemical studies of PDE2 [81, 240, 258-260]. cAMP and cGMP compete for the same binding sites on both the GAF-B regulatory and catalytic domains [81, 240, 241]. The affinity of cNs to the catalytic domain (horizontal transitions in the state diagram) are modulated by regulatory allosteric interactions (vertical transitions). As supported by experimental studies [81, 240, 258], occupancy of the PDE2 GAF-B regulatory domain by either cN induces a conformational change from a low-activity closed configuration to a high-activity open configuration, better exposing the catalytic site to substrates. The

competitive nature of the binding reaction is highlighted by the symmetry of the model with respect to the vertical and horizontal transitions. Microscopic reversibility is conserved in all four closed loops of the model.

The PDE3 model (Fig. 2.2C) is based on competitive inhibition of cNs, observed both in vivo and in vitro [96, 105, 254]. PDE3A1 has PKA phosphorylation sites. Studies on activation of PDE3 via PKA-mediated phosphorylation have been performed primarily using non-cardiac tissues [254, 261-265]. In bovine cardiac muscle, Harrison et al. failed to detect significant changes in cAMP hydrolysis as a result of PKA-mediated phosphorylation of PDE3, despite the fact that PDE3 phosphorylation by PKA was observed [266]. In adult rat cardiac myocytes, total cellular activity of PDE3 in vivo did not increase upon inhibition of PKA by H89 or PKI [267]. PDE3A1 has recently been shown to participate in the SERCA/PLB/AKAP signalosome, where phosphorylation by PKA promotes its targeting to the signalosome, where it may modulate cAMP levels in a highly localized manner [268]. In light of [267] and [268], we assumed that the functional consequences of PKA-induced phosphorylation of PDE3 relate to its participation in this spatially confined signalosome, which is a level of compartmentalization not described in our model. Therefore, in our work we did not distinguish the roles of PKA-phosphorylated vs. non-phosphorylated PDE3.

The PDE4 model (Fig. 2.2D) is based upon the following two experimental results. First, both the non-phosphorylated and phosphorylated (the red encircled P represents the phosphate group) forms contribute significantly to cAMP hydrolysis in vitro [130] and in cardiac myocytes [267]. Second, affinity for cAMP remains the same whether or not PDE4 is phosphorylated by PKA; however, the maximum rate of

hydrolysis is elevated ~ 1.4 fold by PKA-mediated phosphorylation [130, 134]. Activation of PDE4 via PKA-mediated phosphorylation in cardiac myocytes is more well established in literature [269-271] based on studies of purified proteins [130, 134] and from in vivo data from cardiac myocytes [272-274]. As a result, activation of PDE4 via PKA-mediated phosphorylation is included in current model the model.

Appendix B. Supplementary Material for the cN Signaling Network Model

B.1. Symbol definitions

B.1.1. Definition of symbols for signaling network components

	Symbol	Representation
		Pathway cross-talk
1	cN	Cyclic Nucleotide, either cAMP or cGMP (second messenger)
2	cNs	Cyclic Nucleotides, both cAMP and cGMP (second messengers)
3	5′-AMP	Adenosine 5′-Monophosphate. Hydrolyzed cAMP, after breakage of the 3′- cyclic phosphate bond of cAMP
4	5′-GMP	Guanosine 5′-Monophosphate. Hydrolyzed cGMP, after breakage of the 3′- cyclic phosphate bond of cGMP
5	PDE	Phosphodiesterase, enzyme that catalyzes the breakage of phosphodiester bond
6	PDEs	Phosphodiesterases/ Phosphodiesterase Isoenzymes. Multiple gene families of Phosphodiesterases
7	PDE1	Phosphodiesterase gene family 1
8	PDE2	Phosphodiesterase gene family 2
9	PDE3	Phosphodiesterase gene family 3

10	PDE4	Phosphodiesterase gene family 4
11	PDE5	Phosphodiesterase gene family 5
		β-adrenergic pathway
12	β-AR	β-Adrenergic Receptor
13	βARK	β-Adrenergic Receptor Kinase
14	Gs	Stimulatory G-protein
15	AC	Adenylyl Cyclase
16	ATP	Adenosine Triphosphate
17	ADP	Adenosine Diphosphate
18	cAMP	Cyclic Adenosine-3′,5′ Monophosphate (second messenger)
19	PKA	Protein Kinase A (cAMP-dependent protein kinase)
20	PKA-I	PKA, Type I
21	RI	Regulatory subunit of PKA-I
22	PKACI	Catalytic subunit of PKA-I
23	PKA-II	PKA, Type II
24	RII	Regulatory subunit of PKA-II
25	PKACII	Catalytic subunit of PKA-II
		NO/cGMP/PKG pathway
26	NO	Nitric Oxide
27	NOS	Nitric Oxide Synthase
28	sGC	Soluble Guanylate Cyclase
29	GTP	Guanosine Triphosphate
30	GDP	Guanosine Diphosphate

31	cGMP	Cyclic Guanosine-3′, 5′-Monophosphate (second messenger)
32	PKG-I	Protein Kinase G (cGMP-dependent protein kinase), Type I
		Signaling Network Responses
33	Cross-talk response	Indirect response of one pathway when the other is stimulated. Changes in β-adrenergic responses upon NO stimulation and/or changes in NO/cGMP/PKG pathway responses upon β-adrenergic stimulation.
34	Direct response	Direct response of the pathway upon stimulation. Changes in β-adrenergic responses upon stimulation of the β-adrenergic pathway and/or changes in NO/cGMP/PKG pathway responses upon its own stimulation.

Table B.1. Definition of symbols for signaling network components.

B.1.2. Definition of symbols for pharmacological drugs

	Symbol	Full Name	Effects
7	ISO	Isoproterenol	β-AR agonist
8	NE	Norepinephrine	β-AR agonist. Neurotransmitter
9	SNAP	(±)-S-Nitroso-N-acetylpenicillamine	NO donor
10	IBMX	3-isobutyl-1-methylxanthine	Non-specific PDE inhibitor
11	EHNA	Erythro-9-(2-Hydroxy-3-Nonyl) Adenine	PDE2 inhibitor
12	Cilo	Cilostamide	PDE3 inhibitor

13	Rol	Rolipram	PDE4 inhibitor
14	Sil	Sildenafil	PDE5 inhibitor
15	PKI	Protein Kinase Inhibitor	Kinase inhibitor

Table B.2. List of pharmacological drugs.

B.2. Equations

The model of Zhao et al. [127] is expanded to include mechanistic descriptions of cGMP dynamics. Centered upon cN signal dynamics, the entire network model can be viewed as composed of 5 modules: ***A)*** portions of the β-AR pathway governing cAMP synthesis, from ligand binding to β-AR to the activation of AC; ***B)*** portions of the NO/cGMP/PKG pathway regulating cGMP synthesis through activation of sGC; ***C)*** pathway crosstalk comprising mechanistic models of PDEs 1–5 regulating cAMP and cGMP degradation; ***D)*** balance Equation for cAMP and cGMP signals, bridging together A) to C); and ***E)*** activation of kinases by cNs. The number of state equations and parameters in each sections of the model is tabulated in Table B.3, as well as parameters and constants for pharmacological reagents and unit conversions (Item ***F)***).

	Component	State Equations	Parameters
A.	β-adrenergic pathway (cAMP synthesis)	11	19
B.	NO/sGC pathway (cGMP synthesis)	9	27
C.	Pathway cross-talk (cN degradation)	13	38
D.	cN balance equations (Net cN dynamics)	4	--

E.	Kinase activation (PKA and PKG)	6	14
	Total (cN Network)	**43**	**98**
F.	Other parameters and constants	--	21
	Total	**43**	**119**

Table B.3. Tabulation of equations and parameters.

For notation, concentrations of signaling species are enclosed by square brackets, "[ ]". Fractions normalized to total concentrations are not enclosed or enclosed with round brackets, "( )". Rates of cN production and degradation are prefixed by lower-case letter "v". In addition, subscript "A" and subscript "G" denote cAMP hydrolysis and cGMP hydrolysis related terms respectively. The definitions of state variables, together with their initial conditions, are tabulated in Sect. B.4. For equations adapted from previous models [71, 129], notations are preserved as much as possible as the original literature.

B.2.1. Equations for β-adrenergic pathway

Equations for the β-adrenergic pathway, governing the production of cAMP, are from Saucerman et al. [71].

Equations for β-AR receptor

$$[L_{tot}] - [LR] - [LRG] - [L] = 0 \quad (22)$$

$$[\beta_1 AR_{act}] - [LR] - [LRG] - [RG] - [\beta_1 AR] = 0 \quad (23)$$

$$[G_{stot}] - [RG] - [LRG] - \left[G_{s\beta\gamma}\right] - [G_s] = 0 \quad (24)$$

$$\frac{d([\beta_1 AR_{act}])}{dt} = \{k_{\beta ARK-}[\beta_1 AR_{S464}] - k_{\beta ARK+}([LR] + [LRG])\} \ldots$$

$$+ \{k_{PKA-}[\beta_1 AR_{S301}] - k_{PKA+}([PKACI][\beta_1 AR_{act}])\} \quad (25)$$

$$\frac{d([\beta_1 AR_{S464}])}{dt} = k_{\beta ARK+}([LR] + [LRG]) - k_{\beta ARK-}[\beta_1 AR_{S464}] \quad (26)$$

$$\frac{d([\beta_1 AR_{S301}])}{dt} = k_{PKA+}[PKAC_I][\beta_1 AR_{act}] - k_{PKA-}[\beta_1 AR_{S301}] \quad (27)$$

Where:

$[LR] = [L][\beta_1 AR]/K_L$; $[LRG] = [L][\beta_1 AR][G_s]/(K_L K_R)$; $[RG] = [\beta_1 AR][G_s]/K_c$

Equations for Gs activation

$$\frac{d([G_{s\alpha GTPtot}])}{dt} = k_{gact}([RG] + [LRG]) - k_{hyd}[G_{s\alpha GTPtot}] \quad (28)$$

$$\frac{d([G_{s\beta\gamma}])}{dt} = k_{gact}([RG] + [LRG]) - k_{reassoc}[G_{s\alpha GDP}][G_{s\beta\gamma}] \quad (29)$$

$$\frac{d([G_{s\alpha GDP}])}{dt} = k_{hyd}[G_{s\alpha GTPtot}] - k_{reassoc}[G_{s\alpha GDP}][G_{s\beta\gamma}] \quad (30)$$

Equations for cAMP production

For the following equations, terms governing the pharmacological drug, Forskolin (Fsk), are removed from the original model by Saucerman et al. [71] as Fsk is not studied in the present model.

$$[G_{s\alpha GTPtot}] - [G_{s\alpha GTP}] - [G_{s\alpha GTP}{:}AC] = 0 \quad (31)$$

$$[AC_{tot}] - [G_{s\alpha GTP}{:}AC] - [AC] = 0 \quad (32)$$

$$vp_A = \frac{k_{AC_{basal}}[AC][ATP]}{k_{m_{AC_{basal}}} + [ATP]} + \frac{k_{AC_{Gs\alpha}}[AC{:}G_{s\alpha}GTP][ATP]}{k_{m_{GsaGTP}} + [ATP]}$$

Where $[G_{s\alpha GTP}{:}AC] = [G_{s\alpha GTP}][AC]/K_{Gs\alpha}$

B.2.2. Equations for NO/sGC pathway

Equations for NO delivery

$$\frac{d[Donor_{NO}]}{dt} = -k_{D_{donor}} \cdot [Donor_{NO}]^{n_{donor}} \quad (33)$$

$$J_{NO} = C_{diff_{NO}} \frac{([NO]_o - [NO]_i)}{w_{sL}}$$

$$\frac{d[NO]_o}{dt} = v_{donorNO} - \frac{A_{cell}}{V_{perf}} J_{NO} - v_{D_{NOo}} \quad (34)$$

$$\frac{d[NO]_i}{dt} = v_{NOS} + \frac{A_{cell}}{V_{cell}} J_{NO} - v_{D_{NOi}} \quad (35)$$

Where

$v_{donorNO} = k_{D_{donor}}[Donor_{NO}]^{n_{donor}} \cdot f_{donor}$,

$v_{D_{NOo}} = k_{D_{NO\_O2}} \cdot [O_2][NO]_o^{\,2}$,

$v_{D_{NOi}} = k_{D_{NO\_O2}} \cdot [O_2][NO]_i^{\,2} - k_{D_{NO\_SO}} \cdot [O_2^{\cdot -}][NO]_i$,

$A_{cell} = 2 \cdot (l_{cell} \cdot w_{cell} + h_{cell} \cdot w_{cell} + h_{cell} \cdot l_{cell})$,

$V_{cell} = l_{cell} \cdot w_{cell} \cdot h_{cell}$, and

$V_{cell} = 3.142 * r_{rube}^2 * l_{cell} - V_{cell}$.

Equations for NO regulation of sGC

Equations governing NO regulation of sGC remains the same as the original model of Batchelor, et al. [129].

$$\frac{d(sGC)}{dt} = k_{-1_{sGC}}(NOsGC) + k_{6_{sGC}}(GC^*) - k_{1_{sGC}}[NO](sGC) - k_{-6_{sGC}}(sGC) \quad (36)$$

$$\frac{d(NOsGC)}{dt} =$$

$$k_{1_{sGC}}[NO](sGC) + k_{-2_{sGC}}(NOsGC^*) - k_{-1_{sGC}}(NOsGC) - k_{2_{sGC}}(NOsGC) \quad (37)$$

$$\frac{d(NOsGC^*)}{dt} = k_{2_{sGC}}(NOsGC) + k_{-3_{sGC}}(NOsGC^*NO) \ldots$$

$$- k_{-2_{sGC}}(NOsGC^*) - k_{3_{sGC}}[NO](NOsGC^*) \quad (38)$$

$$\frac{d(NOsGC^*NO)}{dt} = k_{3_{sGC}}[NO](NOsGC^*) + k_{-4_{sGC}}[NO](GC^*NO) \ldots$$

$$- k_{-3_{sGC}}(NOsGC^*NO) - k_{4_{sGC}}(NOsGC^*NO) \quad (39)$$

$$\frac{d(sGC^*NO)}{dt} = k_{4_{sGC}}(NOsGC^*NO) + k_{-5_{sGC}}[NO](sGC^*) \ldots$$

$$- k_{-4_{sGC}}[NO](sGC^*NO) - k_{5_{sGC}}(sGC^*NO) \quad (40)$$

$$\frac{d(sGC^*)}{dt} = k_{5_{sGC}}(sGC^*NO) + k_{-6_{sGC}}(sGC) - k_{-5_{sGC}}[NO](sGC^*) - k_{6_{sGC}}(sGC^*) \quad (41)$$

Equations for cGMP production

$$vp_G = Vmax_{sGC}\,(NOsGC^*)$$

B.2.3. Equations for phosphodiesterase isoenzymes

The PDE degradation components of Saucerman et al. [71] and Batchelor, et al. [129] are extended to include degradation by five distinctively regulated PDE isoenzymes, PDEs 1–5.

Equations for PDE1

Rate of PDE1 degradation of cAMP as regulated by cGMP (42)

$$vPDE1_A = \frac{Vmax_{PDE1_A}[cAMP]}{km_{PDE1_A}\left(1 + \frac{[cGMP]}{km_{PDE1_G}}\right) + [cAMP]}$$

Rate of PDE1 degradation of cGMP as regulated by cAMP (43)

$$vPDE1_G = \frac{Vmax_{PDE1_G}[cGMP]}{km_{PDE1_G}\left(1 + \frac{[cAMP]}{km_{PDE1_A}}\right) + [cGMP]}$$

Equations for PDE2

Rate of PDE2 cAMP degradation as regulated by cGMP (44)

$$vPDE2_A = \frac{Vmax_{PDE2_A}[cAMP][1 + \frac{[cAMP]}{\rho_{PDE2}k_{a_{PDE2}}} + \frac{[cGMP]}{\omega_{PDE2}k_{b_{PDE2}}}]}{K_{s_{PDE2}}\left[1 + \frac{[cAMP]}{K_{a_{PDE2}}} + \frac{[cAMP][cGMP]}{\epsilon_{PDE2}K_{I_{PDE2}}K_{a_{PDE2}}} + \frac{[cGMP]}{K_{I_{PDE2}}} + \frac{[cGMP]}{K_{b_{PDE2}}} + \frac{[cGMP]^2}{\eta_{PDE2}K_{I_{PDE2}}K_{b_{PDE2}}}\right] + \cdots [cAMP][1 + \frac{[cAMP]}{K_{a_{PDE2}}} + \frac{[cGMP]}{\omega_{PDE2}K_{b_{PDE2}}}]}$$

Rate of PDE2 cGMP degradation as regulated by cAMP (45)

$$vPDE2_G = \frac{Vmax_{PDE2_G}[cGMP][1 + \frac{[cGMP]}{\eta_{PDE2}k_{b_{PDE2}}} + \frac{[cAMP]}{\epsilon_{PDE2}k_{a_{PDE2}}}]}{k_{I_{PDE2}}\left[1 + \frac{[cGMP]}{k_{b_{PDE2}}} + \frac{[cAMP][cGMP]}{k_{s_{PDE2}}k_{b_{PDE2}}} + \frac{[cAMP]}{k_{s_{PDE2}}} + \frac{[cAMP]}{k_{a_{PDE2}}} + \frac{[cAMP]^2}{\rho_{PDE2}k_{s_{PDE2}}k_{a_{PDE2}}}\right] + \cdots [cGMP][1 + \frac{[cGMP]}{k_{b_{PDE2}}} + \frac{[cAMP]}{\epsilon_{PDE2}k_{a_{PDE2}}}]}$$

Equations for PDE3

Rate of PDE3 cAMP degradation, with competitive inhibition by cGMP (46)

$$vPDE3_A = \frac{Vmax_{PDE3_A}[cAMP]}{k_{s_{PDE3}}\left(1 + \frac{[cGMP]}{k_{i_{PDE3}}}\right) + [cAMP]}$$

Rate of PDE3 cGMP degradation, with competitive inhibition by cAMP (47)

$$vPDE3_G = \frac{Vmax_{PDE3_G}[cGMP]}{k_{i_{PDE3}}\left(1 + \frac{[cAMP]}{k_{s_{PDE3}}}\right) + [cGMP]}$$

Equations for PDE4

Fraction of PDE4 phosphorylated by PKA

$$PDE4 = 1 - pPDE4$$

$$\frac{d(pPDE4)}{dt} = k_{PDE4_{PKA}} \cdot [PKAC_{II}] \cdot PDE4 - k_{PDE4_{pp}} \cdot pPDE4 \quad (48)$$

Rate of cAMP hydrolysis by non-phosphorylated and phosphorylated PDE4 (49)

$$vPDE4_A = \frac{Vmax_{PDE4_A} \cdot PDE4 \cdot [cAMP]}{K_{m_{PDE4}} + [cAMP]} + \frac{Vmax_{pPDE4_A} \cdot pPDE4 \cdot [cAMP]}{K_{m_{pPDE4}} + [cAMP]}$$

Equations for PDE5

Equations governing PDE5 activation are modified from the original Batchelor et al. model [129] to explicitly include PKG-mediated phosphorylation.

$$\frac{d(PDE5)}{dt} = k_{-1_{PDE5}}(cGMP{:}PDE5) - k_{1_{PDE5}}(PDE5)[cGMP] \quad (50)$$

$$\frac{d(cGMP{:}PDE5)}{dt} = k_{1_{PDE5}}[cGMP](PDE5) + k_{-2_{PDE5}}(tPDE5^*) \ldots \quad (51)$$

$$- k_{-1_{PDE5}}(cGMP{:}PDE5) - k_{2_{PDE5}}(cGMP{:}PDE5)$$

$$\frac{d(tPDE5^*)}{dt} = k_{2_{PDE5}}(cGMP{:}PDE5) + k_{-3_{PDE5}}(pPDE5^*) \ldots$$

$$- k_{-2_{PDE5}}(tPDE5^*) - k_{3_{PDE5}}(PKG_{I_{active}})(tPDE5^*) \quad (52)$$

$$\frac{d(pPDE5^*)}{dt} = k_{3_{PDE5}}(PKG_{I_{active}})(tPDE5^*) - k_{-3_{PDE5}}(pPDE5^*) \quad (53)$$

cGMP hydrolysis by PDE5 (54)

$$vPDE5_G = \frac{Vmax_{PDE5_G} \cdot tPDE5^* \cdot [cGMP]}{km_{PDE5}+[cGMP]} + \frac{Vmax_{pPDE5_G} \cdot pPDE5^* \cdot [cGMP]}{km_{pPDE5}+[cGMP]}$$

B.2.4. Equations for cyclic nucleotide signal dynamics

The asterisk (*) following the originally defined PDE isoenzyme hydrolytic rate denote the hydrolytic activity after inhibition by a pharmacological inhibitor if applied, as defined by the following section. Otherwise, the hydrolytic rate is defined by previous sections.

Balance equations for cN signals

$$\frac{d[cAMP_{tot}]}{dt} = vp_A - vPDE1_A^* - vPDE2_A^* - vPDE3_A^* - vPDE4_A^* \quad (55)$$

$$\frac{d[cGMP_{tot}]}{dt} = vp_G - vPDE1_G^* - vPDE2_G^* - vPDE3_G^* - vPDE5_G^* \quad (56)$$

Equations for pharmacological inhibition of PDE activities

If applied, the pharmacological inhibitor inhibits the hydrolytic activity of a PDE isoenzyme by the following equations. In this paper, the nonspecific PDE inhibitor (IBMX) is never simultaneously applied with any of the specific inhibitors; therefore, despite the form of the equations, interactions between the two inhibitors, if any, are not modeled.

$$vPDE1_A^* = vPDE1_A/(1 + \frac{[IBMX]}{Ki_{IBMX\_PDE1}})$$

$$vPDE1_G^* = vPDE1_{\mathrm{G}}/(1 + \frac{[IBMX]}{Ki_{IBMX\_PDE1}})$$

$$vPDE2_A^* = vPDE2_{\mathrm{A}}/(1 + \frac{[IBMX]}{Ki_{IBMX\_PDE2}} + \frac{[EHNA]}{Ki_{EHNA}}))$$

$$vPDE2_G^* = vPDE2_{\mathrm{G}}/(1 + \frac{[IBMX]}{Ki_{IBMX\_PDE2}} + \frac{[EHNA]}{Ki_{EHNA}})$$

$$vPDE3_A^* = vPDE3_{\mathrm{A}}/(1 + \frac{[IBMX]}{Ki_{IBMX\_PDE3}} + \frac{[Cilo]}{Ki_{Cilo}})$$

$$vPDE3_G^* = vPDE3_{\mathrm{G}}/(1 + \frac{[IBMX]}{Ki_{IBMX\_PDE3}} + \frac{[Cilo]}{Ki_{Cilo}})$$

$$vPDE4_A^* = vPDE4_{\mathrm{A}}/(1 + \frac{[IBMX]}{Ki_{IBMX\_PDE4}} + \frac{[Roli]}{Ki_{Rol}})$$

$$vPDE5_G^* = vPDE5_{\mathrm{G}}/(1 + \frac{[IBMX]}{Ki_{IBMX\_PDE5}} + \frac{[Sil]}{Ki_{Sil}})$$

Equation for conservation of mass of cAMP

Free [cAMP] is updated from the original model [71] to include the effect of cAMP bound to PDEs. (57)

$$[cAMP] = [cAMP]_{tot} - ([ARC_I] + 2 \cdot [A2RC_I] + 2 \cdot [A2R_I]) \ldots$$
$$-([ARC_{II}] + 2 \cdot [A2RC_{II}] + 2 \cdot [A2R_{II}]) \ldots$$
$$-([APDE2] + 2 \cdot [APDE2A] + [PDE2A] + [GPDE2A] + [APDE2G])$$

where terms in equation are defined in the sections below.

Equation for conservation of mass of cGMP

Free [cGMP] is governed by the following equation.

$$[cGMP] = [cGMP]_{tot} - (2 \cdot [PKG_I{:}\,cGMP2] + 4 \cdot [PKG_I{:}\,cGMP4]) \ldots \quad (58)$$
$$-([GPDE2] + 2 \cdot [GPDE2AG] + [PDE2G] + [GPDE2A] + [APDE2G]) \ldots$$
$$-([GPDE5] + 2 \cdot [tPDE5^*] + 2 \cdot [pPDE5^*])$$

where terms in equation are defined in the sections below.

Equations for cAMP bound to PDEs

cAMP bound to PDE2 is governed by the following equations.

$$[APDE2] = [PDE2]\frac{[cAMP]}{k_{a_{PDE2}}}$$
$$[APDE2A] = [PDE2]\frac{[cAMP]^2}{\rho_{PDE2}k_{s_{PDE2}}k_{a_{PDE2}}}$$
$$[PDE2A] = [PDE2]\frac{[cAMP]}{k_{s_{PDE2}}}$$
$$[GPDE2A] = [PDE2]\frac{[cAMP][cGMP]}{\omega k_{s_{PDE2}}k_{b_{PDE2}}}$$
$$[APDE2G] = [PDE2]\frac{[cAMP][cGMP]}{\varepsilon k_{i_{PDE2}}k_{a_{PDE2}}}$$

Where

$$[PDE2] = \frac{2[PDE2]_{tot}}{D_{PDE2}}/(1 + \frac{[IBMX]}{Ki_{IBMX\_PDE2}} + \frac{[EHNA]}{Ki_{EHNA}})$$

and

$$D_{PDE2} = 1 + \frac{[cAMP]}{k_{a_{PDE2}}} + \frac{[cAMP][cGMP]}{\epsilon_{PDE2}k_{i_{PDE2}}k_{a_{PDE2}}} + \frac{[cGMP]}{k_{i_{PDE2}}} + \frac{[cGMP]}{k_{b_{PDE2}}} + \frac{[cGMP]^2}{\eta_{PDE2}k_{i_{PDE2}}k_{b_{PDE2}}} \ldots + \frac{[cAMP]^2}{\rho_{PDE2}k_{s_{PDE2}}k_{a_{PDE2}}} + \frac{[cAMP]}{k_{s_{PDE2}}} + \frac{[cAMP][cGMP]}{\omega k_{s_{PDE2}}k_{b_{PDE2}}}$$

Equations for cGMP bound to PDEs

cGMP bound to PDE2 is governed by the following equations.

$$[GPDE2] = [PDE2]\frac{[cGMP]}{k_{b_{PDE22}}}$$
$$[GPDE2G] = [PDE2]\frac{[cGMP]^2}{\eta_{PDE2}k_{i_{PDE2}}k_{b_{PDE2}}}$$

$$[PDE2G] = [PDE2]\frac{[cGMP]}{k_{i_{PDE2}}}$$
$$[GPDE2A] = [PDE2]\frac{[cAMP][cGMP]}{\omega k_{s_{PDE2}} k_{b_{PDE2}}}$$
$$[APDE2G] = [PDE2]\frac{[cAMP][cGMP]}{\epsilon_{PDE2} k_{i_{PDE2}} k_{a_{PDE2}}}$$

Where $[PDE2]$ is the same as that defined previously in "Equations for cAMP bound to PDEs".

cGMP bound to PDE5 is governed by the following equations.

$$[GPDE5] = 2 \cdot [PDE5]^*_{tot}(cGMP{:}PDE5)$$
$$[tPDE5^*] = 2 \cdot [PDE5]^*_{tot}(tPDE5^*)$$
$$[pPDE5^*] = 2 \cdot [PDE5]^*_{tot}(pPDE5^*)$$
Where
$$[PDE5]^*_{tot} = [PDE5]_{tot}/(1 + \frac{[IBMX]}{Ki_{IBMX\_PDE5}} + \frac{[Sil]}{Ki_{Sil}})$$

Equations for cGMP bound to PKG

cGMP bound to PKG is governed by the following equations.

$$[PKG_I{:}cGMP2] = [PKG_I]_{tot}(PKG_I{:}cGMP2)$$

$$[PKG_I{:}cGMP4] = [PKG_I]_{tot}(PKG_I{:}cGMP4)$$

B.2.5. Equations for kinase activation

Equations for PKA activation

Equations for PKA-I and PKA-II are from Saucerman et al. [71].

$$2[PKA_{Itot}] - ([RC_I] + [ARC_I] + [A_2RC_I] + [PKAC_I{:}PKI]) - [PKAC_I] = 0 \qquad (59)$$

Where

$$[RC_I] = \frac{K_A K_B}{[cAMP]^2}\frac{[PKAC_I]}{K_D}([PKAC_I] + [PKAC_I{:}PKI])$$

$$[ARC_I] = \frac{K_A}{[cAMP]^2}\frac{[PKAC_I]}{K_D}([PKAC_I] + [PKAC_I{:}PKI])$$

$$[A_2RC_I] = \frac{[PKAC_I]}{K_D}([PKAC_I] + [PKAC_I{:}PKI])$$

$$[A_2R_I] = [PKAC_I] + [PKAC_I{:}PKI]$$

$$[PKAC_I{:}PKI] = \frac{[PKAC_I][PKI_{tot}]}{K_{PKI} + [PKAC_I] + [PKAC_{II}]}$$

PKA-II activation by cAMP and inhibition by PKI are governed by the following equations.

$$2[PKA_{II}tot] - ([RC_{II}] + [ARC_{II}] + [A_2RC_{II}] + [PKAC_{II}{:}PKI]) - [PKAC_{II}] = 0 \quad (60)$$

Where

$$[RC_{II}] = \frac{K_A K_B}{[cAMP]^2}\frac{[PKAC_{II}]}{K_D}([PKAC_{II}] + [PKAC_{II}{:}PKI])$$

$$[ARC_{II}] = \frac{K_A}{[cAMP]^2}\frac{[PKAC_{II}]}{K_D}([PKAC_{II}] + [PKAC_{II}{:}PKI])$$

$$[A_2RC_{II}] = \frac{[PKAC_{II}]}{K_D}([PKAC_{II}] + [PKAC_{II}{:}PKI])$$

$$[A_2R_{II}] = [PKAC_{II}] + [PKAC_{II}{:}PKI]$$

$$[PKAC_{II}{:}PKI] = \frac{[PKAC_{II}][PKI_{tot}]}{K_{PKI} + [PKAC_I] + [PKAC_{II}]}$$

Finally, concentration of pharmacological inhibitor PKI is regulated by the following

$$[PKI] = \frac{K_{PKI}[PKI_{tot}]}{K_{PKI} + [PKAC_I] + [PKAC_{II}]}$$

Equations for PKG activation

$$\frac{d(PKG_I{:}cGMP2)}{dt} = k_{1_{PKGI}}(PKG_I)[cGMP]^{h_{1_{PKGI}}} + k_{-2_{PKGI}}(PKG_I{:}cGMP4) \ldots$$

$$-k_{-1_{PKGI}}(PKG_I{:}cGMP2) - k_{2_{PKGI}}(PKG_I{:}cGMP2)[cGMP]^{h_{2_{PKGI}}} \quad (61)$$

$$\frac{d(PKG_I{:}cGMP4)}{dt} = k_{2_{PKG}}(PKG_I{:}cGMP2)[cGMP]^{h_{2_{PKG}}} - k_{-2_{PKG}}(PKG_I{:}cGMP4)$$

Where $k_{2_{PKGI}} = k^*_{2_{PKGI}} \cdot T_{PKGI}$ and $k_{-2_{PKGI}} = k^*_{-2_{PKGI}} \cdot T_{PKGI}$ (62)

$$(PKG_I) = 1 - (PKG_I{:}cGMP2) - (PKG_I{:}cGMP4) \quad (63)$$

$$(PKG_{I_{active}}) = f_{PKGI}(PKG_I{:}cGMP2) + (PKG_I{:}cGMP4) \quad (64)$$

B.3. Model parameters

All adopted parameters are the same as or fall within the indicated ranges of the original models of Zhao et al. [127], Saucerman et al. [71], and Batchelor et al. [129].

B.3.1. Parameters in β-adrenergic pathway model

All adopted parameters are the same as original model of Zhao et al. [127] and Saucerman et al. [71].

Parameters for β-AR receptor

	Parameter	Representation	Value	Units	Ref.
1	$[\beta_1 AR_{tot}]$	Total concentration of $\beta_1 AR$	0.0132	μM	[71]

2	$[G_{stot}]$	Total concentration of stimulatory G protein	3.83	μM	[71]
3	K_L	Dissociation constant between β_1AR receptor and its ligand	0.285	μM	[71]
4	K_R	Dissociation constant between ligand-bound β_1AR receptor and G-protein	0.062	μM	[71]
5	K_C	Dissociation constant between unbound β_1AR receptor and G-protein	33	μM	[71]
6	$k_{\beta ARK+}$	β_1 AR desensitization by β -arrestin	1.1×10^{-6}	ms^{-1}	[71]
7	$k_{\beta ARK-}$	β_1AR re-sensitization	$2k_{\beta ARK+}$	ms^{-1}	[71]
8	k_{PKA+}	β_1AR desensitization by PKA	3.6×10^{-6}	$\mu M^{-1}ms^{-1}$	[71]
9	k_{PKA-}	β_1AR re-sensitization	$0.62k_{PKA+}$	ms^{-1}	[71]

Table B.4. Parameters for β-adrenergic receptor regulation.

Parameters for Gs activation

	Parameter	Representation	Value	Units	Ref.
1	k_{gact}	$G_{s\alpha}$activation	0.016	ms^{-1}	[71]
2	k_{hyd}	$G_{s\alpha}$hydrolysis	8×10^4	ms^{-1}	[71]
3	$k_{reassoc}$	$G_{s\alpha}$reassociation	1.2	$\mu M^{-1}ms^{-1}$	[71]

Table B.5. Parameters for G-protein activation.

Parameters for cAMP production

	Parameter	Representation	Value	Units	Ref.
1	$[AC_{tot}]$	Total concentration of adenylyl cyclase	0.0497	μM	[71]
2	$[ATP]$	Total concentration of ATP	5×10^3	μM	[71]
3	$K_{Gs\alpha}$	AC activation by $G_{s\alpha}$	315	μM	[71]
4	k_{AC_basal}	Basal AC activity	2×10^{-4}	ms^{-1}	[71]
5	k_{m_basal}	Basal AC affinity for ATP	1.03×10^3	μM	[71]
6	$k_{AC\_Gs\alpha}$	AC activity with $G_{s\alpha}$ activation	8.5×10^2	ms^{-1}	[71]
7	$k_{m\_Gs\alpha GTP}$	$AC: G_{s\alpha}$ affinity for ATP	315	μM	[71]

Table B.6. Parameters for AC catalyzed production of cAMP.

B.3.2. Parameters in NO/sGC model

All adopted parameters are the same or fall within the indicated ranges of the original models of Zhao et al. [127], Saucerman et al. [71], and Batchelor et al. [129].

Parameters for NO delivery model

	Parameter	Representation	Value	Units	Ref.
1	v_{NOS}	Release flux from endogenous NOS	1.8×10^{-8}	$\mu M/ms$	[150, 242]

2	$k_{D_{NO\_O2}}$	Rate of NO degradation when reacting with oxygen (O_2)	9.2×10^{-9}	$\mu M^{-2} ms^{-1}$	[139, 140]
3	$k_{D_{NO\_SO}}$	Rate of NO degradation when reacting with superoxide ($O_2^{\cdot -}$)	6.5	$\mu M^{-1} ms^{-1}$	[141]
4	$[O_2]$	Oxygen concentration in experimental solution at cell-depth	74	μM	[275]
5	$[O_2^{\cdot -}]$	Superoxide concentration in cardiac myocytes	4.7×10^{-5}	μM	[141]
6	$C_{diff_{NO}}$	Diffusion constant for NO across plasma membrane	1.0	$\mu m^2/ms$	[276]
		NO donor SNAP			
7	n_{donor}	Order of reaction for NO donor decomposition	1.548	--	[135]
8	$k_{D_{donor}}$	Rate of NO Donor decomposition	1.116×10^{-7}	$\mu M^{1-n_{dono}} ms^{-1}$	[136]
9	f_{donor}	Moles of NO released per mole of NO donor	1	--	[137, 138]
		Cell dimensions			
10	w_{sL}	Thickness of the sarcolemma	8×10^{-3}	μm	[277]

		(cardiac cell membrane)			
11	l_{cell}	Length of ARVM	140	μm	[6]
12	w_{cell}	Width of ARVM	33	μm	[6]
13	h_{cell}	Height of ARVM	14	μm	[6]
		Experimental Setup			
14	r_{tube}	Radius of capillary tube	125	μm	[128]

Table B.7. Parameters for NO liberation by SNAP.

Parameters for NO regulation of sGC model

All parameters listed below are the same as or fall within the identified ranges of the original model [129, 278].

	Parameter	Representation	Value	Units	Ref.
1	$k_{1_{sGC}}$	sGC activation rate	0.3	$\mu M^{-1} ms^{-1}$	[129]
2	$k_{-1_{sGC}}$	sGC deactivation rate	0.006	ms^{-1}	[129]
3	$k_{2_{sGC}}$	sGC activation rate	0.028	ms^{-1}	[129]
4	$k_{-2_{sGC}}$	sGC deactivation rate	0.028	ms^{-1}	[129]
5	$k_{3_{sGC}}$	sGC desensitization rate	0.004	$\mu M^{-1} ms^{-1}$	[129]
6	$k_{-3_{sGC}}$	sGC desensitization rate	1	ms^{-1}	[129]
7	$k_{4_{sGC}}$	sGC desensitization rate	2	ms^{-1}	[129]
8	$k_{-4_{sGC}}$	sGC desensitization rate	1.8×10^{-3}	$\mu M^{-1} ms^{-1}$	[129]
9	$k_{5_{sGC}}$	Rate of recovery from desensitization	7×10^{-7}	ms^{-1}	[129]

10	$k_{-5_{sGC}}$	Fixed by microscopic reversibility	0.163	$\mu M^{-1}ms^{-1}$	[129]
11	$k_{6_{sGC}}$	Rate of recovery from inactivated species	0.001	ms^{-1}	[129]
12	$k_{-6_{sGC}}$	Rate of inactivation	10^{-6}	ms^{-1}	[129]
13	$Vmax_{sGC}$	Maximum rate of cGMP production by sGC	1.3×10^{-4}	$\mu M/ms$	[129]

Table B.8. Parameters for NO regulation of sGC.

B.3.3. Parameters for phosphodiesterase models

Parameters for PDE1 model

	Parameter	Representation	Value	Unit	Ref.
1	km_{PDE1_A}	PDE1 affinity to cAMP	0.98	μM	[5]
2	km_{PDE1_G}	PDE1 affinity to cGMP	0.76	μM	[5]
3	$Vmax_{PDE1_A}$	Maximal homotropic cAMP hydrolytic rate	5×10^{-6}	$\mu M/ms$	FIT
4	$Vmax_{PDE1_G}$	Maximal homotropic cGMP hydrolytic rate	1.3×10^{-6}	$\mu M/ms$	FIT

Table B.9. Parameters for PDE1 model.

Parameters for PDE2 model

	Parameter	Representation	Value	Unit	Ref.
1	$k_{a_{PDE2}}$	Dissociation constants for cAMP binding to GAF-B regulatory domain	0.2286	μM	[240, 241]
2	$k_{b_{PDE2}}$	Dissociation constants for cGMP binding to GAF-B regulatory domain	0.0654	μM	[240, 241]
3	$k_{s_{PDE2}}$	Dissociation constants for cAMP binding to catalytic domain	32.5	μM	[31]
4	$k_{I_{PDE2}}$	Dissociation constants for cGMP binding to catalytic domain	22.2	μM	[31]
5	ρ_{PDE2}	Scaling factor for $k_{s_{PDE2}}$ upon cAMP biding to GAF-B regulatory domain for cAMP-regulated cAMP hydrolysis	0.9791	--	[30]
6	ω_{PDE2}	Scaling factor for $k_{s_{PDE2}}$ upon cGMP biding to GAF-B regulatory domain	0.37	--	[253]
7	ϵ_{PDE2}	Scaling factor for $k_{I_{PDE2}}$ upon cAMP biding to GAF-B regulatory domain cAMP-regulated cGMP hydrolysis	0.67	--	FIT
8	η_{PDE2}	cGMP-activated, cGMP hydrolysis	0.86	--	[241]

		Scaling factor for $k_{I_{PDE2}}$ upon cGMP biding to GAF-B regulatory domain cGMP-regulated cGMP hydrolysis			
9	$Vmax_{PDE2_A}$	Maximum homotropic rate cGMP hydrolysis	2.2×10^{-4}	$\mu M/ms$	FIT
10	$Vmax_{PDE2_G}$	Maximum homotropic rate cGMP hydrolysis	2.4×10^{-4}	$\mu M/ms$	FIT
11	$[PDE2]_{tot}$	Total concentration of PDE2	5×10^{-3}	μM	[72]

Table B.10. Parameters for PDE2 model.

Parameters for PDE3 model

	Parameter	Meaning	Value	Unit	Ref.
1	$k_{s_{PDE3}}$	cAMP affinity to catalytic domain	0.13	μM	[254]
2	$k_{i_{PDE3}}$	cGMP affinity to catalytic domain	0.1	μM	[105]
3	$Vmax_{PDE3_A}$	Maximum rate of cAMP hydrolysis	2.5×10^{-5}	$\mu M/ms$	FIT
4	$Vmax_{PDE3_G}$	Maximum rate of cAMP hydrolysis	5.1×10^{-6}	$\mu M/ms$	FIT

Table B.11. Parameters for PDE3 model.

Parameters for PDE4 model

	Parameter	Representation	Value	Units	Ref.
1	$k_{PDE4_{PKA}}$	Rate of PDE4 phosphorylation	7.5×10^{-3}	$\mu M^{-1} ms^{-1}$	[74]
2	$k_{PDE4_{pp}}$	Rate of PDE4 dephosphorylation	1.5×10^{-3}	ms^{-1}	[74]
3	$k_{m_{PDE4}}$	cAMP affinity to catalytic domain of the non-phosphorylated PDE4	1.12	μM	[130, 134]
4	$k_{m_{pPDE4}}$	cAMP affinity to catalytic domain of the non-phosphorylated PDE4	1.12	μM	[130, 134]
5	$Vmax_{PDE4_A}$	Maximum rate of cAMP hydrolysis by the non-phosphorylated PDE4	1×10^{-4}	$\mu M/ms$	FIT
6	$Vmax_{pPDE4_A}$	Maximum rate of cAMP hydrolysis by the phosphorylated PDE4	1.4 $\cdot Vmax_{PDE4}$	$\mu M/ms$	[130, 134]

Table B.12. Parameters for PDE4 model.

Parameters for PDE5 model

All parameters are the same as or fall within the ranges identified by the original model [129], except PKG phosphorylation rate ($k_{3_{PDE5}}$) and the two parameters for hydrolysis

behavior of phosphorylated PDE5 ($k_{m_{pPDE5}}$ and $Vmax_{pPDE5_G}$). These changes are to account for the incorporation of explicit PKG-mediated phosphorylation of PDE5.

	Parameter	Representation	Value	Units	Ref.
1	$k_{1_{PDE5}}$	cGMP association rate	1.81×10^{-5}	$\mu M^{-1} ms^{-1}$	[129]
2	$k_{-1_{PDE5}}$	cGMP dissociation rate	0.868×10^{-4}	ms^{-1}	[129]
3	$k_{2_{PDE5}}$	Rate of conformation change to active PDE5	0.2×10^{-3}	ms^{-1}	[129]
4	$k_{-2_{PDE5}}$	Rate of conformation change to non-activated PDE5	0.154×10^{-3}	ms^{-1}	[129]
5	$k_{3_{PDE5}}$	Rate of PDE5 phosphorylation by active PKG	1.1×10^{-4}	ms^{-1}	[129]
6	$k_{-3_{PDE5}}$	Rate of PDE5 dephosphorylation	1.21×10^{-6}	ms^{-1}	[129]
7	$k_{m_{PDE5}}$	cGMP affinity to catalytic domain of the non-phosphorylated PDE5	4	μM	[278]
8	$k_{m_{pPDE5}}$	cGMP affinity to catalytic domain of the phosphorylated PDE5	1	μM	[278]
9	$Vmax_{PDE5_G}$	Maximum rate of cGMP hydrolysis by the non-	$3.3 \times 10^{\mp 5}$	$\mu M/ms$	FIT

		phosphorylated PDE5			
10	$Vmax_{pPDE5_G}$	Maximum rate of cGMP hydrolysis by the phosphorylated PDE5	$1.65 \cdot Vmax_{PDE5}$	$\mu M/ms$	[279]
11	$[PDE5]_{tot}$	Total concentration of PDE5	7.7×10^{-3}	μM	[95]

Table B.13. Parameters for PDE5 model.

B.3.4. Parameters for kinase models

All adopted parameters are the same as or fall within the indicated ranges of the original models of Zhao et al. [127], Saucerman et al. [71], and Batchelor et al. [129].

Parameters for PKA activation

	Parameter	Representation	Value	Units	Ref.
1	$[PKA_{Itot}]$	Total concentration of PKA-I	0.59	μM	[71]
2	$[PKA_{IItot}]$	Total concentration of PKA-II	0.025	μM	[71]
3	K_A	Dissociation constant between one cAMP-bound PKA (ARC) and second cAMP (A)	9.14	μM	[71]
4	K_B	Dissociation constant between unbound PKA (RC) and cAMP (A)	1.64	μM	[71]
5	k_D	Dissociation constant between two cAMP bound regulatory subunit (A2R)	4.375	μM	[71]

		and catalytic subunit (C) of PKA			

Table B.14. Parameters for cAMP activation of PKA.

Parameters for PKG-I activation model

	Parameter	Description	Value	Units	Ref.
1	$k_{1_{PKGI}}$	cGMP association with slow high affinity site on PKG-I	2.3×10^{-3}	$\mu M^{-1} ms^{-1}$	[280]
2	$k_{-1_{PKGI}}$	cGMP dissociation from slow high affinity site on PKG-I	1.5×10^{-5}	ms^{-1}	[280]
3	$k^*_{-2_{PKGI}}$	cGMP association with rapid low affinity site on PKG-I	3.3×10^{3}	$\mu M^{-1} ms^{-1}$	[280]
4	$k^*_{2_{PKGI}}$	cGMP dissociation from rapid low affinity site on PKG-I	2.3×10^{-4}	ms^{-1}	[280]
5	T_{PKGI}	Temperature adjustment (from 0◦C to 37◦C) for $k^*_{-2_{PKGI}}$ and $k^*_{2_{PKGI}}$	70	--	[280]
6	f_{PKGI}	Phosphorylation activity of partially-cGMP-bound PKG-I ($PKG_I{:}cGMP2$) as a fraction of fully-cGMP-bound ($PKG_I{:}cGMP4$)	0.6	--	[280]
7	$h_{1_{PKGI}}$	Hill coefficient for slow site	1.55	--	[281]

8	$h_{2_{PKGI}}$	Hill coefficient for fast site	1.7	--	[281]
9	$[PKG_I]_{tot}$	Total Concentration of PKG-I	0.03	μM	[162]

Table B.15. Parameters for cGMP activation of PKG.

B.3.5. Parameters for pharmacological reagents

	Parameter	Representation	Value	Units	Ref.
1	Ki_{IBMX_PDE1}	IC50 of IBMX inhibition of PDE1 activity	11	μM	[255]
2	Ki_{IBMX_PDE2}	IC50 of IBMX inhibition of PDE2 activity	28	μM	[255]
3	Ki_{IBMX_PDE3}	IC50 of IBMX inhibition of PDE3 activity	6	μM	[255]
4	Ki_{IBMX_PDE4}	IC50 of IBMX inhibition of PDE4 activity	30	μM	[130]
5	Ki_{IBMX_PDE5}	IC50 of IBMX inhibition of PDE5 activity	20	μM	[282]
6	Ki_{EHNA}	IC50 of EHNA inhibition of PDE2 activity	0.8	μM	[10]
7	Ki_{Cilo}	IC50 of Cilostamide inhibition of PDE3 activity	5×10^{-3}	μM	[10]
8	Ki_{Rol}	IC50 of Rolipram inhibition of PDE	0.2	μM	[256]

		activity			
9	Ki_{Sil}	IC50 of Sildenafil inhibition of PDE activity	3.5×10^{-3}	μM	[95]
10	Ki_{PKI}	Inhibitory constant of PKI to PKA	2×10^{-4}	μM	[71]

Table B.16. Inhibitory constants of pharmacological inhibitors.

	Parameter	Representation	Value	Units	Ref.
1	$[L_{tot}]$	Total concentration of ligand to β-adrenergic receptor (e.g. isoproterenol (ISO))	0..100	μM	[71]
2	$[SNAP]$	Concentration of nitric oxide donor, SNAP	0…100	μM	[63]
3	$[IBMX]$	Concentration of PDE inhibitor, IBMX	100	μM	[71, 82]
4	$[EHNA]$	Concentration of PDE2 inhibitor, EHNA	10	μM	[63]
5	$[Cilo]$	Concentration of PDE3 inhibitor, Cilostamine	1	μM	[85]
6	$[Roli]$	Concentration of PDE4 inhibitor, Rolipram	10	μM	[85]
7	$[Sil]$	Concentration of PDE5 inhibitor, Sildenafil	0.1	μM	[63]
8	$[PKI_{tot}]$	Concentration of PDE inhibitor, IBMX	0.18	μM	[71]

Table B.17. Typical concentrations of pharmacological inhibitors.

B.3.6. Constants for Unit Conversions

	Parameter	Original Unit	Converted Unit	Multiplication Factor	Ref.
1	cf_{pmolMg_uM}	$pmol/mg\ protein$	μM	0.18	[6]
2	$cf_{pmolGWetWt\_uM}$	$pmol/g\ wet\ weight$	μM	2.43×10^3	[6]
3	$cf_{pmolCell\_pmolMg}$	$pmol/100{,}000\ cells$	$pmol/mg\ protein$	0.361	[71]

Table B.18. Constants for unit conversions.

B.4. State variable initial conditions

Initial conditions for state variables reflect basal conditions, where no pharmacological drugs are applied externally or internally to the cell. The values are obtained from steady state of the model ran from a preliminary set of initial conditions. For the preliminary initial conditions, experimental values are assigned whenever possible, such as the initial values for [cAMP] and [cGMP]. When experimental measures are not readily available, all components are assumed to be in their non-activated states, and all PDE activities are assumed to be zero. When the model is run to steady state from the preliminary initial conditions to obtain current initial conditions, the states with experimental measurements remained in the experimentally recorded range. Whenever possible for states adapted from previous models, the final initial conditions are ensured to be similar to the original models [71, 129].

	State Variables	Representation	Initial Value	Units	Ref.
1	$[Donor_{NO}]$	NO donor	0	μM	--
2	$[NO]_o$	NO outside of the cell	0.0001	μM	[95, 150, 242]
3	$[NO]_i$	NO inside the cell	0.0001	μM	[95, 150, 242]
4	$[L]$	Ligand to β-AR (ISO)	0	μM	--
5	$[\beta AR]$	β-AR	0.01	μM	[71]
6	$[Gs]$	Stimulatory G-protein	3.83	μM	[71]

7	$[\beta_1 AR_{act}]$	Activated β-receptor	0.01	μM	[71]
8	$[\beta_1 AR_{S464}]$	Desensitized β -AR by β-receptor kinase	0	μM	[71]
9	$[\beta_1 AR_{S301}]$	Desensitized β-AR by PKA-I	0.0016	μM	[71]
10	$[G_{saGTPtot}]$	Total concentration of Gs with GTP bound to its α-subunit	0.024	μM	[71]
11	$[G_{saGDP}]$	Gs with GDP bound to its α-subunit	0.0006	μM	[71]
12	$[G_{sb\gamma}]$	β- and ϒ-subunits of Gs	0.0248	μM	[71]
13	$[G_{saGTP}]$	Free Gs with GTP bound to α-subunit	0.021	μM	[71]
14	$[AC]$	Adenylyl Cyclase	0.047	μM	[71]
15	(sGC)	Free sGC	0.98	--	[129]
16	$(NOsGC)$	sGC bound with 1 NO	0.028	--	[129]
17	$(NOsGC^*)$	Activated sGC with 1 NO bound	0.028	--	[129]
18	$(NOsGC^*NO)$	sGC bound with 2 NO	0	--	[129]
19	(sGC^*NO)	NO-bound inactivated sGC	0.084	--	[129]
20	(sGC^*)	NO-free inactive sGC	0.001	--	[129]
21	$vPDE1_A^*$	Rate of cAMP hydrolysis by PDE1	0	$\mu M /ms$	--
22	$vPDE1_G^*$	Rate of cGMP hydrolysis by PDE1	0	$\mu M /ms$	--

23	$vPDE2_A^*$	Rate of cAMP hydrolysis by PDE2	0	$\mu M /ms$	--
24	$vPDE2_A^*$	Rate of cGMP hydrolysis by PDE2	0	$\mu M /ms$	--
25	$vPDE3_A^*$	Rate of cAMP hydrolysis by PDE3	0	$\mu M /ms$	--
26	$vPDE3_G^*$	Rate of cGMP hydrolysis by PDE3	0	$\mu M /ms$	--
27	$(pPDE4)$	PKA-phosphorylated PDE4	0.11	--	--
28	$vPDE4_A^*$	Rate of cAMP hydrolysis by PDE4	0	$\mu M /ms$	--
29	$(PDE5)$	Free PDE5	0.96	--	--
30	$(cGMP{:}PDE5)$	cGMP-bound PDE5	0.002	--	[129]
31	$(tPDE5^*)$	Stimulated cGMP-bound PDE5	0.003	--	[129]
32	$(pPDE5^*)$	PKG phosphorylated PDE5 (active)	0.027	--	[129]
33	$vPDE5_G^*$	Rate of cGMP hydrolysis by PDE5	0	$\mu M /ms$	[129]
34	$[cAMP_{tot}]$	Total cAMP	0.50	μM	[71]
35	$[cAMP]$	Free cAMP	0.16	μM	[71]
36	$[cGMP_{tot}]$	Total cGMP	0.017	μM	[71]
37	$[cGMP]$	Free cGMP	0.01	μM	[128]
38	$[PKAC_I]$	Dissociated active fragment of	0.086	μM	[71]

		PKA-I			
39	$[PKAC_{II}]$	Dissociated active fragment of PKA-II	0.025	μM	[71]
40	$(PKG_I{:}\,cGMP2)$	PKG-I bound with 2 cGMP	0.10	--	--
41	$(PKG_I{:}\,cGMP4)$	PKG-I bound with 4 cGMP (active)	0.006	--	--
42	(PKG_I)	Free PKG-I	0.89	--	--
43	$(PKG_{I_{activity}})$	PKG-I activity	0.063	--	--

Table B.19. Initial conditions of state variables.

B.5. Formulation of new model components

B.5.1. Model formulation for PDE5

As shown in Fig.B.1, our PDE5 model is adapted from that of Batchelor et al. [129]. Same as the original model, PDE5 are modeled as dimers of two identical subunits [61, 65, 71, 79, 80]. For simplicity, model schematics (Fig.B.1) represent one monomer subunit of PDE5. Binding of cGMP to the PDE5 GAF-A regulatory domain allosterically activates the enzyme [129]. The PKG-phosphorylated PDE5 has increased catalytic rate and increased cGMP-affinity when compared to the non-phosphorylated active species [128, 130-134]. In the original model, the forward transition rate between the phosphorylated and non-phosphorylated species (k_{3_5}) represented the PKG-mediated

phosphorylation of PDE5 (Fig.B.1); however, PKG is not explicitly included in the transition rate [129]. Here, we incorporated cGMP-activated PKG to the forward transition rate between the phosphorylated and non-phosphorylated species (Fig.B.1). The PDE5 parameters are tabulated in Table B.16.

Fig.B.1. State diagram of PDE5 activation.

PDE5 monomer subunits are shown with conserved catalytic domains (ovals, denoted by "C") and varying regulatory domains (varied shaped, denoted by "R"). Active site within the catalytic domain that bind cGMP is represented by semi-circular sockets; GAF-A regulatory domain is shown by open rectangular sockets. cGMP is shown by blue circles. As shown, PDE5 is allosterically activated by cGMP binding to its regulatory domain. The PKG phosphorylated form has increased catalytic rate and increased cGMP-affinity compared to the non-phosphorylated active species. PDE5 model is adapted from that of Batchelor et al. [129]. For clarity, the subscript "PDE5" in parameter names is omitted from the schematic, instead only "5" is shown.

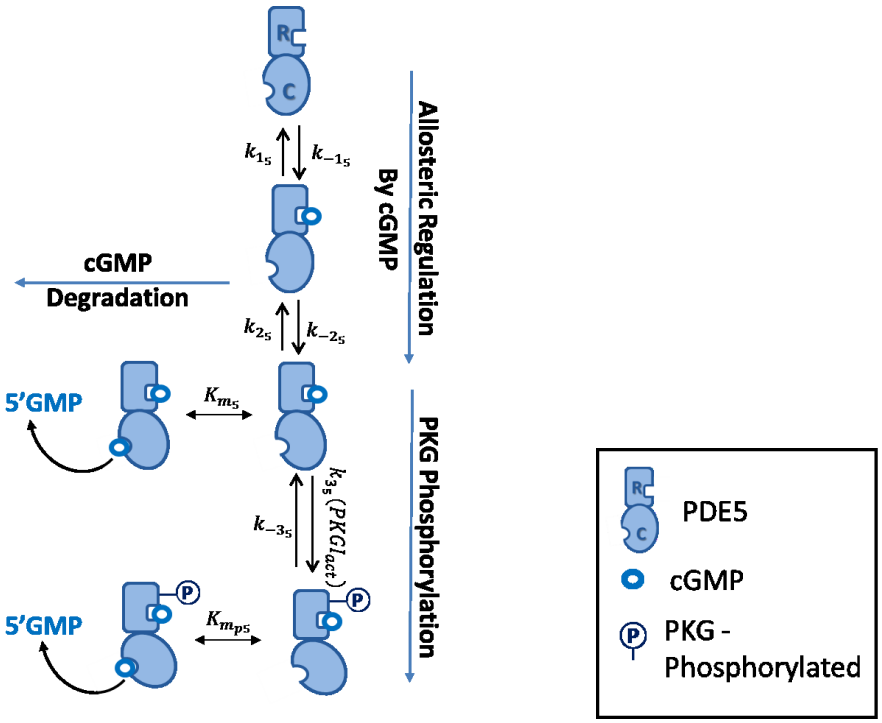

B.5.2. Model formulation for PKG.

Fig.B.2 shows the model schematic for cGMP-dependent activation of PKG-I, the isoform expressed in cardiac myocyte [283]. PKG-I are homodimers, with two identical subunits [284]. Experiments support the modeled two-step activation process (Fig.B.2), that cGMP tend to bind to the high affinity sites (top two semi-circles) first before occupying the low affinity sites (bottom two semi-circles) [281]. In addition, for both the low and high affinity allosteric sites, full occupancy by two cGMP induces the conformation change required for PKG-I activation [281]. Upon binding of two cGMP each to the high and low affinity binding pockets of its N-terminal regulatory domain, the phosphotransferase activity of PKG-I increases (Fig.B.2) due to release of inhibition of the catalytic center by the N-terminal auto-inhibitory domain [66]. Partially bound PKG-I

($PKG_I: 2cG$) is 50-70% active, whereas fully bound PKG ($PKG_I: 4cG$) is fully active [284]. The PDE5 parameters are tabulated in Table B.18.

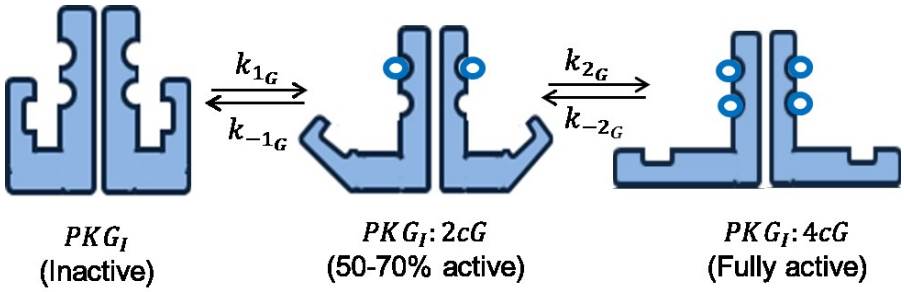

Fig.B.2. State diagram of PKG-I activation by cGMP.

Model schematic for the two-step activation process of PKG-I by cGMP. PKG-I are homodimers, with two identical subunits. The four allosteric sites are shown using semi-circular circles, with the two high affinity and two low affinity sites shown on top and bottom respectively. The catalytic sites are shown using rectangular sockets. cGMP is denoted by blue circles. PKG-I is activated by cGMP binding to its allosteric domains, which induces conformational changes that exposes the catalytic domain (rectangular sockets). For clarity, the subscript "PKG" in parameter names is omitted from the schematic, instead only "G" is shown.

B.5.3. Modeling NO delivery

A minimal model for the delivery and regulation of NO is developed. The NO balance equation (Equation 13) is adapted from previous models by Schmidt et al. [139], Ramamurthi et al. [140], and Kar and Kavdia [141], in which NO decay follows second order kinetics with respect to NO and first order with respect to O_2 [139, 140] and superoxide ($O_2^{\cdot-}$) [141]. The NO release kinetic from the decomposition of donor SNAP

is modeled according to existing literature [135-138]. Diffusion of NO from cell exterior, across the cell membrane, into the intra-cellular compartment is governed by Fick's Law. For simplification, linear [NO] gradient across cell boundary is assumed, justified by the thinness of sarcolemma [277]. In addition, cardiac myocytes are approximated to be rectangular in shape, with dimensions consistent with available measurements [6]. In addition, NO flux (V_{NOS}) endogenous to the cardiac myocyte contributes to NO accumulation, as Nitric Oxide Synthase (NOS) catalyzes the production of NO from L-arginine [285]. The specific value of V_{NOS} is chosen so that basal [cGMP] is ~ 10nM according to Götz et al. [100] and endogenous [NO] is within the lower range of that identified by literature for biological tissues [95, 150, 242]. Typically, NO donor is perfused through a capillary tube with the cardiac myocyte being placed at the mouth of the tube. In these cases, donor concentration is assumed to be constant as the donor is continuously supplemented despite its continuous natural decay.

B.5.4. Modeling the effects of PDE inhibitors

A minimal model of inhibitor-PDE interaction is constructed (Sect. B.2.4), using similar approaches to that in Batchelor et al. [129]. The effect of an inhibitor is modeled to directly attenuate the hydrolytic rate of PDEs with IC50 reported by experiments (Table B.19). This reflects the output of typical biochemical experiments characterizing the inhibitor: the decrease of PDE activity by applying various concentration of the inhibitor as a fraction of its activity without the inhibitor (e.g. [10]). We assume, for a given inhibitor, the PDE-bound inhibitor does not effectively change the total concentration of free inhibitor yet to interact with the PDE. This assumption is justified by the fact that the typical concentration of applied pharmacological PDE inhibitors (Table B.20) far exceeds

that of their targets [71]. Immediate unset and termination is assumed for all drug applications, such that the time course of application resembles a square wave. In addition, perfect drug specificity is assumed for each specific inhibitor. Effects of all inhibitors to their targets are assumed to be instantaneous, so that the observed temporal dynamics are solely due to that of signaling components intrinsic to the cell.

B.6. Model constraints and additional validations

Each PDE model is optimized individually to in vitro data obtained from purified PDEs (Fig.B.3 and conditions specified in Sect. B.6.1). For a given PDE isoenzyme model, all constraints for that PDE are used simultaneously (i.e. included in the same cost function), together with the ranges for parameters imposed by experiments whenever available (Sect. B.3.3 Tables). Similarly for the PKG and NO liberation models, all constraints are used simultaneously for each model, together with the ranges for parameters imposed by experiments (Sect. B.3.3 Tables). Subsequently, the relative proportions of the PDEs were fit to data shown in Fig.B.2. Each optimization minimizes the value of a cost function that captures the distance between the data points and the corresponding simulation results through the least-squares best fit method. All data points used for developing the new model components in this paper are weighed equally in the optimization. All optimizations are performed in MATLAB (MathWorks Inc.) using the function, fmincon, utilizing the interior-point optimization algorithm.

B.6.1. Constraints for PDE models

The parameters for the PDE models are constrained by the data shown in Fig.B.3. In addition, they are constrained to ranges identified by experiments whenever available (referenced in Sect. B.3.3). The constraint data in Fig.B.3A–C (dotted symbols) used to obtain the validation relationships shown in manuscript Fig. 3.2A–D were from the same studies but at different concentrations. All plots in Fig. 3.3 are presented in a way that preserves their original appearance in the source literature.

To constrain parameters for PDEs 1, 3, and 4, Eqs. 21-22, 25-26, and 27-28 are fitted to data shown in Fig.B.3A-B, D, and E respectively, together with the ranges of parameter values imposed by experiments (referenced in Sect. B.3.3). The modified PDE5 model (Eqs. 29-33) of Batchelor et al. [129] is constrained by PDE5 activation data from Corbin et al. [132] to pin-point exact parameter values within the ranges identified by experimental data (referenced in Sect. B.3.3).

For the PDE2 model, the following constraints are imposed simultaneously to fit Eqs. 23 and 24, in addition to that shown in Fig.B.3C. The parameters are defined in Table B.10.

1. Parameters $K_{a_{PDE2}}$ and $K_{b_{PDE2}}$ are constrained to the ranges identified by [240, 241] and parameters $K_{s_{PDE2}}$ and $K_{I_{PDE2}}$ to those identified by [31].
2. The scaling factors, ρ_{PDE2}, ω_{PDE2}, ϵ_{PDE2}, and η_{PDE2}, are constrained to the ranges of (0, 1), because cN binding to GAF-B regulatory domain increases cN binding affinity to catalytic domain (i.e. decreases dissociation constant). In other words, cN allosteric regulation produces positive cooperativity [30, 241].

3. cAMP-mediated scaling factors (ρ_{PDE2} and ϵ_{PDE2}) are required to take on values that are greater than their corresponding cGMP-mediated scaling factors (ω_{PDE2} and η_{PDE2}) as experiments show less sensitivity of PDE2 to cAMP allosteric regulation [95].
4. The apparent EC50 concentration for cAMP (measured in the absence of cGMP), is constrained to be greater than that for cGMP (measured in the absence of cAMP) [95].
5. The maximal cAMP hydrolysis under cGMP regulation is constrained to occur at [cGMP] above 2 μM [93, 241].
6. Microscopic reversibility is satisfied for each closed loop of the PDE2 model (Fig. 2.2B of Zhao et al. [127]).

Fig.B.3. Constraints for PDE models.

Dotted symbols are experimental data (obtained from purified PDEs); lines are from simulations. ***(A)*** PDE1 cAMP hydrolysis rate (normalized to the maximum rate achieved) is constrained to normalized data from Yan et al. [87] under 3.125 μM [cGMP]. ***(B)*** Normalized PDE1 cGMP hydrolysis rate is constrained to normalized data from Yan et al. [87] under 3.125 μM [cAMP]. ***(C)*** Effects of various [cAMP] on PDE2 cGMP hydrolysis rates, with 0.2 μM [cGMP], is constrained by data from Russell et al. [142]. Rates are normalized by the cGMP rates at 0.2 μM [cGMP] measured without cAMP. ***(D)*** The PDE3 model is constrained to normalized data from Movsesian et al. [238]. The dashed line is fit to rates measured without cGMP (hollow dots), and solid line to rates measured with 0.05 μM [cGMP] (filled dots). ***(E)*** PDE4 model is constrained to normalized data from Wang et al. [239]. ***(F)*** Simulation from the PDE5 model (line) versus PDE5 activity data (dots) from Corbin et al. [132].

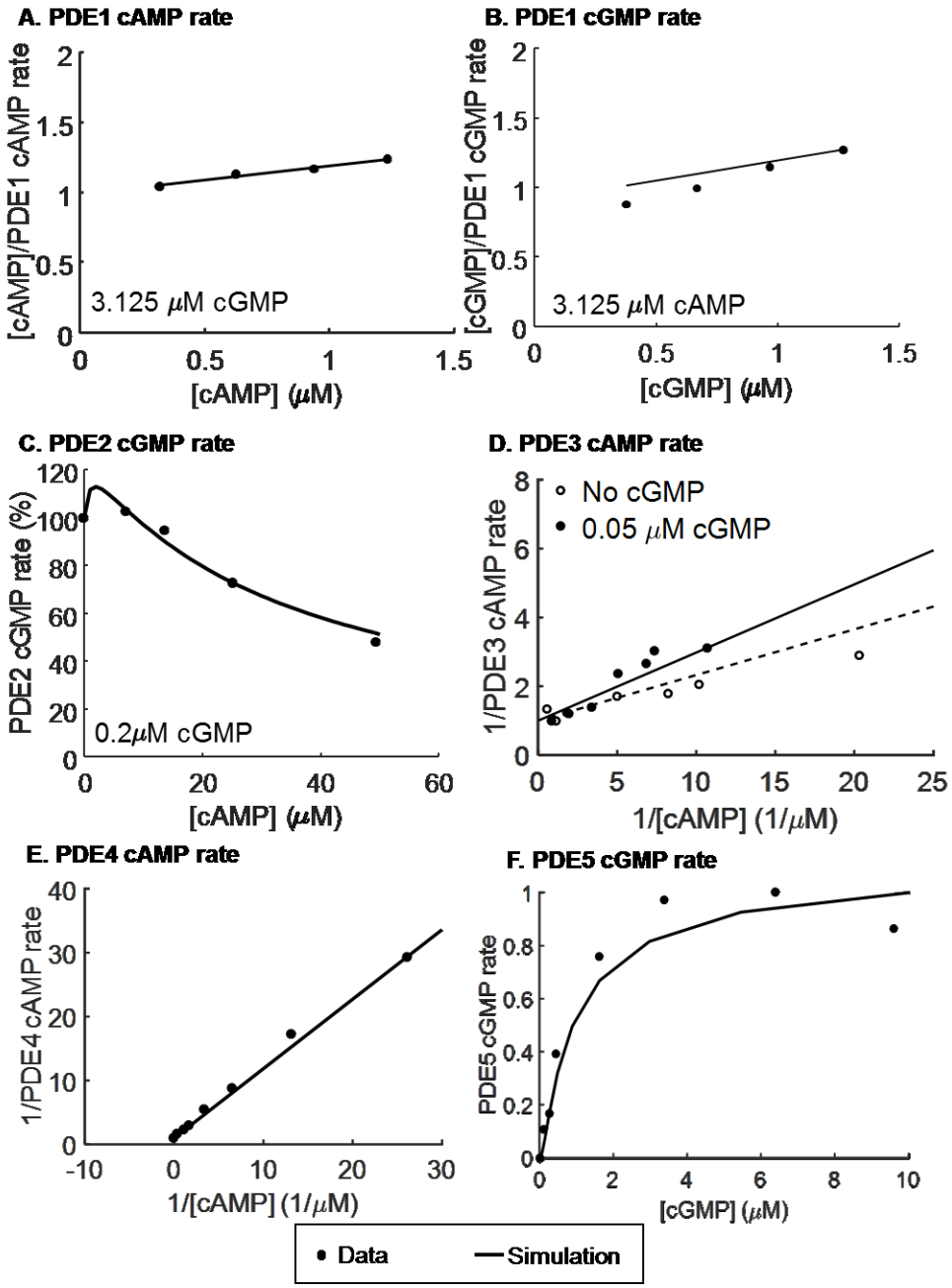

B.6.2. Model constraints for PDE activities.

Data from Adult Rat Ventricular Myocytes (ARVMs) obtained by Verde et al. [86] and Rochais et al. [85] are shown in gray and black respectively in Fig.B.4A. The lower two,

closely-matching data sets from Verde et al. [86] and the data averages from Rochais et al. [85] are used to constrain the rates of cAMP hydrolysis by PDEs 1 – 4, namely parameters $Vmax_{PDE1_A}$, $Vmax_{PDE2_A}$, $Vmax_{PDE3_A}$, and $Vmax_{PDE4_A}$. In addition, the constraint that the hydrolysis rate of PKA-phosphorylated PDE4 ($Vmax_{pPDE4_A}$) is 1.4 times that of non-phosphorylated PDE4 [130, 245] is applied simultaneously.

As shown in Fig.B.4B, cGMP hydrolysis rates (parameters $Vmax_{PDE1_G}$, $Vmax_{PDE2_G}$, $Vmax_{PDE3_G}$, and $Vmax_{PDE5_G}$) of PDEs 1, 2, 3, and 5 are constrained by [cGMP] measured upon applications of inhibitors of all PDEs, PDE2, PDE5 (IBMX, EHNA, Sil respectively) from Castro et al. [82]. In addition, the constraint that the hydrolysis rate of PKG-phosphorylated PDE5 ($Vmax_{pPDE5_G}$) is 1.65 times that of non-phosphorylated PDE5 [132, 133, 279, 286] is applied simultaneously.

Fig.B.4. Constraints for maximal PDE degradation rates.

(A) Data used for constraining cAMP hydrolysis rates ($Vmax$'s) of PDEs 1 – 4 are shown, with the specific PDE inhibited indicated on the abscissa. Percent increase in [cAMP] against total cAMP hydrolyzed (as measured by the non-specific PDE inhibitor, IBMX) upon PDE2, PDE3, and PDE4 inhibition (with inhibitors EHNA, Cilo, and Rol respectively) are shown from Verde et al. [86] (gray) and Rochais et al. [85] (black). Simulation results are show in blue. Data from Verde et al. [86] are displayed in accordance with the original figure, with averages indicated by bar graph. The lower two, closely-matching data sets from Verde et al. [86] and the data averages from Rochais et al. [85] are used to constrain the rates of cAMP hydrolysis by PDEs 1 – 4 to avoid biasing the model. All data are obtained from ARVMs under basal condition (i.e. without

ISO). ***(B)*** Constraints for relative proportion of cGMP hydrolysis rates ($Vmax$'s) of PDEs 1 – 5 respectively. Model results (gray bars) versus [cGMP] measured by Castro et al. [82] (dots) when the activities of all PDEs, PDE2, PDE5, and PDEs 2 and 5 are inhibited by applications of respectively IBMX, EHNA, Sil, and simultaneous EHNA and Sil). Data are obtained under stimulation by 100 μM NO donor, SNAP in ARVM cardiac myocytes.

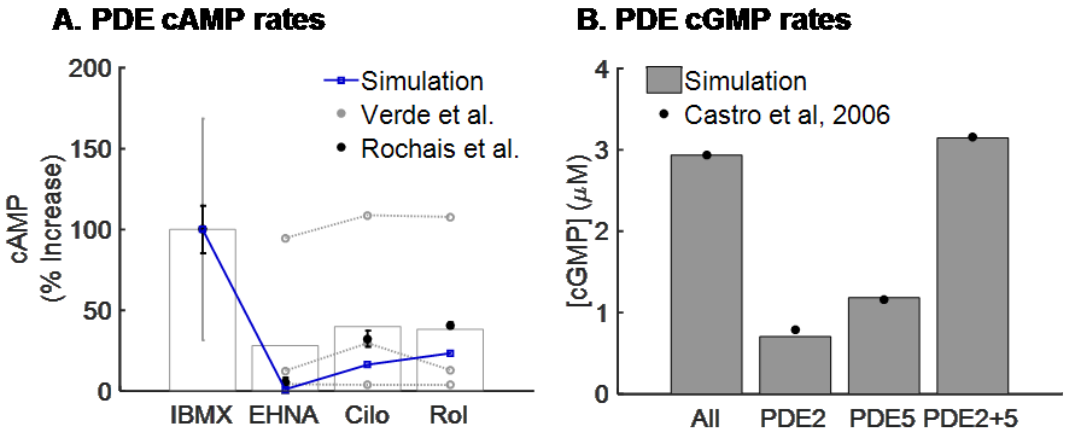

B.6.3. Additional model constraints

As shown in Fig.B.5, activation of PKG-I activity by cGMP (Eqs. 40–43) is constrained by data of Corbin et al. [280] to pin-point the exact values of parameters from the ranges identified by experiments (referenced in Sect. B.3.4). In addition, the EC50 is consistent with reported experimental averages [95, 284].

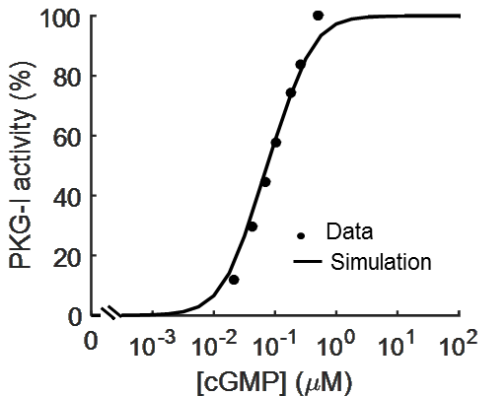

Fig.B.5. Constraint for PKG model.

Simulated PKG activity (line) as a function of [cGMP] versus normalized data of Corbin et al. [280] (dots) obtained from purified PKG.

In order to pin-point exact parameter values from the ranges identified by experiments (referenced in Sect. B.3.2), [NO] reached by perfusion of NO donor (SNAP) (Eqs. 12–14) is constrained to data measured by Vila-Petroff [143] (Fig.B.6).

Fig.B.6. Constraint for Model for NO release from SNAP.

Simulated [NO] accumulation from various [SNAP] (NO donor) after 20 minutes of perfusion (line) versus data of Villa-Petroff et al. [143] (dots), which obtained from physiological solution containing cardiac myocytes.

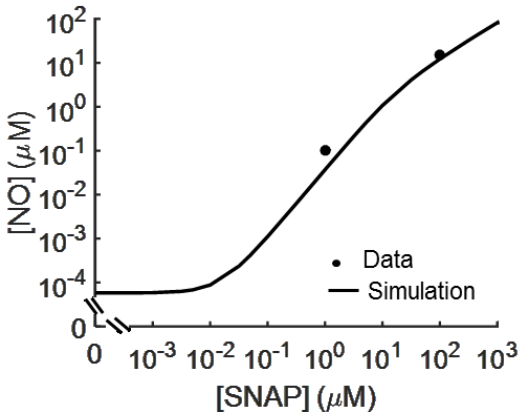

B.6.4. Additional Model Validations

We define "model validations" as predictions made using the model that agree with experimental data not included in the fitting process.

When only one cN is present in the reaction system, the model-produced PDE2 EC50s (half activation points) for cAMP and cGMP hydrolysis also agree with experimental averages [29, 91-95, 107]. In addition, the sigmoidal shapes of the hydrolysis curves agree with experiments [91-93].

Fig.B.7. Experimental validation of PDE2 model.

Experimental data predicted by the model. EC50 concentrations of cAMP (black color scheme) and cGMP hydrolysis (gray color scheme) by PDE2 versus experimental averages [29, 91-95, 107].

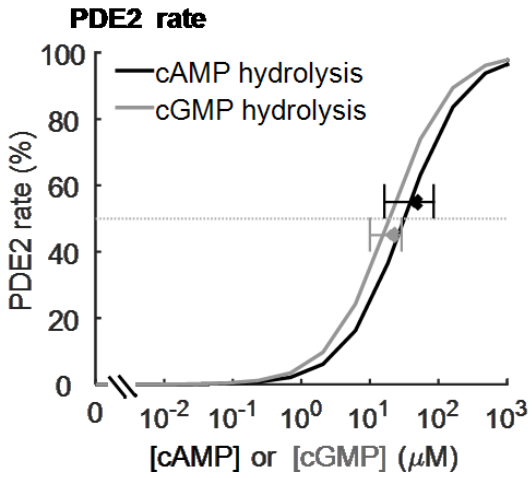

We define "model validations" as predictions made using the model that agree with experimental data not included in the fitting process.

Fig.B.8 below provides additional validation of the contribution of isoform-specific PDEs in regulating [cAMP] upon activation of β1-AR (i.e. β2-AR stimulation is inhibited by ICI [85]). Model closely replicates [cAMP] time course measured under PDE3 inhibitor (Cilo), PDE4 inhibitor (Rol), and non-specific PDE inhibitor (IBMX), under ISO stimulation, as measured by Rochais et al. [85] from ARVMs.

Fig.B.8. Experimental validation of cAMP dynamics.

Experimental data predicted by the model. Simulated [cAMP] time course measured under PDE3 inhibitor (Cilo, 1 μM), PDE4 inhibitor (Rol, 10 μM), and non-specific PDE inhibitor (IBMX, 100 μM), under 5 μM [ISO] stimulation (black line) is compared to that measured by Rochais et al. [85] in ARVMs (gray dots). β2-AR antagonist (ICI, 1 μM) was also applied in the experiment by Rochais et al. [85], but not simulated by the model.

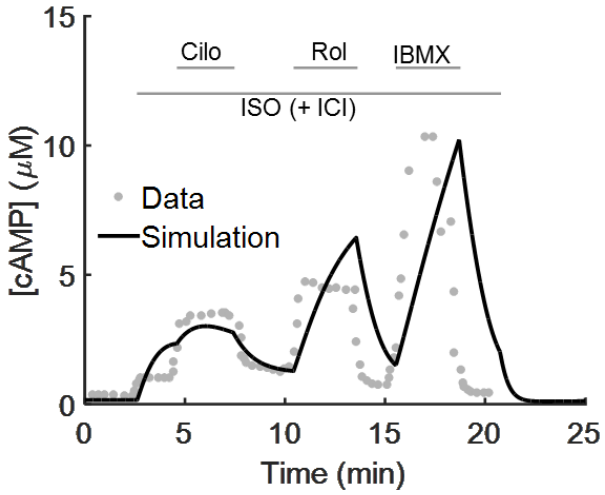

Potential causes of the slight discrepancy between data and simulation may be the following:

1) We assumed instantaneous application and termination of drug application (i.e. a square wave of drug concentration against time), which may not fully represent the influx and efflux of drugs in this complex experimental setup.

2) We employed a very simplistic model of PDE inhibition by specific PDE inhibitors (Sect. B.3.3), with the assumption that the inhibitors will instantaneously ablate target activity.

3) The data include inhibition of β2-AR from simultaneous application of ICI with ISO, which is not included in the model. However, it may serve as a good estimate of whole-cell cAMP dynamics.

4) We assumed a very simplistic approach to estimate [cAMP] from CNGC signals, using the calibration curve of the probe (C460W/E583M) against [cAMP] from Rich et al. [246] as referenced in Rochais et al. [85].

B.7. Additional result figures

B.7.1. Cross-talk responses

Fig.B.9. Characterization of cross-talk responses.

(A)–(C) Percent increase in [cAMP], PKA-I and PKA-II activation in response to low, medium, and high levels of SNAP perfusion (5 nM, 50nM, and 500 nM [SNAP]) for 30 minutes relative to those without SNAP but with the same [ISO]. ***(D)*** and ***(E)*** Percent increases in [cGMP] and PKG activation in response to increasing [ISO] relative to those measured without ISO but with the same [SNAP].

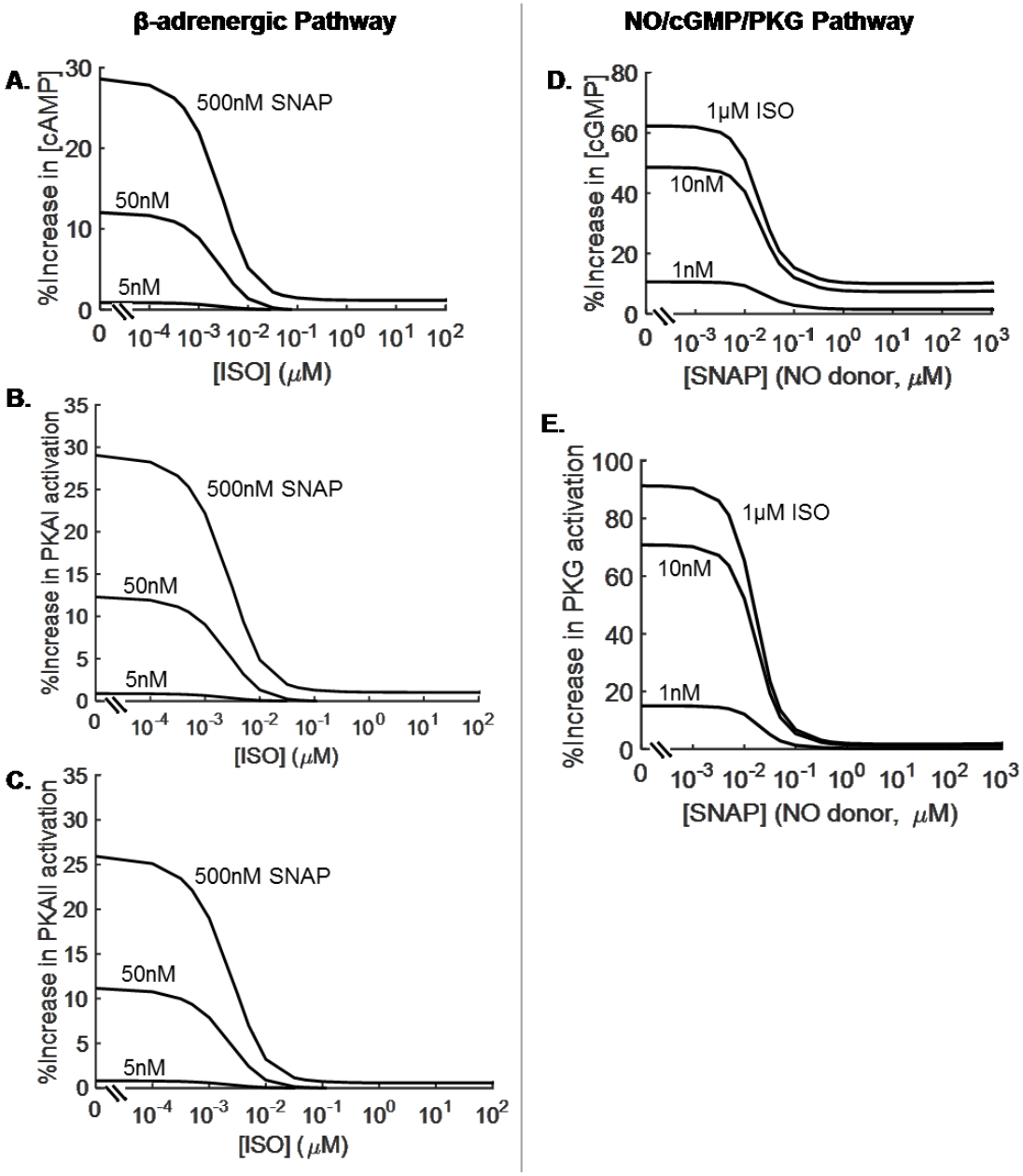
β-adrenergic Pathway
NO/cGMP/PKG Pathway
A.
%Increase in [cAMP]
500nM SNAP
50nM
5nM
[ISO] (μM)
B.
%Increase in PKAI activation
500nM SNAP
50nM
5nM
[ISO] (μM)
C.
%Increase in PKAII activation
500nM SNAP
50nM
5nM
[ISO] (μM)
D.
%Increase in [cGMP]
1μM ISO
10nM
1nM
[SNAP] (NO donor, μM)
E.
%Increase in PKG activation
1μM ISO
10nM
1nM
[SNAP] (NO donor, μM)

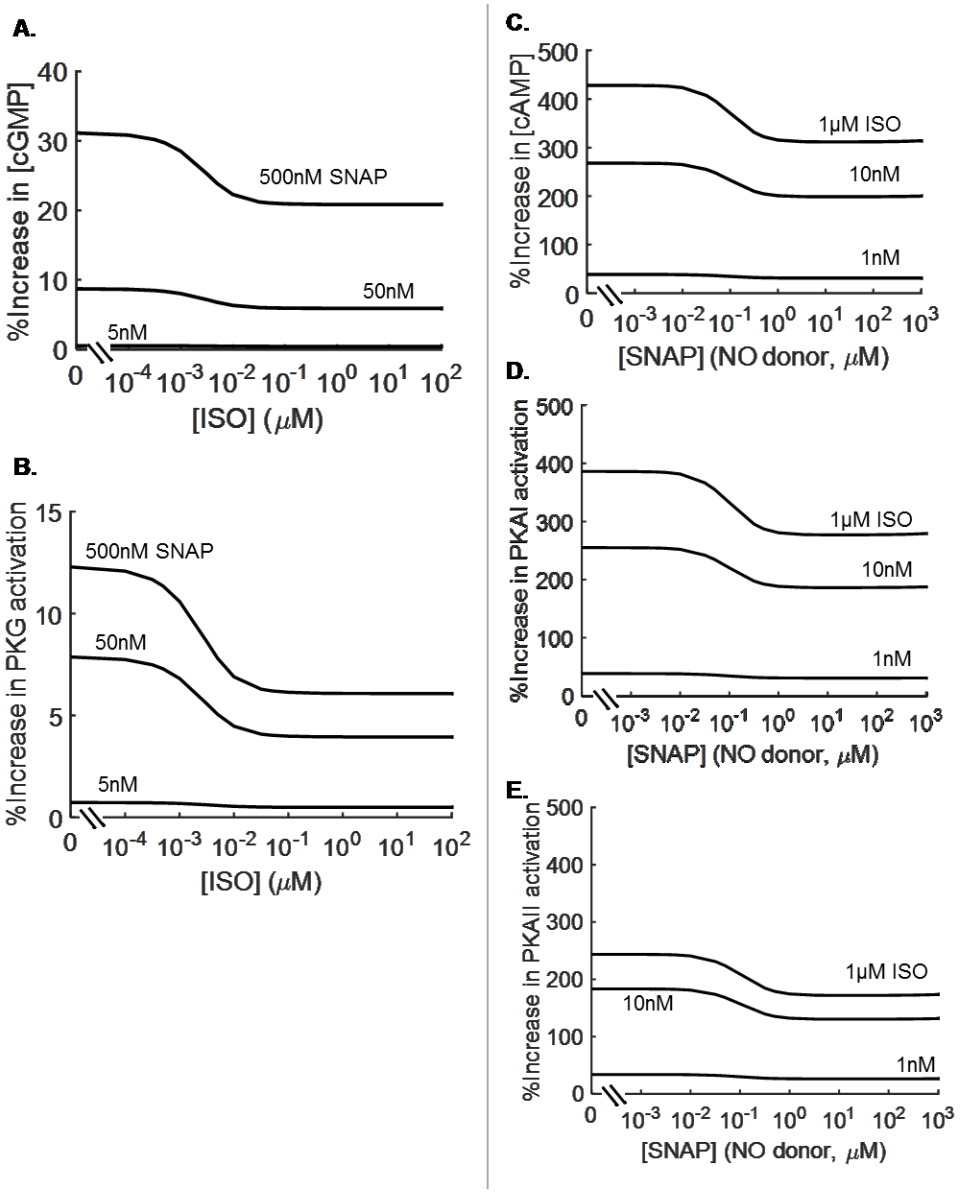

Fig.B.10. Characterization of cross-talk responses.

(A) and ***(B)*** Percent increase in [cGMP] and PKG activation in response to low, medium, and high levels of SNAP perfusion (5 nM, 50nM, and 500 nM [SNAP]) for 30 minutes relative to those without SNAP but with the same [ISO]. ***(C)*** – ***(E)*** Percent increases in [cAMP], PKA-I, and PKA-II activation in response to increasing [ISO] relative to those measured without ISO but with the same [SNAP].

B.7.2. PDE2-PDE5 coupling

Fig.B.11. NO/cGMP/PKG pathway responses under PDE2 inhibition.

All simulation data shown are percent increases upon PDE2 inhibition relative to their respective values prior to inhibition under the same [SNAP] (50 nM) without ISO stimulation. Varying degrees of PDE2 inhibition (20%, 50%, and 90%) is simulated with simultaneous SNAP application under the indicated [ISO] for 30 min. ***(A)*** Percent increases in cGMP hydrolysis rates of PDEs 1 – 3 and 5 upon 90% PDE2 inhibition are shown in black, red, blue, and cyan respectively. ***(B) – (D)*** respectively, percent increase in PDE5 cGMP rates, [cGMP], and PKG activation upon 20%, 50%, and 90% PDE2 inhibition.

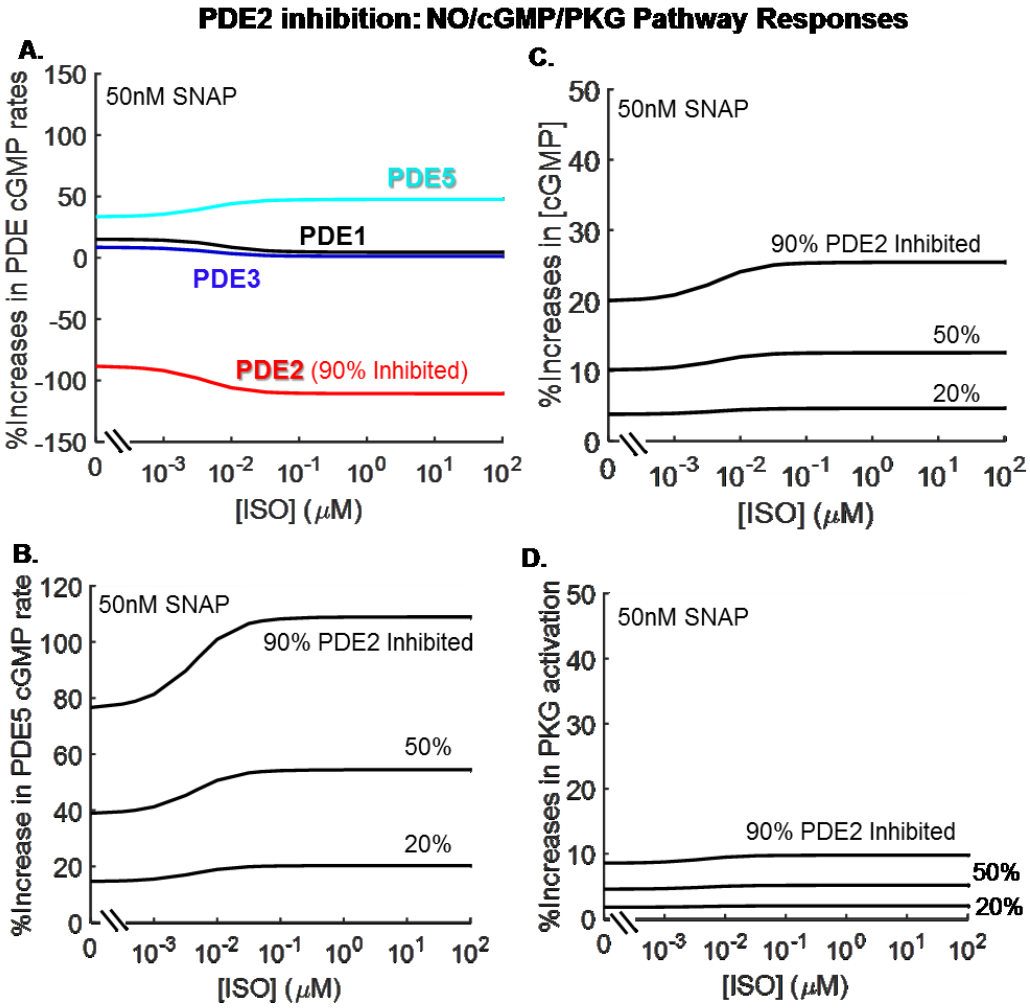
PDE2 inhibition: NO/cGMP/PKG Pathway Responses
A.
%Increases in PDE cGMP rates
50nM SNAP
PDE5
PDE1
PDE3
PDE2 (90% Inhibited)
[ISO] (μM)
C.
%Increases in [cGMP]
50nM SNAP
90% PDE2 Inhibited
50%
20%
[ISO] (μM)
B.
%Increase in PDE5 cGMP rate
50nM SNAP
90% PDE2 Inhibited
50%
20%
[ISO] (μM)
D.
%Increases in PKG activation
50nM SNAP
90% PDE2 Inhibited
50%
20%
[ISO] (μM)

B.7.3. PDE state occupancy

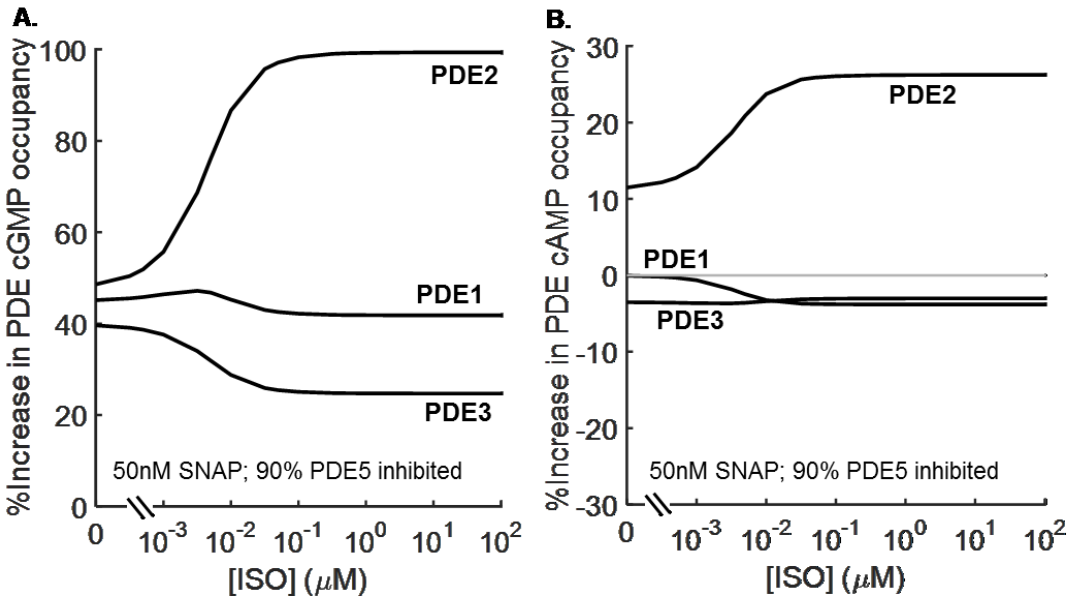

Fig.B.12. PDE state occupancy under PDE5 inhibtion.

All simulation data shown are percent increases upon PDE5 inhibition (90%) relative to their respective values prior to inhibition under the same [SNAP] (50 nM) without ISO stimulation. ***(A)*** Percent increase in catalytic domains occupied by cGMP for PDEs 1 – 3 upon 90% PDE5 inhibition. ***(B)*** Percent increase in catalytic domains occupied by cAMP for PDEs 1 – 3 upon 90% PDE5 inhibition. The horizontal gray line indicates places with no increase, thus dividing increase from decreases in occupancy.

B.8. Model conditions

B.8.1. Conditions for figure generation

All figures are generated using the same set of equations, parameters, and initial conditions as specified by the above sections.

B.8.2. Presentation of cGMP-related data

- For Fig. 3.3C – D, recording of [cGMP] by CNGC probes [82, 128] were converted to actual concentrations by interpolating against calibration curve of the specific probes used [246], as referenced by the original literature [82, 128]. Linear interpolations of recorded signals in cardiac myocytes were performed against the original calibration data of the cGMP probe reported in Rich et al. [246].
- [NO] are calculated with various [SNAP] using the current model, which is validated by Fig.B.6.
- NO donor, SNAP, is used for all experiments [82, 128, 143] used for model validation. This is because of the relatively simple release kinetics of SNAP compared to other NO donors and the availability of experimental data in cardiac myocytes.
- The slight discrepancies between simulation and experimental data in Fig. 3.3C are likely the result of simplifying assumptions above and in modeling drug application and actions, detailed in Sect. B.5.4.

B.9. Species and temperature information

B.9.1. Species

The majority of the data used in parameterization of our model is from rat ventricular myocytes. If not available, we used data from hear tissues of other species whenever possible. Species information for figures is tabulated in Table B.20. Additional species information can be found in our baseline models Zhao et al. [127] and Saucerman et al. [71].

B.9.2. Temperature

The temperatures at which data shown in figures were collected are listed in Table B.20 below. Some of the experiments cited in this paper were performed at 30◦C and others at room temperature (~25◦C). No model equation has explicit temperature dependence.

	Figure	Species	Assay Temp. (◦C)	Ref.
	Manuscript			
1	Fig. 3.2A PDE1 cAMP rate	Mouse PDE1 clones	Pre-warmed	[87]
2	Fig. 3.2B PDE1 cGMP rate	Mouse PDE1 clones	Pre-warmed	[87]
3	Fig. 3.2C PDE2 cAMP rate	Rat ventricular myocytes	--	[88]
4	Fig. 3.2D PDE2 cAMP rate	Rat heart	--	[142]

5	Fig. 3.2E PDE3 cAMP rate	Human heart PDE3 clones	30	[96]
6	Fig. 3.2F PDE3 cAMP rate	Human heart PDE3 clones	30	[96]
7	Fig. 3.3A [ISO] vs. [cAMP]	Rat ventricular myocytes	25	[97, 98]
8	Fig. 3.3B cAMP dynamics	Rat ventricular myocytes	25	[99, 143]
9	Fig. 3.3C [cGMP] dose-response	Rat ventricular myocytes	Room	[82, 128]
10	Fig. 3.3D [cGMP] dynamics	Rat ventricular myocytes	Room	[82]
11	Fig. 3.3E [cGMP] dynamics under specific PDE inhibitors	Rat ventricular myocytes	Room	[82]
	Supplement			
12	Fig.B.3A PDE1 cAMP rate constraint	Mouse PDE1 clones	Pre-warmed	[87]
13	Fig.B.3B PDE1 cGMP rate constraint	Mouse PDE1 clones	Pre-warmed	[87]
14	Fig.B.3C PDE2 constraint	Rat heart	--	[142]
15	Fig.B.3D PDE3 constraint	Human ventricular tissue	30	[238]
16	Fig.B.3E PDE4 constraint	Human PDE4	23	[239]

		clones		
17	Fig.B.3F PDE5 constraint	Rat lung	30	[132]
18	Fig.B.4A PDE cAMP constraint	Rat ventricular myocytes	Room	[85, 86]
19	Fig.B.4B PDE cGMP constraint	Rat ventricular myocytes	Room	[82]
20	Fig.B.5 PKG constraint	Bovine lung	30	[280]
21	Fig.B.6 SNAP constraint	Physiological solution containing rat ventricular myocytes	25	[143]
22	Fig.B.8 cAMP dynamics validation	Rat ventricular myocytes	Room	[85]

Table B.20. Species and temperature information for relevant figures.

Appendix C. Supplementary Material for the cN Signaling–LCC Model

C.1. Symbols definition

C.1.1. Definition of symbols for signaling network components

	Symbol	Representation
		Pathway cross-talk
1	cN	Cyclic Nucleotide, either cAMP or cGMP (second messenger)
2	cNs	Cyclic Nucleotides, both cAMP and cGMP (second messengers)
3	5′-AMP	Adenosine 5′-Monophosphate. Hydrolyzed cAMP, after breakage of the 3′- cyclic phosphate bond of cAMP
4	5′-GMP	Guanosine 5′-Monophosphate. Hydrolyzed cGMP, after breakage of the 3′- cyclic phosphate bond of cGMP
5	PDE	Phosphodiesterase, enzyme that catalyzes the breakage of phosphodiester bond
6	PDEs	Phosphodiesterases/ Phosphodiesterase Isoenzymes. Multiple gene families of Phosphodiesterases
7	PDE1	Phosphodiesterase gene family 1
8	PDE2	Phosphodiesterase gene family 2
9	PDE3	Phosphodiesterase gene family 3
10	PDE4	Phosphodiesterase gene family 4

11	PDE5	Phosphodiesterase gene family 5
		β-adrenergic pathway
12	β-AR	β-Adrenergic Receptor
13	βARK	β-Adrenergic Receptor Kinase
14	Gs	Stimulatory G-protein
15	AC	Adenylyl Cyclase
16	ATP	Adenosine Triphosphate
17	ADP	Adenosine Diphosphate
18	cAMP	Cyclic Adenosine-3′,5′ Monophosphate (second messenger)
19	PKA	Protein Kinase A (cAMP-dependent protein kinase)
20	PKA-I	PKA, Type I
21	RI	Regulatory subunit of PKA-I
22	PKACI	Catalytic subunit of PKA-I
23	PKA-II	PKA, Type II
24	RII	Regulatory subunit of PKA-II
25	PKACII	Catalytic subunit of PKA-II
		NO/cGMP/PKG pathway
26	NO	Nitric Oxide
27	NOS	Nitric Oxide Synthase
28	sGC	Soluble Guanylate Cyclase
29	GTP	Guanosine Triphosphate
30	GDP	Guanosine Diphosphate
31	cGMP	Cyclic Guanosine-3′, 5′-Monophosphate (second messenger)

32	PKG-I	Protein Kinase G (cGMP-dependent protein kinase), Type I

Table C.1. Definition of symbols for signaling network components.

C.1.2. Definition of symbols for kinase phosphorylation of L-Type calcium channel

	Symbol	Representation
1	LCC	L-type Ca^{2+} channel
2	VDI	Voltage Dependent Inactivation
3	CDI	Ca^{2+} Dependent Inactivating
4	PP1	Protein Phosphatase 1
5	PP2A	Protein Phosphatase 2A

Table C.2. Definition of symbols associated with L-type Ca^{2+} channel gating.

C.1.3. Definition of symbols for pharmacological drugs

	Symbol	Full Name	Effects
1	ISO	Isoproterenol	β-AR agonist
2	NE	Norepinephrine	β-AR agonist. Neurotransmitter
3	SNAP	(±)-S-Nitroso-N-acetylpenicillamine	NO donor
4	IBMX	3-isobutyl-1-methylxanthine	Non-specific PDE inhibitor
5	EHNA	Erythro-9-(2-Hydroxy-3-Nonyl) Adenine	PDE2 inhibitor
6	Cilo	Cilostamide	PDE3 inhibitor

7	Rol	Rolipram	PDE4 inhibitor
8	Sil	Sildenafil	PDE5 inhibitor

Table C.3. List of pharmacological drugs.

C.2. Equations

The cN cross-talk signaling network model of Zhao et al. [175] is functionally integrated to a LCC model of Greenstein & Winslow [176], originally developed by Jafri et. al. [181]. Centered upon cN signal dynamics, the signaling network model [127] is composed of 5 modules: ***A)*** portions of the β-adrenergic pathway governing cAMP synthesis, from ligand binding to β-AR to the activation of AC; ***B)*** portions of the NO/cGMP/PKG pathway regulating cGMP synthesis through activation of sGC; ***C)*** pathway crosstalk comprising mechanistic models of PDEs 1 – 5 regulating cAMP and cGMP degradation, originally developed by Zhao et al. [127]; ***D)*** balance equation for cAMP and cGMP signals, bridging together A) to C); and ***E)*** activation of kinases by cNs. The model for kinase regulation of LCC gating is composed of 2 components: ***F)*** PKA and PKG-mediated phosphorylation of LCC regulating channel availability and distribution of gating modes; and ***G)*** stochastic simulation of LCC gating in distinct gating modes. The number of state equations and parameters in each sections of the model is tabulated in Table C.4, as well as parameters and constants for pharmacological reagents and unit conversions (Item ***H)***).

	Component	States	Parameters
A.	β-adrenergic pathway (cAMP synthesis)	11	19

B.	NO/sGC pathway (cGMP synthesis)	9	27
C.	Pathway cross-talk (cN degradation)	13	38
D.	cN balance equations (Net cN dynamics)	4	--
E.	Kinase activation (PKA and PKG)	6	14
	Total (cN Network)	**43**	**98**
F.	Kinase Phosphorylation of LCC	6	8
G.	LCC channel gating	14×4=96	23
	Total (LCC Regulation)		
H.	Other parameters and constants	--	5
	Total	**145**	**129**

Table C.4. Tabulation of equations and parameters.

For notation, concentrations of signaling species are enclosed by square brackets, "[ ]". Fractions normalized to total concentrations are not enclosed or enclosed with round brackets, "( )". Rates of cN production and degradation are prefixed by lower-case letter "v". The definitions of state variables, together with their initial conditions, are tabulated in Sect. IVA. For equations adapted from previous models [71, 127, 129, 175], notations are preserved as much as possible as the original literature.

C.2.1. Equations for cN cross-talk signaling network

All parameters listed below are the same as the original cN cross-talk signaling network model of Zhao et al. [175]. The state variables of kinase activation ($[PKAC_{II}]$ and $(PKG_{I_{active}})$) provide inputs to PKA-PKG-LCC Model below.

C.2.2. Equations for PKA-PKG-LCC model

The PKA-PKG-LCC Model calculates the proportion of channels available for gating and that of channels gating in each of the four gating modes.

Channel availability

$$f_{avail} = \frac{\frac{0.16}{1+e^{[-30\cdot((PKACII)-0.6))]}} + 0.28}{\frac{1.4}{1+e^{[-20\cdot((PKG_{act})-0.8)]}} + 1} \quad (65)$$

where

$(PKACII) = [PKACII]/(2 \cdot [PKAIItot])$
is the fraction of PKA-II activated by cAMP as regulated by the cN cross-talk signaling network.

Number of LCCs available is determined by

$$N_{avail} = N_{LCC\_s} \cdot f_{avail} \quad (66)$$

Mode switching

$$\frac{d(LCCa)}{dt} = k_{PP2A}(LCCa\_A) + k_{PP2A}(LCCa\_G) - (k_{LCCa\_A} + k_{LCCa\_G}) \cdot (LCCa) \quad (67)$$

$$\frac{d(LCCa\_A)}{dt} = k_{LCCa\_A}(LCCa) + k_{PP2A}(LCCa\_AG) - (k_{PP2A} + k_{LCCa\_G}) \cdot (LCCa\_A) \quad (68)$$

$$\frac{d(LCCa\_AG)}{dt} = k_{LCCa\_G}(LCCa_A) + k_{LCCa\_A}(LCCa_G) - 2 \cdot k_{PP2A} \cdot (LCCa\_AG) \quad (69)$$

$$\frac{d(LCCa\_G)}{dt} = k_{LCCa\_G}(LCCa) + k_{PP1}(LCCa\_AG) - (k_{LCCa\_A} + k_{PP2A}) \cdot (LCCa\_G) \quad (70)$$

Where

$k_{LCCa\_A} = k_{cat_{PKA}} \cdot (PKACII)$

$k_{LCCa\_G} = k_{cat_{PKG}} \cdot (PKG_{act})$

$k_{PP2A} = Vmax_{PP2A} \cdot (PP2A)$

Number of LCCs gating in each mode is determined by

$$N_{modei} = N_{avail} \cdot f_{modei}, i = \{1, 2, G, AG\} \quad (71)$$

Where

$f_{mode1} = (LCCa)$, $f_{mode2} = (LCCa\_A)$, $f_{mode\_G} = (LCCa\_G)$, and $f_{mode\_AG} = (LCCa\_AG)$

are determined by Equations .

C.2.3. Equations for L-type calcium channel model

LCC Markov processes

The baseline LCC model is adopted from Greenstein and Winslow [176], originally developed by Jafri et al. [181]. Stochastic stimulation of LCC model is achieved through the Gillespie algorithm [47]. Briefly, for each time step, dt, a uniform random variable is generated and is used to determine which state the Markov processes (Fig.) transitions into, if a transition occurs.

The PKA-PKG-LCC model defined above determines the proportion of channels gating in each mode (N_{modei}). Channel gating in each gating mode ($mode_i, i = \{1,\ 2,\ G, AG\}$) is defined with the same Markov process defined in Fig. 4.1B, but with distinct gating parameters (f_{modei} and g_{modei}) as defined in Table C.7.

Transition rates for mode switching & voltage activation (Fig. 4.1A) are defined as follows:

$\alpha = 2.0e^{0.012(V_m - 35)}$

$\beta = 0.0882e^{-0.05(V_m - 35)}$

$\alpha' = a\alpha$

$\beta' = \beta / b$

$\gamma = \gamma_0 [Ca^{2+}]_{ss}$

Transition rates for voltage-dependent inactivation (Fig. 4.1B) are defined as follows:

$$y_\infty = \frac{0.4}{1 + e^{\frac{V_m + 12.5}{5}}} + 0.6$$

$$\tau_y = \frac{340}{1 + e^{\frac{V_m + 30}{12}}} + 60$$

$k_{b,y} = y_\infty / \tau_y$

$k_{b,y} = (1 - y_\infty) / \tau_y$

Channel opening

For a channel to be open, it must occupy State 6 or 12 in the Markov process defined in Fig. 4.1A, and it must occupy State 1 of Fig. 4.1B. Let $isopen(mode_i, j_{LCC})$ be the indicator variable determining whether the ith channel in $mode_i$ is open or closed, that is

$isopen(mode_i, j_{LCC}) = 1$, if the channel is open;
otherwise,

$isopen(mode_i, j_{LCC}) = 0$, indicating the channel is closed.

L-type Ca^{2+} current

If a LCC is open, the channel Ca^{2+} conductance is given by

$$i_{LCC\_open} = P_{LCC} \frac{4V_m F^2}{RT} \frac{\left([Ca^{2+}]_i e^{2V_m F/(RT)} - 0.341[Ca^{+2}]_o\right)}{e^{2V_m F/(RT)} - 1} \quad (72)$$

The current passing through the jth LCC gating in Modei is

$$I_{LCC,j_{LCC}} = isopen(mode_i, j_{LCC}) \cdot i_{LCC\_open} \quad (73)$$

Whole-cell I_{CaL}, normalized by whole-cell capacitance, is given by the summation of unitary Ca^{2+} currents over all LCCs

$$I_{CaL} = \frac{1}{C_{SA}} \frac{N_{LCC}}{N_{LCC\_s}} \cdot \sum_{mode_i}^{i=\{1,2,G,AG\}} \sum_{j_{LCC}=1}^{N_{modei}} I_{LCC,j_{LCC}} \quad (74)$$

In addition, the current flux is calculated as

$$J_{LCC} = -\frac{C_{SA}}{2FV_{ds}} \cdot I_{CaL} \quad (75)$$

C.3. Model parameters

C.3.1. Parameters for cN cross-talk signaling model

All parameters are the same as the original cN cross-talk signaling network model of Zhao et al. [175].

C.3.2. Parameters for PKA-PKG-LCC model

Phosphorylating rate of LCC by active PKG is assumed to be same as that of PKA (i.e. $k_{cat\_PKG} = k_{cat\_PKA}$). This assumption is discussed in C.6.2.

Parameter	Representation	Value	Units	Ref.

1	$(LCC)_{total}$	Total L-type Ca channel	100	%	--
2	$Vmax_{PP1}$	PP1 dephosphorylation rate	1.561×10^{-2}	$units\ substrate\ /unit\ PP1/ms$	[79]
3	$r_{LCC_{PP1}}$	Units of PP1 tethered to LCC	5	$units\ LCC/PP1$	[79]
4	$Vmax_{PP2A}$	PP2A dephosphorylation rate	1.199×10^{-3}	$units\ substrate\ /units\ PP2A\ /msec$	[79]
5	ε_{PP2A}	PP2A : LCC	0.6	$units\ PP2A\ /unit\ substrate$	[79]
6	k_{PP2A}	PP2A dephosphorylation rate	$\varepsilon_{PP2A} \cdot Vmax_{PP2A}$	$msec^{-1}$	[79]
7	k_{cat_PKA}	PKA phosphorylation rate	2.7×10^{-4}	$msec^{-1}$	[74]
8	k_{cat_PKG}	PKG phosphorylation rate	2.7×10^{-4}	$msec^{-1}$	--

Table C.5. Parameters for PKA-PKG-LCC model.

C.3.3. Parameters for L-type calcium channel model

Baseline LCC model (Mode 1)

All parameters are the same as that of the original model of Greenstein et al. [176].

Parameter	Representation	Value	Units	Ref.

1	f	LCC transition rate into open state	0.85	ms^{-1}	[176]
2	g	LCC transition rate	2.0	ms^{-1}	[176]
3	f'	LCC transition rate	0.005	ms^{-1}	[176]
4	g'	LCC transition rate	7.0	ms^{-1}	[176]
5	a	LCC mode transition parameter	2.0	--	[176]
6	b	LCC mode transition parameter	1.9356	--	[176]
7	γ_0	LCC mode transition parameter	0.44	$mM^{-1}ms$	[176]
8	ω	LCC mode transition parameter	0.02158	ms^{-1}	[176]

Table C.6. Parameters for baseline L-type Ca^{2+} channel Markov model.

C.3.4. Parameters changes for gating modes

Table C.7 tabulates how f and g (defined in Table C.6) are altered to obtain parameters, f_{modei} and g_{modei}, for each LCC gating mode. The remaining parameter values are the same as that listed in Table C.6.

	Gating Mode	Parameter Adjusted	Ref.
1	Mode 1	N/A	[176]
2	Mode A	$g/10$	[79, 180]

3	Mode G	$f/2$	[186]
4	Mode AG	$g/10$ and $f/2$ (i.e. PKA changes + PKG changes)	[160]

Table C.7. Parameters adjusted for kinase-induced L-type Ca^{2+} channel gating modes.

C.3.5. Parameters for L-type calcium current

	Parameter	Representation	Value	Units	Ref.
1	P_{CaL}	L-type Ca^{2+} channel permeability to Ca^{2+} (unitary)	9.13×10^{-13}	$cm^3 s^{-1}$	[176]
2	C_{SA}	Capacitance of the cell surface	153.4	pF	[176]
3	F	Faraday's constant	96.5	$C/mmol$	[176]
4	T	Temperature	310	K	[176]
5	R	Universal gas constant	8.314	$\frac{J}{mol \cdot K}$	[176]
6	$[Ca^{2+}]_o$	Extracellular Ca^{2+} concentration	2	mM	[176]
7	$N_{LCC_{tot}}$	Total number of L-type Ca^{2+} channels in the cell	50,000	--	[176]

Table C.8. Parameters for L-type Ca^{2+} current.

C.4. Simulation conditions

Initial conditions for state variables reflect basal conditions, in which no pharmacological drugs are applied externally or internally to the cell. The values are obtained from steady state of the model ran from a preliminary set of initial conditions. For the preliminary initial conditions, experimental values are assigned whenever possible, such as the initial values for [cAMP] and [cGMP]. When experimental measures are not readily available, all components are assumed to be in their non-activated states, and all PDE activities are assumed to be zero. When the model is run to steady state from the preliminary initial conditions to obtain current initial conditions, the states with experimental measurements remained in the experimentally recorded range. Whenever possible for states adapted from previous models, the final initial conditions are ensured to be similar to the original models [71, 129].

C.4.1. State variable initial conditions

	State Variables	Representation	Initial Value	Units	Ref.
		cN Signaling Network			
1	$[Donor_{NO}]$	NO donor	0	μM	--
2	$[NO]_o$	NO outside of the cell	0.0001	μM	[95, 150, 242]
3	$[NO]_i$	NO inside the cell	0.0001	μM	[95, 150, 242]
4	$[L]$	Ligand to β-AR (ISO)	0	μM	--

5	$[\beta AR]$	β-AR	0.01	μM	[71]
6	$[Gs]$	Stimulatory G-protein	3.83	μM	[71]
7	$[\beta_1 AR_{act}]$	Activated β-receptor	0.01	μM	[71]
8	$[\beta_1 AR_{S464}]$	Desensitized β-AR by β-receptor kinase	0	μM	[71]
9	$[\beta_1 AR_{S301}]$	Desensitized β -AR by PKA-I	0.0016	μM	[71]
10	$[G_{saGTPtot}]$	Total concentration of Gs with GTP bound to its α-subunit	0.024	μM	[71]
11	$[G_{saGDP}]$	Gs with GDP bound to its α-subunit	0.0006	μM	[71]
12	$[G_{s\beta\gamma}]$	β- and ϒ-subunits of Gs	0.0248	μM	[71]
13	$[G_{saGTP}]$	Free Gs with GTP bound to α-subunit	0.021	μM	[71]
14	$[AC]$	Adenylyl Cyclase	0.047	μM	[71]
15	(sGC)	Free sGC	0.98	--	[129]
16	$(NOsGC)$	sGC bound with 1 NO	0.028	--	[129]
17	$(NOsGC^*)$	Activated sGC with 1 NO bound	0.028	--	[129]
18	$(NOsGC^*NO)$	sGC bound with 2 NO	0	--	[129]
19	(sGC^*NO)	NO-bound inactivated sGC	0.084	--	[129]
20	(sGC^*)	NO-free inactive sGC	0.001	--	[129]
21	$vPDE1_A^*$	Rate of cAMP hydrolysis by PDE1	0	$\mu M/ms$	--
22	$vPDE1_G^*$	Rate of cGMP hydrolysis by PDE1	0	$\mu M/ms$	--
23	$vPDE2_A^*$	Rate of cAMP hydrolysis by PDE2	0	$\mu M/ms$	--
24	$vPDE2_A^*$	Rate of cGMP hydrolysis by PDE2	0	$\mu M/ms$	--

25	$vPDE3_A^*$	Rate of cAMP hydrolysis by PDE3	0	$\mu M/ms$	--
26	$vPDE3_G^*$	Rate of cGMP hydrolysis by PDE3	0	$\mu M/ms$	--
27	$(pPDE4)$	PKA-phosphorylated PDE4	0.11	--	--
28	$vPDE4_A^*$	Rate of cAMP hydrolysis by PDE4	0	$\mu M/ms$	--
29	$(PDE5)$	Free PDE5	0.96	--	--
30	$(cGMP:PDE5)$	cGMP-bound PDE5	0.002	--	[129]
31	$(tPDE5^*)$	Stimulated cGMP-bound PDE5	0.003	--	[129]
32	$(pPDE5^*)$	PKG phosphorylated PDE5 (active)	0.027	--	[129]
33	$vPDE5_G^*$	Rate of cGMP hydrolysis by PDE5	0	$\mu M/ms$	[129]
34	$[cAMP_{tot}]$	Total cAMP	0.50	μM	[71]
35	$[cAMP]$	Free cAMP	0.16	μM	[71]
36	$[cGMP_{tot}]$	Total cGMP	0.017	μM	[71]
37	$[cGMP]$	Free cGMP	0.01	μM	[128]
38	$[PKAC_I]$	Dissociated active fragment of PKA-I	0.086	μM	[71]
39	$[PKAC_{II}]$	Dissociated active fragment of PKA-II	0.025	μM	[71]
40	$(PKG_I:cGMP2)$	PKG-I bound with 2 cGMP	0.10	--	--
41	$(PKG_I:cGMP4)$	PKG-I bound with 4 cGMP (active)	0.006	--	--
42	(PKG_I)	Free PKG-I	0.89	--	--
43	$(PKG_{I_{activity}})$	PKG-I activity	0.063	--	--
		Regulation of L-Type Calcium Channel			
44	f_{avail}	Fraction of LCCs	1	--	

		available for gating		
45	$f_{unavail}$	Fraction of LCCs that are unavailable for gating	0	--
46	(LCC)	Non-phosphorylated LCC	1	--
47	(LCC_A)	PKA-phosphorylated LCC	0	--
48	(LCC_AG)	PKA- and PKG-phosphorylated LCC α-subunit	0	--
49	(LCC_G)	PKG-phosphorylated LCC	0	--
50	I_{LCC}	Ca^{2+} current through a single LCC	0	pA
51	i_{LCC_open}	Ca^{2+} conductance of a single open LCC	0	pA
52	I_{CaL}	Whole cell L-type Ca^{2+} current	0	
53	J_{LCC}	Whole cell L-type Ca^{2+} flux	0	

Table C.9. Initial conditions for state variables.

In addition, all LCCs are assumes to start in State 1 for the 12 state model (Fig. 4.1A) and State 1 of the VDI process (Fig. 4.1B).

C.4.2. Simulation parameters

	Parameter	Representation	Value	Unit
1	dt	Time step for Monte Carlo simulation of	0.01	$msec$
2	N_{LCC_s}	Total number of LCC simulated	500	--
3	$tspan$	Duration of each sweep	320	$msec$
4	V_m	Voltage clamp protocol		mV
5	$[Ca^{2+}]$	Ca^{2+} clamp concentration	4	μM

Table C.10. Simulation parameters.

C.4.3. Conditions for figure generation

All figures are generated using the same set of equations, parameters, and initial conditions as specified by the above sections.

C.5. Basis for model and simulations

C.5.1. Gating parameters

Let X_i be a random variable representing time spent in a given State i (also known as the dwell time or sojourn time in State i) of the Markov processes constituting the LCC model [176]. Then, it is exponentially distributed with the probability density function (pdf)

$$f(x_i) = \lambda e^{-\lambda x_i},$$

where time constant $\lambda = \sum_{j \neq i} r_{i,j}$, that is sum of exit rates ($r_{i,j}$) out of State i. Expectation of X_i or mean dwell time is defined as

$$E(X_i) = \frac{1}{\sum_{i=1}^{n} ri,j}$$

That is the reciprocal of the sum of exit rates out of State i.

As a result, the gating parameters are changed according to fold changes of the given gating mode with respect to that of basal as shown in Table C.7.

C.5.2. Theoretical distribution of open/closed times

As explained above, the theoretical distribution for open times in Fig.C.1 are produced according to exponential distribution with exit rate from the open state (State 6) as parameters:

$$f(x_i) = ge^{-gx_i} \text{ for Mode 1}$$
$$f(x_i) = (\frac{g}{10})e^{-(\frac{g}{10})x_i} \text{ for Mode A}$$
$$f(x_i) = ge^{-gx_i} \text{ for Mode G}$$
$$f(x_i) = (\frac{g}{10})e^{-(\frac{g}{10})x_i} \text{ for Mode AG}$$

The pdf above in each case is scaled by the total number of openings recorded, in order to match the simulation data.

C.5.3. Best-fit to open/closed time histograms

Each histogram shown is also fitted according to the following functions through minimum least squares optimization:

Open Time (Single exponential fit)

$$f(x) = c_o \cdot \exp\left(-\frac{1}{\tau_o} * t_{open}\right)$$

Close Time (Double exponential fit)

$$f(x) = c_f \cdot \exp\left(-\frac{1}{\tau_{cf}} \cdot t_{closed}\right) + c_s * \exp\left(-\frac{1}{\tau_{cf}} \cdot t_{closed}\right)$$

The produced probability in each case is scaled by the total number of openings recorded, in order to match the simulation data. The variables above are defined in Table C.11.

	Symbol	Unit	Name	Representation
1	$nbin$	--	Number of bins	Number of divisions for histograms
			Open Times	
2	$\bar{t_o}$	ms	Mean open time	Average duration of LCC openings
3	τ_o	ms	Time constant	Time constant of open times from single exponential fit on open-time histograms
4	c_o	ms	Normalization factor	Constant multiplier of exponential fit on open-time histograms

5	t_{open}	ms	Open times	Duration of each LCC openings
			Close Times	
6	$\overline{t_c}$	ms	Mean closed time	Average duration of LCC closings
7	τ_{cf}	ms	Fast time constants	Time constant of short close times from double exponential fit on close-time histograms
8	τ_{cs}	ms	Slow time constants	Time constant of long close times from double exponential fit on close-time histograms
9	c_f	ms	Normalization factor	Constant multiplier of exponential fit on short components of closed-time histograms
10	c_s	ms	Normalization factor	Constant multiplier of exponential fit on long components of closed-time histograms
11	t_{close}	ms	Closed Times	Duration of each LCC closings
			Others	
12	T_1	ms	First latency	Time from the beginning of the test pulse to the first opening of the channel

Table C.11. Parameters for histograms and least square fits.

C.6. Additional result figures

C.6.1. Supplementary simulations

Fig.C.1. LCC single channel open and closed time distribution.

Currents are elicited from a holding potential of - 80 mV to 0 mV for 200 msec. For each mode, distributions histograms are assembled from simulation of 500 independent LCCs. **(A) – (D)** Distribution of channel open times for Mode 1, A, G and AG respectively. In addition, the theoretical distribution (black line), best-fit mono-exponential distribution (dotted line), and distribution mean (vertical dashed line with annotation) are shown. **(E) – (H)** Distribution of channel closed time for Mode 1, A, G, and AG respectively. The best-fit mon-exponential distributions (solid line) are shown together with its fast (steep dotted line) and slow (dotted line) exponential components. Distribution mean (vertical dashed line with annotation) are shown.

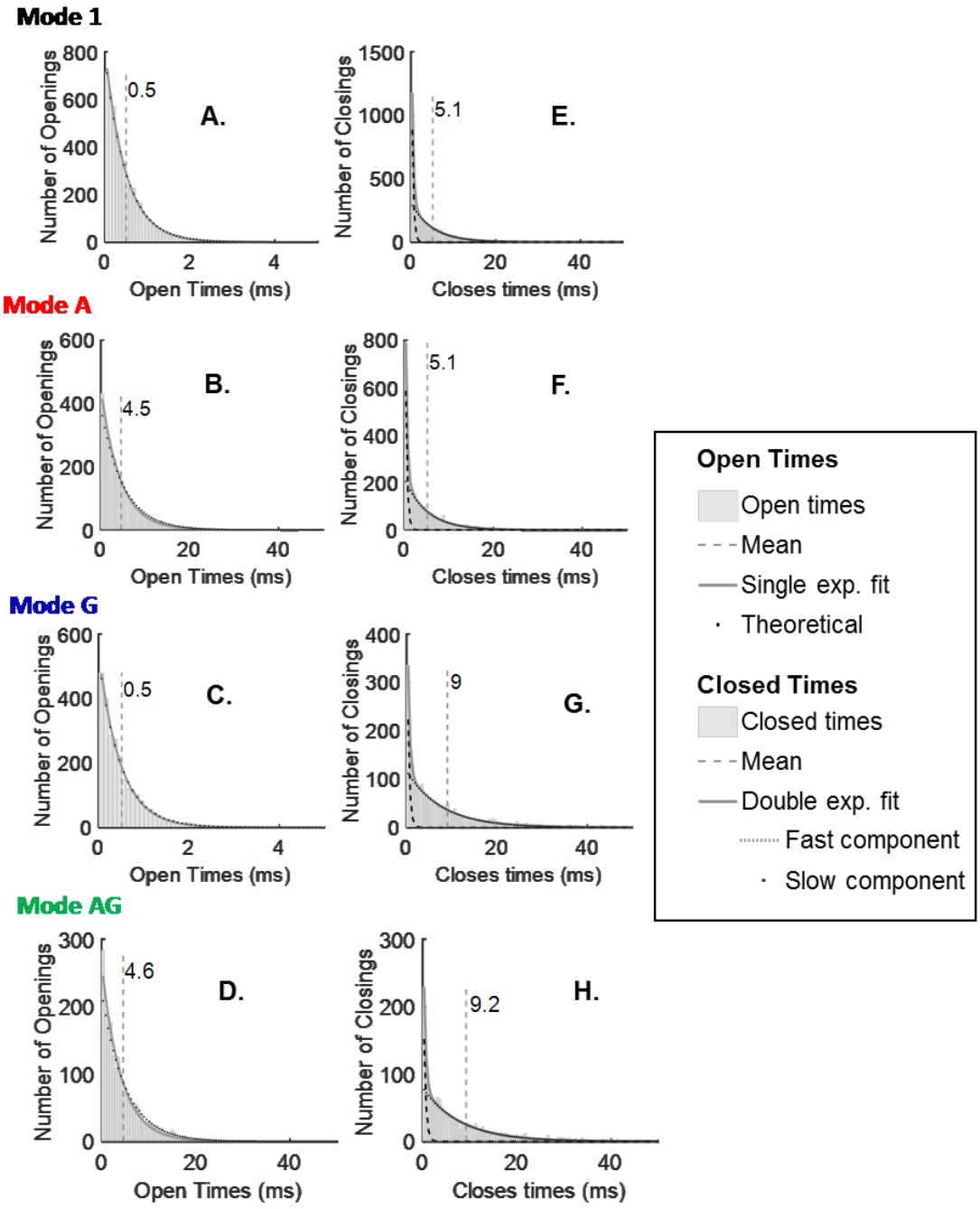

Fig.C.2A: All four PDE subtypes determine the response of ICaL to β-adrenergic stimulation, with the rank order of potency PDE4 > PDE3 > PDE2 > PDE1. This result is consistent with that by Verde et al. [86].

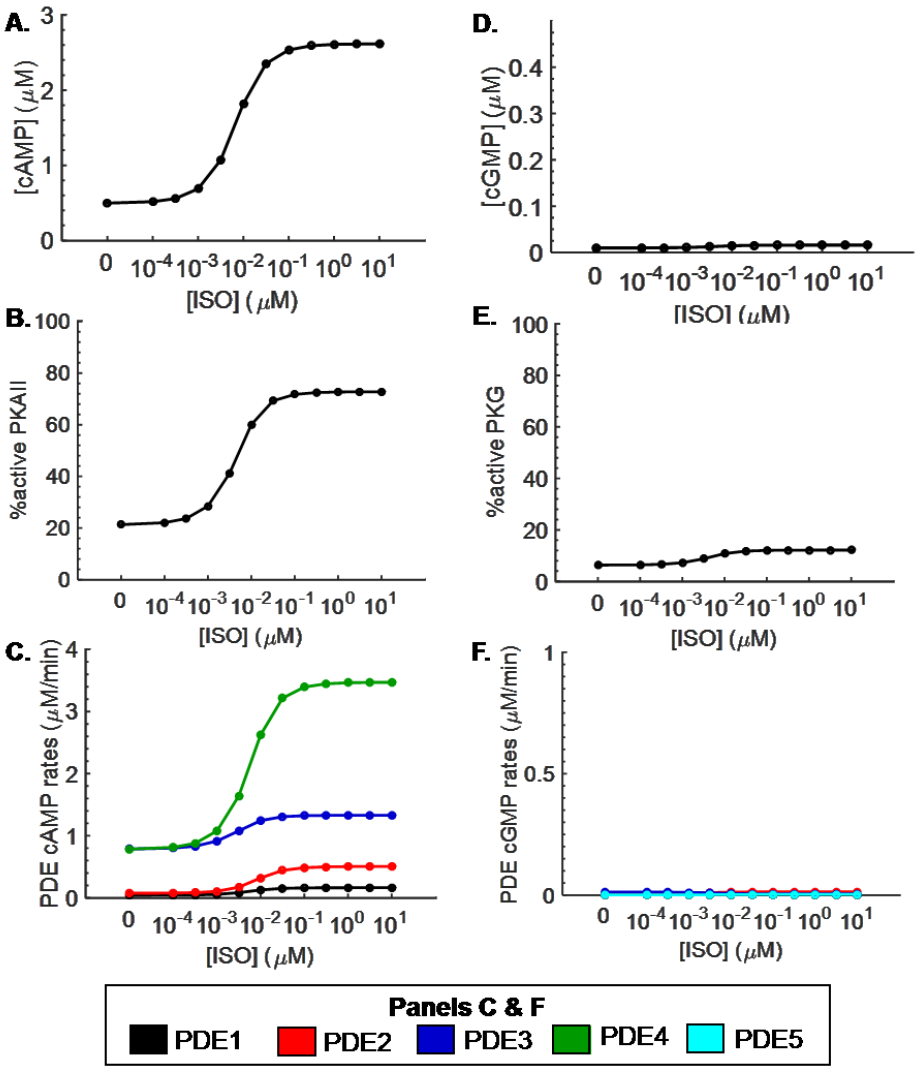

Fig.C.2. cN regulation of β-adrenergic stimulation.

(A) – (C) Responses within the β-adrenergic pathway, with [cAMP], percent PKA-II activated, and PDE cAMP hydrolysis rates shown respectively. **(D) – (F)** Responses within the NO/cGMP/PKG pathway are shown respectively for [cGMP], percent PKG activated, and PDE cGMP hydrolysis rates. (B) and (E) The hydrolysis rates for PDEs 1, 2, 3, 4, and 5 are shown in black, red, blue, green, and cyan respectively.

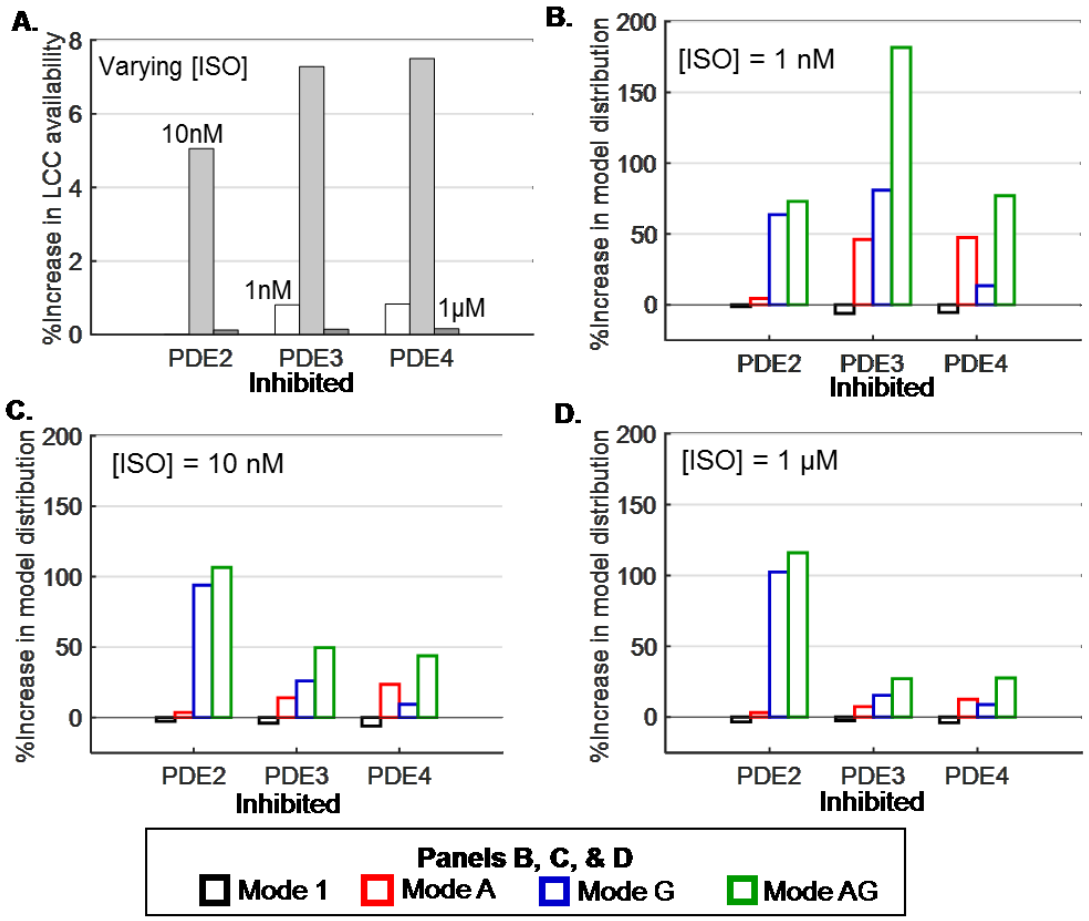

Fig.C.3. LCC gating mode changes by PDE inhibition under β-adrenergic stimulation.

Individual inhibitions of PDE 2, 3, and 4 (x-axis) under [ISO] of 1 nM (white), 10 nM (grey), and 1 μM (dark grey). Percent increases in model responses are shown with respect to those prior to the indicated PDE inhibition. For PDE 2, 3, and 4 inhibition respectively, 10 μM EHNA, 1 μM Cilo, and 0.3 μM Rol have been applied in accordance with Verde et al. [86]. (A) Percent increases in LCC availability. (B), (C), and (D) respectively, percent increases in proportions of channels gating in each mode under 1 nM, 10 nM, and 1 μM [ISO]. Percent increases in gating modes, Mode 1, A, G, and AG are shown in black, red, blue, and green outlines bars respectively.

C.6.2. Sensitivity analysis

In the absence of experimental data, this study assumed that PKG phosphorylation rate of LCC is equal to that of PKA (i.e. $k_{cat\_PKG} = k_{cat\_PKA}$). In order to see the way the unknown parameter k_{cat_PKG}affects our study, we performed sensitivity analysis ($\overline{k_{cat_{PKG}}}$) on this parameter. Fig.C.4-Fig.C.6 and Fig.C.7- Fig.C.9 show simulations results after increasing and decreasing $k_{cat_PKG}$by a factor of ten. In order, the figures in the aforementioned two sets of figures correspond to Fig. 4.5, Fig.C.2, and Fig. 4.6 that has been generated using original set of parameters. Comparing the results from this sensitivity analysis and figures from the original model, ten-fold variations in k_{cat_PKG} do not produce significant changes in model outputs on LCC currents, LCC gating, or cN cross-talk signaling. As a result, uncertainty of the value of k_{cat_PKG} due to the lack of experimental data does not affect the results and findings from this paper.

Fig.C.4-Fig.C.6 shows model simulation under the condition that $\overline{k_{cat_{PKG}}} = k_{cat\_PKG} \times 10$.

Fig.C.4. Sensitivity analysis ($\mathbf{k_{cat\_PKG} \times 10}$) on redistribution of LCC gating modes.

Simulation performed with PKG phosphorylation rate of LCC multiplied by ten (i.e. $\overline{k_{cat_{PKG}}} = k_{cat\_PKG} \times 10$). Figure corresponds to Fig.C.7 with $\overline{k_{cat_{PKG}}} = k_{cat\_PKG} \div 10$ and Fig. 5 with original set of parameters. LCC gating behavior under varying [ISO] (no SNAP) (A–C) and under varying [SNAP] with 10 μM ISO and without ISO (D–G). **(A)** Percent increases in Peak I_{CaL} under varying [ISO] over basal I_{CaL} (no ISO) (grey line) versus data by Katsube et al. [169] (black dots). (E) Peak I_{CaL} under varying [SNAP]

without ISO (black) and with 10 µM [ISO] (grey). **(B)** and **(E)** Percent of LCCs available corresponding to (A) and (D) respectively. Percent of LCCs gating in Mode 1 (black), Mode A (red), Mode G (blue), Mode AG (green) are shown in for varying [ISO] (C), varying [SNAP] **(F)**, and varying [SNAP] under simultaneous ISO stimulation (10 µM) **(G)**.

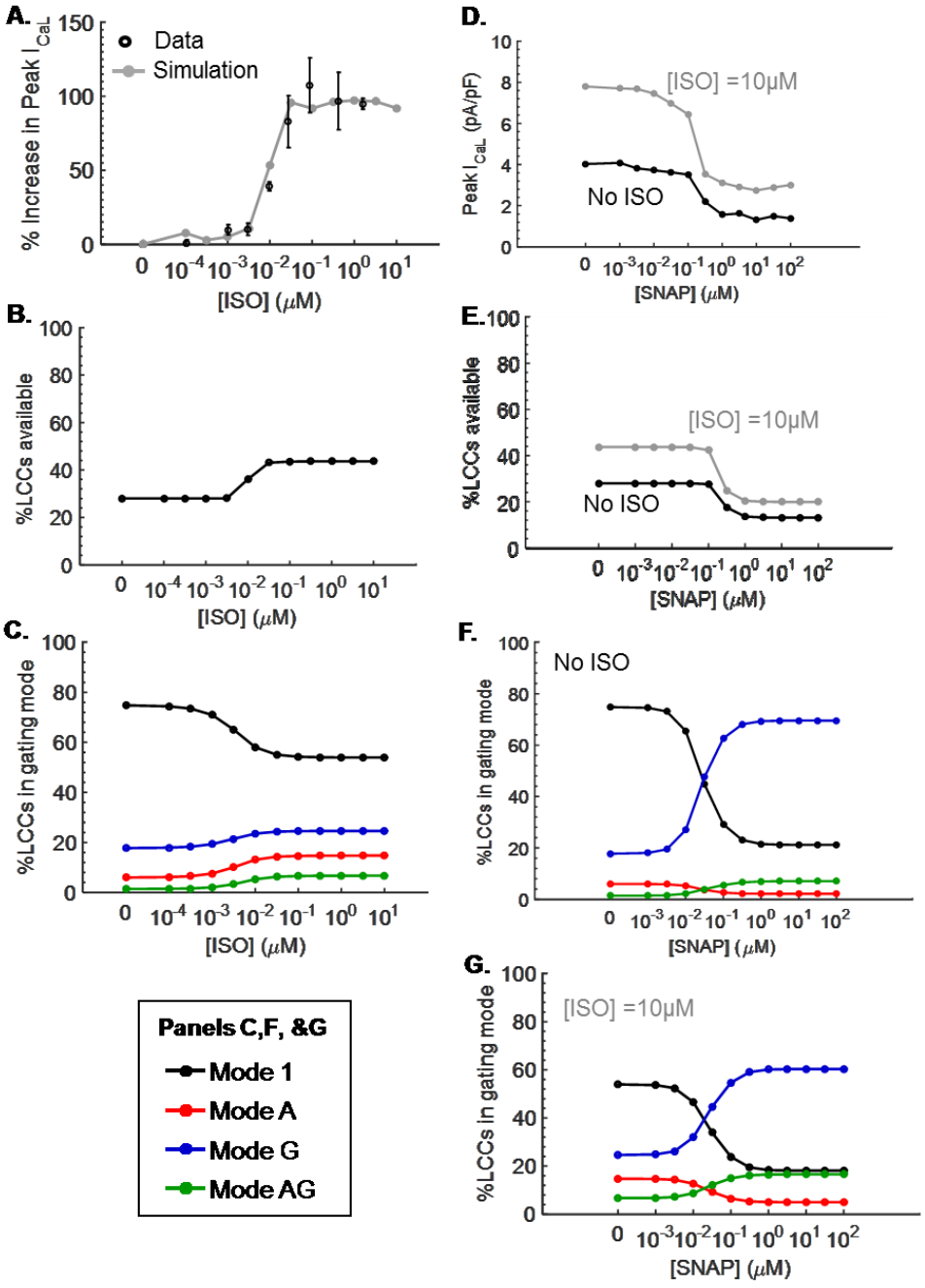

Fig.C.5. Sensitivity analysis ($\mathbf{k_{cat\_PKG} \times 10}$) on cN regulation of β-adrenergic stimulation.

Simulation performed with PKG phosphorylation rate of LCC multiplied by ten (i.e. $\overline{k_{cat_{PKG}}} = k_{cat\_PKG} \times 10$). Figure corresponds to Fig.C.8 with $\overline{k_{cat_{PKG}}} = k_{cat\_PKG} \div 10$ and Fig.C.2 with original set of parameters. **(A) – (C)** Responses within the β-adrenergic pathway, with [cAMP], percent PKA-II activated, and PDE cAMP hydrolysis rates shown respectively. **(D) – (F)** Responses within the NO/cGMP/PKG pathway are shown respectively for [cGMP], percent PKG activated, and PDE cGMP hydrolysis rates. (B) and (E) The hydrolysis rates for PDEs 1, 2, 3, 4, and 5 are shown in black, red, blue, green, and cyan respectively.

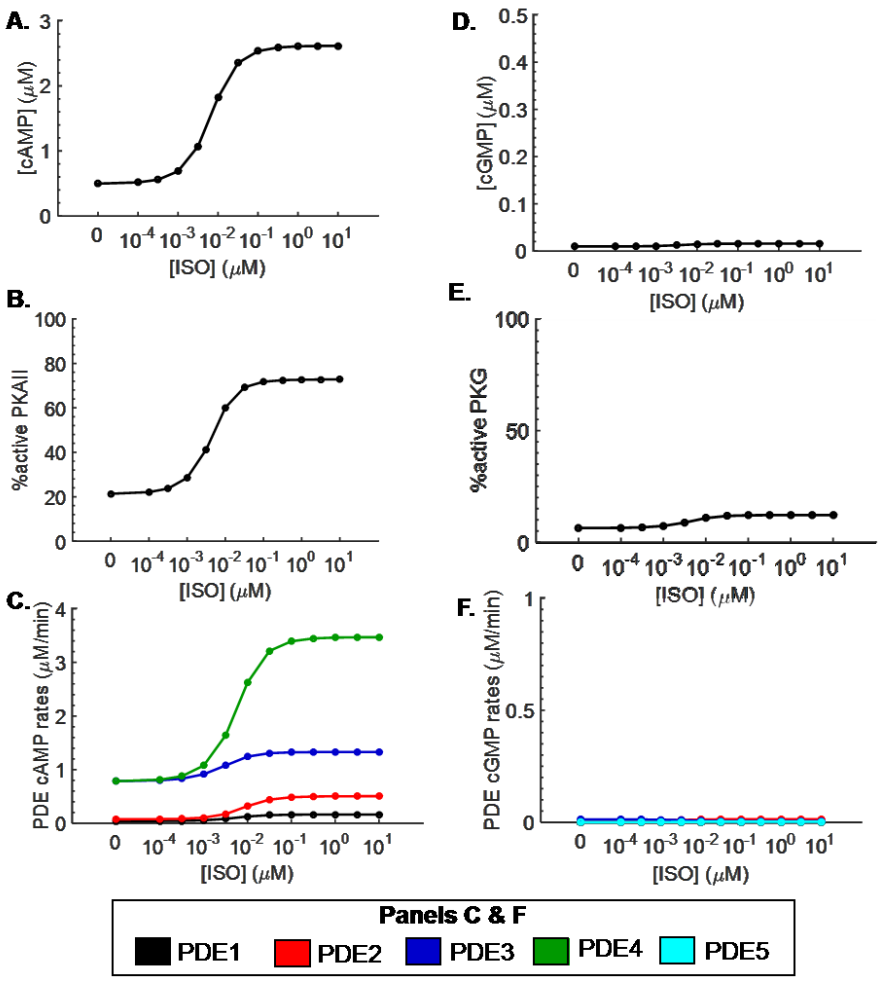

Fig.C.6. Sensitivity analysis ($k_{cat\_PKG} \times 10$) on role of cN cross-talk in LCC regulation.

Simulation performed with PKG phosphorylation rate of LCC multiplied by ten (i.e. $\overline{k_{cat_{PKG}}} = k_{cat\_PKG} \times 10$). Figure corresponds to Fig.C.9 with $\overline{k_{cat_{PKG}}} = k_{cat\_PKG} \div 10$ and Fig. 6 with original set of parameters. **(A)** and **(B)** respectively, [cAMP] and percent active PKA-II under varying [SNAP] without (black) and with ISO (10 μM). **(C)** cAMP hydrolysis rates for PDEs 1, 2 ,3 and 4 (black, red, blue, and green respectively) for simulation without ISO. **(D)** Similar to C, for simulation with ISO. **(E)** and **(F)**

respectively, [cGMP] and percent active PKG under varying [SNAP] without (black) and with ISO (10 µM). **(G)** and **(H)** The cGMP hydrolysis rates for PDEs 1, 2 ,3 and 5 (black, red, blue, and cyan respectively) for simulation without and with ISO respectively.

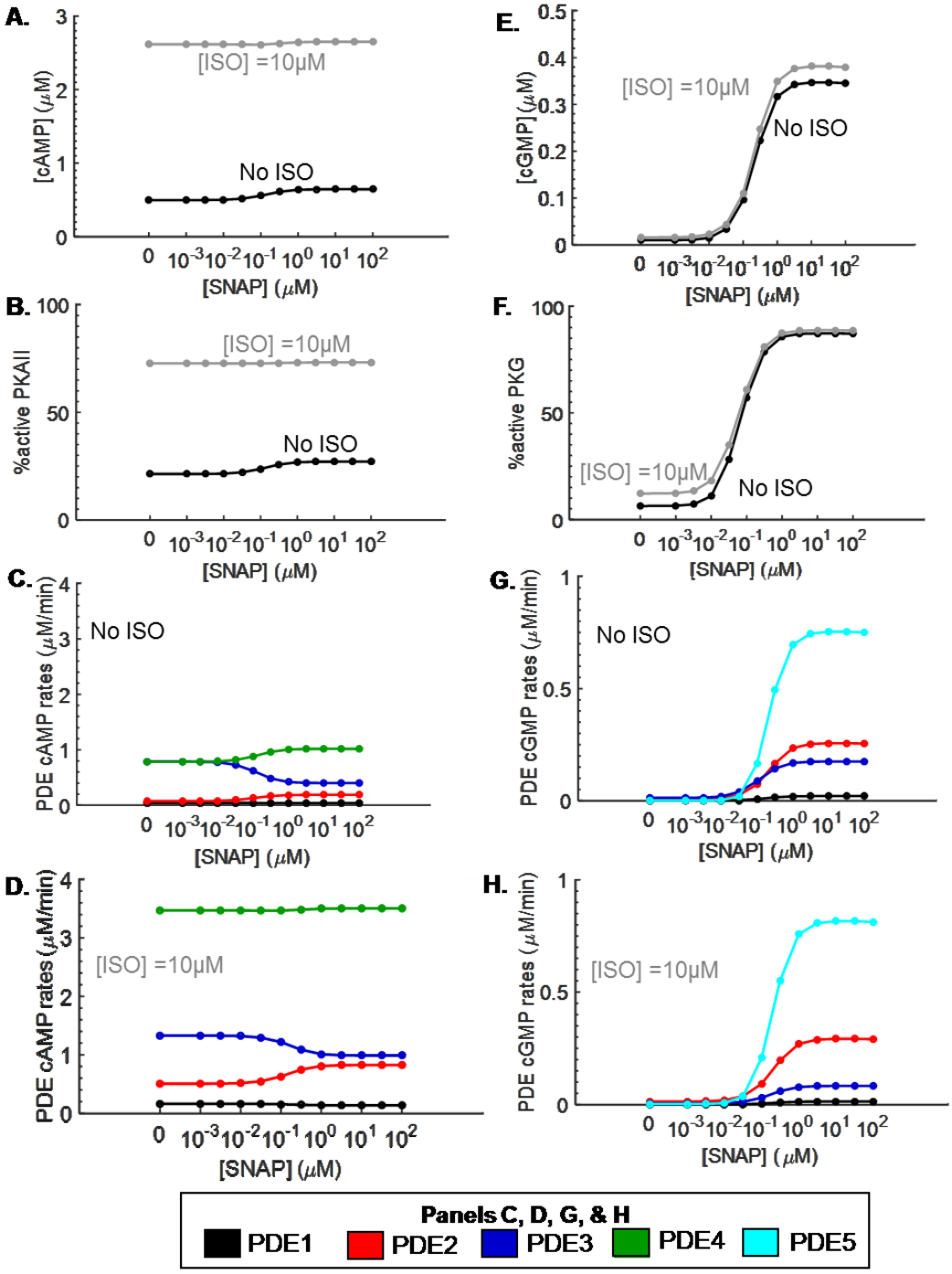

Fig.C.7- Fig.C.9 shows model simulation under the condition that $\overline{k_{cat_{PKG}}} = k_{cat\_PKG} \div 10$.

Fig.C.7. Sensitivity analysis ($\mathbf{k_{cat\_PKG}} \div \mathbf{10}$) on redistribution of LCC gating modes.

Simulation performed with PKG phosphorylation rate of LCC divided by ten (i.e. $\overline{k_{cat_{PKG}}} = k_{cat\_PKG} \div 10$). Figure corresponds to Fig.C.4 with $\overline{k_{cat_{PKG}}} = k_{cat\_PKG} \times 10$ and Fig. 4.6 with original set of parameters.

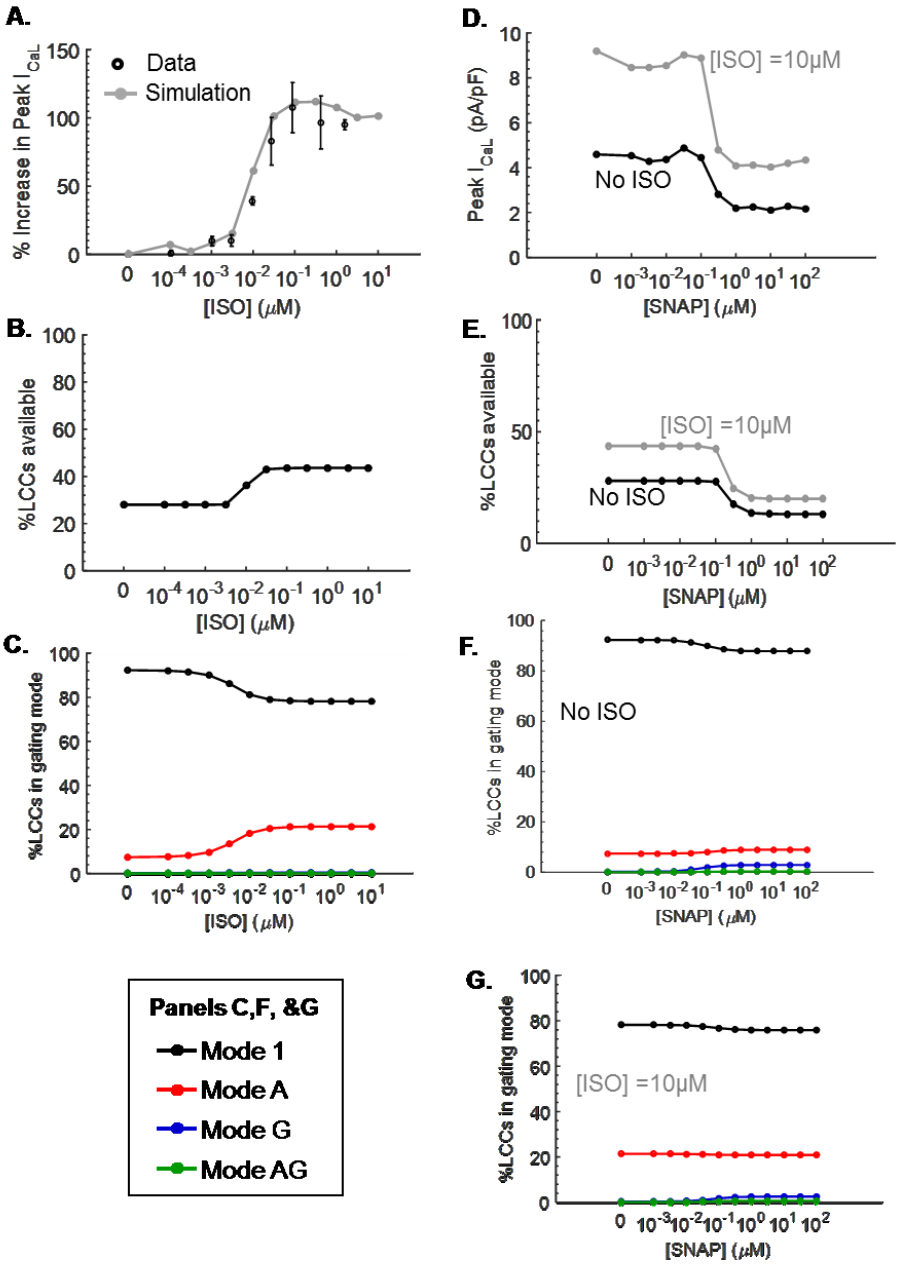
A.
Data
Simulation
% Increase in Peak I_{CaL}
[ISO] (μM)
B.
%LCCs available
[ISO] (μM)
C.
%LCCs in gating mode
[ISO] (μM)
Panels C,F, &G
Mode 1
Mode A
Mode G
Mode AG
D.
Peak I_{CaL} (pA/pF)
[ISO] =10μM
No ISO
[SNAP] (μM)
E.
%LCCs available
[ISO] =10μM
No ISO
[SNAP] (μM)
F.
%LCCs in gating mode
No ISO
[SNAP] (μM)
G.
%LCCs in gating mode
[ISO] =10μM
[SNAP] (μM)

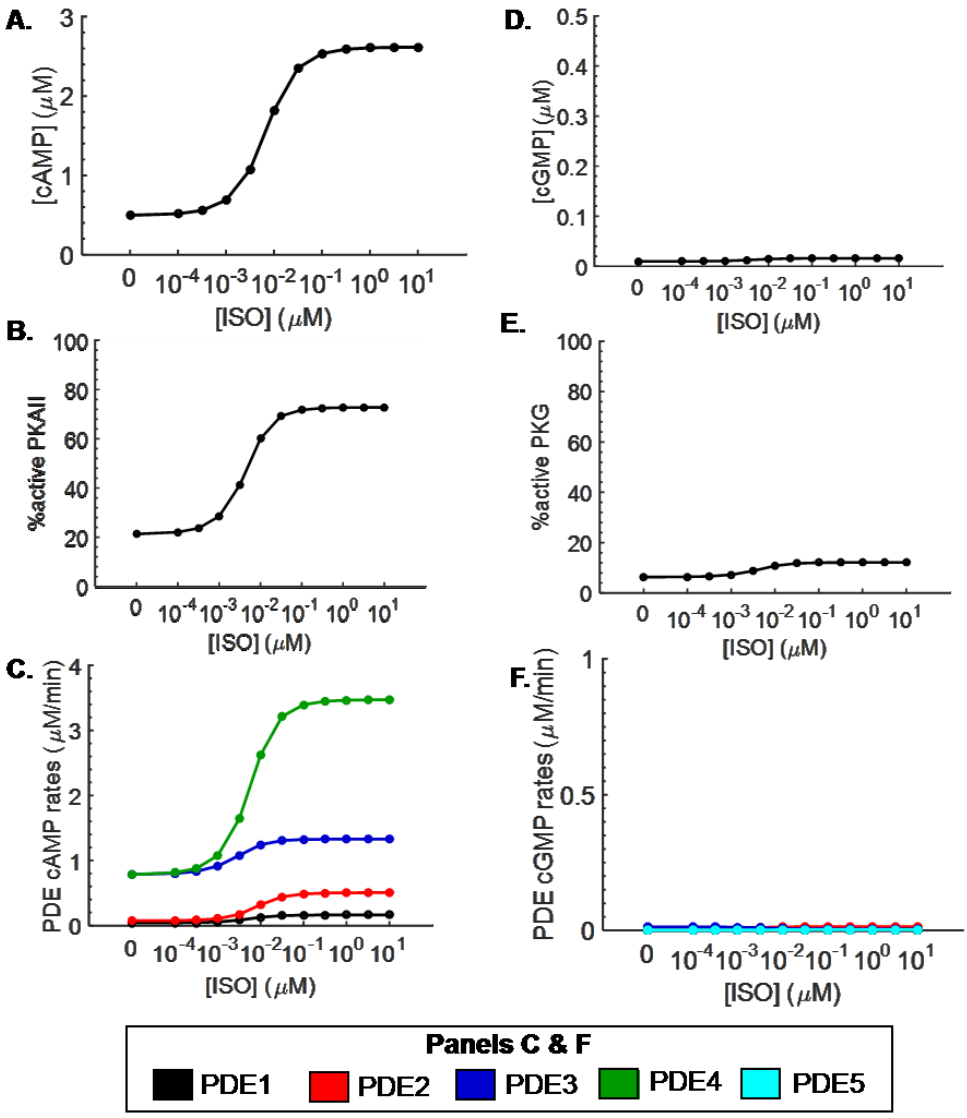

Fig.C.8. Sensitivity analysis ($\mathbf{k_{cat\_PKG} \div 10}$) on cN regulation of β-adrenergic stimulation.

Simulation performed with PKG phosphorylation rate of LCC divided by ten (i.e. $\overline{k_{cat_{PKG}}} = k_{cat\_PKG} \div 10$). Figure corresponds to Fig.C.5 with $\overline{k_{cat_{PKG}}} = k_{cat\_PKG} \times 10$ and Fig.C.2 with original set of parameters.

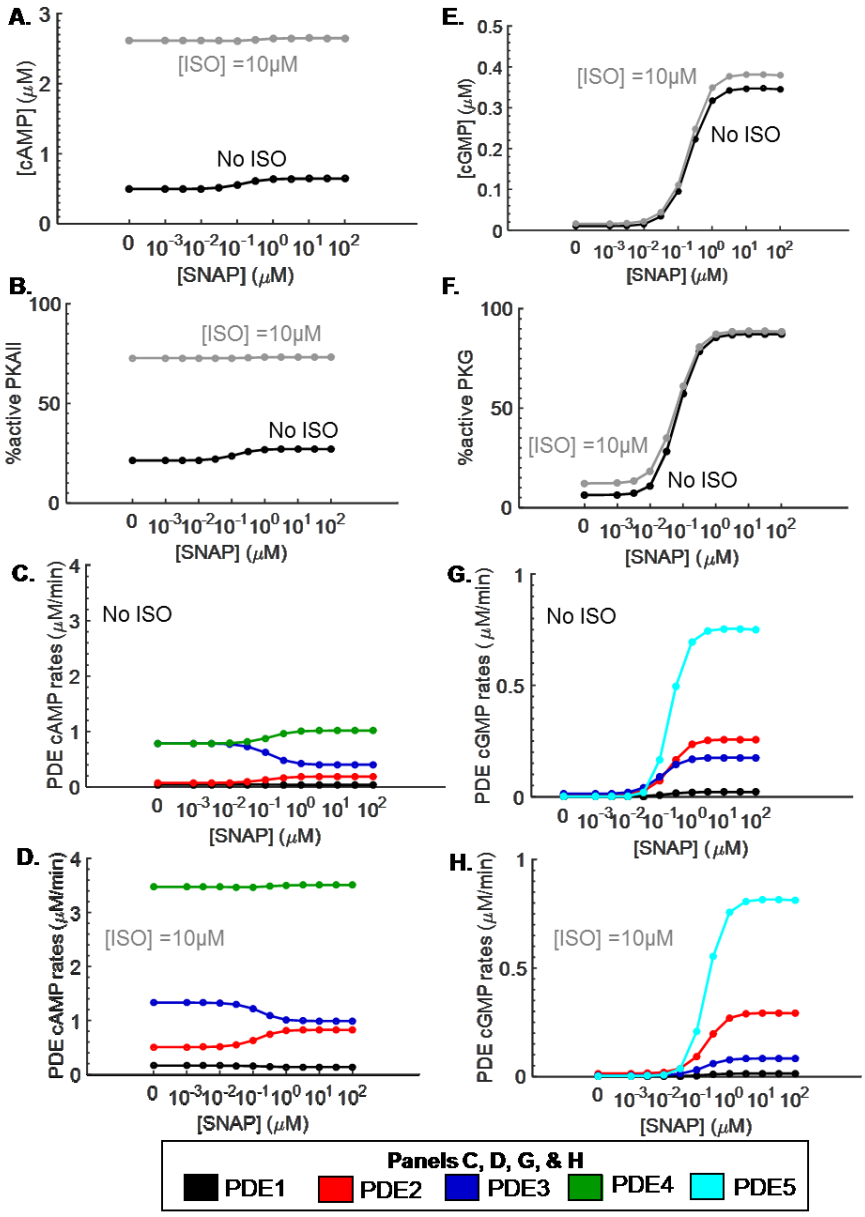

Fig.C.9. Sensitivity analysis ($k_{cat\_PKG} \div 10$) on role of cN cross-talk in LCC regulation.

Simulation performed with PKG phosphorylation rate of LCC divided by ten (i.e. $\overline{k_{cat_{PKG}}} = k_{cat\_PKG} \div 10$). Figure corresponds to Fig.C.6 with $\overline{k_{cat_{PKG}}} = k_{cat\_PKG} \times 10$ and Fig. 4.5 with original set of parameters.

C.6.3. Model Ca2+ concentration

In our model simulations, [Ca^{2+}] is clamped at 4 μM. Due to the presence of Ca^{2+} buffer, EGTA, in experimental solutions, free [Ca^{2+}] is unlikely to be higher than 10 μM for total [Ca^{2+}] less than 5 mM (**Error! Reference source not found.**A), as estimated using on-ine program MaxChelator ® by Bers et al. [191]. Consequently, we tested the effect of varying [Ca^{2+}] below 10 μM on I_{CaL} using the LCC model from Greenstein and Winslow [171]. In order to eliminate stochastic variations in channel current due to the random openings and closings of LCCs, we implemented the LCC model using deterministic ordinary differential equations (ODEs), so that the average LCC behavior is well reflected. We then clamped [Ca^{2+}] from 1 nM to 10 μM. As shown in **Error! Reference ource not found.**B, while the kinetics of I_{CaL} inactivation is greatly influenced by [Ca^{2+}], peak I_{CaL} is not affected much. We chose 4 μM [Ca^{2+}] to reflect a median level of impact of CDI on peak I_{CaL} (**Error! Reference source not found.**B). Our study analyzes peak $ICaL$ only, not its kinetics; the particular choice of 4 μM [Ca^{2+}] over other values, while do change the precise values of peak I_{CaL} reported, do not affect our key findings.

Fig.C.10. [Ca^{2+}] in the model.

(A) Free [Ca^{2+}] from 10 mM EGTA buffering is calculated according to Bers et al. [191] using the on-line program MaxChelator ® [191] with the indicated total [Ca^{2+}] on the abscissa. **(B)** I_{CaL} obtained under varying [Ca2+] from 1 nM to 10 μM. Currents are elicited from a holding potential of - 80 mV to 0 mV for 150 msec. In order to eliminate stochastic variations, LCC model from Greenstein and Winslow [171] is implemented using deterministic ODEs.

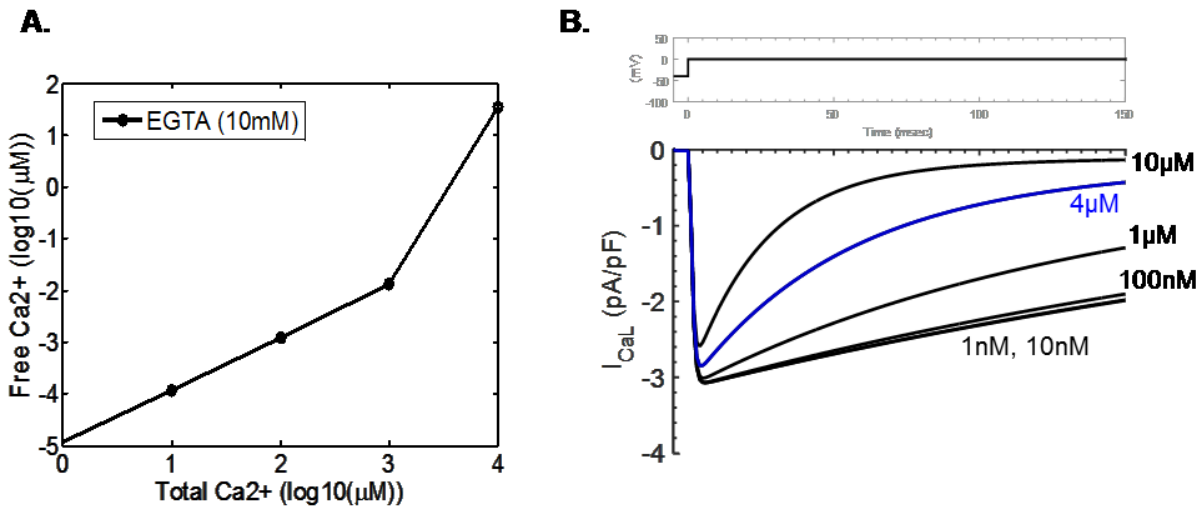
A.
EGTA (10mM)
Free Ca2+ (log10(μM))
Total Ca2+ (log10(μM))
B.
(mV)
Time (msec)
10μM
4μM
1μM
100nM
1nM, 10nM
I_CaL (pA/pF)

Appendix D.Acknowledgements

D.1. Research funding

The author is grateful to the funding from Natural Sciences and Engineering Research Council (NSERC) of Canada scholarships, CGS M-377616-2009 (1 year) and PGSD3-405041-2011 (3 years).

D.2. Thesis proposal committee

The author is grateful to the guidance of the thesis proposal committee:

Name	Lab	Primary Department	Institution
Gordon Tomaselli (Chair)	Ion Channels & electrical remodeling in structural heart disease	Cardiology	Johns Hopkins University
Natalia Trayanova	Computational Cardiology Lab	Biomedical Engineering	Johns Hopkins University
Raimond Winslow (PI)	Winslow Lab	Biomedical Engineering	Johns Hopkins University

Table D.1. Thesis proposal committee members.

D.3. Research lab and institute

The author thanks the members of the Institute of Computational Medicine (ICM) for their support. The author also appreciates the opportunity to interact with the members of the Winslow Lab: Dr. Raimond Winslow (PI), Dr. Joseph Greenstein, Lulu Chu, Mark Walker, Bhaskar Chennuri, Dr. Sonia Cortassa, Dr. Pegy Foteinou, Dr. Rob Kazmierski, Dr. Laura Gauthier, Dr. An-Chi Wei, Dr. Yasmin Hashambhoy, Dr. Troy Anderson, Tejas Mehta, and Aagam Shah.

D.4. Research correspondences

The author is grateful to the guidance of the following mentors for their support of the research project:

Name	**Lab**	**Primary Department**	**Institution**
Raimond Winslow (PI)	Winslow Lab	Biomedical Engineering	Johns Hopkins University
Brian O'Rourke	O'Rourke Lab	Cardiology	Johns Hopkins University
Natalia Trayanova	Computational Cardiology Lab	Biomedical Engineering	Johns Hopkins University
Joseph Greenstein	Winslow Lab	Biomedical Engineering	Johns Hopkins University
Sonia Cortassa	Winslow Lab	Cardiology	Johns Hopkins

			University
David Kass	Cardiac hypertrophy and failure	Cardiology	Johns Hopkins University
Nazareno Paolocci	Nitrogen and oxygen reactive species on cardiac function	Cardiology	Johns Hopkins University
David Yue	Calcium Signals Lab	Biomedical Engineering	Johns Hopkins University
Jeffrey Saucerman	Cardiac Systems Biology Lab	Biomedical Engineering	University of Virginia
Jason Yang	Synthetic and Systems Biology	Biomedical Engineering	Boston University
Vincent Manganiello	Biochemical Physiology	National Heart, Lung, and Blood Institute	National Institute of Health
Sharon Francis	Cyclic nucleotide signaling pathways	Molecular Physiology and Biophysics	Vanderbilt University
Jackie Corbin	Cyclic nucleotide signaling pathways	Molecular Physiology and Biophysics	Vanderbilt University
Jennifer Busch	Cyclic nucleotide signaling pathways	Biology	Wheaton College

Jayvardhan Pandit	Pharmacokinetics (PDE2)	Pfizer Global R&D	Pfizer Inc.
Dave Nettleton	Metabolism and Pharmacokinetics (PDE2)	R&D	Novartis Inc.
Frank Menniti	Small molecule therapeutics for cognitive disorders (PDE2)	Basic Pharmaceutical Sciences	West Virginia University Mnemosyne Pharmaceuticals, Inc.
Viacheslav Nikolaev	Molecular imaging of cAMP and cGMP in Heart Failure	Heart Center	University of Gottingen
Rodolphe Fischmeister	Signaling and Cardiac Pathophysiology Lab	Pharmacology	University of Paris
Gregoire Vandecasteele	Signaling and Cardiac Pathophysiology Lab	Pharmacology	University of Paris
Jerome Levroy	Signaling and Cardiac Pathophysiology	Pharmacology	University of Paris
Stephan Herzig	Voltage-gated Ca2+ channels	Pharmacology	Cologne University
Jan Matthes	Voltage-gated Ca2+ channels	Pharmacology	Cologne University

Elza Kuzmenkina	Voltage-gated Ca2+ channels	Pharmacology	Cologne University
Joachim E. Schultz	Phosphodiesterase Pharmacology	Pharmaceutical Biochemistry	University of Tubingen
Thomas M. Lincoln	NO and cGMP signaling in VSM	Physiology	University of South Alabama
Franz Hofmann	Signal Transduction and Function of cGMP/PKG	Pharmacology and Toxicology	Technische Universitat Munchen
Daniel Gillespie	Stochastic Algorithms and Simulation	---	Dan T Gillespie Consulting
Achilles Pappano	Voltage-gated Ca2+ channels	Cell Biology	University of Connecticut

Table D.2. Research correspondences.

D.5. Graduate Board Oral (GBO) examination

The author appreciates all friends who helped preparing for the GBO. The author is grateful to the guidance of the following mentors at Johns Hopkins University for their efforts in conducting the GBO examination:

Name	Course	Primary Department
GBO Committee		

Raimond Winslow (PI)	Cardiac Electrophysiology	Biomedical Engineering
Lawrence Schramm	Neural Systems & Special Sciences (Medical School)	Biomedical Engineering
John Wierman (GBO Chair)	Stochastic Processes	Applied Mathematics & Statistics
Sanjeev Khudanpur	Random Signals Analysis	Electrical & Computer Engineering
Junghoon Lee	Medical Imaging Systems	Electrical & Computer Engineering
Joseph Greenstein (Alternate)	Cardiac Electrophysiology	Biomedical Engineering
Douglas Robinson (Alternate)	Molecules and Cells (Medical School)	Cell Biology
Mentors		
Brian O'Rourke	Cardiac Electrophysiology	Cardiology
Rajini Rao	Molecules and Cells (Medical School)	Physiology
Mary Blue	Neural Systems & Special Sciences (Medical School)	Kennedy Krieger Institute
AbdEl-Monem El-Sharkawy	Medical Imaging Systems	Radiology

Table D.3. Graduate Board Oral (GBO) examination committee and contacts.

D.6. Mentors in lab rotations

The author appreciates the guidance of the following mentors during rotation in their labs or associated labs at Johns Hopkins University:

Name	Lab	Primary Department
Jerry Prince	Image Analysis and Communication Lab (IACL)	Electrical & Computer Engineering
Dzung Pham	Neuroradiology	Radiology
Elliot McVeigh	Dynamic Imaging Lab	Biomedical Engineering
Daniel Herzka	Dynamic Imaging Lab	Biomedical Engineering
Robert G. Weiss	Weiss Lab	Heart & Vascular Institute
Katherine Wu	Cardiology	Heart & Vascular Institute
Susumu Mori	Brain Anatomical MRI Lab	Radiology

Table D.4. Mentors in lab rotations.

D.7. Mentors for teaching assistantships

The author thanks the following mentors for their guidance as a teaching assistant in their courses at Johns Hopkins University:

Name	Course	Primary Department
Michael Beer	Models and Simulation (Undergrad Year 2)	Biomedical Engineering

Joel Bader	Systems Bioengineering III (Undergrad Year 4/Graduate)	Biomedical Engineering

Table D.5. Mentors for teaching assistantships.

D.8. Instructors and teaching assists in courses taken

The author is grateful to the course instructors, lab and workshop instructors, teaching assistants, and patients who volunteered for clinical and scientific discussions, even though not all can be named.

Lead Instructor	**Course**	**Department**
Medical School Courses		
Mark F. Teaford	Human Anatomy	Functional Anatomy & Evolution
Kenneth Ross	Human Anatomy – Head & Neck	Functional Anatomy & Evolution
David Weishampel	Human Anatomy – Limbs	Functional Anatomy & Evolution
Valerie DeLeon	Human Anatomy – Embryology	Functional Anatomy & Evolution
Jon Lorsch	Molecules & Cells - Macromolecules	Biophysics & Biophysical Chemistry
Jeremy Nathans	Molecules & Cells – Molecular	Molecular Biology &

	Biology & Genetics	Genetics
Joy Yang	Molecules & Cells – Cell Physiology	Cell Biology
Peter Pedersen	Molecules & Cells – Metabolism	Biological Chemistry
Daniel Raben	Molecules & Cells – Metabolism	Biological Chemistry
Philip A. Cole	Pharmacology	Pharmacology
David Newman-Toker	Neural Systems & Special Senses (NSS) – NSS & Anatomy	Neurology
Nick Maragakis	NSS – General Sensory & Motor	Neurology
Albert Jun	NSS – Special Sensory & Motor	Ophthalmology
Nicoline Schiess	NSS – Multi-System Diseases	Neurology
Systems Biology		
Emad Boctor	Medical Imaging – Ultrasound & Nuclear Medicine	Radiology
Junghoon Lee	Medical Imaging – X-ray & CT	Electrical & Computer Engineering
AbdEl-Monem El-Sharkawy	Medical Imaging - MRI	Radiology
Eric Young	Models of the Neuron (Audit)	Biomedical Engineering
Engineering Theory		

Sanjeev Khudanpur	Random Signals Analysis	Electrical & Computer Engineering
Howard Weinert	Digital Signal Processing	Electrical & Computer Engineering
John Wierman	Stochastic Processes	Applied Mathematics & Statistics
Shih-Ping Han	Numerical Analysis	Applied Mathematics & Statistics
Pablo Iglesias	Linear Systems (Audit)	Electrical & Computer Engineering
Sridevi Sarma	Non-Linear Systems (Audit)	Biomedical Engineering

Table D.6. Lead course instructors for courses taken.

Appendix E. Bibliography and Reference Cited

[1] Mozaffarian D, Benjamin EJ, Go AS, Arnett DK, Blaha MJ, Cushman M, et al. Heart Disease and Stroke Statistics—2015 Update: A Report From the American Heart Association. Circulation. 2015;131:e29-e322.

[2] Mudd JO, Kass DA. Tackling heart failure in the twenty-first century. Nature. 2008;451:919-28.

[3] Marín-García J. Cyclic Nucleotides Signaling (Second Messengers) and Control of Myocardial Function: Effects of Heart Failure. Heart Failure: Humana Press; 2010. p. 161-9.

[4] Tomaselli GF, Marbán E. Electrophysiological remodeling in hypertrophy and heart failure. Cardiovascular research. 1999;42:270-83.

[5] Bers DM. Cardiac excitation–contraction coupling. Nature. 2002;415:198-205.

[6] Bers DM. Excitation Contraction Coupling and Cardiac Contractile Force. 2nd ed. Dordrecht: Kluwer Academic Publishers; 2001.

[7] Greenstein JL, Hinch R, Winslow RL. Mechanisms of Excitation-Contraction Coupling in an Integrative Model of the Cardiac Ventricular Myocyte. Biophysical Journal. 2006;90:77-91.

[8] Tsai EJ, Kass DA. Cyclic GMP signaling in cardiovascular pathophysiology and therapeutics. Pharmacology & Therapeutics. 2009;122:216-38.

[9] Takimoto E. Cyclic GMP-dependent signaling in cardiac myocytes. Circulation Journal. 2012;76:1819-25.

[10] Antos LLK, Schmidt HH, Hoffmann F, Stasch J-P. cGMP: generators, effectors and therapeutic implications: Springer; 2009.

[11] Cohen P. Protein kinases—the major drug targets of the twenty-first century? Nature Reviews Drug Discovery. 2002;1:309-15.

[12] Graves JD, Krebs EG. Protein Phosphorylation and Signal Transduction. Pharmacology & Therapeutics. 1999;82:111-21.

[13] Katz A. Physiology of the Heart: Wolters Kluwer Health; 2011.

[14] Boerrigter G, Lapp H, Burnett JC. Modulation of cGMP in heart failure: a new therapeutic paradigm. cGMP: Generators, Effectors and Therapeutic Implications: Springer; 2009. p. 485-506.

[15] Massion PB, Pelat M, Belge C, Balligand J-L. Regulation of the mammalian heart function by nitric oxide. Comparative Biochemistry and Physiology Part A: Molecular & Integrative Physiology. 2005;142:144-50.

[16] Hammond J, Balligand J-L. Nitric oxide synthase and cyclic GMP signaling in cardiac myocytes: From contractility to remodeling. Journal of molecular and cellular cardiology. 2012;52:330-40.

[17] Zaccolo M, Movsesian MA. cAMP and cGMP Signaling Cross-Talk Role of Phosphodiesterases and Implications for Cardiac Pathophysiology. Circulation Research. 2007;100:1569-78.

[18] Stangherlin A, Gesellchen F, Zoccarato A, Terrin A, Fields LA, Berrera M, et al. cGMP Signals Modulate cAMP Levels in a Compartment-Specific Manner to Regulate Catecholamine-Dependent Signaling in Cardiac MyocytesNovelty and Significance. Circulation Research. 2011;108:929-39.

[19] Champion HC, Skaf MW, Hare JM. Role of nitric oxide in the pathophysiology of heart failure. The Role of Nitric Oxide in Heart Failure: Springer; 2004. p. 81-92.

[20] Balligand J-L. Regulation of cardiac β-adrenergic response by nitric oxide. Cardiovascular research. 1999;43:607-20.

[21] Takimoto E, Champion HC, Belardi D, Moslehi J, Mongillo M, Mergia E, et al. cGMP Catabolism by Phosphodiesterase 5A Regulates Cardiac Adrenergic Stimulation by NOS3-Dependent Mechanism. Circulation Research. 2005;96:100-9.

[22] SENZAKI H, SMITH1 CJ, JUANG GJ, ISODA T, MAYER SP, OHLER A, et al. Cardiac phosphodiesterase 5 (cGMP-specific) modulates β-adrenergic signaling in vivo and is down-regulated in heart failure. The FASEB Journal. 2001;15:1718-26.

[23] Mongillo M, Tocchetti CG, Terrin A, Lissandron V, Cheung Y-F, Dostmann WR, et al. Compartmentalized phosphodiesterase-2 activity blunts β-adrenergic cardiac inotropy via an NO/cGMP-dependent pathway. Circulation Research. 2006;98:226-34.

[24] Abi-Gerges A, Richter W, Lefebvre F, Mateo P, Varin A, Heymes C, et al. Decreased Expression and Activity of cAMP Phosphodiesterases in Cardiac Hypertrophy and Its Impact on β-Adrenergic cAMP Signals. Circulation Research. 2009;105:784-92.

[25] Stangherlin A, Zaccolo M. cGMP-cAMP interplay in cardiac myocytes: a local affair with far-reaching consequences for heart function. Biochem Soc Trans. 2012;40:11-4.

[26] Weiss HR, Gong GX, Straznicka M, Yan L, Tse J, Scholz PM. Cyclic GMP and cyclic AMP induced changes in control and hypertrophic cardiac myocyte function interact through cyclic GMP affected cyclic-AMP phosphodiesterases. Canadian journal of physiology and pharmacology. 1999;77:422-31.

[27] Moalem J, Weiss HR, Davidov T, Rodriguez R, Molino B, Lazar MJ, et al. Heart Failure Reduces Both the Effects and Interaction Between Cyclic GMP and Cyclic AMP. Journal of Surgical Research. 2006;134:300-6.

[28] Mehel H, Emons J, Vettel C, Wittköpper K, Seppelt D, Dewenter M, et al. Phosphodiesterase-2 Is Up-Regulated in Human Failing Hearts and Blunts β-Adrenergic Responses in Cardiomyocytes. Journal of the American College of Cardiology. 2013;62:1596-606.

[29] Omori K, Kotera J. Overview of PDEs and their regulation. Circulation Research. 2007;100:309-27.

[30] Beavo JA. Cyclic nucleotide phosphodiesterases: functional implications of multiple isoforms. Physiological Reviews. 1995;75:725-48.

[31] Francis SH, Corbin JD, Bischoff E. Cyclic GMP-hydrolyzing phosphodiesterases. cGMP: Generators, Effectors and Therapeutic Implications: Springer; 2009. p. 367-408.

[32] Lugnier C. Cyclic nucleotide phosphodiesterase (PDE) superfamily: a new target for the development of specific therapeutic agents. Pharmacology & Therapeutics. 2006;109:366-98.

[33] Tamargo J, Caballero R, Gómez R, Delpón E. Cardiac electrophysiological effects of nitric oxide. Cardiovascular research. 2010;87:593-600.

[34] Saucerman JJ, McCulloch AD. Cardiac β-Adrenergic Signaling. Annals of the New York Academy of Sciences. 2006;1080:348-61.

[35] Wollert KC, Drexler H. Regulation of cardiac remodeling by nitric oxide: focus on cardiac myocyte hypertrophy and apoptosis. Heart failure reviews. 2002;7:317-25.

[36] Perera RK, Nikolaev VO. Compartmentation of cAMP signalling in cardiomyocytes in health and disease. Acta Physiologica. 2013.

[37] Lohse MJ, Engelhardt S, Eschenhagen T. What is the role of β-adrenergic signaling in heart failure? Circulation Research. 2003;93:896-906.

[38] Ding B, Abe J-i, Wei H, Xu H, Che W, Aizawa T, et al. A positive feedback loop of phosphodiesterase 3 (PDE3) and inducible cAMP early repressor (ICER) leads to cardiomyocyte apoptosis. Proceedings of the National Academy of Sciences of the United States of America. 2005;102:14771-6.

[39] Lehnart SE, Wehrens XH, Reiken S, Warrier S, Belevych AE, Harvey RD, et al. Phosphodiesterase 4D deficiency in the ryanodine-receptor complex promotes heart failure and arrhythmias. Cell. 2005;123:25-35.

[40] Molina CE, Leroy J, Richter W, Xie M, Scheitrum C, Lee I-O, et al. Cyclic Adenosine Monophosphate Phosphodiesterase Type 4 Protects Against Atrial Arrhythmias. Journal of the American College of Cardiology. 2012;59:2182-90.

[41] Ding B, Abe J-i, Wei H, Huang Q, Walsh RA, Molina CA, et al. Functional Role of Phosphodiesterase 3 in Cardiomyocyte Apoptosis: Implication in Heart Failure. Circulation. 2005;111:2469-76.

[42] Abi-Gerges A, Richter W, Lefebvre F, Mateo P, Varin A, Heymes C, et al. Decreased expression and activity of cAMP phosphodiesterases in cardiac hypertrophy and its impact on β-adrenergic cAMP signals. Circulation research. 2009;105:784-92.

[43] Mehel H, Emons J, Vettel C, Wittköpper K, Seppelt D, Dewenter M, et al. Phosphodiesterase-2 is up-regulated in human failing hearts and blunts β-adrenergic responses in cardiomyocytes. Journal of the American College of Cardiology. 2013;62:1596-606.

[44] Knight W, Yan C. Cardiac cyclic nucleotide phosphodiesterases: function, regulation, and therapeutic prospects. Hormone and metabolic research= Hormon-und Stoffwechselforschung= Hormones et metabolisme. 2012;44:766.

[45] Yan C, Ding B, Shishido T, Woo C-H, Itoh S, Jeon K-I, et al. Activation of extracellular signal-regulated kinase 5 reduces cardiac apoptosis and dysfunction via inhibition of a phosphodiesterase 3A/inducible cAMP early repressor feedback loop. Circulation research. 2007;100:510-9.

[46] Kostic M, Erdogan S, Rena G, Borchert G, Hoch B, Bartel S, et al. Altered expression of PDE1 and PDE4 cyclic nucleotide phosphodiesterase isoforms in 7-oxo-prostacyclin-preconditioned rat heart. Journal of molecular and cellular cardiology. 1997;29:3135-46.

[47] Gillespie DT. Exact stochastic simulation of coupled chemical reactions. The journal of physical chemistry. 1977;81:2340-61.

[48] Guazzi M. Clinical Use of Phosphodiesterase-5 Inhibitors in Chronic Heart Failure. Circulation: Heart Failure. 2008;1:272-80.

[49] Benitah J-P, Alvarez JL, Gómez AM. L-type Ca 2+ current in ventricular cardiomyocytes. Journal of molecular and cellular cardiology. 2010;48:26-36.

[50] Maurice DH, Ke H, Ahmad F, Wang Y, Chung J, Manganiello VC. Advances in targeting cyclic nucleotide phosphodiesterases. Nature Reviews Drug Discovery. 2014;13:290-314.

[51] Sutherland EW, Rall T. The relation of adenosine-3', 5'-phosphate and phosphorylase to the actions of catecholamines and other hormones. Pharmacological Reviews. 1960;12:265-99.

[52] Beavo JA, Brunton LL. Cyclic nucleotide research -- still expanding after half a century. Nat Rev Mol Cell Biol. 2002;3:710-8.

[53] Dzimiri N. Regulation of β-adrenoceptor signaling in cardiac function and disease. Pharmacological Reviews. 1999;51:465-502.

[54] Smith M, Drummond G, Khorana H. Cyclic Phosphates. IV. 1 Ribonucleoside-3', 5'Cyclic Phosphates. A General Method of Synthesis and Some Properties. Journal of the American Chemical Society. 1961;83:698-706.

[55] Ashman D, Lipton R, Melicow MM, Price T. Isolation of adenosine 3′, 5′-monophosphate and guanosine 3′, 5′-monophosphate from rat urine. Biochemical and Biophysical Research Communications. 1963;11:330-4.

[56] Kots AY, Martin E, Sharina IG, Murad F. A short history of cGMP, guanylyl cyclases, and cGMP-dependent protein kinases. cGMP: Generators, Effectors and Therapeutic Implications: Springer; 2009. p. 1-14.

[57] Kuo J, Greengard P. Cyclic nucleotide-dependent protein kinases, IV. Widespread occurrence of adenosine 3′, 5′-monophosphate-dependent protein kinase in various tissues and phyla of the animal kingdom. Proceedings of the National Academy of Sciences. 1969;64:1349-55.

[58] Ignarro LJ, Buga GM, Wood KS, Byrns RE, Chaudhuri G. Endothelium-derived relaxing factor produced and released from artery and vein is nitric oxide. Proceedings of the National Academy of Sciences. 1987;84:9265-9.

[59] Balligand J-L, Kelly RA, Marsden PA, Smith TW, Michel T. Control of cardiac muscle cell function by an endogenous nitric oxide signaling system. Proceedings of the National Academy of Sciences. 1993;90:347-51.

[60] Rall T, Sutherland EW. Formation of a cyclic adenine ribonucleotide by tissue particles. Journal of Biological Chemistry. 1958;232:1065-76.

[61] Francis SH, Blount MA, Corbin JD. Mammalian cyclic nucleotide phosphodiesterases: molecular mechanisms and physiological functions. Physiological reviews. 2011;91:651-90.

[62] Kass DA, Takimoto E, Nagayama T, Champion HC. Phosphodiesterase regulation of nitric oxide signaling. Cardiovascular research. 2007;75:303-14.

[63] Fischmeister R, Castro LR, Abi-Gerges A, Rochais F, Jurevičius J, Leroy J, et al. Compartmentation of Cyclic Nucleotide Signaling in the Heart The Role of Cyclic Nucleotide Phosphodiesterases. Circulation Research. 2006;99:816-28.

[64] Nobelprize.org. Nobel Media AB. <http://wwwnobelprizeorg/faq/questions_in_categoryphp?id=22>. 2014. Web. 1 Apr 2016.

[65] Conti M, Beavo J. Biochemistry and physiology of cyclic nucleotide phosphodiesterases: essential components in cyclic nucleotide signaling. Annu Rev Biochem. 2007;76:481-511.

[66] Hofmann F, Bernhard D, Lukowski R, Weinmeister P. cGMP Regulated Protein Kinases (cGK). In: Schmidt HHW, Hofmann F, Stasch J-P, editors. cGMP: Generators, Effectors and Therapeutic Implications: Springer Berlin Heidelberg; 2009. p. 137-62.

[67] Conti M, Mika D, Richter W. Cyclic AMP compartments and signaling specificity: Role of cyclic nucleotide phosphodiesterases. The Journal of General Physiology. 2014;143:29-38.

[68] Miller CL, Yan C. Targeting cyclic nucleotide phosphodiesterase in the heart: therapeutic implications. Journal of cardiovascular translational research. 2010;3:507-15.

[69] Zhang M, Koitabashi N, Nagayama T, Rambaran R, Feng N, Takimoto E, et al. Expression, activity, and pro-hypertrophic effects of PDE5A in cardiac myocytes. Cellular Signalling. 2008;20:2231-6.

[70] Zoraghi R, Corbin JD, Francis SH. Properties and functions of GAF domains in cyclic nucleotide phosphodiesterases and other proteins. Molecular pharmacology. 2004;65:267-78.

[71] Saucerman JJ, Brunton LL, Michailova AP, McCulloch AD. Modeling β-Adrenergic Control of Cardiac Myocyte Contractility in Silico. Journal of Biological Chemistry. 2003;278:47997-8003.

[72] Iancu RV, Jones SW, Harvey RD. Compartmentation of cAMP signaling in cardiac myocytes: a computational study. Biophysical Journal. 2007;92:3317-31.

[73] Kraeutler M, Soltis A, Saucerman J. Modeling cardiac β-adrenergic signaling with normalized-Hill differential equations: comparison with a biochemical model. BMC systems biology. 2010;4:157.

[74] Yang JH, Saucerman JJ. Phospholemman is a negative feed-forward regulator of Ca^{2+} in β-adrenergic signaling, accelerating β-adrenergic inotropy. Journal of molecular and cellular cardiology. 2012;52:1048-55.

[75] Heijman J, Volders PG, Westra RL, Rudy Y. Local control of β-adrenergic stimulation: Effects on ventricular myocyte electrophysiology and Ca^{2+}-transient. Journal of molecular and cellular cardiology. 2011;50:863-71.

[76] Saucerman JJ, Healy SN, Belik ME, Puglisi JL, McCulloch AD. Proarrhythmic Consequences of a KCNQ1 AKAP-Binding Domain Mutation: Computational Models of Whole Cells and Heterogeneous Tissue. Circulation research. 2004;95:1216-24.

[77] Massion PB, Balligand JL. Modulation of cardiac contraction, relaxation and rate by the endothelial nitric oxide synthase (eNOS): lessons from genetically modified mice. The Journal of Physiology. 2003;546:63-75.

[78] Keef KD, Hume JR, Zhong J. Regulation of cardiac and smooth muscle Ca2+channels (CaV1.2a,b) by protein kinases2001.

[79] Hashambhoy YL, Winslow RL, Greenstein JL. CaMKII-Induced Shift in Modal Gating Explains L-Type Ca^{2+} Current Facilitation: A Modeling Study. Biophysical Journal. 2009;96:1770-85.

[80] Segel IH. Enzyme kinetics: Wiley, New York; 1975.

[81] Martinez SE, Wu AY, Glavas NA, Tang X-B, Turley S, Hol WGJ, et al. The two GAF domains in phosphodiesterase 2A have distinct roles in dimerization and in cGMP binding. Proceedings of the National Academy of Sciences. 2002;99:13260-5.

[82] Castro LRV, Verde I, Cooper DMF, Fischmeister R. Cyclic Guanosine Monophosphate Compartmentation in Rat Cardiac Myocytes. Circulation. 2006;113:2221-8.

[83] Herget S, Lohse MJ, Nikolaev VO. Real-time monitoring of phosphodiesterase inhibition in intact cells. Cellular Signalling. 2008;20:1423-31.

[84] Nikolaev VO, Gambaryan S, Engelhardt S, Walter U, Lohse MJ. Real-time Monitoring of the PDE2 Activity of Live Cells: HORMONE-STIMULATED cAMP HYDROLYSIS IS FASTER THAN HORMONE-STIMULATED cAMP SYNTHESIS. Journal of Biological Chemistry. 2005;280:1716-9.

[85] Rochais F, Abi-Gerges A, Horner K, Lefebvre F, Cooper DM, Conti M, et al. A specific pattern of phosphodiesterases controls the cAMP signals generated by different Gs-coupled receptors in adult rat ventricular myocytes. Circulation research. 2006;98:1081-8.

[86] Verde I, Vandecasteele G, Lezoualc'h F, Fischmeister R. Characterization of the cyclic nucleotide phosphodiesterase subtypes involved in the regulation of the L‐type Ca2+ current in rat ventricular myocytes. British Journal of Pharmacology. 1999;127:65-74.

[87] Yan C, Zhao AZ, Bentley JK, Beavo JA. The Calmodulin-dependent Phosphodiesterase Gene PDE1C Encodes Several Functionally Different Splice Variants in a Tissue-specific Manner. Journal of Biological Chemistry. 1996;271:25699-706.

[88] Prigent A, Fougier S, Nemoz G, Anker G, Pacheco H, Lugnier C, et al. Comparison of cyclic nucleotide phosphodiesterase isoforms from rat heart and bovine aorta: Separation and inhibition by selective reference phosphodiesterase inhibitors. Biochemical pharmacology. 1988;37:3671-81.

[89] Beavo J, Hardman JG, Sutherland EW. Stimulation of adenosine 3', 5'-monophosphate hydrolysis by guanosine 3', 5'-monophosphate. Journal of Biological Chemistry. 1971;246:3841-6.

[90] Komas N, Le Bec A, Stoclet J-C, Lugnier C. Cardiac cGMP-stimulated cyclic nucleotide phosphodiesterases: effects of cGMP analogues and drugs. European Journal of Pharmacology: Molecular Pharmacology. 1991;206:5-13.

[91] Yamamoto T, Yamamoto S, Osborne J, Manganiello V, Vaughan M, Hidaka H. Complex effects of inhibitors on cyclic GMP-stimulated cyclic nucleotide phosphodiesterase. Journal of Biological Chemistry. 1983;258:14173-7.

[92] Martins TJ, Mumby M, Beavo J. Purification and characterization of a cyclic GMP-stimulated cyclic nucleotide phosphodiesterase from bovine tissues. Journal of Biological Chemistry. 1982;257:1973-9.

[93] Whalin ME, Strada SJ, Thompson W. Purification and partial characterization of membrane-associated type II (cGMP-activatable) cyclic nucleotide phosphodiesterase from rabbit brain. Biochimica et Biophysica Acta (BBA)-Molecular Cell Research. 1988;972:79-94.

[94] Osadchii OE. Myocardial phosphodiesterases and regulation of cardiac contractility in health and cardiac disease. Cardiovascular drugs and therapy. 2007;21:171-94.

[95] Francis SH, Busch JL, Corbin JD. cGMP-Dependent Protein Kinases and cGMP Phosphodiesterases in Nitric Oxide and cGMP Action. Pharmacological Reviews. 2010;62:525-63.

[96] He R, Komas N, Ekholm D, Murata T, Taira M, Hockman S, et al. Expression and characterization of deletion recombinants of two cGMP-inhibited cyclic nucleotide phosphodiesterases (PDE-3). Cell biochemistry and biophysics. 1998;29:89-111.

[97] Vila Petroff MG, Egan JM, Wang X, Sollott SJ. Glucagon-Like Peptide-1 Increases cAMP but Fails to Augment Contraction in Adult Rat Cardiac Myocytes. Circulation Research. 2001;89:445-52.

[98] Kuznetsov V, Pak E, Robinson RB, Steinberg SF. β2-Adrenergic Receptor Actions in Neonatal and Adult Rat Ventricular Myocytes. Circulation Research. 1995;76:40-52.

[99] Zaccolo M, Pozzan T. Discrete microdomains with high concentration of cAMP in stimulated rat neonatal cardiac myocytes. Science. 2002;295:1711-5.

[100] Götz KR, Sprenger JU, Perera RK, Steinbrecher JH, Lehnart SE, Kuhn M, et al. Transgenic mice for real-time visualization of cGMP in intact adult cardiomyocytes. Circulation research. 2014;114:1235-45.

[101] Mongillo M, McSorley T, Evellin S, Sood A, Lissandron V, Terrin A, et al. Fluorescence Resonance Energy Transfer–Based Analysis of cAMP Dynamics in Live Neonatal Rat Cardiac Myocytes Reveals Distinct Functions of Compartmentalized Phosphodiesterases. Circulation research. 2004;95:67-75.

[102] Johnson W, Katugampola S, Able S, Napier C, Harding S. Profiling of cAMP and cGMP phosphodiesterases in isolated ventricular cardiomyocytes from human hearts: comparison with rat and guinea pig. Life sciences. 2012;90:328-36.

[103] Méry PF, Pavoine C, Pecker F, Fischmeister R. Erythro-9-(2-hydroxy-3-nonyl)adenine inhibits cyclic GMP-stimulated phosphodiesterase in isolated cardiac myocytes. Molecular pharmacology. 1995;48:121-30.

[104] Boess FG, Hendrix M, van der Staay F-J, Erb C, Schreiber R, van Staveren W, et al. Inhibition of phosphodiesterase 2 increases neuronal cGMP, synaptic plasticity and memory performance. Neuropharmacology. 2004;47:1081-92.

[105] Hambleton R, Krall J, Tikishvili E, Honeggar M, Ahmad F, Manganiello VC, et al. Isoforms of Cyclic Nucleotide Phosphodiesterase PDE3 and Their Contribution to cAMP Hydrolytic Activity in Subcellular Fractions of Human Myocardium. Journal of Biological Chemistry. 2005;280:39168-74.

[106] Christ T, Galindo-Tovar A, Thoms M, Ravens U, Kaumann AJ. Inotropy and L-type Ca2+ current, activated by β1- and β2-adrenoceptors, are differently controlled by phosphodiesterases 3 and 4 in rat heart. British Journal of Pharmacology. 2009;156:62-83.

[107] Bethke T, Meyer W, Schmitz W, Scholz H, Stein B, Thomas K, et al. Phosphodiesterase inhibition in ventricular cardiomyocytes from guinea‐pig hearts. British Journal of Pharmacology. 1992;107:127-33.

[108] Torphy TJ, Undem B. Phosphodiesterase inhibitors: new opportunities for the treatment of asthma. Thorax. 1991;46:512-23.

[109] Reneerkens OA, Rutten K, Steinbusch HW, Blokland A, Prickaerts J. Selective phosphodiesterase inhibitors: a promising target for cognition enhancement. Psychopharmacology. 2009;202:419-43.

[110] Boswell‐Smith V, Spina D, Page CP. Phosphodiesterase inhibitors. British Journal of Pharmacology. 2006;147:S252-S7.

[111] Takimoto E, Champion HC, Li M, Belardi D, Ren S, Rodriguez ER, et al. Chronic inhibition of cyclic GMP phosphodiesterase 5A prevents and reverses cardiac hypertrophy. Nature medicine. 2005;11:214-22.

[112] Houslay MD, Schafer P, Zhang KYJ. Keynote review: Phosphodiesterase-4 as a therapeutic target. Drug Discovery Today. 2005;10:1503-19.

[113] Yan C, Miller CL, Abe J-i. Regulation of phosphodiesterase 3 and inducible cAMP early repressor in the heart. Circulation Research. 2007;100:489-501.

[114] Menniti FS, Faraci WS, Schmidt CJ. Phosphodiesterases in the CNS: targets for drug development. Nat Rev Drug Discov. 2006;5:660-70.

[115] Rahnama'i MS, Ückert S, Hohnen R, van Koeveringe GA. The role of phosphodiesterases in bladder pathophysiology. Nature Reviews Urology. 2013;10:414-24.

[116] Richter W, Xie M, Scheitrum C, Krall J, Movsesian MA, Conti M. Conserved expression and functions of PDE4 in rodent and human heart. Basic research in cardiology. 2011;106:249-62.

[117] Lehnart SE, Marks AR. Phosphodiesterase 4D and heart failure: a cautionary tale. Expert Opin Ther Targets. 2006;10:677-88.

[118] Terasaki W, Appleman M. The role of cyclic GMP in the regulation of cyclic AMP hydrolysis. Metabolism. 1975;24:311-9.

[119] Bode DC, Kanter JR, Brunton LL. Cellular distribution of phosphodiesterase isoforms in rat cardiac tissue. Circulation research. 1991;68:1070-9.

[120] Perera RK, Sprenger JU, Steinbrecher JH, Hübscher D, Lehnart SE, Abesser M, et al. Microdomain Switch of cGMP-Regulated Phosphodiesterases Leads to ANP-Induced Augmentation of β-Adrenoceptor-Stimulated Contractility in Early Cardiac Hypertrophy. Circulation research. 2015;116:1304-11.

[121] Saucerman JJ, Greenwald EC, Polanowska-Grabowska R. Mechanisms of cyclic AMP compartmentation revealed by computational models. The Journal of General Physiology. 2014;143:39-48.

[122] Edwards HV, Christian F, Baillie GS. cAMP: novel concepts in compartmentalised signalling. Seminars in cell & developmental biology: Elsevier; 2012. p. 181-90.

[123] Kritzer MD, Li J, Dodge-Kafka K, Kapiloff MS. AKAPs: the architectural underpinnings of local cAMP signaling. Journal of molecular and cellular cardiology. 2012;52:351-8.

[124] Mika D, Leroy J, Vandecasteele G, Fischmeister R. PDEs create local domains of cAMP signaling. Journal of molecular and cellular cardiology. 2012;52:323-9.

[125] Ahmad F, Shen W, Vandeput F, Szabo-Fresnais N, Krall J, Degerman E, et al. Regulation of SERCA2 activity by PDE3A in human myocardium: Phosphorylation-dependent interaction of PDE3A1 with SERCA2. Journal of Biological Chemistry. 2015:jbc. M115. 638585.

[126] Lu Z, Xu X, Hu X, Lee S, Traverse JH, Zhu G, et al. Oxidative stress regulates left ventricular PDE5 expression in the failing heart. Circulation. 2010;121:1474-83.

[127] Zhao CY, Greenstein JL, Winslow RL. Interaction between phosphodiesterases in the regulation of the cardiac β-adrenergic pathway. Journal of molecular and cellular cardiology. 2015;88:29-38.

[128] Castro LRV, Schittl J, Fischmeister R. Feedback Control Through cGMP-Dependent Protein Kinase Contributes to Differential Regulation and Compartmentation of cGMP in Rat Cardiac Myocytes. Circulation Research. 2010;107:1232-40.

[129] Batchelor AM, Bartus K, Reynell C, Constantinou S, Halvey EJ, Held KF, et al. Exquisite sensitivity to subsecond, picomolar nitric oxide transients conferred on cells by guanylyl cyclase-coupled receptors. Proceedings of the National Academy of Sciences. 2010;107:22060-5.

[130] MacKenzie SJ, Baillie GS, McPhee I, MacKenzie C, Seamons R, McSorley T, et al. Long PDE4 cAMP specific phosphodiesterases are activated by protein kinase A ‐ mediated phosphorylation of a single serine residue in Upstream Conserved Region 1 (UCR1). British Journal of Pharmacology. 2002;136:421-33.

[131] Leroy J, Abi-Gerges A, Nikolaev VO, Richter W, Lechêne P, Mazet J-L, et al. Spatiotemporal Dynamics of β-Adrenergic cAMP Signals and L-Type Ca2+ Channel Regulation in Adult Rat Ventricular Myocytes Role of Phosphodiesterases. Circulation Research. 2008;102:1091-100.

[132] Corbin JD, Turko IV, Beasley A, Francis SH. Phosphorylation of phosphodiesterase ‐ 5 by cyclic nucleotide ‐ dependent protein kinase alters its catalytic and allosteric cGMP ‐ binding activities. European Journal of Biochemistry. 2000;267:2760-7.

[133] Rybalkin SD, Rybalkina IG, Feil R, Hofmann F, Beavo JA. Regulation of cGMP-specific phosphodiesterase (PDE5) phosphorylation in smooth muscle cells. Journal of Biological Chemistry. 2002;277:3310-7.

[134] Sette C, Conti M. Phosphorylation and Activation of a cAMP-specific Phosphodiesterase by the cAMP-dependent Protein Kinase INVOLVEMENT OF SERINE 54 IN THE ENZYME ACTIVATION. Journal of Biological Chemistry. 1996;271:16526-34.

[135] Ferrero R, Rodríguez-Pascual F, Miras-Portugal MT, Torres M. Comparative effects of several nitric oxide donors on intracellular cyclic GMP levels in bovine chromaffin cells: correlation with nitric oxide production. British Journal of Pharmacology. 1999;127:779-87.

[136] Sigma-Aldrich. S-Nitroso-N-acetyl-DL-penicillamine. Production Information. Saint Louis, Missouri2007.

[137] Miller MR, Megson IL. Recent developments in nitric oxide donor drugs. British Journal of Pharmacology. 2007;151:305-21.

[138] Al-Sa'doni H, Ferro A. S-Nitrosothiols: a class of nitric oxide-donor drugs. Clinical science. 2000;98:507-20.

[139] Schmidt K, Desch W, Klatt P, Kukovetz WR, Mayer B. Release of nitric oxide from donors with known half-life: a mathematical model for calculating nitric oxide concentrations in aerobic solutions. Naunyn-Schmiedeberg's Archives of Pharmacology. 1997;355:457-62.

[140] Ramamurthi A, Lewis RS. Measurement and Modeling of Nitric Oxide Release Rates for Nitric Oxide Donors. Chemical Research in Toxicology. 1997;10:408-13.

[141] Kar S, Kavdia M. Modeling of biopterin-dependent pathways of eNOS for nitric oxide and superoxide production. Free Radical Biology and Medicine. 2011;51:1411-27.

[142] Russell TR, Terasaki WL, Appleman MM. Separate Phosphodiesterases for the Hydrolysis of Cyclic Adenosine 3',5'-Monophosphate and Cyclic Guanosine 3',5'-Monophosphate in Rat Liver. Journal of Biological Chemistry. 1973;248:1334-40.

[143] Vila-Petroff MG, Younes A, Egan J, Lakatta EG, Sollott SJ. Activation of distinct cAMP-dependent and cGMP-dependent pathways by nitric oxide in cardiac myocytes. Circulation Research. 1999;84:1020-31.

[144] Shan X, Quaile MP, Monk JK, French B, Cappola TP, Margulies KB. Differential Expression of PDE5 in Failing and Nonfailing Human Myocardium. Circulation: Heart Failure. 2012;5:79-86.

[145] Pokreisz P, Vandenwijngaert S, Bito V, Van den Bergh A, Lenaerts I, Busch C, et al. Ventricular phosphodiesterase-5 expression is increased in patients with advanced heart failure and contributes to adverse ventricular remodeling after myocardial infarction in mice. Circulation. 2009;119:408-16.

[146] Nagendran J, Archer SL, Soliman D, Gurtu V, Moudgil R, Haromy A, et al. Phosphodiesterase type 5 is highly expressed in the hypertrophied human right ventricle, and acute inhibition of phosphodiesterase type 5 improves contractility. Circulation. 2007;116:238-48.

[147] Hare JM. Nitric oxide and excitation–contraction coupling. Journal of molecular and cellular cardiology. 2003;35:719-29.

[148] Murad F. Nitric Oxide and Cyclic GMP in Cell Signaling and Drug Development. New England Journal of Medicine. 2006;355:2003-11.

[149] Rastaldo R, Pagliaro P, Cappello S, Penna C, Mancardi D, Westerhof N, et al. Nitric oxide and cardiac function. Life sciences. 2007;81:779-93.

[150] Thomas DD, Ridnour LA, Isenberg JS, Flores-Santana W, Switzer CH, Donzelli S, et al. The chemical biology of nitric oxide: Implications in cellular signaling. Free Radical Biology and Medicine. 2008;45:18-31.

[151] Simon JN, Duglan D, Casadei B, Carnicer R. Nitric oxide synthase regulation of cardiac excitation–contraction coupling in health and disease. Journal of molecular and cellular cardiology. 2014;73:80-91.

[152] Ziolo MT, Kohr MJ, Wang H. Nitric oxide signaling and the regulation of myocardial function. Journal of molecular and cellular cardiology. 2008;45:625-32.

[153] Zhang YH, Casadei B. Sub-cellular targeting of constitutive NOS in health and disease. Journal of molecular and cellular cardiology. 2012;52:341-50.

[154] Wahler GM, Dollinger SJ. Nitric oxide donor SIN-1 inhibits mammalian cardiac calcium current through cGMP-dependent protein kinase. American Journal of Physiology-Cell Physiology. 1995;268:C45-C54.

[155] Barouch LA, Harrison RW, Skaf MW, Rosas GO, Cappola TP, Kobeissi ZA, et al. Nitric oxide regulates the heart by spatial confinement of nitric oxide synthase isoforms. Nature. 2002;416:337-9.

[156] Jiang L, Gawler D, Hodson N, Milligan C, Pearson H, Porter V, et al. Regulation of cloned cardiac L-type calcium channels by cGMP-dependent protein kinase. Journal of Biological Chemistry. 2000;275:6135-43.

[157] Yang L, Liu G, Zakharov SI, Bellinger AM, Mongillo M, Marx SO. Protein kinase G phosphorylates Cav1. 2 α1c and β2 subunits. Circulation Research. 2007;101:465-74.

[158] Fiedler B, Lohmann SM, Smolenski A, Linnemüller S, Pieske B, Schröder F, et al. Inhibition of calcineurin-NFAT hypertrophy signaling by cGMP-dependent protein kinase type I in cardiac myocytes. Proceedings of the National Academy of Sciences. 2002;99:11363-8.

[159] Carabelli V, D'Ascenzo M, Carbone E, Grassi C. Nitric oxide inhibits neuroendocrine CaV1 L-channel gating via cGMP-dependent protein kinase in cell-attached patches of bovine chromaffin cells. The Journal of Physiology. 2002;541:351-66.

[160] Klein G, Drexler H, Schröder F. Protein kinase G reverses all isoproterenol induced changes of cardiac single L-type calcium channel gating. Cardiovascular research. 2000;48:367-74.

[161] Schröder F, Klein G, Fiedler B, Bastein M, Schnasse N, Hillmer A, et al. Single L-type Ca2+ channel regulation by cGMP-dependent protein kinase type I in adult cardiomyocytes from PKG I transgenic mice. Cardiovascular research. 2003;60:268-77.

[162] Méry PF, Lohmann SM, Walter U, Fischmeister R. Ca^{2+} current is regulated by cyclic GMP-dependent protein kinase in mammalian cardiac myocytes. Proceedings of the National Academy of Sciences. 1991;88:1197-201.

[163] Sumii K, Sperelakis N. cGMP-Dependent Protein Kinase Regulation of the L-Type Ca2+ Current in Rat Ventricular Myocytes. Circulation research. 1995;77:803-12.

[164] Harvey RD, Hell JW. Ca< sub> V</sub> 1.2 signaling complexes in the heart. Journal of molecular and cellular cardiology. 2013;58:143-52.

[165] Zhang M, Takimoto E, Lee D-i, Santos CX, Nakamura T, Hsu S, et al. Pathological cardiac hypertrophy alters intracellular targeting of phosphodiesterase type 5 from nitric oxide synthase-3 to natriuretic peptide signaling. Circulation. 2012;126:942-51.

[166] Lee DI, Zhu G, Sasaki T, Cho G-S, Hamdani N, Holewinski R, et al. Phosphodiesterase 9A controls nitric-oxide-independent cGMP and hypertrophic heart disease. Nature. 2015;519:472-6.

[167] Takimoto E, Belardi D, Tocchetti CG, Vahebi S, Cormaci G, Ketner EA, et al. Compartmentalization of cardiac β-adrenergic inotropy modulation by phosphodiesterase type 5. Circulation. 2007;115:2159-67.

[168] Winslow RL, Rice J, Jafri S, Marban E, O'Rourke B. Mechanisms of altered excitation-contraction coupling in canine tachycardia-induced heart failure, II Model studies. Circulation Research. 1999;84:571-86.

[169] Katsube Y, Yokoshiki H, Nguyen L, Sperelakis N. Differences in isoproterenol stimulation of Ca^{2+} current of rat ventricular myocytes in neonatal compared to adult. European journal of pharmacology. 1996;317:391-400.

[170] Stern MD. Theory of excitation-contraction coupling in cardiac muscle. Biophysical Journal. 1992;63:497.

[171] Greenstein JL, Winslow RL. An integrative model of the cardiac ventricular myocyte incorporating local control of Ca 2+ release. Biophysical Journal. 2002;83:2918-45.

[172] Winslow RL, Cortassa S, O'Rourke B, Hashambhoy YL, Rice JJ, Greenstein JL. Integrative modeling of the cardiac ventricular myocyte. Wiley Interdisciplinary Reviews: Systems Biology and Medicine. 2011;3:392-413.

[173] Allen DG, Kentish JC. The cellular basis of the length-tension relation in cardiac muscle. Journal of molecular and cellular cardiology. 1985;17:821-40.

[174] Rice JJ, Winslow RL, Hunter WC. Comparison of putative cooperative mechanisms in cardiac muscle: length dependence and dynamic responses. American Journal of Physiology-Heart and Circulatory Physiology. 1999;276:H1734-H54.

[175] Zhao CY, Greenstein JL, Winslow RL. Roles of phosphodiesterases in the regulation of the cardiac cyclic nucleotide cross-talk signaling network. Journal of molecular and cellular cardiology. 2016;91:215-27.

[176] Greenstein JL, Winslow RL. An Integrative Model of the Cardiac Ventricular Myocyte Incorporating Local Control of Ca2+ Release. Biophysical Journal. 2002;83:2918-45.

[177] O'Rourke B, Kass DA, Tomaselli GF, Kääb S, Tunin R, Marbán E. Mechanisms of Altered Excitation-Contraction Coupling in Canine Tachycardia-Induced Heart Failure, I: Experimental Studies. Circulation Research. 1999;84:562-70.

[178] Tanskanen AJ, Greenstein JL, O'Rourke B, Winslow RL. The Role of Stochastic and Modal Gating of Cardiac L-Type Ca2+ Channels on Early After-Depolarizations. Biophys J. 2005;88:85-95.

[179] Yue DT, Herzig S, Marban E. Beta-adrenergic stimulation of calcium channels occurs by potentiation of high-activity gating modes. Proceedings of the National Academy of Sciences. 1990;87:753-7.

[180] Greenstein JL, Tanskanen AJ, Winslow RL. Modeling the Actions of β-Adrenergic Signaling on Excitation—Contraction Coupling Processes. Annals of the New York Academy of Sciences. 2004;1015:16-27.

[181] Jafri MS, Rice JJ, Winslow RL. Cardiac Ca2+ dynamics: the roles of ryanodine receptor adaptation and sarcoplasmic reticulum load. Biophysical Journal. 1998;74:1149-68.

[182] Zhao CY, Greenstein JL, Winslow RL. Regulation of the Cardiac β-Adrenergic Pathway via cAMP-cGMP Competition. Biophysical Journal. 2014;108:260a.

[183] Gerhardstein BL, Puri TS, Chien AJ, Hosey MM. Identification of the sites phosphorylated by cyclic AMP-dependent protein kinase on the β2 subunit of L-type voltage-dependent calcium channels. Biochemistry. 1999;38:10361-70.

[184] van der Heyden MA, Wijnhoven TJ, Opthof T. Molecular aspects of adrenergic modulation of cardiac L-type Ca2+ channels. Cardiovascular research. 2005;65:28-39.

[185] Ganesan AN, Maack C, Johns DC, Sidor A, O'Rourke B. β-Adrenergic Stimulation of L-type Ca2+ Channels in Cardiac Myocytes Requires the Distal Carboxyl Terminus of α1C but Not Serine 1928. Circulation Research. 2006;98:e11-e8.

[186] Tohse N, Sperelakis N. cGMP inhibits the activity of single calcium channels in embryonic chick heart cells. Circulation Research. 1991;69:325-31.

[187] Tohse N, Nakaya H, Kanno YT. Cyclic GMP ‐ mediated inhibition of L ‐ type Ca2+ channel activity by human natriuretic peptide in rabbit heart cells. British Journal of Pharmacology. 1995;114:1076-82.

[188] Grassi C, D'Ascenzo M, Azzena GB. Modulation of Ca v 1 and Ca v 2.2 channels induced by nitric oxide via cGMP-dependent protein kinase. Neurochemistry international. 2004;45:885-93.

[189] Wiechen K, Yue D, Herzig S. Two distinct functional effects of protein phosphatase inhibitors on guinea-pig cardiac L-type Ca2+ channels. The Journal of Physiology. 1995;484:583-92.

[190] Hashambhoy YL, Greenstein JL, Winslow RL. Role of CaMKII in RyR leak, EC coupling and action potential duration: A computational model. Journal of molecular and cellular cardiology. 2010;49:617-24.

[191] Bers DM, Patton CW, Nuccitelli R. Chapter 1 - A Practical Guide to the Preparation of Ca2+ Buffers. In: Michael W, editor. Methods in Cell Biology: Academic Press; 2010. p. 1-26.

[192] Kameyama M, Hofmann F, Trautwein W. On the mechanism of β-adrenergic regulation of the Ca channel in the guinea-pig heart. Pflügers Archiv. 1985;405:285-93.

[193] Grushin K, Nenov M, Dynnik V, Semushina S, Pakhomova I, Murashev A, et al. Role of the NO-cGMP cascade in regulation of L-type Ca2+ currents in isolated cardiomyocytes. Biochemistry (Moscow) Supplement Series A: Membrane and Cell Biology. 2008;2:243-52.

[194] Abi‐Gerges N, Fischmeister R, Méry PF. G protein‐mediated inhibitory effect of a nitric oxide donor on the L‐type Ca2+ current in rat ventricular myocytes. The Journal of Physiology. 2001;531:117-30.

[195] Best JM, Kamp TJ. Different subcellular populations of L-type Ca²⁺ channels exhibit unique regulation and functional roles in cardiomyocytes. Journal of molecular and cellular cardiology.52:376-87.

[196] Levi RC, Alloatti G, Penna C, Gallo MP. Guanylate-cyclase-mediated inhibition of cardiac I Ca by carbachol and sodium nitroprusside. Pflügers Archiv. 1994;426:419-26.

[197] Shirayama T, Pappano AJ. Biphasic effects of intrapipette cyclic guanosine monophosphate on L-type calcium current and contraction of guinea pig ventricular myocytes. Journal of Pharmacology and Experimental Therapeutics. 1996;279:1274-81.

[198] Mubagwa K, Shirayama T, Moreau M, Pappano A. Effects of PDE inhibitors and carbachol on the L-type Ca current in guinea pig ventricular myocytes. American Journal of Physiology-Heart and Circulatory Physiology. 1993;265:H1353-H63.

[199] Imai Y, Jiang B, Pappano AJ. Mechanism for muscarinic inhibition of ICa (L) is determined by the path for elevating cyclic AMP in cardiac myocytes. Cardiovascular research. 2001;51:331-43.

[200] Levi RC, Alloatti G, Fischmeister R. Cyclic GMP regulates the Ca-channel current in guinea pig ventricular myocytes. Pflügers Archiv-European Journal of Physiology. 1989;413:685-7.

[201] Ziolo MT, Lewandowski SJ, Smith JM, Romano FD, Wahler GM. Inhibition of cyclic GMP hydrolysis with zaprinast reduces basal and cyclic AMP‐elevated L‐type calcium current in guinea‐pig ventricular myocytes. British Journal of Pharmacology. 2003;138:986-94.

[202] Kumar R, Namiki T, Joyner RW. Effects of cGMP on L-type calcium current of adult and newborn rabbit ventricular cells. Cardiovascular research. 1997;33:573-82.

[203] Ziolo MT, Harshbarger CH, Roycroft KE, Smith JM, Romano FD, Sondgeroth KL, et al. Myocytes isolated from rejecting transplanted rat hearts exhibit a nitric oxide-mediated reduction in the calcium current. Journal of molecular and cellular cardiology. 2001;33:1691-9.

[204] Haddad G, Sperelakis N, Bkaily G. Regulation of the calcium slow channel by cyclic GMP dependent protein kinase in chick heart cells. Mol Cell Biochem. 1995;148:89-94.

[205] Gallo MP, Ghigo D, Bosia A, Alloatti G, Costamagna C, Penna C, et al. Modulation of guinea-pig cardiac L-type calcium current by nitric oxide synthase inhibitors. The Journal of Physiology. 1998;506:639-51.

[206] Gallo MP, Malan D, Bedendi I, Biasin C, Alloatti G, Levi RC. Regulation of cardiac calcium current by NO and cGMP-modulating agents. Pflügers Archiv. 2001;441:621-8.

[207] Grushin K, Nenov M, Dynnik V, Semushina S, Pakhomova I, Murashev A, et al. Role of the NO-cGMP Cascade in the Regulation of L-type Ca2+ Current in Isolated Cardiomyocytes. BIOLOGICHESKIE MEMBRANY. 2008;25:377-87.

[208] Wang H, Kohr MJ, Traynham CJ, Ziolo MT. Phosphodiesterase 5 restricts NOS3/Soluble guanylate cyclase signaling to L-type Ca2+ current in cardiac myocytes. Journal of molecular and cellular cardiology. 2009;47:304-14.

[209] Wang H, Kohr MJ, Wheeler DG, Ziolo MT. Endothelial nitric oxide synthase decreases β-adrenergic responsiveness via inhibition of the L-type Ca2+ current2008.

[210] Kokubun S, Reuter H. Dihydropyridine derivatives prolong the open state of Ca channels in cultured cardiac cells. Proceedings of the National Academy of Sciences. 1984;81:4824-7.

[211] Zhao CY, Greenstein JL, Winslow RL. Mechanisms of Phosphodiesterase Interactions in Cardiac Cyclic Nucleotide Cross-Talk Signaling Network. 1st Annual Meeting of Biophysical Society of Canada. 2015:122.

[212] Houslay MD, Adams DR. PDE4 cAMP phosphodiesterases: modular enzymes that orchestrate signalling cross-talk, desensitization and compartmentalization. Biochemical Journal. 2003;370:1-18.

[213] Baillie GS. Compartmentalized signalling: spatial regulation of cAMP by the action of compartmentalized phosphodiesterases. FEBS journal. 2009;276:1790-9.

[214] Zaccolo M. Phosphodiesterases and compartmentalized cAMP signalling in the heart. European Journal of Cell Biology. 2006;85:693-7.

[215] Nikolaev VO, Bünemann M, Schmitteckert E, Lohse MJ, Engelhardt S. Cyclic AMP Imaging in Adult Cardiac Myocytes Reveals Far-Reaching β1-Adrenergic but Locally Confined β2-Adrenergic Receptor–Mediated Signaling. Circulation research. 2006;99:1084-91.

[216] Steinberg SF, Brunton LL. Compartmentation of G protein-coupled signaling pathways in cardiac myocytes. Annual Review of Pharmacology and Toxicology. 2001;41:751-73.

[217] Wong W, Scott JD. AKAP signalling complexes: focal points in space and time. Nat Rev Mol Cell Biol. 2004;5:959-70.

[218] Michel JJC, Scott JD. AKAP mediated signal transduction. Annual Review of Pharmacology and Toxicology. 2002;42:235-57.

[219] Oess S, Icking A, Fulton D, Govers R, Müller-Esterl W. Subcellular targeting and trafficking of nitric oxide synthases. Biochemical Journal. 2006;396:401-9.

[220] Zhang YH, Casadei B. Sub-cellular targeting of constitutive NOS in health and disease. Journal of molecular and cellular cardiology.52:341-50.

[221] Mika D, Leroy J, Vandecasteele G, Fischmeister R. PDEs create local domains of cAMP signaling. Journal of molecular and cellular cardiology.52:323-9.

[222] Catterall WA. Structure and regulation of voltage-gated Ca2+ channels. Annual review of cell and developmental biology. 2000;16:521-55.

[223] Josephson IR, Guia A, Lakatta EG, Lederer WJ, Stern MD. Ca2+ ‐ dependent components of inactivation of unitary cardiac L ‐ type Ca2+ channels. The Journal of Physiology. 2010;588:213-23.

[224] Ferreira G, Yi J, Ríos E, Shirokov R. Ion-dependent Inactivation of Barium Current through L-type Calcium Channels. The Journal of General Physiology. 1997;109:449-61.

[225] Limpitikul WB, Dick IE, Joshi-Mukherjee R, Overgaard MT, George Jr AL, Yue DT. Calmodulin mutations associated with long QT syndrome prevent inactivation of cardiac L-type Ca2 + currents and promote proarrhythmic behavior in ventricular myocytes. Journal of molecular and cellular cardiology. 2014;74:115-24.

[226] Shaw RM, Colecraft HM. L-type calcium channel targeting and local signalling in cardiac myocytes. Cardiovascular research. 2013;98:177-86.

[227] Saucerman JJ, Bers DM. Calmodulin binding proteins provide domains of local Ca²⁺ signaling in cardiac myocytes. Journal of molecular and cellular cardiology.52:312-6.

[228] Cannell MB, Kong CHT. Local control in cardiac excitation-contraction coupling. Journal of molecular and cellular cardiology.52:298-303.

[229] Tanskanen AJ, Greenstein JL, Chen A, Sun SX, Winslow RL. Protein geometry and placement in the cardiac dyad influence macroscopic properties of calcium-induced calcium release. Biophysical Journal. 2007;92:3379-96.

[230] Winslow RL, Rice J, Jafri S. Modeling the cellular basis of altered excitation–contraction coupling in heart failure. Progress in Biophysics and Molecular Biology. 1998;69:497-514.

[231] Bender AT, Beavo JA. Cyclic nucleotide phosphodiesterases: molecular regulation to clinical use. Pharmacological Reviews. 2006;58:488-520.

[232] Kass DA. Heart Failure: A PKGarious Balancing Act. Circulation. 2012:CIRCULATIONAHA. 112.124909.

[233] Gauthier LD, Greenstein JL, Winslow RL. Toward an integrative computational model of the guinea pig cardiac myocyte. Frontiers in physiology. 2012;3.

[234] Winslow RL, Trayanova N, Geman D, Miller MI. Computational medicine: translating models to clinical care. Science Translational Medicine. 2012;4:158rv11-rv11.

[235] Kuhn M. Cardiology: A big-hearted molecule. Nature. 2015;519:416-7.

[236] Amanfu RK, Saucerman JJ. Cardiac Models in Drug Discovery and Development: A Review. 2011;39:379-95.

[237] Winslow RL, Trayanova N, Geman D, Miller MI. Computational Medicine: Translating Models to Clinical Care. Science Translational Medicine. 2012;4:158rv11.

[238] Movsesian MA, Smith CJ, Krall J, Bristow MR, Manganiello VC. Sarcoplasmic reticulum-associated cyclic adenosine 5'-monophosphate phosphodiesterase activity in normal and failing human hearts. The Journal of Clinical Investigation. 1991;88:15-9.

[239] Wang P, Myers JG, Wu P, Cheewatrakoolpong B, Egan RW, Billah MM. Expression, Purification, and Characterization of Human cAMP-Specific Phosphodiesterase (PDE4) Subtypes A, B, C, and D. Biochemical and Biophysical Research Communications. 1997;234:320-4.

[240] Wu AY, Tang X-B, Martinez SE, Ikeda K, Beavo JA. Molecular Determinants for Cyclic Nucleotide Binding to the Regulatory Domains of Phosphodiesterase 2A. Journal of Biological Chemistry. 2004;279:37928-38.

[241] Jäger R, Schwede F, Genieser H-G, Koesling D, Russwurm M. Activation of PDE2 and PDE5 by specific GAF ligands: delayed activation of PDE5. British Journal of Pharmacology. 2010;161:1645-60.

[242] Hall CN, Garthwaite J. What is the real physiological NO concentration in vivo? Nitric Oxide. 2009;21:92-103.

[243] Iancu RV, Ramamurthy G, Warrier S, Nikolaev VO, Lohse MJ, Jones SW, et al. Cytoplasmic cAMP concentrations in intact cardiac myocytes. American Journal of Physiology-Cell Physiology. 2008;295:C414.

[244] Beavo J, Bechtel P, Krebs E. Activation of protein kinase by physiological concentrations of cyclic AMP. Proceedings of the National Academy of Sciences. 1974;71:3580-3.

[245] De Arcangelis V, Soto D, Xiang Y. Phosphodiesterase 4 and phosphatase 2A differentially regulate cAMP/protein kinase a signaling for cardiac myocyte contraction under stimulation of β1 adrenergic receptor. Molecular pharmacology. 2008;74:1453-62.

[246] Rich TC, Tonia ET, Rohan JG, Schaack J, Karpen JW. In vivo assessment of local phosphodiesterase activity using tailored cyclic nucleotide–gated channels as cAMP sensors. The Journal of General Physiology. 2001;118:63-78.

[247] Hohl CM, Li Q. Compartmentation of cAMP in adult canine ventricular myocytes. Relation to single-cell free Ca2+ transients. Circulation research. 1991;69:1369-79.

[248] MINNEMAN KP, HEGSTRAND LR, MOLINOFF PB. The pharmacological specificity of beta-1 and beta-2 adrenergic receptors in rat heart and lung in vitro. Molecular pharmacology. 1979;16:21-33.

[249] Lukowski R, Krieg T, Rybalkin SD, Beavo J, Hofmann F. Turning on cGMP-dependent pathways to treat cardiac dysfunctions: boom, bust, and beyond. Trends in Pharmacological Sciences. 2014;35:404-13.

[250] Mohan P, Brutsaert DL, Paulus WJ, Sys SU. Myocardial contractile response to nitric oxide and cGMP. Circulation. 1996;93:1223-9.

[251] Ono K, Trautwein W. Potentiation by cyclic GMP of beta-adrenergic effect on Ca2+ current in guinea-pig ventricular cells. The Journal of Physiology. 1991;443:387-404.

[252] Vandeput F, Wolda SL, Krall J, Hambleton R, Uher L, McCaw KN, et al. Cyclic Nucleotide Phosphodiesterase PDE1C1 in Human Cardiac Myocytes. Journal of Biological Chemistry. 2007;282:32749-57.

[253] Rosman GJ, Martins TJ, Sonnenburg WK, Beavo JA, Ferguson K, Loughney K. Isolation and characterization of human cDNAs encoding a cGMP-stimulated 3′,5′-cyclic nucleotide phosphodiesterase. Gene. 1997;191:89-95.

[254] Degerman E, Belfrage P, Manganiello VC. Structure, Localization, and Regulation of cGMP-inhibited Phosphodiesterase (PDE3). Journal of Biological Chemistry. 1997;272:6823-6.

[255] Brunkhorst D, der Leyen Hv, Meyer W, Nigbur R, Schmidt-Schumacher C, Scholz H. Relation of positive inotropic and chronotropic effects of pimobendan, UD-CG 212 Cl, milrinone and other phosphodiesterase inhibitors to phosphodiesterase III inhibition in guinea-pig heart. Naunyn-Schmiedeberg's Archives of Pharmacology. 1989;339:575-83.

[256] MacKenzie SJ, Houslay MD. Action of rolipram on specific PDE4 cAMP phosphodiesterase isoforms and on the phosphorylation of cAMP-response-element-binding

protein (CREB) and p38 mitogen-activated protein (MAP) kinase in U937 monocytic cells. Biochem J. 2000;347:571-8.

[257] Loughney K, Martins TJ, Harris EAS, Sadhu K, Hicks JB, Sonnenburg WK, et al. Isolation and Characterization of cDNAs Corresponding to Two Human Calcium, Calmodulin-regulated, 3′,5′-Cyclic Nucleotide Phosphodiesterases. Journal of Biological Chemistry. 1996;271:796-806.

[258] Pandit J, Forman MD, Fennell KF, Dillman KS, Menniti FS. Mechanism for the allosteric regulation of phosphodiesterase 2A deduced from the X-ray structure of a near full-length construct. Proceedings of the National Academy of Sciences. 2009;106:18225-30.

[259] Erneux C, Miot F, Van Haastert PJ, Jastorff B. The binding of cyclic nucleotide analogs to a purified cyclic GMP-stimulated phosphodiesterase from bovine adrenal tissue. J Cyclic Nucleotide Protein Phosphor Res. 1985;10:463-72.

[260] Manganiello VC, Tanaka T, Murashima S. Cyclic GMP-stimulated cyclic nucleotide phosphodiesterases. Cyclic nucleotide phosphodiesterases: Structure, regulation and drug action. 1990;2:61-85.

[261] Smith CJ, Vasta V, Degerman E, Belfrage P, Manganiello V. Hormone-sensitive cyclic GMP-inhibited cyclic AMP phosphodiesterase in rat adipocytes. Regulation of insulin-and cAMP-dependent activation by phosphorylation. Journal of Biological Chemistry. 1991;266:13385-90.

[262] Pyne N, Cooper M, Houslay M. Identification and characterization of both the cytosolic and particulate forms of cyclic GMP-stimulated cyclic AMP phosphodiesterase from rat liver. Biochem J. 1986;234:325-34.

[263] Lopez-Aparicio P, Rascon A, Manganiello VC, Karl-Erik A, Belfrage P, Degerman E. Insulin induced phosphorylation and activation of the cGMP-inhibited cAMP phosphodiesterase in human platelets. Biochemical and Biophysical Research Communications. 1992;186:517-23.

[264] Macphee C, Reifsnyder D, Moore T, Lerea K, Beavo J. Phosphorylation results in activation of a cAMP phosphodiesterase in human platelets. Journal of Biological Chemistry. 1988;263:10353-8.

[265] Rascón A, Lindgren S, Stavenow L, Belfrage P, Andersson K-E, Manganiello VC, et al. Purification and properties of the cGMP-inhibited cAMP phosphodiesterase from bovine aortic smooth muscle. Biochimica et Biophysica Acta (BBA)-Molecular Cell Research. 1992;1134:149-56.

[266] Harrison SA, Reifsnyder DH, Gallis B, Cadd GG, Beavo JA. Isolation and characterization of bovine cardiac muscle cGMP-inhibited phosphodiesterase: a receptor for new cardiotonic drugs. Molecular pharmacology. 1986;29:506-14.

[267] Rochais F, Vandecasteele G, Lefebvre F, Lugnier C, Lum H, Mazet J-L, et al. Negative Feedback Exerted by cAMP-dependent Protein Kinase and cAMP Phosphodiesterase on Subsarcolemmal cAMP Signals in Intact Cardiac Myocytes: AN IN VIVO STUDY USING ADENOVIRUS-MEDIATED EXPRESSION OF CNG CHANNELS. Journal of Biological Chemistry. 2004;279:52095-105.

[268] Ahmad F, Shen W, Vandeput F, Szabo-Fresnais N, Krall J, Degerman E, et al. Regulation of sarcoplasmic reticulum Ca2+ ATPase 2 (SERCA2) activity by phosphodiesterase 3A (PDE3A) in human myocardium: phosphorylation-dependent interaction of PDE3A1 with SERCA2. J Biol Chem. 2015;290:6763-76.

[269] Vandecasteele G, Rochais F, Abi-Gerges A, Fischmeister R. Functional localization of cAMP signalling in cardiac myocytes. Biochemical Society Transactions. 2006;34:484-8.

[270] Houslay MD, Baillie GS, Maurice DH. cAMP-Specific Phosphodiesterase-4 Enzymes in the Cardiovascular System A Molecular Toolbox for Generating Compartmentalized cAMP Signaling. Circulation research. 2007;100:950-66.

[271] Houslay MD, Adams DR. PDE4 cAMP phosphodiesterases: modular enzymes that orchestrate signalling cross-talk, desensitization and compartmentalization. Biochem J. 2003;370:1-18.

[272] Dodge KL, Khouangsathiene S, Kapiloff MS, Mouton R, Hill EV, Houslay MD, et al. mAKAP assembles a protein kinase A/PDE4 phosphodiesterase cAMP signaling module. The EMBO journal. 2001;20:1921-30.

[273] Dodge-Kafka KL, Soughayer J, Pare GC, Michel JJC, Langeberg LK, Kapiloff MS, et al. The protein kinase A anchoring protein mAKAP coordinates two integrated cAMP effector pathways. Nature. 2005;437:574-8.

[274] Mika D, Richter W, Westenbroek RE, Catterall WA, Conti M. PDE4B mediates local feedback regulation of β1-adrenergic cAMP signaling in a sarcolemmal compartment of cardiac myocytes. Journal of Cell Science. 2014;127:1033-42.

[275] Kavdia M, Lewis RS. Nitric Oxide Delivery in Stagnant Systems via Nitric Oxide Donors: A Mathematical Model. Chemical Research in Toxicology. 2002;16:7-14.

[276] Denicola A, Souza JM, Radi R, Lissi E. Nitric oxide diffusion in membranes determined by fluorescence quenching. Archives of biochemistry and biophysics. 1996;328:208-12.

[277] McNutt NS. Ultrastructure of the myocardial sarcolemma. Circulation Research. 1975;37:1-13.

[278] Halvey EJ, Vernon J, Roy B, Garthwaite J. Mechanisms of activity-dependent plasticity in cellular nitric oxide-cGMP signaling. Journal of Biological Chemistry. 2009;284:25630-41.

[279] Francis SH, Bessay EP, Kotera J, Grimes KA, Liu L, Thompson WJ, et al. Phosphorylation of isolated human phosphodiesterase-5 regulatory domain induces an apparent conformational change and increases cGMP binding affinity. Journal of Biological Chemistry. 2002;277:47581-7.

[280] Corbin JD, Døskeland SO. Studies of two different intrachain cGMP-binding sites of cGMP-dependent protein kinase. Journal of Biological Chemistry. 1983;258:11391-7.

[281] Wolfe L, Francis SH, Landiss LR, Corbin JD. Interconvertible cGMP-free and cGMP-bound forms of cGMP-dependent protein kinase in mammalian tissues. Journal of Biological Chemistry. 1987;262:16906-13.

[282] Fink TL, Francis SH, Beasley A, Grimes KA, Corbin JD. Expression of an Active, Monomeric Catalytic Domain of the cGMP-binding cGMP-specific Phosphodiesterase (PDE5). Journal of Biological Chemistry. 1999;274:34613-20.

[283] Feil R, Lohmann SM, de Jonge H, Walter U, Hofmann F. Cyclic GMP-Dependent Protein Kinases and the Cardiovascular System: Insights From Genetically Modified Mice. Circulation Research. 2003;93:907-16.

[284] Francis SH, Corbin JD. Cyclic Nucleotide-Dependent Protein Kinases: Intracellular Receptors for cAMP and cGMP Action. Critical Reviews in Clinical Laboratory Sciences. 1999;36:275-328.

[285] Stuehr DJ, Griffith OW. Mammalian Nitric Oxide Synthases. Advances in Enzymology and Related Areas of Molecular Biology: John Wiley & Sons, Inc.; 2006. p. 287-346.

[286] Mullershausen F, Russwurm M, Koesling D, Friebe A. In vivo reconstitution of the negative feedback in nitric oxide/cGMP signaling: role of phosphodiesterase type 5 phosphorylation. Molecular biology of the cell. 2004;15:4023-30.

Appendix F. Curriculum Vitae

Educational History

Ph.D. expected	2016	Program in Biomedical Engineering Mentor: Raimond L. Winslow, Ph.D.	Johns Hopkins School of Medicine
B.S.	2009	Systems Design Engineering	University of Waterloo

Other Professional Experience

Team Member	2015	JHU Bootcamp for Technology Entrepreneurs
Participant	2013	GPU Computing Symposium and Workshop, NVIDIA
Team Member	2012	Johns Hopkins Biotech Business Case Competition
Participant	2010	Cardiology Rounds, JHU SOM
Participant	2010	Your Research Career Workshop, JHU SOM
Research Rotation	2009-2010	Lab of Dr. Jerry L. Prince, JHU
Participant	2009-2010	Research Integrity and Ethics, JHU SOM
Trainee	2009-2010	Medical School, JHU SOM
Quantitative Analyst	2007-2008	TD Asset Management (TDAM)
Research Assistant	2007	Lab of Dr. Ed Jernigan, University of Waterloo
Research Experimenter	2007	Northern Digital Inc. (NDI)
Research Technician	2006	Lab of Dr. Marshall Sussman, University Health Network/Mount Sinai Hospital (UHN/MSH)
Trend Analyst	2005	Research In Motion (RIM)

Quality Assurance Coordinator 2005 National Cash Register (NCR)

Scholarships/Fellowships

Natural Sciences and Engineering Research Council (NSERC) of Canada,

Post Graduate Scholarship – Doctoral (PGS-D), PGSD3-405041-2011

2011-2014, $63,000 CAD

Awarded through national competitions based on academic excellence, research potential, and communication, interpersonal and leadership abilities

Natural Sciences and Engineering Research Council (NSERC) of Canada

Alexander Graham Bell Canada Graduate Scholarship (CGS), CGS M-377616-2009

Post Graduate Scholarship (PGS) (granted in place of CGS for tenure outside of Canada). 2009, $17,500 CAD

Awarded through national competitions based on academic excellence, research potential, and communication, interpersonal and leadership abilities

Academic and other Honors

2015	Travel Award	Biophysical Society of Canada (BSC)
2015	Travel Award	Graduate Student Association, JHU SOM
2007	Undergraduate Student Research Award (USRA)	Natural Sciences and Engineering Research Council (NSERC) of Canada
2004-2009	Queen Elizabeth II Aiming for the Top	Ministry of Training, Colleges and Universities, ON, Canada

	Scholarship	
2004-2009	Dean's Honors List	University of Waterloo
2006	CVRD Inco Limited Award	University of Waterloo
2006	Outstanding Work Term Report	University of Waterloo
2006	Outstanding Work Term Report	University of Waterloo
2004	Alumni @ Microsoft Engineering Entrance Scholarship	University of Waterloo
2004	English Language Proficiency Prize	University of Waterloo
2004	Certificate of Distinction from the President	University of Waterloo

Publications

Zhao, CY, Greenstein, JL, Winslow, RL (2016) Mechanisms of the cyclic nucleotide cross-talk Signaling Network in Cardiac L-Type Calcium Channel Regulation. (In preparation).

Zhao, CY, Greenstein, JL, Winslow, RL (2016) Roles of phosphodiesterases in the regulation of the cardiac cyclic nucleotide cross-talk signaling network. J Mol. & Cell. Card. 91:215-27.

Zhao, CY, Greenstein, JL, Winslow, RL (2015) Interaction between phosphodiesterases in the regulation of the cardiac β-adrenergic pathway. J Mol. & Cell. Card. 88:29-38.

Andreisek, G., White, LM, Theodoropoulos, JS, Naraghi, A, Young, N, **Zhao, CY**, Mamisch, TC, Sussman, MS (2010) Synthetic-echo time post-processing technique

for generating images with variable T_2-weighted contrast: diagnosis of meniscal and cartilage abnormalities of the knee. Radiology 254 (1): 188-199.

Posters/Abstracts

Zhao, CY, Greenstein, JL, Winslow, RL (2016) Regulation of the cardiac L-type calcium channel by the cyclic nucleotide cross-talk signaling network. 60th Annual Meeting of Biophysical Society, Baltimore, MD, USA, March, 2016. (Abstract and Platform Presentation)

Zhao, CY, Greenstein, JL, Winslow, RL (2015) Mechanisms of phosphodiesterase interactions in cardiac cyclic nucleotide cross-talk signaling network. 1st Annual Meeting of Biophysical Society of Canada, Waterloo, ON, Canada, July, 2015. (Abstract and Poster)

Zhao, CY, Greenstein, JL, Winslow, RL (2014) Regulation of the β-Adrenergic pathway via cAMP-cGMP competition. 59th Annual Meeting of Biophysical Society, Baltimore, MD, USA, March, 2014. (Abstract and Poster)

Zhao, CY, Greenstein, JL, Winslow, RL (2014) Roles of phosphodiesterases in cyclic nucleotide cross-talk in cardiac myocytes. 59th Annual Meeting of Biophysical Society, Baltimore, MD, USA, March, 2014. (Abstract and Poster)

Zhao, CY, Chen, D, Carass, A, Chen, M, Bogovic, J, Prince, J (2010) A Java application for manually editing cortical label. Proc. 16th Annual International Conference on Human Brain Mapping, Barcelona, Spain. June, 2010. (Abstract and Poster)

Zhao, CY, Carass, A, Chen, M, Bogovic, J, Chen, D, Prince, J (2010) A protocol for manual correction of gyral-based cortical labels. Proc. 16th Annual International Conference on Human Brain Mapping, Barcelona, Spain, June, 2010. (Abstract and Poster)

Service and Leadership

2010-Present	Volunteer for community, departmental, and institutional events
2012-2013	Representative for Department of Biomedical Engineering, Graduate Representative Organization (GRO), JHU
2012	Teaching Assistant for Systems Bioengineering III (580.429)
2012	Teaching Assistant for Biological Models and Simulation (580.223)

Claire Yunzhu Zhao

Claire Yunzhu Zhao (née Yunzhu Zhao) was born on August 30th, 1986 in Beijing, China. After moving around worldwide in early childhood, her family left China again in 2000, this time, to Riverside, CA, USA. Equipped with little English and lots of guts, she began study at John W. North High School. After eight months, her family landed in Toronto, ON, Canada, where she completed high school at Jarvis Collegiate Institute. Claire's interests in mathematics, science and engineering led her to University of Waterloo, Waterloo, ON in 2004 for Systems Design Engineering with a focus in Statistics. Besides coursework, she was exposed to a variety of disciplines in her co-op experiences, from image analysis in University Health Networks (UHN), to R&D in special measurement systems at Northern Digital Inc. (NDI), to statistics analysis in TD Asset Management (TDAM), among others. These rewarding experiences encouraged Claire to pursue a Ph.D. in biomedical engineering at Johns Hopkins University (JHU), Baltimore, MD, USA, which she began after earning Bachelor's with Honors in 2009. During graduate school, she became involved with the Graduate Student Organization (GRO), serving as representative for the Department of Biomedical Engineering from 2012-2013. She is an active member in the JHU Ballet Program, ballroom clubs, and JHU Recreation, with additional involvements in other clubs. She also participated in community services and business competitions hosted by JHU. It was with the support of her loving parents and friends that Claire was able to persevere, in the midst of several challenges, a number of lab rotations, and a majority of first year of medical school, in her Ph.D. research on signal transduction via the cyclic nucleotide cross-talk signaling network in the cardiac myocyte.